Influence of Spatial Constraints in Non-crystalline Regions on the Polymer Dynamics in Semi-crystalline Polyethylene: a Solid State NMR Study

Dissertation
zur Erlangung des Grades

”Doktor der Naturwissenschaften”

am Fachbereich Chemie, Pharmazie und Geowissenschaften der
Johannes Gutenberg-Universität Mainz
vorgelegt von

Yefeng Yao
geboren in Jiangsu, P. R. China

Mainz 2007

To my family

Abstract

A broad variety of solid state NMR techniques were used to investigate the chain dynamics in several polyethylene (PE) samples, including ultrahigh molecular weight PEs (UHMW-PEs) and low molecular weight PEs (LMW-PEs). Via changing the processing history, i.e. melt/solution crystallization and drawing processes, these samples gain different morphologies, leading to different molecular dynamics.

Due to the long chain nature, the molecular dynamics of polyethylene can be distinguished in local fluctuation and long range motion. With the help of NMR these different kinds of molecular dynamics can be monitored separately. In this work the local chain dynamics in non-crystalline regions of polyethylene samples was investigated via measuring $^{1}H-^{13}C$ heteronuclear dipolar coupling and ^{13}C chemical shift anisotropy (CSA). By analyzing the motionally averaged $^{1}H-^{13}C$ heteronuclear dipolar coupling and ^{13}C CSA, the information about the local anisotropy and geometry of motion was obtained.

Taking advantage of the big difference of the ^{13}C T_1 relaxation time in crystalline and non-crystalline regions of PEs, the 1D ^{13}C MAS exchange experiment was used to investigate the cooperative chain motion between these regions. The different chain organizations in non-crystalline regions were used to explain the relationship between the local fluctuation and the long range motion of the samples.

In a simple manner the cooperative chain motion between crystalline and non-crystalline regions of PE results in the experimentally observed diffusive behavior of PE chain. The morphological influences on the diffusion

motion have been discussed. The morphological factors include lamellar thickness, chain organization in non-crystalline regions and chain entanglements. Thermodynamics of the diffusion motion in melt and solution crystallized UHMW-PEs is discussed, revealing entropy-controlled features of the chain diffusion in PE. This thermodynamic consideration explains the counterintuitive relationship between the local fluctuation and the long range motion of the samples. Using the chain diffusion coefficient, the rates of jump motion in crystals of the melt crystallized PE have been calculated. A concept of ”effective” jump motion has been proposed to explain the difference between the values derived from the chain diffusion coefficients and those in literatures.

The observations of this thesis give a clear demonstration of the strong relationship between the sample morphology and chain dynamics. The sample morphologies governed by the processing history lead to different spatial constraints for the molecular chains, leading to different features of the local and long range chain dynamics. The knowledge of the morphological influence on the microscopic chain motion has many implications in our understanding of the α-relaxation process in PE and the related phenomena such as crystal thickening, drawability of PE, the easy creep of PE fiber, etc.

Zusammenfassung

Im Rahmen der vorliegenden Arbeit wurden viele verschiedene Festkörper-NMR-Techniken verwendet, um die Kettendynamik verschiedener Polyethylenproben zu untersuchen. Durch Variation der thermischen Vorgeschichte chemisch identischer Proben, z.B. Schmelz- oder Lösungskristallisation und Verstreckung, können die Proben unterschiedliche Morphologien erhalten, welche die molekulare Dynamik der Kettenmoleküle bestimmt.

Aufgrund der Länge der Polymere können in Polyethylen lokale Fluktuationen einzelner Monomereinheiten von diffusiven Translatiosbewegungen unterschieden werden. Dies geschieht mit Hilfe von Festkörper-NMR-Experimenten, welche lokale Bewegungsprozesse in den nicht-kristallinen Bereichen der Polyethyleneproben durch Messungen der heteronuklearen dipolaren Kopplung (D_{IS}) zwischen direkt Benachbarten ^{1}H und ^{13}C Kernspins und der chemischen Verschiebungsanisotropie (CSA) der ^{13}C Kernspins in den CH_2 Gruppen des Polymers erfassen. Durch die Analyse der Bewegungsmittelung der beiden tensoriellen Größen (D_{IS} und CSA), kann die lokale Anisotropie molekularen Fluktuationen bestimmt sowie geometrische Information über die lokalen Bewegungsprozesse gewonnen werden.

Der große Unterschied der ^{13}C T_1 Relaxationszeiten in den kristallinen und nicht-kristallinen Bereichen der Probe ermöglicht die Beobachtung diffusiver kooperativer Translationsprozesse der Polyethylenketten durch einfache eindimensionale ^{13}C MAS Austauschexperimente. Das unterschiedliche Verhalten der lokalen Fluktuationen und der kooperativen Translationsbewegung lieferte dabei detaillierte Information über die morphologischen Unterschiede der Proben.

Die beobachtete Kettentranslation zwischen kristallinen und nicht-kristallinen Bereichen resultiert aus der kollektiven Bewegung des Polymers und lässt Rückschlüsse auf morphologische Größen wie Lamellendicke der Polyethylenkristallite, die Kettenorganisation in nicht-kristallinen Bereichen sowie die Verschlaufung der Polymerketten zu. Eine thermodynamische Betrachtung der Kettendiffusion in Schmelz- und lösungskristallisierten Polyethylenproben mit sehr hohem Molekulargewicht (UHMW-PE) zeigt entropisch bestimmte Aspekte der Kettendiffusion in Polyethylen auf. Die thermodynamische Betrachtung ist auch in der Lage die konterintuitive Relation zwischen lokalen Fluktuationen der Polymerketten in nicht-kristallinen Bereichen und

kooperativen Translationsbewegung zu erklären. Aus den ermittelten Diffusionskoeffizienten können Sprungraten für die Ketten in den Kristalliten berechnet werden, deren Diskrepanz zu Literaturwerten durch das Konzept von "effektiven" Sprüngen erklärt werden kann.

In dieser Arbeit konnte der direkte Zusammenhang zwischen der Morphologie semikristalliner Polymer und deren dynamischen Verhalten aufgezeigt werden. So werden durch eine unterschiedliche Prozessierungen eines Polymers unterschiedliche Morphologien erzeugt, welche aufgrund unterschiedlicher räumlicher Einschränkungen zu verschiedenen dynamischen Prozessen führt, was sich in einer Vielzahl von wichtigen Eigenschaften wie z.B. Langzeitstabilität oder Verstreckbarkeit manifestiert.

Abbreviations and Acronyms

1D	one dimensional
2D	one dimensional
ACQ	acquisition
AHT	average Hamiltonian theory
CP	cross polarization
CS	chemical shift
CSA	chemical shift anisotropy
CW	continuous wave
DD	dipolar decoupling
DQ	double quantum
DSC	differential scanning calorimetry
EX	exchange
ext	external
FID	free induction decay
FT	fourier transformation
int	internal
LAB	laboratory frame
LMW	low molecular weight
MAS	magic-angle spinning

MF	molecular frame
MQ	multiple-quantum
NMR	nuclear magnetic resonance
NOE	nuclear Overhauser effect
PAF	principal axes frame
PE	polyethylene
REDOR	rotational echo, double resonance
REREDOR	rotor encoded rotational echo, double resonance
RF	radio frequency
ROT	rotor frame
S/N	signal-to-noise
SAT	saturation
SAXS	small-angle X-ray scattering
sec	secular approximation
SP	single pulse
SUPER	separation of undistorted powder patterns by effortless recoupling
TEM	transmission electron microscopy
WAXD	wide-angle X-ray diffraction
UHMW	ultrahigh molecular weight

Contents

Motivation

Chain diffusion between crystalline and non-crystalline regions is an important dynamic process related to polymer crystal thickening, polymer melting, polymer drawing process and so on. In semi-crystalline polymers below the glass transition temperature, T_g, chain diffusion is strongly quenched. Increasing temperature above T_g, chain diffusion can take place between crystalline and non-crystalline regions below the melting point T_m of the crystalline regions. For linear polyethylenes, the mechanical relaxation measurements show that chain diffusion between crystalline and non-crystalline regions happens at the temperature $\sim 90^{\circ}C$, which is called the α-transition temperature of PE (Chapter 5, [Strobl 97]). The presence of chain diffusion in PEs gives a microscopic explanation for the mechanical α-process of PE.

The chain diffusion motion traverses between crystalline and non-crystalline regions. Hence, it requires cooperativity of the molecular motion between crystalline and non-crystalline regions. In polymer crystals, due to the restriction of the crystal lattice molecular chains often undergo a well defined motion. For polyethylene, it has been found that the chain units in the crystal can only perform a "helical jump", that is, the chain units undergo a 180° rotation with a translation by one CH_2 unit. The sites and angles involved in the jump motion are defined by the crystal lattice. Due to the chain connectivity, the sequential jump motions of individual units in the crystal then result in the translational movement of the whole crystalline stem along the crystallographic *c*-axis. Again, due to the chain connectivity, the chain movement in the crystallites will lead to the motion of the connected non-crystalline chain units, which consists of the non-crystalline portion of chain diffusion motion. However, to move a chain unit from non-crystalline regions into crystalline regions often involves changes in the non-crystalline regions like the change of chain conformations, which then lead to some energy/entropy barrier for the movement. Following this point, a question arises

whether or not chain diffusion can be facilitated via decreasing the energy/entropy barrier involved in this motion.

This question becomes of particular interest with respect to the morphological effect on the molecular dynamics of non-crystalline chains. The morphology of polymers usually depends on the chemical nature and the crystallization condition of the sample. For linear polyethylene, it has been found that different crystallization conditions can yield completely different sample morphologies. If crystallized from the melt, where the conditions are far from equilibrium, part of chains form thin plate-like lamellae and the rest form non-crystalline regions, which are usually described as a random coil. Whereas, if crystallized from a dilute solution, where the conditions are close to equilibrium, the polymer chains are known to form crystal lamellae by chain folding and the fold regions give rise to the non-crystalline regions. Compared to melt crystallized PE samples, the non-crystalline chains of a solution crystallized sample usually contain less entanglements but more local restriction, which most likely results from the chain folding structure, a point will be discussed in this thesis. However, the chain diffusion motion of solution crystallized samples seems to be facilitated by the chain folding structure, as indicated by the high drawability of the solution crystallized sample. The high drawability usually can not be observed in the melt crystallized sample. Since the drawability of PE is strongly related to the chain diffusion between crystalline and non-crystalline region [Hu 99b], the different morphologies and different drawability in the melt and solution crystallized PE samples thus give a implication about the morphological effect on the chain diffusion motion.

The aim of this thesis is to investigate the morphological effect on the chain diffusion in PEs by means of solid state NMR. As already mentioned above, the chain diffusion results from the sequential motion of individual chain units. The great advantage of NMR techniques is its capability to monitor these two kinds of molecular motions separately, even though both motions span a broad frequency range. Furthermore, solid state NMR can give detailed information about the motional features of individual chain unit, i.e. the frequency, the geometry. The latter is very useful in order to trace the spatial restriction of the chain units. With the knowledge of spatial restriction combined with the relevant chain diffusion behavior, the morphological effect on the chain diffusion can then be derived.

Chapter 1

Theoretical Basis of NMR

1.1 General introduction

The first nuclear magnetic resonance (NMR) phenomenon was reported independently by Bloch and Purcell [Bloch 46, Purcell 46], in 1946. Based on this phenomenon, NMR spectroscopy was developed. Since the resonance frequencies of nuclear spins are very sensitive to the chemical surrounding, NMR spectroscopy is mostly applied in the chemistry already shortly after the invention. However, throughout the first few decades, NMR spectroscopy utilized the technique known as the continuous-wave (CW), which is a time consuming way for the signal acquisition and usually suffers from poor signal-to-noise (S/N) ratio. A major breakthrough of NMR was achieved in 1970s. At that time people found that the initially used CW method could be replaced by the pulsed Fourier transform (FT) technique [Ernst 65, Ernst 66]. Via the pulsed FT technique a far better resolution and sensitivity in NMR spectra can be achieved. Furthermore, the pulsed FT technique gives one the opportunity to manipulate nearly arbitrarily the interactions and generate specific long-lived coherent states. These virtues originate the development of various modern NMR techniques, including two- or multi-dimensional spectroscopy and multiple quantum methods [Ernst 87].

In general, based on the states of sample NMR is roughly divided into solution NMR and solid state NMR. In contrast to solution NMR, where fast molecular random tumbling averages out all anisotropic interactions, solid state NMR always deals with the anisotropic interactions existing in solids, which usually give very strong line-broadening in the spectra. Hence, in order to obtain high resolution NMR spectra in

solids, the anisotropic interactions have to be ”removed”. Considering the formulae of the NMR interactions, removing the anisotropic interactions can be achieved either by manipulating the spatial part, which in fact is the basis of the magic angle spinning (MAS) technique, or by manipulating the spin part, which is the basis of all kinds of decoupling techniques, such as all multipulse techniques, high power heteronuclear decoupling, and so on. In solid state NMR practice these two kinds of manipulation are often combined to optimize the resolution. The achievement of high resolution solid state NMR spectra, however, results from a loss of information. The anisotropic interactions, although they seem to be hindrance of high resolution and good S/N, actually contain a lot of information on structure and dynamics of molecules. To avoid this penalty a lot of so-called recoupling methods have been developed in the last decades, which subtly combine the manipulations from sample rotation and RF pulses, providing the high resolution spectrum as well as the information of anisotropic interactions.

The NMR phenomenon and the mechanism behind have been well studied and covered in several classic NMR books [Abragam 61, Mehring 83, Schmidt-Rohr 94]. In this chapter a short overview of the basic NMR theory will be presented. We will focus our interest on the theoretical description of NMR interactions and how to manipulate them, which provides the basis for a better understanding of the NMR techniques given later. Afterwards a detailed analysis of two ”recoupling” pulse sequences will be given, which are the main techniques used for the investigations in this thesis.

1.2 Density operator and Liouville-von Neumann equation

In NMR, we deal with the dynamics of N coupled spins. In quantum mechanics, the state of spin can be fully described by the wave function $|\psi_{spin}\rangle$, which obeys the time-dependent Schrödinger equation:

$$\frac{d}{dt}|\psi_{spin}(t)\rangle = -\mathbf{i}\hat{H}_{spin}|\psi_{spin}(t)\rangle \tag{1.1}$$

where $\hat{H}_{spin}$ is called the nuclear spin Hamiltonian, containing all interactions related to the nuclear spin.

However, applying the time-dependent Schrödinger equation (Eq. 1.1) to a real spin system one has to deal with a great number of spins separately then combine the results to get a macroscopic property. This procedure works only in principle. To avoid this problem one can use the density operator method to describe the behavior of entire ensemble, without referring to the individual spin states. The density operator $\hat{\rho}$ is defined as:

$$\hat{\rho} = \overline{|\psi\rangle\langle\psi|} \tag{1.2}$$

where the overbar denotes an average over all ensemble members. The density operator $\hat{\rho}$ can be represented by the density matrix, with the matrix elements given by:

$$\rho_{ij} = \langle i|\hat{\rho}|j\rangle = \overline{c_i^* c_j} \tag{1.3}$$

where $|i\rangle$ denotes the eigenstate of the nuclear spin Hamiltonian. In this matrix the diagonal elements ρ_{ii} give the probability of the spin system occupying the state $|i\rangle$. The off-diagonal elements are the ensemble-averaged complex amplitudes of coherence, resulting from the superpositions of different eigenstates. The quantum order of these coherences depends on the change in the magnetic quantum number of the corresponding eigenstates.

With the help of density operator one can derive the Liouville-von Neumann equation:

$$\frac{d}{dt}\hat{\rho}(t) = -\mathbf{i}[\hat{H}_{spin}, \hat{\rho}(t)] \tag{1.4}$$

Its formal solution can be written:

$$\hat{\rho}(t) = \hat{U}(t)\hat{\rho}(0)\hat{U}^{\dagger}(t) \tag{1.5}$$

where $\hat{U}(t)$ is called the time evolution unity operator (or propagator):

$$\hat{U}(t) = \hat{T}e^{-\mathbf{i}\int_0^t \hat{H}_{spin}(t')dt'} \tag{1.6}$$

Here, $\hat{T}$ is the Dyson time-ordering operator. It defines a prescription for evaluating the exponential function in the case where the Hamiltonians do not commute at different time. For the time independent Hamiltonian, $\hat{T}$ can be skipped and Eq. (1.6) can be

written:

$$\hat{U}(t) = e^{-\mathrm{i}\hat{H}_{spin}t} \tag{1.7}$$

The expectation value of an observable operator $\hat{A}$ thus can be obtained by evaluating the trace of the product of the operator and density operator:

$$\langle \hat{A} \rangle_{\rho} = Tr[\hat{A} \cdot \hat{\rho}(t)] \tag{1.8}$$

Combining Eq. (1.5), (1.7) and (1.8), it's clear that the observation in NMR in fact is the result of the time evolution of spin interactions.

1.3 NMR interactions and spectra

The spin interactions in NMR can be roughly divided in external and internal ones. The external spin interactions include the Zeeman interaction and the interaction with radio frequency (RF) pulses. The internal spin interactions include the quadrupole interaction, chemical shift, dipole-dipole interaction and indirect spin-spin coupling (or J-coupling):

$$\hat{H}_{spin} = \underbrace{\hat{H}_z + \hat{H}_{RF}}_{\hat{H}_{ext}} + \underbrace{\hat{H}_Q + \hat{H}_{dd} + \hat{H}_{cs} + \hat{H}_J}_{\hat{H}_{int}} \tag{1.9}$$

In solid state NMR the J-coupling is usually very small. Therefore, the J-coupling will not be discussed in this thesis.

1.3.1 Tensor and internal NMR interaction

The Hamiltonian of internal spin interaction has a general form as:

$$\hat{H}_{int} = -\gamma\hbar\underline{\hat{I}} \cdot \underline{\underline{A_{loc}}} \cdot \underline{\hat{J}} \tag{1.10}$$

where $\underline{\underline{A_{loc}}}$ is a second rank tensor, which describes the orientation dependence of the internal spin interaction. $\underline{\hat{J}}$ is the ultimate source which interacts with $\underline{\hat{I}}$. For example, in the case of chemical shift $\underline{\hat{J}}$ is the external magnetic field $\underline{B_0}$; in the case of dipole-dipole coupling it is the another nuclear spin, and so on.

The tensor $\underline{\underline{A_{loc}}}$ can be described with a 3×3 matrix in Cartesian coordinate:

$$\underline{\underline{A}} = \begin{pmatrix} A_{11} & A_{12} & A_{13} \\ A_{21} & A_{22} & A_{23} \\ A_{31} & A_{32} & A_{33} \end{pmatrix} \tag{1.11}$$

The form of this matrix depends on the choice of the axis frame. It is possible to chose an axis frame where the matrix of $\underline{\underline{A}}$ is diagonalized. This axis frame is called the principal axis frame (PAF) of $\underline{\underline{A}}$. In this case, the tensor $\underline{\underline{A^{PAF}}}$ has a form as:

$$\underline{\underline{A^{PAF}}} = \begin{pmatrix} A_{11}^{PAF} & 0 & 0 \\ 0 & A_{22}^{PAF} & 0 \\ 0 & 0 & A_{33}^{PAF} \end{pmatrix} \tag{1.12}$$

The three numbers along the diagonal of the matrix are called the principal values of $\underline{\underline{A^{PAF}}}$, where A_{11}^{PAF} usually is the principal value associated with the principal frame x axis and the rest may be deduced by analogy. These three principle values are frequently expressed in terms of the isotropic value σ_{iso}, anisotropy δ, and asymmetry η. These three quantities are defined as follows:

$$\sigma_{iso} = \frac{1}{3}(A_{11}^{PAF} + A_{22}^{PAF} + A_{33}^{PAF}) \tag{1.13}$$

$$\delta = A_{33}^{PAF} - \sigma_{iso} \tag{1.14}$$

$$\eta = (A_{22}^{PAF} - A_{11}^{PAF})/A_{33}^{PAF} \tag{1.15}$$

When dealing with rotations in NMR, the irreducible spherical representation for the tensor is often chosen, which has a great advantage in describing the rotation of a tensor. The details of the transformation between Cartesian and irreducible spherical tensor representation have been summarized in Appendix (A). Here we give directly the irreducible spherical representation for the Hamiltonian of internal spin interaction:

$$\hat{H}_{int} = \underline{\underline{A_{loc}}} \cdot \underline{\underline{\hat{T}}} = \sum_{k=0}^{2} \sum_{q=-k}^{k} (-1)^q A_{kq} \hat{T}_{k-q} \tag{1.16}$$

where $\hat{T}_{k-q}$ is the component of irreducible spherical spin tensor operator with rank k and order $-q$. When dealing with the tensor rotation this irreducible spherical representation gives a great simplification, as shown in the later part of this chapter. However, in the following section various NMR interactions will be discussed using mainly the Cartesian tensor representation, since this representation is easy to read and understand.

1.3.2 Zeeman interaction and secular approximation

The Zeeman interaction is the strongest interaction in almost all NMR experiments. It is the interaction between a nuclear spin with $I \neq 0$ and an external static magnetic field, $\underline{B_0}$. Assuming the applied field is along z axis, the Hamiltonian of the Zeeman interaction $\hat{H}_z$ reads as:

$$\hat{H}_z = -\gamma\hbar\underline{\hat{I}} \cdot \underline{B_0} = -\gamma\hbar B_0 \hat{I}_z = \hbar\omega_L \hat{I}_z \tag{1.17}$$

Due to the operator $\hat{I}_z$, the Zeeman interaction causes an energy splitting in $2I+1$ energy levels. For a spin with $I = \frac{1}{2}$, two energy states occur in the magnet with the energies $E_{\frac{1}{2},\pm\frac{1}{2}} = \mp\frac{1}{2}\gamma\hbar B_0$. The energy difference between these two states then is $\Delta E = |\gamma\hbar B_0|$ and $\omega_L = -\gamma B_0$ is called the Larmor frequency. For instance, in a 11.7T magnetic field the Larmor frequency of ^{1}H is 500 MHz. Note that the sign of ω_L can be considered as the direction of spin precession.

The Zeeman interaction causes the so-called secular or high-field approximation. Almost in all NMR experiments $\hat{H}_z$ always is the dominating interaction. Therefore, all the internal interactions can be considered as a small perturbation of $\hat{H}_z$. From the perturbation theory, it is known that the energy of the perturbed system to the first order relates to the wave functions of the perturbed system to $0th$ order, and the $0th$-order wave functions of a perturbed system are simply the eigenfunctions of the dominant Hamiltonian. Suppose that the spin Hamiltonian $\hat{H}_{spin}$ has a form as:

$$\hat{H}_{spin} = \underbrace{\hat{H}_z}_{0th} + \underbrace{\hat{H}_{int}}_{1st} \tag{1.18}$$

Applying perturbation theory to $\hat{H}_{spin}$, the internal spin Hamiltonian $\hat{H}_{int}$ will be split into two parts, the secular part $\hat{H}'_{int}$, which commutes with $\hat{H}_z$, and the non-secular

part $\hat{H}''_{int}$, which does not commutes with $\hat{H}_z$. Since the non-secular part $\hat{H}''_{int}$ has no importance in determining the energy levels of the spin system, it can be neglected and Eq. (1.18) can be re-written as:

$$\hat{H}_{spin} \cong \hat{H}_z + \hat{H}'_{int} \tag{1.19}$$

The approximation inside Eq. (1.19) is the secular approximation. Based on this approximation the internal spin Hamiltonian in the irreducible spherical representation have a concise form as:

$$\hat{H}'_{int} = A_{00}\hat{T}_{00} + A_{10}\hat{T}_{10} + A_{20}\hat{T}_{20} \tag{1.20}$$

Comparison between Eq. (1.20) and Eq. (1.16) shows that all the non-secular terms with $m \neq 0$ have been left out. (However, it doesn't means that these non-secular terms have no effects on NMR. Actually, most of them are related to the relaxation process in NMR.) The part $A_{10}\hat{T}_{10}$ in Eq. (1.20) is antisymmetric and thus has no contribution in NMR. Therefore, it also can be left out [Mehring 83]. In the end after the secular approximation the internal spin Hamiltonian gains a very simple formula:

$$\hat{H}'_{int} = A_{00}\hat{T}_{00} + A_{20}\hat{T}_{20} \tag{1.21}$$

1.3.3 The effect of RF pulses and the rotating frame

In NMR the 'pulse' in fact is just a kind of electromagnetic radiation, generated by the radio frequency (RF) coil. Assuming that the RF coil is put in the x-y plane of the laboratory reference frame, where the z-axis is parallel to $\underline{B_0}$, one can write the Hamiltonian of the pulse with an amplitude $2B_{RF}$ as:

$$\hat{H}_{RF} = -2\gamma_I B_{RF} cos(\omega_{RF} t + \phi_p)\hat{I}_x \tag{1.22}$$

where ϕ_p is the phase of the pulse. For the simplification reason, we will assume $\phi_p = 0$ in the following discussion.

In order to see the effect of RF pulse one could do a frame transformation to get rid of the time dependence of the RF Hamiltonian in Eq. (1.22). First one could rewrite

Eq. (1.22) as (omitting the phase ϕ_p):

$$\hat{H}_{RF} = -\gamma_I B_{RF}(e^{-\omega_{RF}t} + e^{\omega_{RF}t})\hat{I}_x \tag{1.23}$$

Applying the frame transformation from the laboratory frame to the frame rotating at the Larmor frequency ω_L yields:

$$\hat{H}_{RF,R} = e^{\omega_L t} \cdot [-\gamma_I B_{RF}(e^{-\omega_{RF}t} + e^{\omega_{RF}t})\hat{I}_x] \tag{1.24}$$

If the RF frequency ω_{RF} is equal to the Larmor frequency ω_L, Eq. (1.24) can be simplified as:

$$\begin{aligned} \hat{H}_{RF,R} &= -\gamma_I B_{RF}\hat{I}_x - \gamma_I B_{RF} e^{2\omega_L t}\hat{I}_x & (1.25)\\ &\approx -\gamma_I B_{RF}\hat{I}_x & (1.26) \end{aligned}$$

The approximation from Eq. (1.25) to Eq. (1.26) is reasonable, because the second term in Eq. (1.25) oscillates at $2\omega_L$. Defining $\omega_{nut} = -\gamma_I B_{RF}$ as the nutation frequency of the RF field, the $\hat{H}_{RF,R}$ can be written as:

$$\hat{H}_{RF,R} = \omega_{nut}\hat{I}_x \tag{1.27}$$

The typical value of the nutation frequency $|\omega_{nut}/2\pi|$ is in the range 1-200 kHz, which is three to four orders of magnitude smaller than the Larmor frequency. However, compared with the internal spin interactions, this magnitude is strong enough to manipulate the internal spin interactions in NMR.

In the above discussion the concept of the rotating frame is introduced. The rotating frame in NMR usually denotes a frame rotating at the Larmor frequency, which is chosen to extract the time dependence of the Zeeman interaction. However, when one moves from the laboratory frame to the rotating frame, the spin interactions will change their formulae, since the rotating frame is not a frame of inertia. To get the formulae of the spin interactions in the rotating frame, one has to apply a frame transformation to the spin Hamiltonians. A formal treatment of the frame transformation is given in Appendix (B.2).

1.3.4 Chemical shift

Chemical shift represent the indirect interaction of the external magnetic field and the nuclear spins, through the influence of surrounding electrons. The mechanism of chemical shift is indicated in Fig. (1.1).

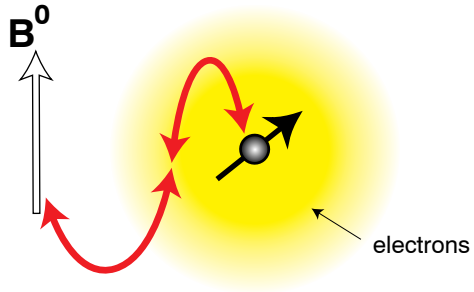

Figure 1.1: *The mechanism of chemical shift. When a sample is put into a magnetic field, the electrons that surround a nucleus will react to produce a secondary field, which will change the resonance frequency of the nuclear spin. The frequency change from this mechanism is chemical shift.*

Based on the mechanism above, the Hamiltonian of chemical shift can be written as:

$$\hat{H}_{cs} = \gamma\hbar\hat{\underline{I}}\cdot\underline{\underline{\sigma}}\cdot\underline{B_0} \tag{1.28}$$

where $\underline{B_0}$ is the external magnetic field and $\underline{\underline{\sigma}}$ is the chemical shielding tensor, which has the following form in its PAF:

$$\underline{\underline{\sigma}} = \sigma_{iso} + \Delta\cdot\begin{pmatrix} -\frac{1+\eta}{2} & 0 & 0 \\ 0 & -\frac{1-\eta}{2} & 0 \\ 0 & 0 & 1 \end{pmatrix} \tag{1.29}$$

The definitions of σ_{iso}, Δ and η follow that in Eq. (1.13), (1.14) and (1.15).

If the external magnetic filed $\underline{B_0}$ is much stronger than the chemical shift interaction, one could apply the secular approximation for the chemical shift interaction. Then the Hamiltonian of chemical shift in Eq. (1.28) gains the orientation dependence. Assuming that $\underline{B_0}$ has a direction along z-axis in the laboratory frame, $\hat{H}_{cs}$ can be expressed

as:

$$\hat{H}_{cs} = -\hbar\omega_L \left[\sigma_{iso} + \frac{1}{2}\Delta(3cos^2\theta - 1 - \eta sin^2\theta cos2\phi)\right]\hat{I}_z \tag{1.30}$$

where ω_L is equal to $-\gamma B_0$ and the polar angle $(\theta,\ \phi)$ defines the direction of $\underline{B_0}$ in PAF, as shown in Fig. (1.2).

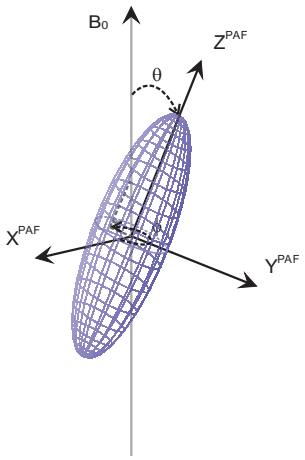

Figure 1.2: *The definition of the tensor orientation.* θ *is the angle between the z-axis of PAF and* $\underline{B_0}$. ϕ *is the angle between the x-axis of PAF and the projection of* $\underline{B_0}$ *in the x-y plane of PAF.*

According to Eq. (1.30), it is clear that the Hamiltonian of chemical shift consists of two parts. One is the isotropic part σ_{iso}, which has no orientation dependence. The other is the anisotropic part $\frac{1}{2}\Delta(3cos^2\theta - 1 - \eta sin^2\theta cos2\phi)$ and has an orientation dependence. The total frequency change due to the chemical shift, ω^*_{cs}, is the summation of these two parts:

$$\omega^*_{cs} = -\omega_L \left[\sigma_{iso} + \frac{1}{2}\Delta(3cos^2\theta - 1 - \eta sin^2\theta cos2\phi)\right] \tag{1.31}$$

It should be noted here that ω^*_{cs} actually is not the chemical shift appearing in NMR spectra. In NMR spectra the chemical shift δ (ppm) is a relative frequency shift, which is defined as:

$$\delta = \frac{\omega - \omega_{ref}}{\omega_{ref}} \cdot 10^6 = \frac{\sigma^{LAB}_{zz}(ref) - \sigma^{LAB}_{zz}}{1 - \sigma^{LAB}_{zz}(ref)} \cdot 10^6 \approx [\sigma^{LAB}_{zz}(ref) - \sigma^{LAB}_{zz}] \cdot 10^6 \tag{1.32}$$

where ω is the resonance frequency of the spin of interest and ω_{ref} is the resonance frequency of the same spin in the reference compound.

Therefore, with the definition in Eq. (1.32) the relative chemical shift ω_{cs} in NMR spectra has a formula as:

$$\omega_{cs} = \delta_{iso} + \frac{1}{2}\Delta_{cs}(3cos^2\theta - 1 - \eta_{cs}sin^2\theta cos2\phi) \tag{1.33}$$

where the isotropic part δ_{iso} is called the isotropic chemical shift and the anisotropic part $\frac{1}{2}\Delta_{cs}(3cos^2\theta - 1 - \eta_{cs}sin^2\theta cos2\phi)$ is called the chemical shift anisotropy (CSA). Comparing Eq. (1.31) with Eq. (1.33), the Larmor frequency ω_L disappears in Eq. (1.33), which means that the relative chemical shift ω_{cs} is independent of the external magnetic field.

1.3.5 Dipole-dipole interaction

The dipole-dipole interaction is also called the dipolar interaction or the dipolar coupling. Its origin is easy to visualize. Each nuclear spin is magnetic and generates a magnetic field, they can interact with each other through space, as shown in Fig. (1.3):

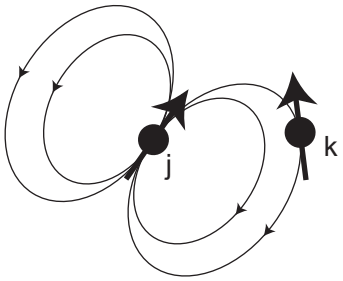

Figure 1.3: *Spin k interacts with spin j via the magnetic field generated by spin j.*

From Fig. (1.3) one can see that this interaction is directly through space, without involving the electron clouds. This situation is distinct from scalar (J) coupling, which is an indirect coupling of the nuclear spins via electron clouds.

One can write the expression for the Hamiltonian of the dipole-dipole interaction:

$$\hat{H}_{dd} = \underline{\hat{I}} \cdot \underline{\underline{D}} \cdot \underline{\hat{S}} \tag{1.34}$$

where the coupling tensor $\underline{\underline{D}}$ in its PAF has the symmetric form:

$$\underline{\underline{D}} = -2D \cdot \begin{pmatrix} -\frac{1}{2} & 0 & 0 \\ 0 & -\frac{1}{2} & 0 \\ 0 & 0 & 1 \end{pmatrix} \tag{1.35}$$

The prefactor 2 is from the normalization of the spin part and the coupling constant D is given by:

$$D = -\hbar \frac{\mu_0}{4\pi} \frac{1}{r^3} \gamma_I \gamma_S \tag{1.36}$$

where μ_0 denotes the vacuum permeability, γ_I and γ_S are the magnetogyric ratios of the spin I and S, and r is the distance between spins.

Constructing the Hamiltonian of dipole-dipole interaction in the laboratory frame with the z-direction defined by the external field $\underline{B_0}$, results a complicated formula as:

$$\begin{aligned} \hat{H}_{dd} &= -\hbar \frac{\mu_0}{4\pi} \gamma_I \gamma_S \left(\frac{\hat{\underline{I}} \cdot \hat{\underline{S}}}{r^3} - 3 \frac{(\hat{\underline{I}} \cdot \underline{r})(\hat{\underline{S}} \cdot \underline{r})}{r^5} \right) \\ &= -\hbar \frac{\mu_0}{4\pi} \frac{1}{r^3} \gamma_I \gamma_S \left(A + B + C + D + E + F \right) \end{aligned} \tag{1.37}$$

where the so-called dipolar alphabet is given by:

$$A = (3cos^2\theta - 1)\hat{I}_z\hat{S}_z \tag{1.38}$$

$$B = -\frac{1}{4}(3cos^2\theta - 1)(\hat{I}_+\hat{S}_- + \hat{I}_-\hat{S}_+) \tag{1.39}$$

$$C = -\frac{3}{2} sin\theta cos\theta e^{-\mathbf{i}\phi}(\hat{I}_z\hat{S}_+ + \hat{I}_+\hat{S}_z) \tag{1.40}$$

$$D = -\frac{3}{2} sin\theta cos\theta e^{+\mathbf{i}\phi}(\hat{I}_z\hat{S}_- + \hat{I}_-\hat{S}_z) \tag{1.41}$$

$$E = -\frac{3}{4} sin^2\theta e^{-2\mathbf{i}\phi}(\hat{I}_+\hat{S}_+) \tag{1.42}$$

$$F = -\frac{3}{4} sin^2\theta e^{+2\mathbf{i}\phi}(\hat{I}_-\hat{S}_-) \tag{1.43}$$

where $\underline{r}$ is the vector between the two spins and the polar angle $(\theta,\ \phi)$ are defined similarly as that in Fig. (1.2).

When a strong external magnetic field $\underline{B_0}$ is applied to the spin system, the formula of the dipole-dipole interaction in Eq. (1.37) is simplified because of the secular approximation. After this approximation, the term A and B are retained, since only these two terms commute with the Zeeman Hamiltonian. The term A always commutes with the Zeeman interaction, whereas the term B commutes only if the two spins cannot be distinguished. This results in the different formulae for homonuclear dipolar interaction and heteronuclear dipolar interaction:

Homonuclear dipolar interaction:

$$\begin{aligned} \hat{H}_{dd}^{homo} &= -\hbar\frac{\mu_0}{4\pi}\frac{1}{r^3}\gamma_I\gamma_I\,(A+B) \\ &= \hbar\omega_D\,[2\hat{I}_{1z}\hat{I}_{2z} - \frac{1}{2}(\hat{I}_{1+}\hat{I}_{2-} + \hat{I}_{1-}\hat{I}_{2+})] \end{aligned} \tag{1.44}$$

Heteronuclear dipolar interaction:

$$\begin{aligned} \hat{H}_{dd}^{hetero} &= -\hbar\frac{\mu_0}{4\pi}\frac{1}{r^3}\gamma_I\gamma_S\,(A) \\ &= \hbar\omega_D\,(2\hat{I}_z\hat{S}_z) \end{aligned} \tag{1.45}$$

where ω_D is given by:

$$\omega_D = \frac{D}{\hbar}\cdot\frac{1}{2}(3cos^2\theta - 1) \tag{1.46}$$

Because of the degeneration of the Zeeman states in the homonuclear case, the term B is still retained in the formula of homonuclear dipolar interaction. The following is an easy explanation for this. Assume that there is an isolated spin pair with the four Zeeman states $\alpha\alpha$, $\alpha\beta$, $\beta\alpha$ and $\beta\beta$. In the homonuclear case, one can easily find that $\alpha\beta$ and $\beta\alpha$ are degenerate. Therefore, any linear combination of $\alpha\beta$ and $\beta\alpha$ could also be an eigenstates of the Zeeman Hamiltonian. For instance, one can construct the two new Zeeman eigenstates as: $\frac{1}{\sqrt{2}}(\alpha\beta \pm \beta\alpha)$. With these two states one finds that the term B has the corresponding eigenvalues, which means that in this case the term B will give some contribution. One could relate the term B with the NMR phenomenon. Actually, the term B describes the so-called "flip-flop" mechanism of spin diffusion. For the heteronuclear case $\alpha\beta$ and $\beta\alpha$ normally are not degenerate. Therefore, the term

B always can be omitted safely in the heteronuclear case.

1.3.6 Quadrupolar interaction

All nuclei with a spin number $I > 1/2$ have a quadrupole interaction, which arises from the interaction of the electric quadrupole moment of nucleus with the gradient of its surrounding electric field at the position of the nucleus. From its definition the quadrupole interaction is an electrostatic interaction and has no relationship with NMR. Yet it can be shown that on deriving the Hamiltonian $\hat{H}_Q$ from quantum mechanics, the terms of spin operators will appear. The formula of quadrupolar interaction can be written as:

$$\hat{H}_Q = \frac{eQ}{2I(2I-1)\hbar}\underline{\hat{I}}\cdot\underline{\underline{V}}\cdot\underline{\hat{I}} \tag{1.47}$$

Here, eQ defines the electric quadrupole moment of nucleus, where e is the proton charge. $\underline{\underline{V}}$ is a second rank traceless tensor, describing the electric field gradient. It's element, $V_{\alpha,\beta}$ $(\alpha,\beta = x,y,z)$, is the gradient of α component of an electric field (E_x,E_y,E_z) in direction β. In its PAF $\underline{\underline{V}}$ is a diagonalized matrix representation, similar to chemical shift anisotropy. But it is important to note that the electric quadrupole interaction is related to the property of the nucleus and change less pronounced with the chemical environment of nucleus.

The strength of the quadrupole interaction varies in a great range. Sometimes the strength of the quadrupole interaction reaches a similar order as the Zeeman interaction. Therefore, it is not always possible to apply the secular approximation to simplify the formula of the quadrupole interaction in Eq. (1.47).

If the quadrupole interaction is much smaller than the Zeeman interaction, the secular approximation can still be used to discard many terms in $\hat{H}_Q$, which do not commute with $\hat{H}_z$. In this case, after the secular approximation the Hamiltonian of the quadrupole interaction has a formula as:

$$\hat{H}_Q = \frac{eQ}{4I(2I-1)\hbar}(eq_{zz}^{LAB})\,[3\hat{I}_z^2 - I\cdot(I+1)] \tag{1.48}$$

where eq_{zz}^{LAB} is the element of the field-gradient tensor $\underline{\underline{V}}$ in the lab frame.

In order to show a clear orientation dependence of $\hat{H}_Q$ in Eq. (1.48), one could define the quadrupole coupling constant, χ_Q, and the asymmetry parameter, η_Q:

$$\chi_Q = \frac{e^2 q_{zz}^{PAF} Q}{\hbar} \tag{1.49}$$

$$\eta_Q = \frac{q_{yy}^{PAF} - q_{xx}^{PAF}}{q_{zz}^{PAF}} \tag{1.50}$$

where the three $q_{\alpha\alpha}^{PAF}$ are the three principle values of $\underline{\underline{V}}$.

Then $\hat{H}_Q$ could be written as:

$$\hat{H}_Q = \omega_Q \left[3\hat{I}_z^2 - I \cdot (I+1)\right] \tag{1.51}$$

with ω_Q defined as:

$$\omega_Q = \frac{\chi_Q}{4I(2I-1)\hbar} \frac{1}{2}(3cos^2\theta - 1 - \eta_Q \, sin^2\theta \, cos2\phi) \tag{1.52}$$

Again, (θ, ϕ) are the polar angles of $\underline{B_0}$ in the PAF of the tensor $\underline{\underline{V}}$.

1.3.7 Spin evolution and NMR spectra

After the introduction of NMR interactions, one can consider how the spins evolve under these interactions. First one has to define the initial state of the spin system. Generally, the initial state of a spin system is the Boltzmann equilibrium state, which is described by:

$$\hat{\rho}(0) = e^{-\hbar\hat{H}/kT} \cong e^{-\hbar\hat{H}_z/kT} \cong 1 - \hbar\hat{H}_z/kT \tag{1.53}$$

Two approximations have be applied in Eq. (1.53). The first one is the secular approximation. The second one is the so-called high temperature approximation. But the name "high temperature" doesn't mean a real high temperature. Actually, this approximation applies very well, when the sample temperature is just higher than a fraction of one

Kelvin. Substituting $\hat{H}_z$ with $-\gamma B_0 \hat{I}_z$, one can write Eq. (1.53) in terms of operators:

$$\begin{aligned} \hat{\rho}(0) &= \hat{1} + \frac{\gamma\hbar B_0}{kT}\hat{I}_z \\ &\sim \frac{\gamma\hbar B_0}{kT}\hat{I}_z \end{aligned} \tag{1.54}$$

The unity operator $\hat{1}$ in Eq. (1.54) can be left out, since it commutes with any other operator and does not evolve in time. Therefore, in the end the initial state of spins I is proportional to the sum of their angular moment $\hat{I}_z$. The coefficient $\frac{\gamma\hbar B_0}{kT}$ tells the effect of the external magnetic field, the temperature and the type of the nuclear spin. In the following discussion this coefficient will be omitted for the simplification reason.

Consider the one pulse experiment shown in Fig. (1.4):

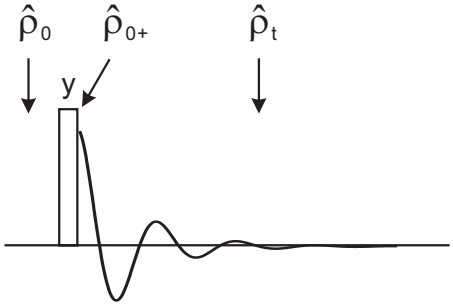

Figure 1.4: *A one pulse experiment.*

Starting from the equilibrium state $\hat{I}_z$, one applies a pulse along the y axis of rotating frame to the system. After this pulse the system gets a new state $\hat{\rho}(0+)$:

$$\hat{\rho}(0+) = \exp(-\mathbf{i}\omega_{nut} t \hat{I}_y)\hat{I}_z \exp(\mathbf{i}\omega_{nut} t \hat{I}_y) \tag{1.55}$$

This new state in fact results from a rotation of $\hat{I}_z$, through the angle $(\omega_{nut} t)$ about the y axis in the rotating frame. With the commutator relation $[\hat{I}_y, \hat{I}_z] = i\hat{I}_x$, one gets a explicit formula for the state after the RF pulse:

$$\hat{\rho}(0+) = \hat{I}_z cos(\omega_{nut} t) + \hat{I}_x sin(\omega_{nut} t) \tag{1.56}$$

If this pulse is a 90° pulse, i.e. $\omega_{nut} t = 90^\circ$, the new state $\hat{\rho}(0+)$ is:

$$\hat{\rho}(0+) = \hat{I}_x \tag{1.57}$$

This state $\hat{I}_x$ usually is called x-magnetization in the classical description. It will evolve under the Hamiltonian $\hat{H}$, giving another new state $\hat{\rho}(t)$:

$$\hat{\rho}(t) = \exp(-\mathbf{i}\hat{H}t)\hat{I}_x\exp(\mathbf{i}\hat{H}t) \tag{1.58}$$

The observed NMR signal $f(t)$ in the time domain then is obtained by taking the trace of $\hat{\rho}(t)$ with the observation operator $\hat{I}^+ = \hat{I}_x + \mathbf{i}\hat{I}_y$:

$$f(t) = Tr[\hat{\rho}(t)\cdot\hat{I}^+] \tag{1.59}$$

And the NMR spectrum $f(\omega)$ is via a Fourier transformation of $f(t)$:

$$f(\omega) = \mathbf{FT}[f(t)] = \mathbf{FT}\{Tr[\hat{\rho}(t)\cdot\hat{I}^+]\} \tag{1.60}$$

According to Eq. (1.59), only the component $\hat{I}_x$ or $\hat{I}_y$ in $\hat{\rho}(t)$ could give rise to an observable signal, which makes difference between the spin evolution under the Hamiltonian linear in $\hat{I}_z$, and the spin evolution under a Hamiltonian bilinear in $\hat{I}_z$. The interested reader is referred to Spiess book for the detail ([Schmidt-Rohr 94], p51).

1.3.8 Two-dimensional (2D) NMR spectroscopy

Up to now only one-dimensional (1D) NMR experiments have been considered. To extend NMR spectroscopy from 1D to 2D, one can introduce a second time variable before the data acquisition in the pulse sequence. An general scheme of 2D NMR experiment is shown in Fig. (1.5).

As shown in the above figure, a typical 2D NMR experiment consists of four periods: preparation, evolution, mixing and detection. The mixing time is not always necessary. The preparation period is to convert the spin system to the desired state for the first time evolution (t_1 time evolution). During the evolution time $t_1 = n\Delta$, the spin system evolves under some internal spin Hamiltonians. In the detection period the signal is detected for each increment of t_1 separately. Therefore, a 2D NMR signal $S(t_1,t_2)$ consists of a series of 1D NMR FIDs, each of which has a different phase factor gaining from the t_1 evolution. Double Fourier transformation of $S(t_1,t_2)$ leads to the 2D NMR spectrum $S(\omega_1,\omega_2)$.

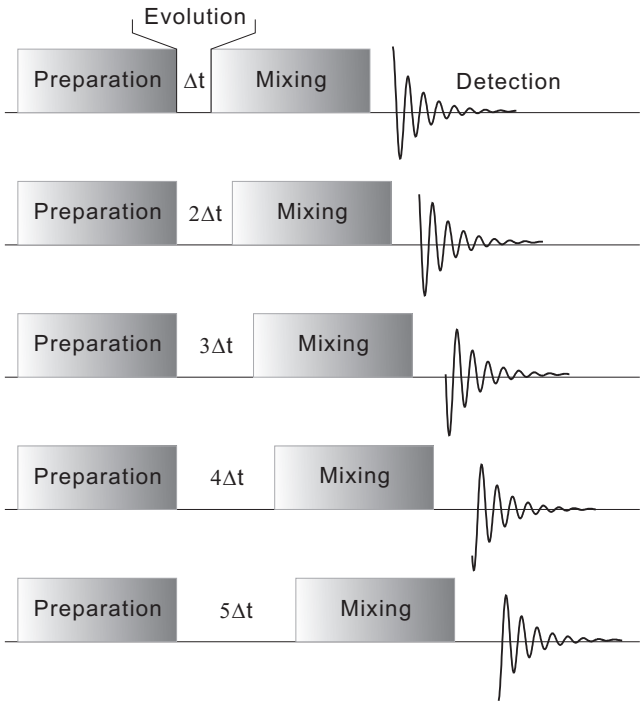

Figure 1.5: *The general scheme of 2D NMR experiment.*

2D NMR spectroscopy covers a huge part of NMR. Basically, it can be divided into three categories: separation experiments, correlation experiments and exchange experiments. Some good overview of these experiments can be found in Spiess book ([Schmidt-Rohr 94], Chapter 6) and Ernst book ([Ernst 87], Chapter 7-9).

1.4 Spin & space manipulations

In NMR people manipulates the NMR interactions or their components for various purposes. Such manipulations can be achieved by operating the spin part of Hamiltonian via RF pulses, or the spatial part via mechanical sample reorientation, or sometimes both at the same time. These three possible ways to manipulate NMR interactions make up of the following three subsections.

1.4.1 Spatial manipulation - magic angle spinning (MAS)

The Magic Angle Spinning (MAS) is a widely used technique in solid state NMR experiments. It operates with the spatial part of a Hamiltonian. The main purpose

of MAS is to achieve the high resolution NMR spectra in solids via removing the anisotropy of the interactions in static powder samples. (Note that the powder sample in NMR always means that the sample consists of many crystallites with random orientations.) Since spin interactions such as chemical shift anisotropy have an orientation dependence, a static powder sample gives broad resonance lines due to the different orientations of the crystallites. The mechanism for MAS to achieve the high resolution is based on the formulae of spin Hamiltonians, which often contain the second Legendre Polynomial $P(\theta) = \frac{1}{2}(3cos\theta^2 - 1)$. If the sample is rotated around an axis, which is tilted with respect to the external field $\underline{B_0}$ by the angle $\theta = 54.7°$, the anisotropy of interactions then is averaged to zero. And this angle $\theta = 54.7°$ is the so-called magic angle.

As described in Eq. (1.21), after the secular approximation the Hamiltonian of an interaction λ in the spherical tensor representation has a form as:

$$\hat{H}_\lambda = A_{00}^{\lambda,LAB}\ \hat{T}_{00} + A_{20}^{\lambda,LAB}\ \hat{T}_{20} \tag{1.61}$$

where the term $A_{00}^{\lambda,LAB}\ \hat{T}_{00}$ is a scalar, corresponding to the isotropic part of λ; the term $A_{20}^{\lambda,LAB}\ \hat{T}_{20}$ is the anisotropic part of λ, which spatial part $A_{20}^{\lambda,LAB}$ is modulated by MAS.

For a specific Hamiltonian it is convenient to take the additional normalization factors from the tensor algebra into account. So, one could have the following formulae for the NMR interactions:

Chemical shift anisotropy

$$\hat{H}_{csa} = \sqrt{\frac{3}{2}} A_{20}^{csa,LAB}\ \hat{T}_{20} \tag{1.62}$$

Dipole-dipole interactions

$$\hat{H}_{dd} = \sqrt{6} A_{20}^{dd,LAB}\ \hat{T}_{20} \tag{1.63}$$

Quadrupole interaction

$$\hat{H}_Q = \sqrt{6} A_{20}^{Q,LAB}\ \hat{T}_{20} \tag{1.64}$$

With these definitions the term $A_{20}^{\lambda,LAB}$ in the above formulae then corresponds to $\hbar \cdot \omega_\lambda$ (e.g. ω_{dd}, ω_Q) in the former discussion.

In order to see the effect of MAS, $A_{20}^{\lambda,LAB}$ needs to be analyzed. Since the interaction tensors are defined in their PAF, it is necessary to transform them to the LAB frame. This generally involves three subsequent rotation transformations given by sets of Euler angles, first from PAF to molecular frame (MF), second from MF to rotor frame (ROT) and finally from rotor frame to laboratory frame (LAB):

$$PAF \xrightarrow[\text{tensor orientation}]{(\alpha_{PC},\beta_{PC},\gamma_{PC})} MF \xrightarrow[\text{powder average}^1]{(\alpha_{MF},\beta_{MF},\gamma_{MF})} Rotor \xrightarrow[\text{MAS}]{(\alpha_{RL},\beta_M,0)} LAB$$

These sequential transformations are easy to carry out via the spherical tensor representation:

$$\begin{aligned} A_{20}^{\lambda,LAB}(t) = \sum_{m=-2}^{2} \left[\sum_{m'=-2}^{2} \left[\sum_{m''=-2}^{2} A_{2m''}^{\lambda,PAF} D_{m''m'}^{(2)}(\Omega_{PC}) \right] D_{m'm}^{(2)}(\Omega_{MF}) \right] \\ \times e^{-\mathbf{i}m\omega_R t} d_{m0}^{(2)}(\beta_M) \end{aligned} \tag{1.65}$$

The full treatment of Eq. (1.65), i.e. the three transformations, is necessary when more than one interaction is considered. Otherwise, a direct transformation from PAF to ROT frame and subsequently to LAB frame is sufficient. In this case, $A_{20}^{\lambda,LAB}(t)$ in Eq. (1.65) can be calculated with setting $\underline{\underline{\hat{A}_2^{\lambda,PAF}}} = \underline{\underline{\hat{A}_2^{\lambda,MF}}}$, leading to the following formula:

$$\begin{aligned} A_{20}^{\lambda,LAB}(t) =& C_1 cos(\gamma + \omega_R t) + C_2 cos(2\gamma + 2\omega_R t) \\ &+ S_1 sin(\gamma + \omega_R t) + S_2 sin(2\gamma + 2\omega_R t) \end{aligned} \tag{1.66}$$

[1] The detail about the powder average can be found in Appendix (E)

where the coefficients C and S (depending on $\delta_\lambda, \eta_\lambda, \alpha_{PAF}$ and β_{PAF}) are given by:

$$\begin{aligned}
C_1 &= -\frac{\delta_\lambda}{\sqrt{2}} sin2\beta_{PAF}(1+\frac{\eta_\lambda}{3}cos2\alpha_{PAF}) \\
C_2 &= \delta_\lambda\Big[\frac{1}{2}sin^2\beta_{PAF} - \frac{\eta_\lambda}{6}(1+cos^2\beta_{PAF})cos2\alpha_{PAF}\Big] \\
S_1 &= \delta_\lambda\eta_\lambda\frac{\sqrt{2}}{3}sin\beta_{PAF}sin2\alpha_{PAF} \\
S_2 &= \delta_\lambda\eta_\lambda\frac{1}{3}cos\beta_{PAF}sin2\alpha_{PAF}
\end{aligned} \tag{1.67}$$

When considering the modulation effect of MAS it is better to have the formulae of Hamiltonians where γ and $\omega_R t$ are separated:

$$\begin{aligned}
A_{20}^{\lambda,LAB}(t) =& \tilde{C}_1 cos(\omega_R t) + \tilde{C}_2 cos(2\omega_R t) \\
&+ \tilde{S}_1 sin(\omega_R t) + \tilde{S}_2 sin(2\omega_R t)
\end{aligned} \tag{1.68}$$

where

$$\begin{aligned}
\tilde{C}_1 &= C_1 cos\gamma + S_1 sin\gamma \\
\tilde{C}_2 &= C_2 cos2\gamma + S_2 sin2\gamma \\
\tilde{S}_1 &= S_1 cos\gamma - C_1 sin\gamma \\
\tilde{S}_2 &= S_2 cos2\gamma + C_2 sin2\gamma
\end{aligned} \tag{1.69}$$

With the formula of $A_{20}^{\lambda,LAB}(t)$ in Eq. (1.66), one can easily write down the averaged Hamiltonian of an interaction λ under MAS:

$$\begin{aligned}
\bar{\hat{H}}_{\lambda,MAS}(t) &= C_\lambda \hat{T}_{20}\,\frac{1}{t}\int_0^t A_{20}^{\lambda,LAB}(t')dt' \\
&= C_\lambda \hat{T}_{20}\,\frac{1}{t}\Phi_\lambda(t)
\end{aligned} \tag{1.70}$$

Note that the prefactor C_λ is added here, whose value depends on the type of the interaction. The isotropic part of $\hat{H}_\lambda$ ($A_{00}^{\lambda,LAB}\ \hat{T}_{00}$) is omitted in Eq. (1.70) since it is not modulated by MAS. The integral of $A_{20}^{\lambda,LAB}(t)$ of t then gives rise to $\Phi_\lambda(t)$, which

shows the phase accumulated from MAS. It is given by:

$$\begin{aligned}\Phi_\lambda(t) =& \frac{C_1}{\omega_R}\Big[sin(\gamma+\omega_R t)-sin\gamma\Big]+\frac{C_2}{2\omega_R}\Big[sin(2\gamma+2\omega_R t)-sin2\gamma\Big]\\ &-\frac{S_1}{\omega_R}\Big[cos(\gamma+\omega_R t)-cos\gamma\Big]-\frac{S_2}{2\omega_R}\Big[cos(2\gamma+2\omega_R t)-cos2\gamma\Big]\end{aligned} \tag{1.71}$$

From the formula of $\Phi_\lambda(t)$, it is easy to know that:

$$\Phi_\lambda|_t^{t+N\tau_R} = 0 \tag{1.72}$$

$$\Phi_\lambda|_{N\tau_R}^{N\tau_R+\frac{\tau_R}{2}} = -\Phi_\lambda|_{N\tau_R+\frac{\tau_R}{2}}^{N\tau_R+\tau_R} \tag{1.73}$$

Here, τ_R is the rotor period.

Eq. (1.72) shows that the acquired phase over N full rotor periods becomes zero, which indicates the averaging effect of MAS. Eq. (1.73) indicates that the acquired phase from the first half rotor period has a same value as that from the second half rotor period, but with the inverted sign, which is the basis of REDOR type recoupling techniques.

With the formula in Eq. (1.70), the evolution of $\hat{\rho}(0)=\hat{I}_x$ under an interaction λ under MAS is given by:

$$\hat{I}_x \xrightarrow{\bar{H}_{\lambda,MAS}(t)t} \hat{I}_x cos\Phi_\Lambda^* + \hat{W} sin\Phi_\Lambda^*,$$

where

$$\begin{aligned}\Phi_{cs}^* &= \omega_{iso}t+\Phi_{csa},\ \ \hat{W}=\hat{I}_y\\ \Phi_{dd}^{(IJ)^*} &= \frac{3}{2}\Phi_{dd,homo},\ \ \hat{I}_x=\hat{I}_x+\hat{J}_x,\ \ \hat{W}=2(\hat{I}_y\hat{J}_z+\hat{I}_z\hat{J}_y)\\ \Phi_{dd}^{(IS)^*} &= \Phi_{dd,hetero},\ \ \hat{W}=2\hat{I}_y\hat{S}_z\\ \Phi_Q^* &= 3\Phi_Q,\ \ \hat{W}=\mathbf{i}(\hat{T}_{21}+\hat{T}_{2-1}) \qquad \text{For} \quad I=1\end{aligned}$$

Note that the acquired phase angles Φ_Λ^* differ from the integrated phase Φ_λ due to the different spin parts $\hat{T}_{20}^\lambda$.

1.4.2 Spin manipulation - RF pulses

RF pulses also can be used to manipulate the spin part of Hamiltonian. The effect of RF pulses can be termed as "rotation in the spin space". To understand the effect of RF pulses the average Hamiltonian theory (AHT) is quite useful. The main point of AHT is to transform away the immediate action of RF pulses via introducing an interaction representation, where the effect of the spin interactions can be calculated to the first order as a simple average. The AHT gives an easy way to determine the net effect of RF pulses. The detail about the AHT will be discussed in Appendix (D). In the following the heteronuclear and homonuclear decoupling are described with the AHT, showing how RF pulses manipulate the spin part of Hamiltonian.

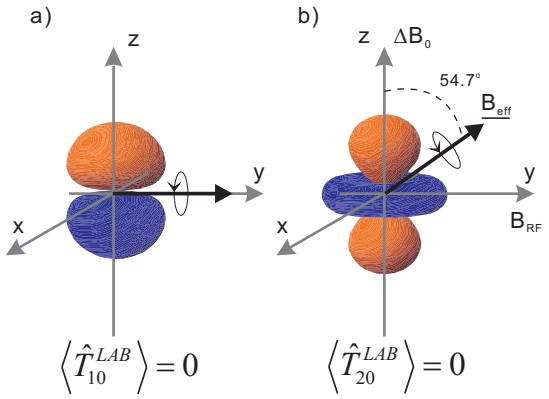

Figure 1.6: *Averaging of first* $(\hat{T}_{10})$*- and second* $(\hat{T}_{20})$*-rank spin operator tensors by continuous rotation around the effective field inclined at* $d_{00}^{(l)}(\beta_m) = 0$.

1.4.2.1 Heteronuclear decoupling

Heteronuclear decoupling is perhaps the simplest example for the rotation of the Hamiltonian in the spin space. Essentially, this decoupling can be considered as a rotation of the first-rank spherical tensor $\hat{T}_{10}$, as shown in Fig. (1.6a).

Assume that a strong RF pulse is applied on the spin I of IS spin system. Following the AHT, one needs a toggling frame which accounts for the RF field. If the RF field was applied along the y-direction of the rotating frame, the heteronuclear dipolar

Hamiltonian in the toggling frame then will have a formula as:

$$\hat{H}^{(IS)}_{dd,T} = \omega^{(IS)}_{dd}\ \hat{S}_z[\hat{I}_z cos(\omega_{RF}t) + \hat{I}_x sin(\omega_{RF}t)] \tag{1.74}$$

Seen from this frame, the operator $\hat{I}_z$ precesses from the z direction through x, $-z$ and $-x$, then back to z. So, the averaged heteronuclear dipolar Hamiltonian over integer precession periods $(n \cdot 2\pi)$ can be written as:

$$\bar{\hat{H}}^{(IS)}_{dd,T} = \omega^{(IS)}_{dd}\ \hat{S}_z \int_0^{n\cdot 2\pi} \frac{d(\omega_{RF}t)}{n\cdot 2\pi}[\hat{I}_z cos(\omega_{RF}t) + \hat{I}_x sin(\omega_{RF}t)] \tag{1.75}$$

It is obvious that $\bar{\hat{H}}^{(IS)}_{dd,T}$ vanishes over integer precession periods $(\omega_{RF}t_p = n\cdot 2\pi)$ and goes to zero for a long irradiation time, i.e. $n \to \infty \Rightarrow \frac{1}{n} \to 0$. It should be noted that, although Eq. (1.75) doesn't show the requirement for the strength of the RF field, to have a proper heteronuclear decoupling the strong RF field is still necessary, which actually is the precondition to make the average Hamiltonian approach in Eq. (1.75) justified. In solid state NMR practice the strength of the RF field must exceed not only the heteronuclear, but also the homonuclear dipolar coupling in order to make Eq. (1.75) justified.

1.4.2.2 Homonuclear decoupling – Lee-Goldburg experiment

Lee-Goldburg experiment [Lee 65] is a continuous version of the homonuclear decoupling via RF pulses. Since it averages the spin part of homonuclear dipolar coupling $\hat{T}_{20}$, which is analogous to $\hat{A}_{20}$ as could be averaged by MAS, Lee-Goldburg experiment can be visualized as "MAS" in the spin space, as shown in Fig. (1.6b).

The Hamiltonian of the homonuclear dipolar interaction can be written in the spherical tensor representation as:

$$\hat{H}^{(IJ)}_{dd} = \sqrt{6} A^{dd,LAB}_{20}\ \hat{T}^{LAB}_{20} \tag{1.76}$$

The spin part $\hat{T}_{20}$ is operated in Lee-Goldburg experiment. The resulting effect can be considered as the transformation of $\hat{T}^{LAB}_{20}$ to the frame rotating around the axis

$(\underline{e_y} cos\beta + \underline{e_z} sin\beta)$, which yields the formula of $\hat{T}_{20}^{T}$ as:

$$\begin{aligned}\hat{T}_{20}^{T} &= \sum_{m=-2}^{2} \hat{T}_{20}^{LAB} D_{0m}^{2}(0,\beta,\omega_{RF}t) \\ &= \hat{T}_{20}^{LAB} \Big\{ \frac{1}{2}(3cos^2\beta - 1) \\ &\quad - sin\beta\ cos\beta\ e^{-i\gamma} + sin\beta\ cos\beta\ e^{+i\gamma} \\ &\quad + sin^2\beta\ e^{-i2\gamma} + sin^2\beta\ e^{+i2\gamma} \Big\}\end{aligned} \tag{1.77}$$

where γ is the equal to $\omega_{RF}t$.

In Lee-Goldburg experiment, the angle β is set to 54.7°, the formula of $\hat{T}_{20}^{T}$ thus only contains the oscillation terms:

$$\hat{T}_{20}^{T} = \hat{T}_{20}^{LAB}\ [\sqrt{\frac{8}{9}}\ sin(\omega_{RF}t) + \frac{2}{3}\ cos(2\omega_{RF}t)] \tag{1.78}$$

So, one can write down the averaged Hamiltonian $\bar{\hat{H}}_{dd,T}^{(IJ)}$ over integer precession periods $(n \cdot 2\pi)$:

$$\begin{aligned}\bar{\hat{H}}_{dd,T}^{(IJ)} &= \sqrt{6}\, A_{20}^{dd,LAB}\ \bar{\hat{T}}_{20}^{T} \\ &= \sqrt{6}\, A_{20}^{dd,LAB}\ \hat{T}_{20}^{LAB} \int_{0}^{n\cdot 2\pi} \frac{d(\omega_{RF}t)}{n\cdot 2\pi} [\sqrt{\frac{8}{9}}\ sin(\omega_{RF}t) + \frac{2}{3}\ cos(2\omega_{RF}t)]\end{aligned} \tag{1.79}$$

Again, similar as the case of the heteronuclear decoupling, $\bar{\hat{H}}_{dd,T}^{(IJ)}$ vanishes for a long irradiation time or over integer precession periods. And to have a proper homonuclear decoupling the strength of the RF field has to be sufficiently strong to avoid the high order of the averaged Hamiltonian.

There are two ways to perform Lee-Goldburg experiment. One is to let the applied RF field have an offset from resonance by $\Delta\omega_{LG} = \sqrt{\frac{1}{2}}\ \omega_{RF}$. Then the effective magnetic field $\underline{B_{eff}}$ will have a direction along the magic angle with the strength $(\omega_{RF}^2 + \Delta\omega_{LG}^2)^{1/2}$. This is the basic principle of the "frequency-shifted LG" (FSLG) experiment. The second way is so-called "phase-modulated LG" (PMLG) [Vinogradov 99]. This achieves LG condition via introducing an additional phase modulation $(\omega_{PMLG}t)$

into the RF pulse. If $\omega_{PMLG} = \sqrt{\frac{1}{2}}\,\omega_{RF}$, then the effective field $\underline{B_{eff}}$ will be along the magic angle. Interested people can find the detail of PMLG in the reference [Vinogradov 99].

1.4.3 Combination of spin & space manipulations

In solid state NMR practice, the spin and space manipulations are usually combined together. A typical example is the cross-polarization (CP) experiment under MAS (the "CP/MAS" experiment), one of the most widely used techniques in solid state NMR. Based on the AHT a short discussion about the CP/MAS experiment will be given in the following section.

1.4.3.1 Cross-polarization under MAS (CP/MAS)

To observe the signals of the dilute spins, such as ^{13}C, ^{29}S$_{\mathrm{i}}$, one often meets the following two problems:
1. The low abundance of nuclei usually give a low signal-to-noise ratio.
2. The relaxation times of low abundance nuclei tend to be very long, which sometimes makes the observation nearly impossible.

Cross-polarization [Hartmann 62] is the technique, which can partially solve these problems and assist in obtaining a spectrum in a reasonable experimental time. The pulse sequence is shown in Fig. (1.7).

The first 90°_{y} pulse puts the ^{1}H magnetization along the x-direction of rotating frame. During the contact pulse, if the Hartmann-Hahn condition $\gamma_H B_1(^1\mathrm{H}) = \gamma_X B_1(\mathrm{X})$ matches, the magnetization then will be transfered from ^{1}H to X spins. The explanation of CP based on the AHT is given in the following.

During the contact pulse of CP experiment, the Hamiltonian acting on the ^{1}H-X spin system is:

$$\hat{H} = \hat{H}_z + \hat{H}_{dd}^{HH} + \hat{H}_{dd}^{HX} + \hat{H}_{RF}^{H} + \hat{H}_{RF}^{X} \tag{1.80}$$

$\hat{H}_z$ can be omitted by introducing the rotating frame. For simplification reasons, the offset and the chemical shift interaction are omitted too. Applying the AHT, one uti-

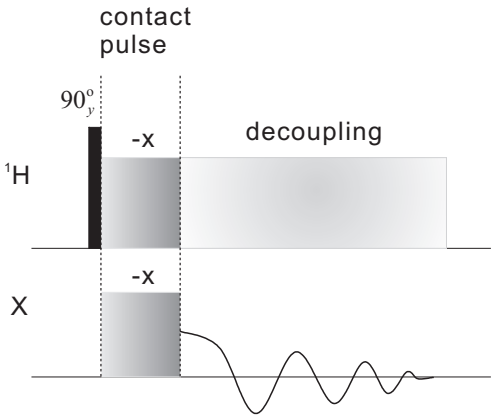

Figure 1.7: *The cross-polarization pulse sequence. The effect of this sequence is the transfer of the polarization from the abundant ^1H spins to X spins via ^1H-X dipole-dipole interaction.*

lizes a "toggling" frame to transform away the effects of the contact pulses:

$$\hat{H}_T = \hat{R}\,(\hat{H}_{dd}^{HH} + \hat{H}_{dd}^{HX})\,\hat{R}^{-1} \tag{1.81}$$

where $\hat{R}$ is given by:

$$\hat{R} = \exp(\mathbf{i}\omega_{RF}^{H} t \hat{I}_x^H)\exp(\mathbf{i}\omega_{RF}^{X} t \hat{I}_x^X) \tag{1.82}$$

In the "toggling" frame the averaged $\bar{\hat{H}}_{dd,T}^{HH}$ has a form as:

$$\begin{aligned}\bar{\hat{H}}_{dd,T}^{HH} &= \omega_{dd}^{H}\int_0^{n\cdot 2\pi}\frac{d(\omega_{RF}^{H}t)}{n\cdot 2\pi} \\ &\quad [3(\hat{I}_z cos\omega_{RF}^{H}t + \hat{I}_y sin\omega_{RF}^{H}t)(\hat{J}_z cos\omega_{RF}^{H}t + \hat{J}_y sin\omega_{RF}^{H}t) - \underline{\hat{I}}\cdot\underline{\hat{J}}\,] \\ &= \omega_{dd}^{H}(3\frac{1}{2}\hat{I}_z\hat{J}_z + 3\frac{1}{2}\hat{I}_y\hat{J}_y - \underline{\hat{I}}\cdot\underline{\hat{J}})\end{aligned} \tag{1.83}$$

With the magic zero condition (Chapter 2, [Schmidt-Rohr 94]), Eq. (1.83) can be written as:

$$\begin{aligned}\bar{\hat{H}}_{dd,T}^{HH} &= \frac{1}{2}(\hat{H}_z^{II} + \hat{H}_y^{II}) \\ &= -\frac{1}{2}\hat{H}_x^{II}\end{aligned} \tag{1.84}$$

where

$$\hat{H}_{\alpha}^{II} = 3\hat{I}_{\alpha}\hat{J}_{\alpha} - \underline{\hat{I}}\cdot\underline{\hat{J}} \tag{1.85}$$

According Eq. (1.84), during the contact pulse the homonuclear dipolar coupling of ^{1}H spins is retained with a scaled factor $-\frac{1}{2}$. Because $\hat{I}_x$ and $\hat{H}_x^{II}$ commute, $[\hat{H}_x^{II}, \hat{I}_x] = 0$, the remaining dipolar coupling will not dephase the magnetization along x-direction. This phenomenon is the so-called "spin lock". And the "locked" ^{1}H magnetization then plays a role as the reservoir for the polarization transfer.

In the toggling frame the heteronuclear dipolar coupling $\hat{H}_{dd}^{HX}$ has a formula as:

$$\begin{aligned}\hat{H}_{dd,T}^{HX} &= \omega_{dd}^{HX}\left[2(\hat{I}_z cos\omega_{RF}^{H}t + \hat{I}_y sin\omega_{RF}^{H}t)(\hat{S}_z cos\omega_{RF}^{X}t + \hat{S}_y sin\omega_{RF}^{X}t)\right] \\ &= \omega_{dd}^{HX}\Big[\underbrace{(\hat{I}_z\hat{S}_z + \hat{I}_y\hat{S}_y)cos(\omega_{RF}^{H} - \omega_{RF}^{X})t + (\hat{I}_y\hat{S}_z - \hat{I}_z\hat{S}_y)sin(\omega_{RF}^{H} - \omega_{RF}^{X})t}_{A} \\ &\quad + \underbrace{(\hat{I}_z\hat{S}_z - \hat{I}_y\hat{S}_y)cos(\omega_{RF}^{H} + \omega_{RF}^{X})t + (\hat{I}_y\hat{S}_z + \hat{I}_z\hat{S}_y)sin(\omega_{RF}^{H} + \omega_{RF}^{X})t}_{B}\Big]\end{aligned} \tag{1.86}$$

In NMR experiments the term A in Eq. (1.86) is usually to be chosen to get the Hartmann-Hahn match. And subsequently the term B becomes a high frequency oscillating which thus can be omitted. Therefore, under the Hartmann-Hahn condition $\hat{H}_{dd,T}^{HX}$ can be simplified as:

$$\begin{aligned}\hat{H}_{dd,T}^{HX} = \omega_{dd}^{HX}[&(\hat{I}_z\hat{S}_z + \hat{I}_y\hat{S}_y)cos(\omega_{RF}^{H} - \omega_{RF}^{X})t \\ &+ (\hat{I}_y\hat{S}_z - \hat{I}_z\hat{S}_y)sin(\omega_{RF}^{H} - \omega_{RF}^{X})t]\end{aligned} \tag{1.87}$$

In a static sample, when the Hartmann-Hahn condition matches, i.e. $\omega_{RF}^{H} = \omega_{RF}^{X}$, $\hat{H}_{dd,T}^{HX}$ becomes time-independent, resulting in a double resonance effect between ^{1}H and X spins. In the case of MAS the situation becomes complicated, because the sample spinning introduces time-dependence into ω_{dd}^{HX}. As shown in Eq. (1.65), under MAS ω_{dd}^{HX} has a modulated formula $\omega_{dd}^{HX}(t)$:

$$\omega_{dd}^{HX}(t) = C_1 cos(\gamma + \omega_R t) + C_2 cos(2\gamma + 2\omega_R t) \tag{1.88}$$

with $C_1 = -\frac{D}{\sqrt{2}} sin2\beta,\ C_2 = \frac{D}{2} sin^2\beta$. Here D is the heteronuclear dipolar coupling constant.

Therefore, under MAS $\hat{H}^{HX}_{dd,T}$ can be written as:

$$\begin{aligned}\hat{H}^{HX}_{dd,T} = &\left[C_1 cos(\gamma + \omega_R t) + C_2 cos(2\gamma + 2\omega_R t)\right] \\ &\cdot \left[(\hat{I}_z\hat{S}_z + \hat{I}_y\hat{S}_y) cos(\omega^H_{RF} - \omega^X_{RF})t + (\hat{I}_y\hat{S}_z - \hat{I}_z\hat{S}_y) sin(\omega^H_{RF} - \omega^X_{RF})t\right]\end{aligned} \tag{1.89}$$

In order to cancel the net oscillatory behaviour of $\hat{H}^{HX}_{dd,T}$, the match conditions changes to $(\omega^H_{RF} - \omega^X_{RF}) = \pm\omega_R$ or $\pm 2\omega_R$, the so-called sideband match conditions [Meier 92]. Whereas, the normal Hartmann-Hahn condition, i.e. $(\omega^H_{RF} - \omega^X_{RF}) = 0$, is not valid any more. Assuming the Hartmann-Hahn condition, $(\omega^H_{RF} - \omega^X_{RF}) = \omega_R$, is fulfilled, the MAS-averaged heteronuclear dipolar coupling $\bar{\hat{H}}^{HX}_{dd,T}$ can be written as:

$$\bar{\hat{H}}^{HX}_{dd,T} = \int_0^{n\cdot 2\pi} \hat{H}^{HX}_{dd,T} \frac{d(\omega_R t)}{n \cdot 2\pi} = \omega^{HX\ *}_{dd} (\hat{I}_z\hat{S}_z + \hat{I}_y\hat{S}_y) \tag{1.90}$$

with

$$\omega^{HX\ *}_{dd} = \frac{1}{2} C_1 cos\gamma = -\frac{D}{2\sqrt{2}} sin2\beta cos\gamma \tag{1.91}$$

Now one could consider how the polarization transfer between ^{1}H and X spins happens. Following the pulse sequence in Fig. (1.7), after the first 90°_y pulse the ^{1}H magnetization is along x-axis. Then during the contact pulses this magnetization evolves under $\bar{\hat{H}}^{HX}_{dd,T}$:

$$\begin{aligned}\rho(t) &= e^{-\mathbf{i}\bar{\hat{H}}^{HX}_{dd,T} t}\ \rho(0)\ e^{\mathbf{i}\bar{\hat{H}}^{HX}_{dd,T} t} \\ &= e^{-\mathbf{i}\omega^{HX\ *}_{dd} t(\hat{I}_z\hat{S}_z + \hat{I}_y\hat{S}_y)}\ \hat{I}_x\ e^{\mathbf{i}\omega^{HX\ *}_{dd} t(\hat{I}_z\hat{S}_z + \hat{I}_y\hat{S}_y)}\end{aligned} \tag{1.92}$$

Evaluating $\rho(t)$ with the Baker-Hausdorff relation ("time-evolution series") yields:

$$\rho(t) = \hat{I}_x \frac{1 + cos(\omega^{HX\ *}_{dd} t)}{2} + \hat{S}_x \frac{1 - cos(\omega^{HX\ *}_{dd} t)}{2} + (\hat{I}_y S_z - I_z S_y) sin(\omega^{HX\ *}_{dd} t) \tag{1.93}$$

The polarization transfer is clearly shown in Eq. (1.93), since $\hat{S}_x$ appears there. The oscillatory behaviour of $\hat{S}_x$, i.e. $\frac{1-cos(\omega^{HX\ *}_{dd} t)}{2}$, resulting from the restriction to isolated

spin pairs, can be observed in the Lee-Goldburg CP (LG-CP) experiment. However, this oscillatory behaviour usually is inconspicuous due to the destructive interference arising from the wide distribution of $\omega_{dd}^{HX\ *}t$ and can be smeared out completely by the homonuclear dipolar coupling which is not averaged out according Eq. (1.84). Note that during CP the prefactor of $\hat{I}_x$, $(\gamma_I B_0/kT)$, is also transferred to $\hat{S}_x$. It means that, comparing with the prefactor of $\hat{S}_x$, $(\gamma_S B_0/kT)$, resulting from a 90° pulse on equilibrium S magnetization, CP makes a signal enhancement γ_I/γ_S.

1.5 Recoupling techniques under MAS

As mentioned before, MAS provides an easy way to obtain high resolution NMR spectra in solids. However, this high resolution is achieved at the expense of eliminating anisotropic spin interactions, which may contain valuable information about molecular structures and dynamics. To avoid this penalty people have developed a lot of techniques, which retain the anisotropic spin interaction as well as the spectral resolution.

One category of these techniques is to manipulate the spatial part of Hamiltonians tactically. The slow MAS and off-magic-angle-spinning (OMAS) belong to this category. The slow MAS usually is applicable for the study of the inhomogeneous interactions, such as chemical shift anisotropy or dipolar coupling of isolated spin pairs. Because of the slow spinning speed, slow MAS spectra consist of the isotropic resonance line accompanied with rotational sidebands appearing at multiples of spin frequency ω_R. The analysis of the sideband intensities yields the information of the inhomogeneous interactions. The OMAS technique usually is to rotate the sample at an angle slightly different from the magic angle. Under OMAS the anisotropic part of the interactions is retained, but scaled down by a factor $\frac{1}{2}(3cos^2\theta_R - 1)$, where θ_R is the angle between rotation axis and the z-axis in the lab frame. Therefore, choosing a suitable spin angle θ_R and spin speed ω_R it is possible to keep the anisotropic resonance lines as well as gain a certain spectral resolution, since the width of anisotropic resonance lines is scaled down.

The second category of techniques is to manipulate the spin and spatial parts of Hamiltonians simultaneously, the so-called recoupling methods. In this case samples are still rotated at the magic angle, but the anisotropic interactions are selectively reintroduced

during certain time, via well-designed pulse scheme cancelling the refocusing effect of MAS. The recoupling methods under MAS are always designed as two dimensional experiments, where the first dimension gives the information of the selectively recoupled anisotropic interaction, whereas the second dimension supplies the high resolution spectrum. Therefore, the aim to have anisotropic spin interaction as well as the spectral resolution is fully achieved with the recoupling methods. Due to this virtue a great variety of recoupling methods have been invented since the last two decades. In the following the principle of recoupling methods under MAS as well as several typical pulse sequences will be discussed in detail.

1.5.1 Principles of recoupling method under MAS

As mentioned in the early part of this chapter, the secular part of the internal spin Hamiltonian has a general form as:

$$\hat{H}'_{int} = A_{00}\hat{T}_{00} + A_{20}\hat{T}_{20} \tag{1.94}$$

where the term $A_{00}\hat{T}_{00}$ is the isotropic part of the interaction and will not be modulated by MAS. The term $A_{20}\hat{T}_{20}$ represents the anisotropic part of the interaction. Because of the orientation dependence of A_{20}, this term is modulated by MAS. The various recoupling methods may choose different schemes to reintroduce different spin anisotropies, but the essential idea behind is similar, that is, synchronous modulation of the spin part $\hat{T}_{20}$ with RF pulses and spatial part A_{20} with MAS creates the net effect of selectively recoupling anisotropic interactions.

Considering the way how to modulate the spin part $\hat{T}_{20}$, various recoupling methods under MAS can be roughly divided to two subcategories. The first one is to modulate $\hat{T}_{20}$ using continuous RF pulses. It means that $\hat{T}_{20}$ and A_{20} are rotated continuously in their respective coordinates. The so-called CN_n^v and RN_n^v recoupling methods belong to this class. Since these CN_n^v and RN_n^v recoupling methods are not used in the work of this thesis, the interested reader is referred to the literature [Levitt 02].

The second one is to modulate $\hat{T}_{20}$ using rotor-synchronized $\delta-$pulses. In this case A_{20} still has a continuous rotation under the magic angle, but $\hat{T}_{20}$ is rotated or "hopped"

around the axis in the spin coordinate by the $\delta-$pulses. A simple example is the REDOR experiment, where the spin part $2\hat{I}_z\hat{S}_z$ changes its sign every half rotor period, as if $\hat{I}_z$ or $\hat{S}_z$ is hopped between their $\pm z$ axis. It should be noted that the recoupling methods mentioned above can be easily extended to the multiple-quantum (MQ) techniques under MAS. Actually the multiple-quantum (MQ) techniques can be considered as a homonuclear version of the recoupling methods.

The chemical shift anisotropy recoupling method - Separation of Undistorted Powder patterns by Effortless Recoupling (SUPER) [Liu 02] - was used in the work of this thesis, which however cannot be classified to any category of the above two recoupling methods. This SUPER experiment uses 360° recoupling pulses to cancel the refocusing effect of MAS at some specific time, which means that the spin part is only rotated continuously at certain time periods. Therefore, this recoupling method is more like a hybrid between the above two categories. Compared with the $\delta-$pulse based CSA recoupling methods, the big advantage of SUPER experiment is the accurate measurement of the asymmetry parameter η of CSA, which hence can supply a full CSA tensor information.

1.5.2 Recoupling pulse sequences

In this section a detailed discussion of two pulse sequences - Rotor-encoded REDOR (REREDOR) [Schnell 01b] and the CSA recoupling experiment (SUPER), will be presented. These two methods allow anisotropic interactions, such as dipolar interaction, CSA, to be measured in a selective and sensitive way. Before introducing REREDOR, the pulse sequence of rotational echo double resonance (REDOR) will be discussed, which actually is the basis of REREDOR.

1.5.2.1 Rotational echo double resonance (REDOR)

REDOR experiment is a ”classical” recoupling technique, which was introduced by Gullion and Schaefer [Gullion 89] for the detection of weak heteronuclear dipolar couplings. The main idea of REDOR is to use a series of well-spaced 180° pulses to prevent the averaging to zero of heteronuclear dipolar coupling by MAS. The pulse scheme of REDOR is given in Fig. (1.8).

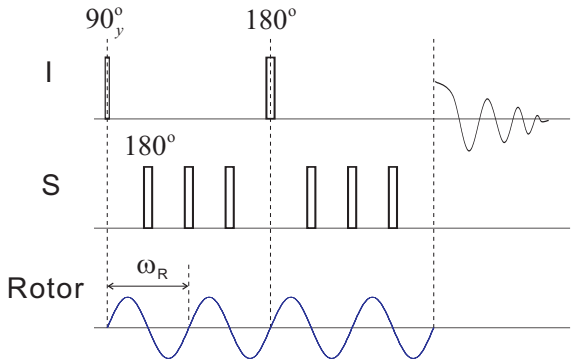

Figure 1.8: *The rotational-echo double resonance (REDOR) pulse sequence.*

Assuming that an isolated *IS* spin system is studied, the first y-pulse makes the magnetization of spin I along x-axis. Afterwards, the magnetization $\hat{I}_x$ is under control of $\hat{H}^I_{cs}$ and $\hat{H}^{IS}_{dd}$. $\hat{H}^I_{cs}$ is linear with $\hat{I}_z$ and will be refocused by the 180° of spin I (the resonance offset will be refocused by the same reason). Therefore, only $\hat{H}^{IS}_{dd}$ will take effects. Under MAS, the heteronuclear dipolar coupling $\hat{H}^{IS}_{dd}$ becomes time-dependent:

$$\hat{H}^{IS}_{dd}(t) = [C_1 cos(\gamma + \omega_R t) + C_2 cos(2\gamma + 2\omega_R t)] \cdot 2\hat{I}_z\hat{S}_z \tag{1.95}$$

with $\quad C_1 = -\frac{D}{\sqrt{2}} sin2\beta,\ C_2 = \frac{D}{2} sin^2\beta$

If one chooses the ω_R-recoupling scheme as shown in Fig. (1.8), the term $C_2 cos(2\gamma + 2\omega_R t)$, oscillating at $2\omega_R$, is still averaged out by MAS and the averaged Hamiltonian over one rotor period can be written as:

$$\begin{aligned} \bar{\hat{H}}^{IS}_{dd} &= \frac{1}{2\pi} \cdot 2 \int_0^{\pi} [C_1 cos(\gamma + \omega_R t)] d(\omega_R t) \cdot 2\hat{I}_z\hat{S}_z \\ &= \frac{\sqrt{2}D}{\pi} sin2\beta sin\gamma \cdot 2\hat{I}_z\hat{S}_z \end{aligned} \tag{1.96}$$

Therefore, during the recoupling period, the evolution of the magnetization can be described as:

$$\begin{aligned} \rho(t) &= e^{-i\bar{\hat{H}}^{IS}_{dd} t}\ \rho(0)\ e^{i\bar{\hat{H}}^{IS}_{dd} t} \\ &= e^{-i\omega^{IS}_{dd}{}^{*} t(2\hat{I}_z\hat{S}_z)}\ \hat{I}_x\ e^{i\omega^{IS}_{dd}{}^{*} t(2\hat{I}_z\hat{S}_z)} \end{aligned} \tag{1.97}$$

with

$$\omega_{dd}^{IS\,*} = \frac{\sqrt{2}D}{\pi} sin2\beta sin\gamma \tag{1.98}$$

Using the time-evolution series to evaluate $\rho(t)$ yields:

$$\rho(t) = \hat{I}_x cos\omega_{dd}^{IS\,*} t + 2\hat{I}_y\hat{S}_z sin\omega_{dd}^{IS\,*} t \tag{1.99}$$

where the time t has to be integral rotor periods, i.e. $t = n\tau_R$.

In the original version of REDOR experiment, to measure heteronuclear dipolar couplings two experiments have to be performed with I as the observed spin in both cases. One is the reference experiment, where the dipolar coupling between the IS spin pairs is refocused at the end of every rotor period, as a normal case under MAS. In the second experiment, this refocusing of the dipolar coupling is prevented by a series of rotor-synchronized 180° pulses applied to one of the spins (S in this case). So, after the recoupling period the magnetization $\hat{I}_x$ will gain a phase angle $\Delta\Phi = \omega_{dd}^{IS\,*} \cdot n\tau_R$, which consequently gives the signal intensity of spin I by a factor $cos\Delta\Phi$. Comparison of this intensity with that from the corresponding reference spectrum yields the value of the involving heteronuclear dipolar coupling.

1.5.2.2 Rotor-encoded REDOR (REREDOR)

Rotor-encoded REDOR experiment is based on the original REDOR scheme, which uses rotor-synchronized $\delta-$pulses to reintroduce heteronuclear dipolar coupling. Usually REREDOR experiment is a two dimensional experiment, where the direct dimension is a high resolution spectrum and the indirect dimension usually gives the information of heteronuclear dipolar coupling via the so-called sidebands patterns. The fast MAS usually is required for this experiment, providing a homonuclear decoupling to simplify the spin system as well as the resolution of the spectrum in the direct dimension. The REREDOR pulse sequence is shown in Fig. (1.9).
As depicted in the above figure, the pulse sequence of REREDOR consists of two REDOR blocks to recouple the heteronuclear dipolar coupling. The indirection dimension, t_1, is inserted after both two REDOR blocks. One purpose to insert the second t_1 time here is to refocus some interactions, which evolve during the t_1 time and gain a phase factor during that time. But this design works only for the interactions which

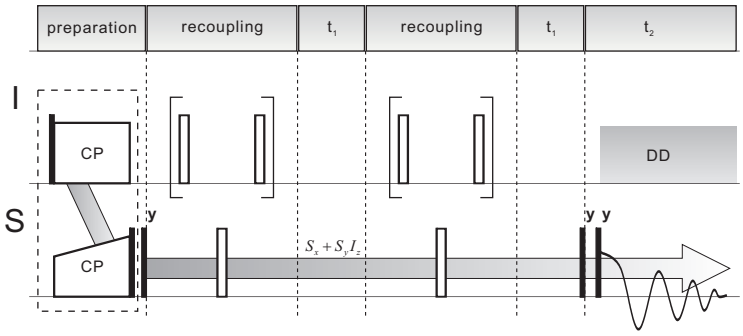

Figure 1.9: *The pulse sequence of CP-based Rotor-encoded REDOR (REREDOR).*

are not modulated by MAS, such as the offset and isotropic chemical shift.

During the preparation period, there usually are two ways to prepare the initial S magnetization. One is via the CP transfer, as shown in the above figure. The other is via the single pulse excitation, which can be done by simply removing the CP block, indicated by a rectangle plotted with dash line in Fig.(1.9).

In spite of the origin of the initial S magnetization, S magnetization will gain a phase factor Φ_1 after a recoupling (ω_R-recoupling) period $n\tau_R$. As mentioned in the section (1.5.2.1), this process can be described as:

$$\hat{S}_x \xrightarrow{\bar{\tilde{H}}_{dd}^{IS}} \hat{S}_x cos\Phi_1 + 2\hat{S}_y\hat{I}_z sin\Phi_1 \tag{1.100}$$

where

$$\bar{\tilde{H}}_{dd}^{IS} = \frac{\sqrt{2}D}{\pi} sin2\beta sin\gamma \cdot 2\hat{I}_z\hat{S}_z \tag{1.101}$$

$$\Phi_1 = \frac{\sqrt{2}D}{\pi} sin2\beta sin\gamma \cdot n\tau_R \tag{1.102}$$

After the first recoupling period, the first t_1 delay is inserted. During this time S magnetization will gain the second phase factor Φ_2:

$$\hat{S}_x cos\Phi_1 + 2\hat{S}_y\hat{I}_z sin\Phi_1 \xrightarrow{-\hat{H}_{dd}^{IS}(t)} \hat{S}_x cos(\Phi_1 - \Phi_2) + 2\hat{S}_y\hat{I}_z sin(\Phi_1 - \Phi_2) \tag{1.103}$$

where $\hat{H}_{dd}^{IS}(t)$ is the MAS modulated heteronuclear dipolar coupling, defined in Eq. (1.95)

and Φ_2 is the accumulated phase during p steps in the t_1 dimension:

$$\Phi_2 = \int_0^{p\cdot\Delta t_1} \hat{H}_{dd}^{IS}(t)dt \tag{1.104}$$

Here, Δt_1 is the increment step in the first dimension. For the generation of spinning sideband patterns, it usually is chosen as $\Delta t_1 = \tau_R/N$.

With the same procedure as above one can calculate the time evolution of the spin system under the action of the whole sequence $\{recoupling - t_1 - recoupling - t_1\}$:

$$\begin{aligned}\hat{S}_x \xrightarrow{\bar{H}_{dd}^{IS}} \xrightarrow{-\hat{H}_{dd}^{IS}(t)} \xrightarrow{-\bar{H}_{dd}^{IS\,\prime}} \xrightarrow{\hat{H}_{dd}^{IS}(t)} \; & \hat{S}_x cos(\Phi_1 - \Phi_2 - \Phi_3 + \Phi_4) \\ & + 2\hat{S}_y\hat{I}_z sin(\Phi_1 - \Phi_2 - \Phi_3 + \Phi_4)\end{aligned} \tag{1.105}$$

Note that $\bar{H}_{dd}^{IS\,\prime}$ is different with $\bar{H}_{dd}^{IS}$ because of the phase factor Φ_2 acquired from the first t_1 delay. By calculation, Φ_3 and Φ_4 are given as:

$$\Phi_3 = 2n\int_{p\Delta t_1}^{\tau_R/2 - p\Delta t_1} C_1 cos(\gamma + \omega_R t)dt \tag{1.106}$$

$$\Phi_4 = \int_{p\cdot\Delta t_1}^{2p\cdot\Delta t_1} \hat{H}_{dd}^{IS}(t)dt \tag{1.107}$$

And C_1 in Eq. (1.106) is equal to $(-\frac{\delta_\lambda}{\sqrt{2}} sin2\beta)$.

Therefore, the amplitude of the recoupled signal is then modulated according to:

$$S(t_1) \propto \langle cos(\Phi_1 - \Phi_2 - \Phi_3 + \Phi_4)\rangle \tag{1.108}$$

where $\langle\cdots\rangle$ denotes the powder average.

Considering the formulae of these phase factors $\Phi_n (n = 1-4)$, one could find the fact that the amplitude modulation of $S(t_1)$ originates only from the rotor spinning, hence is periodic with respect to the rotor period. Due to this periodic property, in principle one only needs to record one rotor period of signal to measure the dipolar coupling, which gives a great benefit to shorter the experiment time.

To extract the dipolar coupling information from $S(t_1)$, one could fit the experimental signal with the simulated one. Two ways can be chosen for the fitting process. One can fit the rotor modulated time signal $S(t_1)$ directly, or fit the sidebands pattern which is obtained from the Fourier transformation of $S(t_1)$. Both give the same results in principle. However, the Fourier transformation for one rotor period of $S(t_1)$ always gives a strong sinc cut-off wiggles. Therefore, practically one usually replicates the recorded signal and concatenates each other prior to the Fourier transformation. With this process the sinc wiggles can be suppressed greatly even without gaussian line-broadening. But one should be aware of that this process also brings some unwanted correlated noise, which may affect the final results.

1.5.2.3 Recoupling CSA – SUPER

SUPER (separation of undistorted powder patterns by effortless recoupling) is an experiment which can obtain undistorted CSA powder patterns under MAS. Unlike most other CSA recoupling pulse sequences, SUPER is insensitive to pulse length imperfections, has no special requirement for the hardware, and hence works well at standard power levels and spinning speeds. The pulse sequence is shown in Fig. (1.10).

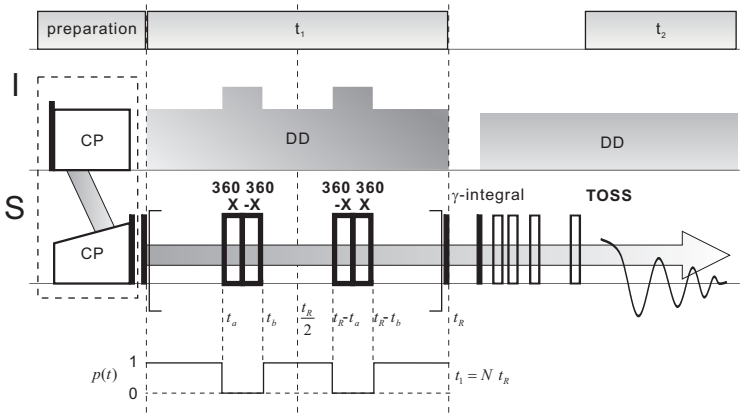

Figure 1.10: *The pulse sequence of SUPER experiment.*

During the preparation period, there are still two ways to create the initial S magnetization. One is via the CP transfer and the other is via the single pulse excitation. And simply removing the CP block, as indicated by a rectangle plotted with dash line in

Fig.(1.10), one switches from CP to single pulse excitation.

The design for the CSA recoupling in SUPER experiment is the 2π-pulse blocks in S channel, which sit symmetrically with respect to the half rotor period t_R, as shown in Fig. (1.10). Based on an assumption $\gamma_S B_{1,S} = \omega_S \gg \omega_R$, MAS modulation during the 2π pulses is negligible, and hence the chemical shift evolution during the 2π pulses is averaged to zero:

$$\bar{\hat{H}}_{cs,T} = \omega_{cs}(t_a)\frac{1}{2\pi}\int_0^{2\pi}[I_z cos(\omega_S t) + I_y cos(\omega_S t)]d(\omega_S t) = 0 \tag{1.109}$$

Due to the resulting "gaps" in the chemical shift evolution, the CSA will not be refocused after one rotor period, i.e., the CSA is recoupled. In order to derive the effective frequency during the recoupling period, one first could write down the time dependence of the CSA frequency under MAS:

$$\begin{aligned}\omega_{csa}(t) =& \tilde{C}_1 cos(\omega_R t) + \tilde{C}_2 cos(2\omega_R t) \\ &+ \tilde{S}_1 sin(\omega_R t) + \tilde{S}_2 cos(2\omega_R t)\end{aligned} \tag{1.110}$$

where $\tilde{C}_n$ and $\tilde{S}_n$ $(n = 1,2)$ are defined in Eq. (1.69). It is easy to know that in the static case $(\omega_R = 0)$:

$$\omega_{csa,stat} = \tilde{C}_1 + \tilde{C}_2 \tag{1.111}$$

With the symmetric design of the 2π-pulse blocks in SUPER experiment, an effective quasi-static anisotropic frequency $\bar{\omega}_{csa}$ can be calculated as:

$$\bar{\omega}_{csa} = \frac{1}{t_R}\int_0^{t_R} p(t)\cdot\omega_{csa}(t)dt \tag{1.112}$$

$$= \chi\cdot\omega_{csa,stat} \tag{1.113}$$

where $p(t) = 0$ when $t_a < t < t_b$ and $(t_R - t_b) < t < (t_R - t_a)$, otherwise $p(t) = 1$, as depicted in Fig. (1.10). And the scaling factor χ is given by:

$$\begin{aligned}&\chi = \frac{1}{t_R}\int_0^{t_R} p(t)\cdot cos(\omega_R t)dt = \frac{1}{t_R}\int_0^{t_R} p(t)\cdot cos(2\omega_R t)dt \\ \Longrightarrow\quad &\chi = \frac{1}{\pi}[sin(\omega_R t_a) - sin(\omega_R t_b)] = \frac{1}{2\pi}[sin(2\omega_R t_a) - sin(2\omega_R t_b)]\end{aligned} \tag{1.114}$$

With Eq. (1.114), one is able to find all the combinations of t_a, t_b and χ. However, as shown in Eq. (1.114) t_a is an implicit function of t_b, which make it inconvenient to search t_a, t_b and χ. In order to avoid this problem, the polynomial approximations of t_b and χ were proposed instead of the harmonics. The interested reader is referred to the literature [Liu 02] for the detail.

Taking into account the isotropic chemical shift as well as the resonance offset, they also get a scaling factor ξ during the recoupling time:

$$\xi = \frac{1}{t_R}\int_0^{t_R} p(t)dt = 1 - 2\frac{t_a - t_b}{t_R} \tag{1.115}$$

Therefore, one can write down the overall effective frequency $\bar{\omega}_1$ during the recoupled evolution period as:

$$\bar{\omega}_1 = \chi\ \omega_{csa,stat} + \xi\ \omega_{iso} \tag{1.116}$$

According to Eq. (1.116), the frequency in the first dimension includes not only the scaled CSA, but also the scaled isotropic chemical shift (combined with the resonance offset). The presence of the later one sometimes could cause a problem. In the case that the isotropic shift appears at the end of the spectral range of the first dimension, the powder patterns could be aliased [Liu 02]. If this case happens, one has to do a shearing procedure to get the proper CSA pattern. However, if the pattern is not aliased the shearing procedure is not necessary. Since the resonance offset is known, one can correct the obtain CSA pattern easily with the known offset term.

As shown in Fig. (1.10), a strong dipolar decoupling is applied on the I spin during the periods of 2π-pulse blocks in S channel. The reason is that, the 2π-pulse blocks could recouple the heteronuclear dipolar coupling too, if the applied RF fields in the two channels match each other, i.e., $\omega_I = \omega_S$. In this case, during the periods of 2π-pulse blocks, the averaged heteronuclear dipolar Hamiltonian can be written as:

$$\begin{aligned}\bar{\hat{H}}_{IS} &= 2\omega_{IS}(t_a)\ \frac{1}{2\pi}\int_0^{2\pi}[\hat{I}_z cos(\omega_S t) + \hat{I}_y sin(\omega_S t)] \\ &\qquad \cdot\ [\hat{S}_z cos(\omega_S t) + \hat{S}_y sin(\omega_S t)]d(\omega_S t) \\ &= \omega_{IS}(t_a)(\hat{I}_z\hat{S}_z + \hat{I}_y\hat{S}_y)\end{aligned} \tag{1.117}$$

This non-vanishing heteronuclear dipolar Hamiltonian will interfere the CSA evolution during the 2π-pulse blocks, resulting in distorted CSA patterns afterwards. Therefore, the sufficiently strong dipolar decoupling has to be applied during the recoupling pulses. In experiment practice, to average the heteronuclear dipolar coupling as well as get a good decoupling usually can be achieved by increasing the RF field on I as:

$$\omega_I = 2\omega_S \tag{1.118}$$

Since the strength of the 2π recoupling pulses is multiples of the rotor spinning frequency, the SUPER experiment is limited at a relatively low MAS frequencies. Hence, it is necessary to suppress MAS spinning sidebands. This is achieved via the four-pulse TOSS (total suppression of spinning sidebands) scheme before detection, as shown in Fig. (1.10). However, the TOSS scheme alone does not give a proper sideband suppression in two-dimensional MAS experiments. Due to this reason the γ-integral block is inserted before the TOSS, which can suppresses sidebands up to the fourth order. About the mechanism of γ-integral one can find the detail in literature [Eden 03].

Chapter 2

Molecular Dynamics and Related NMR Techniques

Solid state NMR provides powerful methods that allow detailed studies of molecular dynamics in a frequency range from *n*Hz to *n*MHz. Generally, fast dynamics (*n*MHz) can be characterized by NMR relaxation time measurements (Chapter 8, [Mehring 83]) and Chapter 5, [Slichter 90]); intermediate dynamics (*n*kHz) can be studied by monitoring dipolar coupling [Saalwachter 02, Schnell 01b] or lineshape analysis (Chapter 6, [Duer 04]); slow dynamics (*n* Hz) can be studied by so-called exchange experiment [Schmidt-Rohr 94].

The discussion in this chapter consists two parts. In the first part a short introduction of motional effects on the spin system will be given. In the second part, the concentration will be focused on the several NMR techniques used in the latter work of this thesis. These NMR techniques include dipolar coupling analysis, lineshape analysis and exchange experiment.

2.1 Motional effects on the spin system

As mentioned in the first chapter, the observed NMR phenomenon is the result of the time evolution of spin interaction. In order to understand the effects of the molecular motions on the spin system, therefore, one could think about motional effects on spin interactions.

2.1.1 Autocorrelation function and correlation time

Generally, dynamic processes can be distinguished as coherent ones or incoherent ones. The mechanical rotation of sample, such as MAS, is a coherent motion. Molecular motions are in general incoherent processes, which are best described by the autocorrelation function $G(\tau)$ [Levitt 01]:

$$G(\tau) = \overline{f(t)f(t+\tau)} \tag{2.1}$$

$f(t)$ denotes the time-dependent position (or orientation) of a molecule and the bar indicates the ensemble average over all the molecules.

$G(\tau)$ is a measure of molecular motions in a sample. The value of $G(\tau)$ depends on the similarity between $f(t)$ and $f(t+\tau)$, which is determined by the time scale of molecular motion. A fast molecular motion results in a big difference between $f(t)$ and $f(t+\tau)$, leading a small value for $G(\tau)$ after the ensemble average of $[f(t)f(t+\tau)]$ over all molecules in the sample. Whereas, a slow molecular motion, which causes less differences between $f(t)$ and $f(t+\tau)$, leads a big value for $G(\tau)$ after the ensemble average.

According to its definition (Eq. 2.1), $G(\tau)$ decays with increasing τ. Often, this decay is assumed to be exponential:

$$G(\tau) = \overline{f(t)^2}\,\exp\left(-\frac{\tau}{\tau_c}\right) \tag{2.2}$$

Here, τ_c is called the correlation time for molecular motion, which provides a value for the time scale of motion. The smaller τ_c, the faster the decay of $G(\tau)$, and the faster the molecular averaging. The inverse of correlation time τ_c^{-1} can be considered as a characteristic frequency of incoherent motion, which is quite useful when one needs to compare the time scale of a molecular motion with the strength of a specific spin interaction. It has to be noted here that τ_c^{-1} is in units of *radians per second*. To write it in units of *cycles per second* or Hz, one should multiply τ_c^{-1} with a factor of $1/2\pi$.

2.1.2 Motional effects on spin interactions

Although motional effects in NMR can be easily observed from experiments, the explanation of motional effects usually is not straightforward. In order to understand motional effects, the knowledge of the relationship between molecular motion and relevant interaction is required.

Generally, different spin interactions are sensitive to different molecular motions. When a motion has its characteristic frequency $\tau_c^{-1}/2\pi$ close to the strength of the spin interaction ω_λ, i.e. $\tau_c^{-1}/2\pi \sim |\omega_\lambda|$, this motion will give a strong modulation to the spin interaction. In other words, this interaction is very sensitive to the molecular motions in this frequency range. The comparison of the motional frequency $\tau_c^{-1}/2\pi$ with the strength of interaction gives a way to evaluate the motional effect on the interaction. By doing this comparison for various molecular motions and various spin interactions, the effects of motion on the spin dynamics are summarized by the following diagram (Fig.(2.1)):

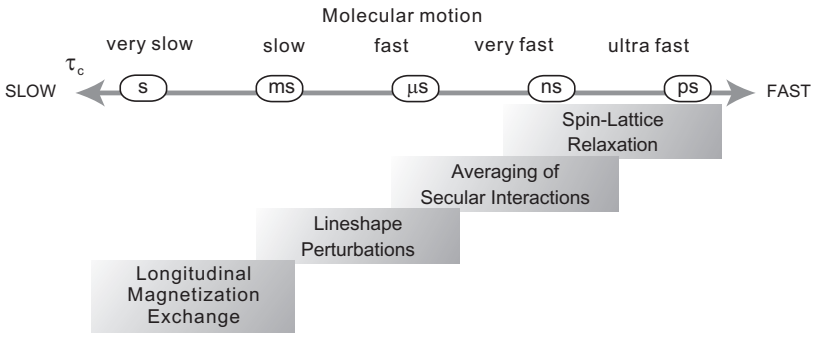

Figure 2.1: *The motional effects and their relevant timescales.*

- *Spin-lattice relaxation.* Very fast motions ($10^6 < \tau_c^{-1}/2\pi < 10^{10}$Hz) usually can induce the spin-lattice relaxation. The relevant spin interaction for the spin-lattice relaxation is the Zeeman interaction, which usually has a strength in the order of tenth to hundredth of MHz. Fast molecular motion in the Zeeman frequency range thus will induce fast fluctuations of the internal spin interactions, giving a strong modulation to Zeeman interaction and thus resulting in the spin-lattice relaxation.

- *Averaging of secular spin interaction*. When the frequency of molecular motion is bigger than the internal spin interaction but smaller than the Zeeman interaction, this kind of molecular motion usually gives a motionally averaged effect on secular parts of internal spin interactions. A typical example is the characteristic reduction of $^{1}H-{}^{13}C$ dipolar coupling constant due to fast molecular motions ($> 10^{4}$Hz).

- *Lineshape perturbations*. Motions with $\tau_c^{-1}/2\pi$ in the order of the internal spin interactions give a strong modulation of lineshape. Frequently, such motions will broaden spectra. However, if the molecular motion is well-regulated, some characteristic lineshapes will appear. Via analyzing the characteristic lineshapes one could extract many useful informations about the relevant molecular motion, such as the frequency and geometry. Attributed to the widely distributed strength of internal spin interactions, molecular motions giving the effect of lineshape perturbation cover a wide frequency range. Usually ^{13}C CSA pattern can be strongly modulated by the motions with $\tau_c^{-1}/2\pi \sim 10^{3}$Hz. Whereas, ^{2}H Pake pattern is sensitive to the motions with $\tau_c^{-1}/2\pi \sim 10^{5}$Hz.

- *Longitudinal magnetization exchange*. Slow motions ($\tau_c^{-1}/2\pi < 10^{3}$Hz) normally do not significantly affect NMR lineshapes. Nevertheless, such slow motions still can be monitored the longitudinal magnetization exchange experiment. However, if the timescale of the motion greatly exceeds the spin-lattice relaxation time of observed nuclear spin, due to the relaxation no motional effects will be shown up in NMR.

2.2 NMR techniques for studying molecular dynamics

Numerous NMR methods are available for the study of molecular dynamics. A wonderful feature of NMR methods is their wide frequency detection range. In the this sections some of these methods and their applications will be discussed. Our attention will be mainly focused on the methods which are used for the study of molecular dynamics in this work.

2.2.1 Relaxation time studies

Relaxation time measurements have been often used to characterize molecular motions in solids. In NMR there are several relaxation times which have to be differentiated such as T_1 and T_2 . T_1 relaxation time(or spin-lattice relaxation time) by definition is the time which excited spins need to recover back to thermal equilibrium state. T_2 relaxation time (or spin-spin relaxation time) normally can be considered as the life time of observed NMR signal. The study and application of these relaxation times are the subjects of several entire books. In this section we will only give a brief discussion for spin-lattice relaxation T_1. For the more detailed description of all kinds of the relaxation times in NMR, the interested reader is referred to the literature [Spiess 78].

2.2.1.1 Spin-lattice relaxation

If spins are placed in a magnetic field without disturbance for a long time, they reach the thermal equilibrium state. The populations in different energy levels obey the Boltzmann distribution at the temperature of environment. RF pulses can disturb the equilibrium state of spin. For example, a π pulse will invert the population distribution, whereas a $\pi/2$ pulse will equalize the populations and create a coherence. The spin-lattice relaxation (or called as the T_1 relaxation) is the process via which the excited spins return to the equilibrium state. The relevant spin interaction in T_1 relaxation process is the Zeeman interaction, indicating that the efficient molecular motion for the relaxation of spin system could be a motion with $\tau_c^{-1}/2\pi \sim \omega_L$. Based on the model of fluctuating local fields, the relationship between the relaxation rate $1/T_1$ and the correlation time of molecular motion τ_c can be expressed generally as follows:

$$T_1^{-1} \propto \frac{\tau_c}{1+(2\pi\omega_L\tau_c)^2} \tag{2.3}$$

With Eq.(2.3) one could plot T_1 against τ_c (Fig. (2.2)), which gives an easy way to analyze the motional effect on T_1 relaxation.
As shown in Fig. (2.2), T_1 has a minimum value, where the correlation time of molecular motion τ_c is equal to $(2\pi\omega_L)^{-1}$. At both sides of the minimum, T_1 has different tendencies against the molecular motion. In the left side, towards the fast motion limit,

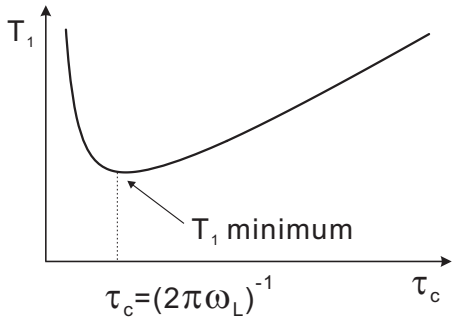

Figure 2.2: *The spin-lattice relaxation time constant T_1 as a function of the correlation time of molecular motion τ_c.*

T_1 increases with increasing molecular dynamics (indicated by the decrease of τ_c). This is the case existing in most liquid samples. Whereas, in the right side of the minimum, the tendency is inverted. T_1 decreases with increasing molecular dynamics. Normally this tendency is true in solids. For example, in semi-crystallized polymers the molecular chains often form thin crystalline lamellae separated by non-crystalline regions. Due to different restrictions from the environment, the molecular chains in crystalline regions are much less mobile that those in non-crystalline regions. Therefore, the ^{13}C T_1 relaxation time in crystalline regions is usually much longer than that in non-crystalline regions. In the case of polyethylene, the ^{13}C T_1 relaxation time in crystalline regions is in the order of 1000s at room temperature, whereas the ^{13}C T_1 relaxation time in non-crystalline regions is often less than 1s.

2.2.1.2 Methods for the spin-lattice relaxation measurement

There are several techniques which could be used to measure T_1. In the following two techniques for T_1 measurement, i.e., the inversion recovery technique and the saturation recovery technique, will be discussed in detail. Other techniques for T_1 measurement could be considered as derivatives of these two techniques.

1. The inversion recovery technique

The inversion recovery technique is designed to determine the system with a short T_1 relaxation time. The sequence is shown in Fig. (2.3).
A π pulse is first applied, which rotates the net nuclear magnetization down to the $-z$

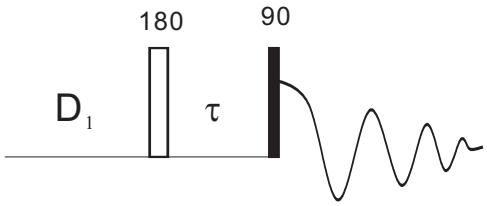

Figure 2.3: *The pulse sequence of inversion recovery experiment.*

axis. During the following time τ, the nuclear magnetization undergoes spin-lattice relaxation and returns toward its equilibrium position along the $+z$ axis. After a time τ, a $\pi/2$ pulse is applied which rotates the longitudinal nuclear magnetization into the $x-y$ plane. Once the nuclear magnetization is present in the $x-y$ plane it will have the precession about the z axis and give a free induction decay (FID). With this pulse scheme, the detected signal intensity $M(\tau)$ is a function of τ:

$$M(\tau) = M_0[1-2\exp(-\tau/\mathrm{T}_1)] \tag{2.4}$$

where M_0 is the initial magnetization after the full relaxation of the spin system during D_1 delay. In order to obtain the value of T_1, one could measure a series of signal intensities using the above pulse sequence but with different time τ. Then fitting the signals to the formula in Eq. (2.4) yields the T_1 value. Fig. (2.4) is an example, showing the determination of the ^{13}C T_1 relaxation time in non-crystalline regions of a UHMW-PE via the inverse recovery experiment. The fitting shows that the ^{13}C T_1 in non-crystalline regions of the polyethylene is ~ 0.6s.

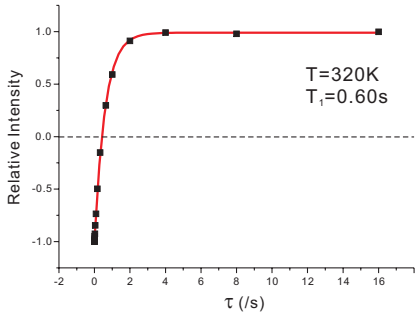

Figure 2.4: *The signal intensity recovery curve from the inversion recovery experiment. The signal intensities is from the ^{13}C in non-crystalline regions of an UHMW-PE, at T=320K and in the field of $B_0 = 13.4T$. The data were fitted to the exponential function in Eq. (2.4).*

2. The saturation recovery technique

Due to its design the inversion recovery technique is not suitable for a system with a long relaxation time. In that case, in order to have an accurate T_1 value D_1 delay in the pulse sequence (Fig. (2.3)) has to be longer than $5 * T_1$, which usually consumes a lot of time for a spin system with a long relaxation time. This is particularly true, when one wants to measure the ^{13}C T_1 relaxation time in solids. The saturation recovery technique can partially solve this problem. The pulse sequence of saturation recovery experiment is shown in Fig. (2.5).

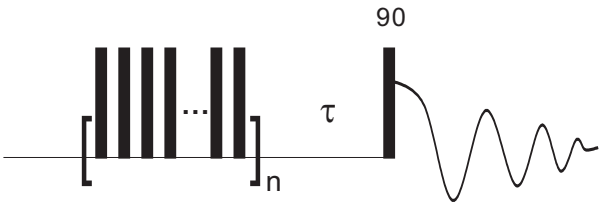

Figure 2.5: *The pulse sequence of saturation recovery experiment.*

In this pulse sequence, a series of $\pi/2$ pulses are applied before τ time in order to saturate all the signal in this channel. During τ time, the nuclear magnetization undergoes spin-lattice relaxation and returns toward its equilibrium position along the $+z$ axis. Then a $\pi/2$ reading pulse is applied after τ time to obtain the signal. Comparing with the inversion recovery technique, one advantage in the saturation recovery technique is that D_1 delay is not needed.

With the pulse scheme in Fig. (2.5), the relationship between the detected signal intensity $M(\tau)$ and the time τ reads as:

$$M(\tau) = M_0[1 - \exp(-\tau/T_1)] \tag{2.5}$$

Here, M_0 is the magnetization after the full relaxation. Again, in order to obtain the value of T_1, one should measure a series of signal intensities but with different time τ, then fit the signals to the formula in Eq. (2.5) to extract the T_1 value.

Fig. (2.6) is the ^{13}C intensity recovery curve of non-crystalline signal of the UHMWPE using the saturation recovery technique. The fitting shows a similar result ~ 0.6s as that from the inversion recovery technique.

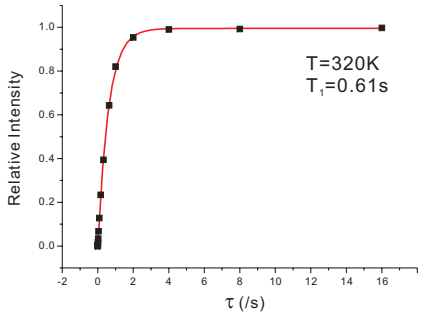

Figure 2.6: *The signal intensity recovery curve from the saturation recovery experiment. The signal intensities is from the ^{13}C in non-crystalline regions of an UHMW-PE, at T=320K and in the field of $B_0 = 13.4T$. The data were fitted to the exponential function in Eq. (2.5).*

In solids, people usually like to measure the T_1 relaxation time of low abundant nuclei with the initial polarization created via cross polarization (CP). The principle of the CP-based techniques is still similar as the inversion recovery technique mentioned above. But the CP-based techniques have a great advantage that the recycle delay in the pulse sequence usually only needs to be $3 * T_1$ of the abundant nucleus such as ^1H. The short delay time thus could save the total experimental time greatly.

2.2.2 $^1H - ^{13}C$ dipolar coupling analysis

Molecular motions can be monitored via $^1H - ^{13}C$ dipolar coupling analysis. The idea of this method is based on the fact that fast intermediate molecular motions ($\tau_c^{-1}/2\pi > 10^4$Hz) usually lead to a characteristic reduction of the observed $^1H - ^{13}C$ dipolar coupling constant. Thus, detecting the reduction degree of coupling constant yields the information of fast intermediate molecular motions. There are many NMR methods available for the detection of $^1H - ^{13}C$ dipolar coupling. In this work we used REREDOR experiment to detect the $^1H - ^{13}C$ dipolar coupling in non-crystalline regions of PE. The detailed discussion of the REREDOR pulse sequence has been given in Chapter 1 (1.5.2.2). In this section we will give some examples to explain how the $^1H - ^{13}C$ dipolar coupling can be modified by fast molecular motions and how one can use the sideband analysis to obtain the dipolar coupling from REREDOR experiment.

2.2.2.1 Motional reduction of $^1H-{}^{13}C$ dipolar coupling

As mentioned already $^1H-{}^{13}C$ dipolar coupling can be modulated by molecular motions. If the motion is fast ($\tau_c^{-1}/2\pi > 10^4$Hz) $^1H-{}^{13}C$ dipolar coupling will get a characteristic reduction in its value. In this section we will give several examples to explain how this characteristic reduction happens.

Consider the dipolar coupling of a typical $^1H-{}^{13}C$ group. Via the neutron diffraction, one knows that the distance between a ^{13}C atom and the direct-bonded ^1H atom is 0.109nm. This internuclear distance corresponds to a direct dipolar coupling of $|\omega_d/2\pi| = 23.3$kHz. Since ^1H in a $^1H-{}^{13}C$ group always has a rapid libration motion around its original site, the experimentally observed dipolar coupling in solids is always less than 23.3kHz. For instance the $^1H-{}^{13}C$ dipolar coupling of the $^1H-{}^{13}C$ group in L-Alanine is $|\omega_d/2\pi| \sim 22$kHz. Furthermore, if a $^1H-{}^{13}C$ group involves more motions, its $^1H-{}^{13}C$ dipolar coupling could decrease further. A typical case can be found in methyl groups, where the fast rotation about its threefold symmetry axis leads to a reduction of the $^1H-{}^{13}C$ dipolar coupling value. Assuming that the angle between the rotation axis and one of the three C-H bonds is 70° as indicated in Fig. (2.7), the $^1H-{}^{13}C$ dipolar coupling in this case would be reduced to $|\omega_d/2\pi| \sim 6.8$kHz.

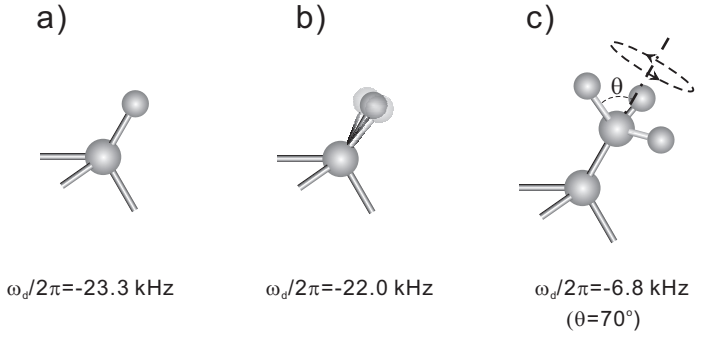

Figure 2.7: *The motional averaging effects on the dipolar coupling of a typical C-H group: (a) a static C-H group; (b) a C-H group with the libration; (c) a C-H group in a methyl group* ($\theta = 70°$).

In this work, the $^1H-{}^{13}C$ dipolar coupling in non-crystalline regions of PEs was studied. It was found that the $^1H-{}^{13}C$ dipolar couplings in non-crystalline regions of PEs varied with crystallization conditions of sample. The variation in the $^1H-{}^{13}C$

dipolar coupling indicates the different molecular dynamics present in non-crystalline regions of the sample, which can be related to the different chain organizations in non-crystalline regions generated during the crystallization process of sample.

2.2.2.2 Sideband analysis in REREDOR

REREDOR experiment can be classified as a 2D experiment. The direct dimension of REREDOR experiment is the ^{13}C MAS spectrum and the indirect dimension results from the rotor-encoding of signal, where the $^{1}H-^{13}C$ dipolar coupling can be derived. In the following, an example will be given to shown how to extract the dipolar coupling from a REREDOR spectrum.

From REREDOR experiment one gets a two dimensional time domain signal $S(t_1,t_2)$. Performing FT for the variable t_2 gives rise to the spectrum $S'(t_1,\omega_2)$, which has a time domain signal in the first dimension and a frequency domain signal in the second dimension. An example of such a spectrum is shown in Fig. (2.8), where Fig. (2.8a) is the two dimensional spectrum $S'(t_1,\omega_2)$; Fig. (2.8b) is the frequency domain signal extracted in the second dimension; and Fig. (2.8c) is the time domain signal extracted in the first dimension. To obtain the dipolar coupling value, one could fit $S'(t_1,\omega_2)$ directly, since this signal contains the information of relevant dipolar coupling as indicated by its formula (Eq. 1.108 in Chapter 1). However, in practice one often choose an alternative to extract the dipolar coupling, that is, performing FT for the variable t_1 in $S'(t_1,\omega_2)$ to create the sideband pattern, then fitting the sideband pattern for the dipolar coupling. Basically, there is no difference between these two procedures. However, if one performs a "concatenation" procedure, i.e. only recording the signal in the first dimension in one or two rotor periods and concatenating the acquired signal to form a new signal for the second FT, an additional attention has to be taken, because the noise in the spectrum will gain some correlations due to the concatenation procedure. Nevertheless, fitting the sideband pattern gives a more straightforward way to extract and compare dipolar couplings. The whole procedure of data analysis in REREDOR experiment is exhibited in Fig. (2.8).

Due to its design, REREDOR experiment is not very suitable for the detection of the molecular motion with a frequency close to the MAS frequency. In the recoupling

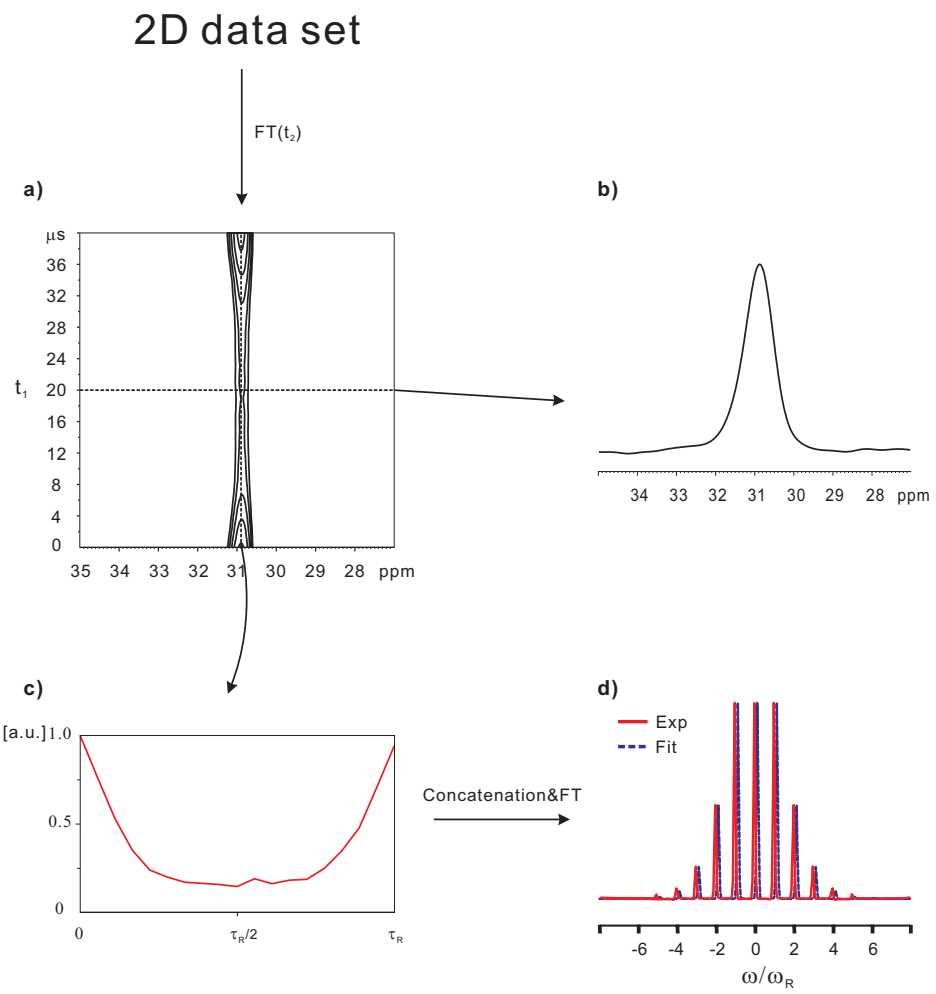

Figure 2.8: *The REREDOR experiment of melt-crystallized UHMW-PE at 25kHz MAS and 320K. The recoupling time is 3 rotor periods,* $\tau_{rcpl} = 3\tau_R$*: (a) the 2D data set after performing FT along the direct dimension; (b) the* ^{13}C *MAS spectrum extracted from a row of (a); (c) the rotor-encoded oscillation signal extracted from a column of (a); (d) the sideband pattern obtained after performing FT on the signal in (c). Before this FT the concatenation process can be done to save experiment time. From this experiment a coupling constant of* $D_{IS}/2\pi = 6.3kHz$ *was obtained in non-crystalline regions of this polyethylene.*

scheme of REREDOR, the MAS and RF pulses are tactically designed to recouple the $^1H - ^{13}C$ dipolar coupling. The efficiency of this recoupling scheme, however, drops down when the frequency of molecular motion is close to the frequency of MAS. The inefficient recoupling will lead to the fast signal decay in the first dimension, which possibly will give some difficulty in the fitting process. Although this case is not very common and varying the MAS frequency can solve this problem to some extend, one

should be aware of this possibility when performing and analyzing REREDOR experiments.

2.2.3 Lineshape analysis

Lineshape analysis techniques usually are different in solid state NMR and solution NMR, although the principle behind is the same. In solution NMR, the lineshape analysis often is used to study the exchange process between two resonant signals. The degree of lineshape perturbation is determined by the difference between the exchange rate k and the difference of the two resonance frequencies $\Delta\omega$ (Chapter 15, [Levitt 02]). In a static solid, however, NMR signals are dominated by anisotropic NMR interactions. For a powder sample where all molecular orientations are present, resonant signals often appear as the so-called "powder pattern". Molecular motions can change the orientation of anisotropic NMR interactions, leading to different degrees of lineshape perturbation. In principle the lineshape perturbation in this case also can be considered as results from the exchange process among different resonant signals caused by molecular motions (Chapter 7, [Schmidt-Rohr 94]). However, depending on the frequency range and motion mode, different molecular motions usually give rise to different lineshape characteristics of resonance. Analyzing the lineshape in this case thus can yield the information about motion frequency as well as the motion geometry. In the following sections a discussion about the lineshape analysis of powder pattern in static solids will be given.

2.2.3.1 Simulating powder pattern

The lineshape in static solids originates from orientation dependence of anisotropic NMR interactions. The different orientation distribution of molecules and, molecular motion changing the molecular orientation, can give changes to the lineshape. For a powder sample, where all molecular orientation are equally weighted, the molecular motion often is the only factor that controls the width of lineshape. To extract the molecular dynamic information from powder pattern, one thus could simulate the powder pattern with the given motion frequency and motion mode. If the simulated pattern matches the experimental one, the motion frequency and motion mode used in the simulation are a candidate for the proper description of molecular motion. In

NMR practice, in order to calculate the lineshape of a powder pattern under conditions of molecular motion, it is common to consider the molecular motion as such a motional process that the involved unit moves between N discrete sites, with the time taken to move between different sites being infinitesimal comparing with the residence time in each site. The following description about the time evolution of spin system under motional processes is based on this model.

In the absence of molecular motion, the time evolution of the transverse magnetization is given by:

$$\frac{dM^i(\theta,\phi;t)}{dt} = M^i(\theta,\phi;t)(\mathbf{i}\omega^i(\theta,\phi) + \mathrm{T}_2^{-1}) \tag{2.6}$$

which has the solution:

$$M^i(\theta,\phi;t) = M_0^i(\theta,\phi)\exp[\mathbf{i}\omega^i(\theta,\phi)t + \mathrm{T}_2^{-1}t] \tag{2.7}$$

θ and ϕ describe the molecular orientation in the external magnetic field $\underline{B_0}$. More precisely, θ and ϕ are the polar angles describing the orientation of $\underline{B_0}$ in the molecular frame (MF), as shown in Fig. (2.9). T_2 is the transverse relaxation time of spins. $\omega^i(\theta,\phi)$ is the resonance frequency of spins in the orientation $[(\theta,\phi),(\alpha_i,\beta_i,\gamma_i)]$. $M_0^i(\theta,\phi)$ is the initial transverse magnetization associated with the particular molecular orientation, which in general is determined by the pulse sequence and generates the transverse magnetization. If the transverse magnetization is generated by a single hard 90° pulse, $M_0^i(\theta,\phi)$ will be the same for all molecular orientations, and thus can be set to 1. The time evolution of net transverse magnetization for the whole powder sample, $M(t)$, is simply obtained from Eq. (2.7) by integrating over all possible molecular orientations described by θ and ϕ:

$$\begin{aligned} M(t) &= \frac{1}{8\pi^2}\int_0^{2\pi} d\phi \int_0^{\pi} sin\theta d\theta\, M(\theta,\phi;t) \\ &= \frac{1}{8\pi^2}\int_0^{2\pi} d\phi \int_0^{\pi} sin\theta d\theta\, M_0^i(\theta,\phi)\exp[\mathbf{i}\omega^i(\theta,\phi)t + \mathrm{T}_2^{-1}t] \end{aligned} \tag{2.8}$$

If molecular reorientations are taken into account with this model, Eq. (2.6) needs to

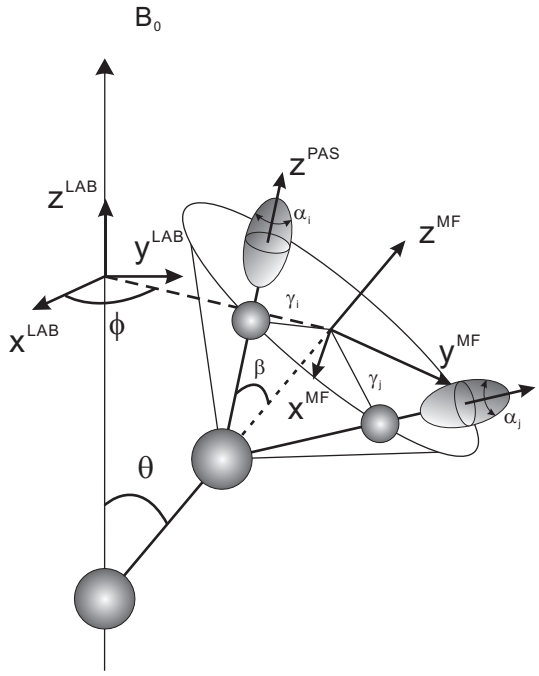

Figure 2.9: *A cone model, defining the polar angles* (θ,ϕ) *for the MF orientation with respect to* $\underline{B_0}$ *and the Euler angles* $(\alpha_n,\beta_n,\gamma_n)$ *for the PAS orientation in MF.*

be modified as:

$$\frac{dM^n(\theta,\phi;t)}{dt} = M^n(\theta,\phi;t)(\mathbf{i}\omega^n(\theta,\phi) + \mathrm{T}_2^{-1} + \Pi) \tag{2.9}$$

Here, $M^n(\theta,\phi;t)$ is an n-dimensional vector, each component being the transverse magnetization from one of the n sites involved in the molecular reorientation process. In Fig. (2.9) two sites denoted as i and j are exemplarily shown. $\omega^n(\theta,\phi)$ is an $n\times n$ diagonal matrix whose elements are the resonance frequencies associated with the n sites for an orientation (θ,ϕ). Π is a $n\times n$ matrix whose elements Π_{ij} are given by:

$$\Pi_{ij} = \Omega_{ij}p_j \qquad \text{and} \qquad \Pi_{ii} = -\sum_{j(\neq i)}^{n-1}\Pi_{ij} \tag{2.10}$$

where Ω_{ij} is the inverse of the correlation time for hopping from the site j to the site i., i.e. $\Omega_{ij} = \tau_{c,ij}^{-1}$, and p_j is the population of site j. The solution to Eq. (2.9) is analogous

to Eq. (2.7). Then the net transverse magnetization reads as:

$$M(t) = \frac{1}{8\pi^2}\int_0^{2\pi} d\phi \int_0^{\pi} sin\theta d\theta \sum_{i=1}^{N} M_0^i(\theta,\phi)L^i(\theta,\phi;t) \tag{2.11}$$

where the propagator $L(\theta,\phi;t)$ is:

$$L^i(\theta,\phi;t) = \exp[\mathbf{i}\omega^i(\theta,\phi)t + \mathrm{T}_2^{-1}t + \Pi] \tag{2.12}$$

For the calculation of ω^i in the site i, it involves two frame transformations in the static case:

$$PAS_i \xrightarrow{(\alpha_i,\beta_i,\gamma_i)} MF \xrightarrow{(\theta,\phi)} LAB \tag{2.13}$$

which can be expressed as the following:

$$\omega_i(\theta,\phi) = \omega_L\ b_0^{MF}\ \underbrace{R^{-1}(\alpha_i,\beta_i,\gamma_i)\sigma_i^{PAF}R(\alpha_i,\beta_i,\gamma_i)}_{\sigma_i^{MF}}\ b_0^{MF'} \tag{2.14}$$

Here, b_0^{MF} is the unit vector of $\underline{B_0}$ in the MF.

An easy way to incorporate Π into calculation is to express Π in a matrix form. For a two-site hopping, it can be expressed as:

$$\Pi = \begin{pmatrix} -\Omega_{ij}\cdot p_i & , & +\Omega_{ij}\cdot p_i \\ +\Omega_{ji}\cdot p_j & , & -\Omega_{ji}\cdot p_j \end{pmatrix} \tag{2.15}$$

where Ω_{ij} is the hopping rate for moving from the site i to the site j and p_i is the population at the site i. For a two-site hopping, Π is a 2×2 matrix. Analogically, for a n-site hopping, Π will be a $n\times n$ matrix.

Therefore, according to the frequency and geometry of motion one can get Π and $\omega^i(\theta,\phi)$ for the spins in every site. With these two parameters one is able to calculate the propagator $L(\theta,\phi;t)$ in Eq. (2.12) omitting T_2 relaxation. The motion modulated pattern then can be obtained by calculating Eq.(2.11).

The above way for the powder pattern simulation is suitable for a motion with τ_c^{-1} comparable with the frequency of related spin interaction. For the τ_c^{-1} of motion significantly bigger than the frequency of related spin interaction, the way to calculate powder pattern can be simplified. This is called the fast motion limit. In this case, the lineshape of powder pattern is governed by the motionally averaged interaction tensor, which can be expressed as:

$$\overline{\sigma^{MF}} = \sum_{i=1}^{n} p_i \cdot \sigma_i^{MF} \tag{2.16}$$

With $\overline{\sigma^{MF}}$, one can easily get the formula for motionally averaged $\omega(\theta,\phi)$:

$$\omega(\theta,\phi) = \overline{\delta}(3cos^2\theta - 1 - \overline{\eta}sin\theta cos2\phi) \tag{2.17}$$

where $\overline{\delta}$ and $\overline{\eta}$ are the anisotropy and asymmetry of motionally averaged tensor $\overline{\sigma^{MF}}$.

Then the powder pattern can be easily achieved after performing the powder average for $\omega(\theta,\phi)$ in Eq. (2.17).

Fig. (2.10) shows an example with the ^{13}C CSA patterns of CH_2 group in PE. As shown in this figure, the ^{13}C CSA pattern shape can be strongly affected by molecular motions. Comparing the experimental and simulated patterns, the information of molecular motion can be obtained.

2.2.3.2 Limitation of lineshape analysis

Lineshape analysis in NMR is a powerful technique, providing fruitful information about molecular dynamics. However, for any kind of analysis which relies on fitting simulated to experimental data, one must be aware that there could be potentially several ”fits”, i.e. different models could give equally good fits to the same experimental data. In the absence of any other data, all of these fits must be considered equally possible descriptions of the actual process. As to lineshape analysis in NMR, although one could use other experiments or some knowledge of the nature of system to reduce such ambiguities, nevertheless, searching for all possible fits is still very important.

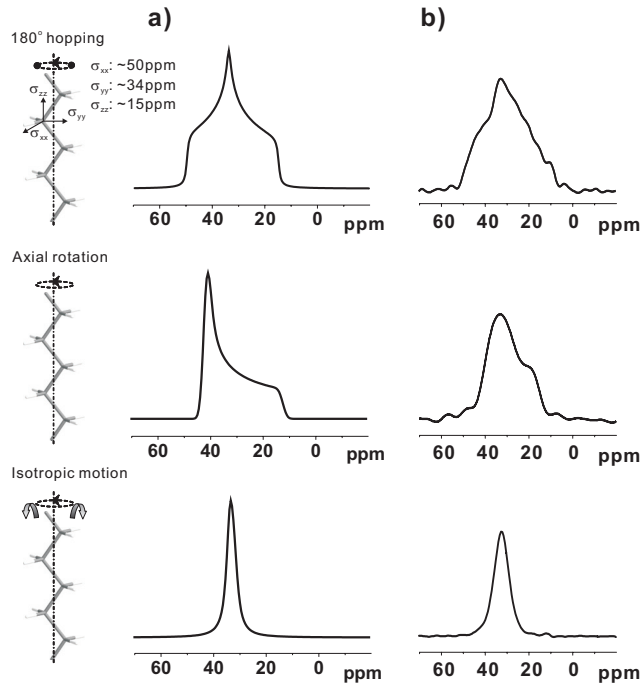

Figure 2.10: ^{13}C *CSA patterns of* CH_2 *group in PE: a): the simulated powder patterns; b): the experimental powder patterns. The tensor orientation of* CH_2 *group in PE is indicated in the left chain model picture:* σ_{xx} *is parallel to the proton-proton internuclear vector,* σ_{yy} *is parallel to the H-C-H angle bisector, and* σ_{zz} *is parallel to the polymer chain axis. The simulated powder patterns were obtained from WEBLAB (http://weblab.mpip-mainz.mpg.de/weblab/weblab.html).*

Lineshape analysis is limited for the analysis of complex motions. In a real system, molecules may undergo various kinds of motions simultaneously. For instance, molecules can rotate about several different axes with different rates at the same time. In this circumstance, the lineshape of powder pattern may become featureless due to a superposition of patterns modulated by different motional components. Therefore, although all the information about molecular motions is still contained in the lineshape, the information about different motional components can not be resolved.

Another problem of lineshape analysis is its model dependency. Lineshape analysis we discussed so far is based on a model for the description of molecular motion. This model assumes that the motion is a hopping between very sharp and deep potential well, i.e. the time for the molecular hopping between different sites is much smaller than the residence time in the given site. Usually, this model works quite well for de-

scribing motional processes. However, it still could fail in some cases. For instance, in the case that the time taken for hopping is comparable to the residence time in the given site, or that each of the hopping sites is ill-defined, this model will not be the proper description of molecular motion. As a result, the model based lineshape analysis in such cases would not yield valid informations for the molecular motion.

2.2.4 Longitudinal magnetization exchange experiment

For the studies of slow motion ($\tau_c^{-1}/2\pi < 10^3$Hz), the longitudinal exchange experiment has been proven to be a very useful method.

The basic principle of exchange experiment is the measurement of the NMR frequency of spins at different times and the detection of slow dynamics through a change in the NMR frequency. Based on this principle, various longitudinal magnetization exchange experiments have been developed [Schmidt-Rohr 94]. These various exchange experiments may look very different since they could be designed for different purposes. But they do share some common features. For instance, the frequency correlation between different dimensions is always achieved via the motion influence on the longitudinal magnetizations. In this section, we will give a concise example of a 2D exchange experiment, showing these common features. A discussion about the 1D ^{13}C exchange experiment, which is used in this work to study the chain diffusion in polyethylenes, will be given afterwards.

2.2.4.1 A basic 2D exchange experiment

The basic pulse sequence scheme of 2D exchange experiment is shown in Fig. (2.11). The design of the pulse sequence is quite simple. First, the transverse magnetization is created by the excitation block, which could be an initial 90° pulse or a CP step. Afterwards, this transverse magnetization is allowed to evolve during the t_1 period under a certain frequency ω_1. At the end of t_1, the magnetization is stored along z (the direction of the external magnetic field $\underline{B_0}$) for the mixing time τ_m, during which some molecular reorientations may occur. After τ_m, the magnetization is turned back to the transverse plane, where it evolves under the frequency ω_2 giving rise to the FID.

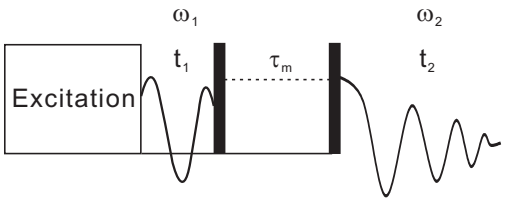

Figure 2.11: *The basic pulse scheme of a 2D exchange experiment*

Performing 2D FT to the time domain signal yields the 2D frequency spectrum. In a usual case, a 2D spectrum consists of a set of diagonal and cross peaks, which describes the correlation between the frequency ω_1 during t_1 and the frequency ω_2 during t_2. To extract the dynamic information from this spectrum, one needs the knowledge about the origin of these peaks, which will be shown in the following. For simplification reasons, the following discussion is based on a two-site exchange process, $A \rightleftharpoons B$.

If no dynamic processes happened in the mixing time τ_m, the frequencies would remain unchanged, $\omega_1 = \omega_2$. The intensities of the signals will be confined to the diagonal line in the 2D spectrum. But if exchange processes happened during the τ_m, the cross peaks at (ω_A, ω_B) and (ω_B, ω_A) would grow up. The appearance of a typical 2D exchange spectrum is illustrated in Fig. (2.12).

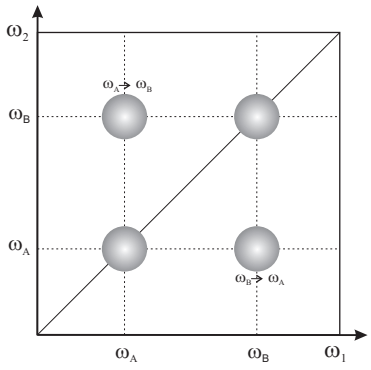

Figure 2.12: *A basic 2D exchange spectrum*

The cross peaks at (ω_A, ω_B) and (ω_B, ω_A) both indicate exchange processes during the time τ_m. In principle these two peaks are attributed to two different processes. For the peak at (ω_A, ω_B), it originates from the motional process which changes the spin frequency from ω_A to ω_B during τ_m, whereas the peak at (ω_B, ω_A) is from the motional

process which changes the spin frequency from ω_B to ω_A during τ_m. For a symmetrical two-site exchange, these two cross peaks have the same intensity. For an unsymmetrical exchange process, these two peaks usually show different intensities.

2D exchange spectra can be used to determine the activation energy of a motion. One knows that varying the mixing time τ_m can lead the change in the intensities of cross peaks. So, by assessing the cross peak intensities as a function of the mixing time τ_m, the correlation time for the related motion can be determined. Determining the correlation times at different temperatures, the activation energy for this motion can be obtained via Arrhenius plot.

2.2.4.2 The 1D ^{13}C exchange experiment on polyethylene

The 1D ^{13}C exchange experiment often used in this work is a simple derivative from the 2D exchange experiment mentioned above. The pulse sequence of the ^{13}C exchange experiment is shown in Fig. (2.13).

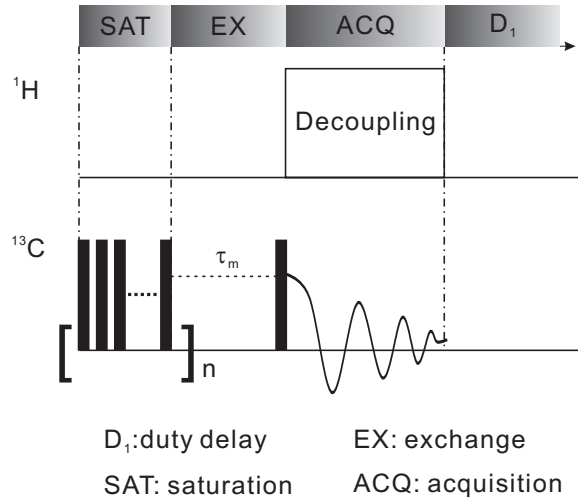

Figure 2.13: *The pulse scheme of ^{13}C exchange experiment*

First a series of 90° pulses is applied to the carbon channel to saturate all the signals. The exchange time τ_m (or mixing time) immediately follows the saturation pulse block. After the exchange time a 90° pulse is applied to read out the signal which grows up during the exchange time. During the acquisition time high power dipolar decoupling

is applied on the ^{1}H channel.

In the work of this thesis, this pulse sequence is used to monitor the chain diffusion between crystalline and non-crystalline regions of polyethylene. The design of this pulse sequence is based on the fact that in polyethylenes the ^{13}C T_1 relaxation time in crystalline regions is much longer than that in non-crystalline regions. Therefore, during the exchange time τ_m, the ^{13}C signal from non-crystalline regions will grow up very quickly because of the short T_1 relaxation time ($\sim 0.6s$). In contrast, the ^{13}C signal from crystalline regions will grow up very slowly due to its long relaxation time ($> 1000s$), if T_1 relaxation is the only mechanism for the increase of signal. However, in polyethylene there is an additional motional process which could lead a fast increment of the crystalline signal, that is the chain diffusion. Consider the structure in a semi-crystalline polyethylene, crystalline and non-crystalline regions are spatially connected. Hence, it is possible for polyethylene chains to translate between crystalline and non-crystalline regions transferring ^{13}C magnetization between them. Fast relaxing non-crystalline regions then serve as a reservoir for the ^{13}C magnetization transfer. Based on this model, monitoring the chain diffusion can be easily achieved via monitoring the increment of crystalline signal as a function of τ_m.

The heteronuclear Overhauser effect (NOE) [Neuhaus 89] has to be considered when using this pulse sequence for the study of the chain diffusion in polyethylenes. As mentioned above, the chain diffusion is monitored by quantifying the growth of ^{13}C crystalline signal during τ_m. The intensity of ^{13}C crystalline signal, however, could be affected by the ^{1}H decoupling during the signal acquisition. If the recycle delay D_1 is not long enough, the saturated ^{1}H will give a NOE enhancement to the ^{13}C non-crystalline signal which grows up during a short τ_m. The ^{13}C crystalline signal could also be affected, since this enhancement factor of NOE can be transfered to crystalline regions via the chain diffusion. An unpleasant property of the NOE enhancement here is its time dependence in the case of transient NOE. For a short τ_m time, the enhancement factor could be quite big, whereas for a long τ_m time the enhancement will become very small or disappear. Therefore, the intensity of ^{13}C crystalline signal will not be accurately quantified any more. To avoid this problem, the recycle time D_1 has to be increased.

Chapter 3

Morphological Effects on Molecular Dynamics in Non-crystalline Regions of Linear UHMW-PE

In this chapter, we will apply various solid-state NMR methods described in the previous chapters to study the molecular motion in PE. Our investigations will be focused on the morphological effects on the chain dynamics in non-crystalline regions of linear UHMW-PEs. The discussion in this chapter consists of four parts. In the beginning, a short introduction of basic knowledge about PE including crystal structure, morphology and chain dynamics will be given. Afterwards, the morphology of the solution crystallized UHMW-PE will be discussed shortly. The main part of the work in this chapter represents the NMR study of the local chain dynamics and the long range chain diffusive motion in the UHMW-PE samples crystallized from melt and solution. In the last part conclusions derived from the experimental observations will be given.

Several solid state NMR techniques were used in this work to monitor the chain dynamics in UHMW-PEs. The local dynamic behavior of chain segments was monitored via analyzing the motionally reduced $^{1}H-^{13}C$ dipolar coupling constant and the lineshape of the ^{13}C CSA pattern. The long range chain diffusive motion between crystalline and non-crystalline regions was investigated using the 1D ^{13}C MAS exchange experiment.

3.1 Introduction to PE

The introduction of PE in this section includes the crystalline structures, possible morphologies, and chain diffusive motion between crystalline and non-crystalline regions. These basic knowledges may help one to have a better understanding of the latter results.

3.1.1 Crystalline structure

PE is a typical semicrystalline polymer. Depending on crystallization conditions, it can form three crystal types: orthorhombic, monoclinic and hexagonal [Corbeij-Kurel 01, Rastogi 05]. Among these crystal structures the most stable one is the orthorhombic crystal. The arrangement of polyethylene chains in the orthorhombic crystal is illustrated in Fig. (3.1).

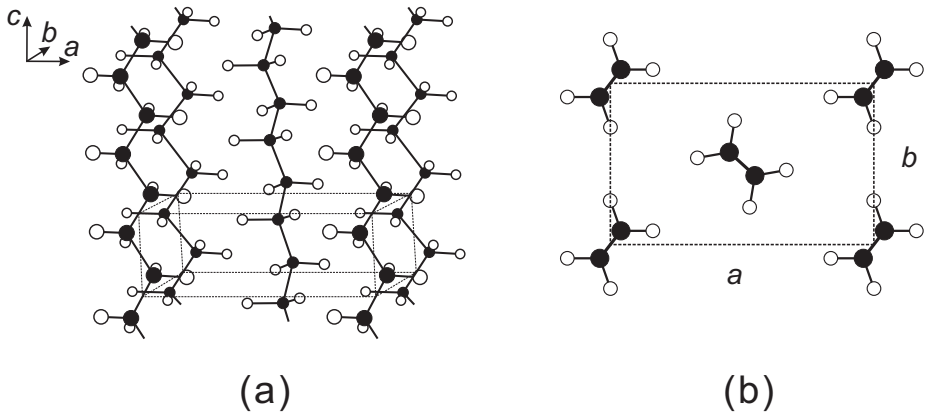

Figure 3.1: *Crystal structure of orthorhombic PE. (a) General view of unit cell; (b) Projection of unit cell parallel to the chain direction, c. (● carbon atoms, ○ hydrogen atoms.)*

As shown in Fig. (3.1), the unit cell of PE contains two monomers and has dimensions of $a = 7.40\mathring{A},\ b = 4.93\mathring{A},\ c = 2.534\mathring{A}$ [Sperling 92]. Due to the energy requirement and steric interactions the PE chains in the unit cell take the all-trans conformation, i.e. the planar zig-zag. And the backbones of polymer chains lie parallel to the crystallographic *c* axis. The chain position in the cell is held by the secondary van der Waals interaction between the chain segments. The angle between the zig-zag plane and the crystallographic *a* or *b* axes is determined by the interactions between H atoms on the

neighbor PE chains.

For the formation of monoclinic and hexagonal crystals of PE, usually some special conditions are needed [Corbeij-Kurel 01]. The monoclinic crystal can be formed by mechanical deformation of an orthorhombic crystal. In a monoclinic crystal the molecules are still in the form of a planar zig-zag and the chain direction and crystal density are virtually unchanged. The difference between the orthorhombic and monoclinic crystals is just the way how the molecules are packed in the unit cells. The hexagonal phase usually can be found in long chain paraffins. For PE this structure is metastable at atmospheric pressure. However, people have observed the hexagonal phase in linear PE at the elevated pressure and temperature ($P > 4kbar$, $T > 250\ ^{\circ}C$) [Corbeij-Kurel 01], where the hexagonal phase is a thermodynamically stable state.

3.1.2 Morphology

Generally, the morphology is defined as the spatial arrangement of distinguishable phases in a matter. In polymer the formation of phase, i.e. shape, size and content, usually is governed by a balance between the kinetics and thermodynamics during crystallization. In this section several typical morphologies of PE and their corresponding crystallization conditions will be discussed. Our interest will be mainly focused on the morphologies developed from the quiescent crystallization, i.e. melt and solution crystallizations.

Solution and melt crystallization usually form different morphologies in PE. It is a well-established and proven fact that when a linear PE sample is crystallized from dilute solution, it forms thin crystalline lamellae with the chain axis, i.e. the crystallographic *c* axis in the lattice, approximately perpendicular to the lamellar surfaces [Organ 85, Rastogi 97]. The lamellar thickness is found to be in the range of 10-30 nm, which usually is much smaller than the length of a fully extended chain. Formation of such crystals invoked the concept known as chain folding, that is, long chains fold back and forth to form crystalline lamellae and fold regions give rise to non-crystalline regions. Concerning the way how PE chains fold back from non-crystalline regions and re-entry into crystalline lamellae, people have proposed several models, which are illustrated in Fig. (3.2).

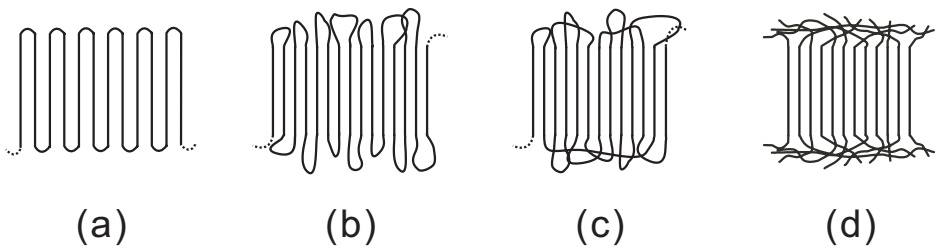

Figure 3.2: *Schematic representation of models of PE morphologies. (a) adjacent re-entry with sharp folds; (b) adjacent re-entry with loose folds; (c) random re-entry; (d) switchboard model*

The model (a) and (b) in Fig. (3.2) are called the adjacent re-entry mode, which means that the chains travel from the crystalline lamellae to the non-crystalline region and then fold back with a re-entry into the same crystallite through the neighbouring exit point. These two models usually are used to describe the morphology of PE crystallized from dilute solution, where the fully disentangled chains can easily organize themselves to make regular chain folding during the crystallization process. The non-crystalline regions are formed by the chain folds in these two cases.

The model (c) and (d) in Fig. (3.2) usually are supposed to be close to the morphology of PE developed from melt crystallization [Flory 62]. In melt crystallization, crystals are formed from completely random and highly entangled molecular chains. Due to the kinetic reason it is almost impossible for the chains to get disentangled and form the regular folds as occurring in solution crystallization process. Therefore, if crystallized from melt, polymer chains are most likely to either fold back with a random re-entry or traverse the non-crystalline region between the different crystallites. The morphologies developed in melt crystallization thus are close to the random re-entry model (c) and the switchboard model (d) [Billmeyer 84].

3.1.3 Chain diffusion in PE

The chain diffusion between crystalline and non-crystalline regions in PE has been recognized for a long time. The existence of this motion gives a good explanation for the origin of the α process of PE (Chapter 5, [Strobl 97]). The first conclusive proof of this motion was given by solid state NMR experiments in the early 1990s

[Schmidt-Rohr 91], where the existence of this diffusive motion was clearly demonstrated in 1D/2D ^{13}C exchange experiments.

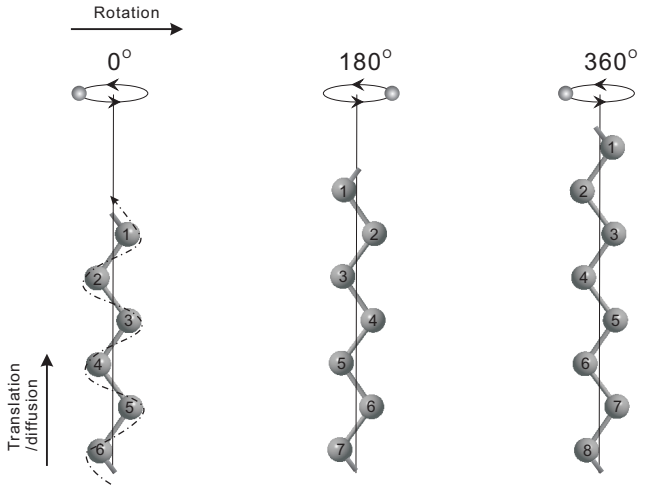

Figure 3.3: *Helical jump of PE chain (all-trans) in crystallites, involving in each step a* 180° *rotation and a translation by one CH_2 unit. The jump sites involved in this motion are defined by the PE crystal lattice. All these sites are energetically equivalent.*

The chain diffusion of PE in nature is a motion that traverses crystalline and non-crystalline regions. It requires the involved chain segments having a cooperative movement in crystalline regions as well as non-crystalline regions. It is well known that chain units in PE crystals have the so-called ”helical jump”, that is, the chain units undergo a 180° rotation with a translation by one CH_2 unit and the sites and angles involved in the jump are defined by the crystal lattice [Reneker 62, Mansfield 78]. Because of the chain connectivity, the jump motions of individual units generate the translative movement of the whole stem along the crystallographic *c*-axis in crystals. Due to the random nature of jump motion this translative motion of the chain stem is considered as a diffusive motion. The jump motion and the consequential chain diffusion are illustrated in Fig. (3.3).

Sample morphology can has a strong influence on the chain diffusive motion, which is illustrated in Fig. (3.4). Three kinds of morphologies are shown in Fig. (3.4): (a) the adjacent re-entry model; (b) the random re-entry model; (c) the switchboard model. If considering the pathway of moving chain, it is easy to imagine that the organization of chains in the interphase between crystalline and non-crystalline regions will be a

bottle neck for this motion. The chain portion in the interphase connects less ordered non-crystalline chains with fully ordered crystalline chains. Then, when a chain segment travels through the interphase, it will have an energy barrier as well as an entropy barrier. The energy barrier originates from the conformation change involved in the motion and the entropy barrier results from the situation that the chain segment moves between non-crystalline regions (high entropy) and crystalline regions (low entropy). Therefore, if the energy barrier of the motion stays constant or at a certain temperature the energy barrier of the motion become less important, the entropy barrier will play an important role. Following this point, the partially ordered non-crystalline chains such as the chain folds in the adjacent re-entry model (3.4a) could favor the chain diffusion due to the less entropy penalty.

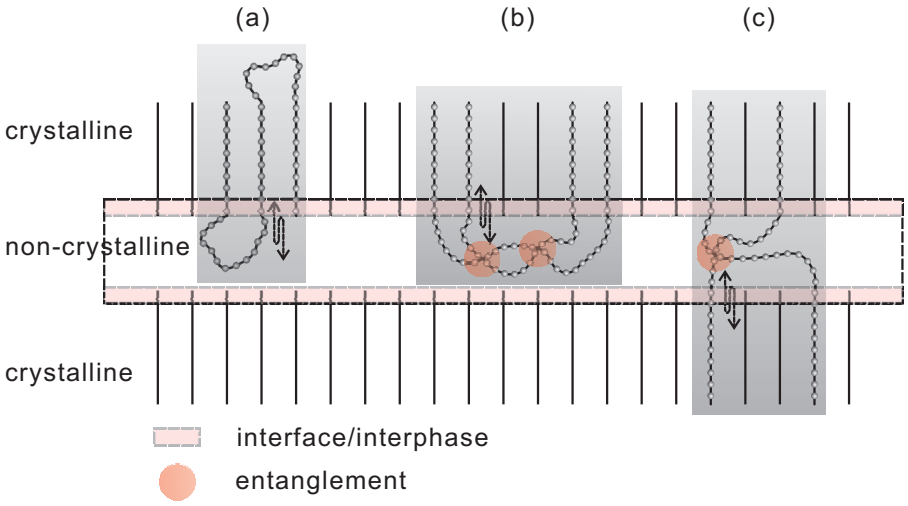

Figure 3.4: *The morphological effects on the chain diffusive motion. Three kinds of morphologies are indicated in this figure: (a) the adjacent re-entry model (with hard folds and loose folds); (b) the random re-entry model; (c) the switchboard model. These three models contain different interphases and different degree of chain entanglements.*

PE samples with different morphologies usually contain different degrees of chain entanglements in their non-crystalline regions. But the influence of chain entanglements on the chain diffusion seems to depend on the diffusion distance. If diffusing a long distance, the chain entanglements will play an important role. Generally, for PE melts

the distance between two entanglement points of a polymer chain is about 300 backbone chain atoms [Porter 66]. In solid the distance between two entanglement points of PE chains will be less than 300 backbone chain atoms, since after crystallization chain entanglements are confined in non-crystalline regions. Nevertheless, chain entanglements will not show strong effects on a short range chain diffusion. However, if the diffusion distance exceeds the entanglement distance, a strong hindrance from chain entanglements will show up since the polymer chain needs a long time to get disentangled for its moving.

3.2 Morphology of the solution crystallized UHMW-PE

Two samples used for the study in this chapter were made from a same UHMW-PE powder, but crystallized in different ways. One is crystallized from the dilute solution called SC-PE, the other is crystallized from melt called MC-PE. It is well known that the melt-crystallized sample forms a random non-crystalline region with fully entangled chains, whereas the solution crystallized sample can form a relatively ordered non-crystalline region with chain folds [Organ 85, Gedde 04]. Fig. (3.5) shows a TEM of SC-PE used in this study.

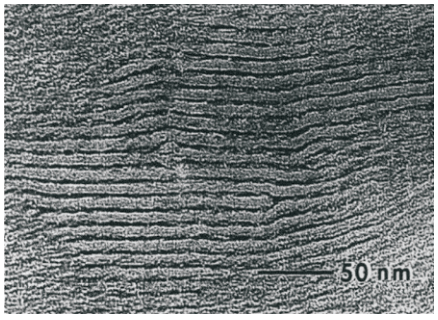

Figure 3.5: *Transmission electron micrograph of solution crystallized UHMW-PE (SC-PE). The stacked lamellae have a thickness of* $\sim$ 12*nm.*

The TEM in the figure shows that SC-PE consists of well-stacked lamellar structure possessing a uniform lamellar thickness of $\sim$ 12nm. The non-crystalline regions are shown as the dark lines in the TEM, which have a thickness around 4nm.

3.3 Local chain dynamics in non-crystalline regions of UHMW-PEs

As already mentioned above, SC-PE and MC-PE contain different morphologies developed during different crystallization processes. It is reasonable to anticipate that due to their morphologies the different chain mobilities are present in non-crystalline regions of these sample. Fig. (3.6a, b) exhibits ^{13}C-CP/MAS spectra of SC-PE and MC-PE, where the NMR signal at $\sim$33 ppm arises from all-trans conformations present in crystalline regions [Earl 79, Vanderhart 81]. In contrast, chains segments in non-crystalline regions are free to adopt various conformations and the molecular dynamics present in these areas leads to fast exchange between these conformations. The NMR signal of these units is observed as a broad peak at about $\sim$31 ppm, the position and the width depending the conformation statistics and the accessibility of the conformational space to dynamic processes present in non-crystalline areas [Earl 79]. The broad non-crystalline peak of SC-PE indicates that non-crystalline chains of SC-PE undergo a strong local restriction hindering the conformation exchange, whereas this strong local restriction does not exist in non-crystalline regions of MC-PE, since it shows a quite sharp non-crystalline peak. The normalized intensity of crystalline signal in the CP/MAS spectra suggests lower crystallinity in the melt crystallized sample, a point that will be discussed later. An accurate quantification of the crystallinity via CP/MAS is hampered by the dependence of the polarization transfer efficiency on the heteronuclear dipolar couplings present in the samples.

These heteronuclear dipolar couplings may differ due to different segmental mobility caused by dynamic processes of polymer chains in non-crystalline areas depending on the crystallization procedure of the sample. In order to quantify these heteronuclear dipolar couplings, a rotor encoded REDOR method has been applied. The resulting spinning sideband patterns for the two samples taken at the isotropic chemical shift of the non-crystalline signals are shown in Fig. (3.6c, d). The broad profile of the spinning sidebands of non-crystalline regions in SC-PE compared to MC-PE is indicative of stronger heteronuclear dipolar coupling in non-crystalline regions of SC-PE. The quantitative analysis of the sideband patterns provides an effective residual heteronuclear coupling constant of 9.1 kHz for the non-crystalline component in SC-PE in relation to 6.3 kHz for MC-PE. The higher effective coupling in SC-PE results from

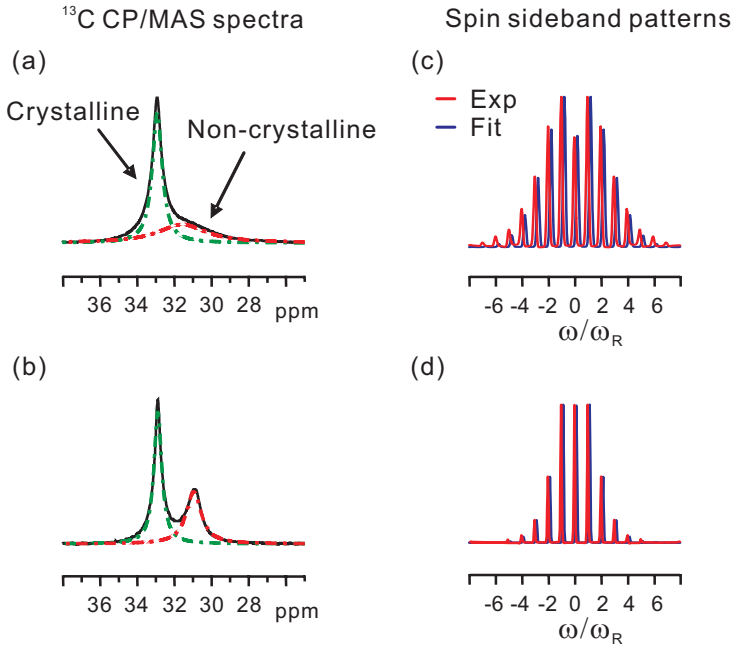

Figure 3.6: *The solid state ^{13}C CP/MAS spectra and the spinning sideband patterns of $^{1}H-^{13}C$ spin pairs in non-crystalline regions. The ^{13}C CP/MAS spectra were measured at 6 kHz MAS, T=320K. The REREDOR experiment was measured at 25 kHz MAS, T=320K, and 3 rotor periods for the recoupling time. (a) the ^{13}C CP/MAS spectrum of SC-PE. Two components are shown in the spectrum. The red dash line is the non-crystalline peak ($\sim$ 31ppm) and the green one is the crystalline peak ($\sim$ 33ppm). (b) the ^{13}C CP/MAS spectrum of MC-PE. (c) the spinning sideband pattern of non-crystalline regions in SC-PE. (d) the spinning sideband pattern of non-crystalline regions in MC-PE. For the spinning sideband patterns, the underlying blue ones were simulated with a dipolar coupling constant of $D_{IS}/2\pi = 9.1$ kHz for SC-PE and 6.3 kHz for MC-PE.*

a more anisotropic molecular motion and thus indicates a more restricted local chain dynamics in non-crystalline regions. However, the sideband analysis of dipolar recoupling schemes does not provide more detailed geometrical information on the dynamic processes which could be obtained from the static powder line shape of the ^{13}C chemical shift anisotropy (CSA).

The SUPER method has been chosen to obtain the static ^{13}C CSA pattern of non-crystalline regions separated from the static line-shape of crystalline PE. The ^{13}C CSA patterns of the two samples recorded at T = 320 K are shown in Fig. (3.7). The pat-

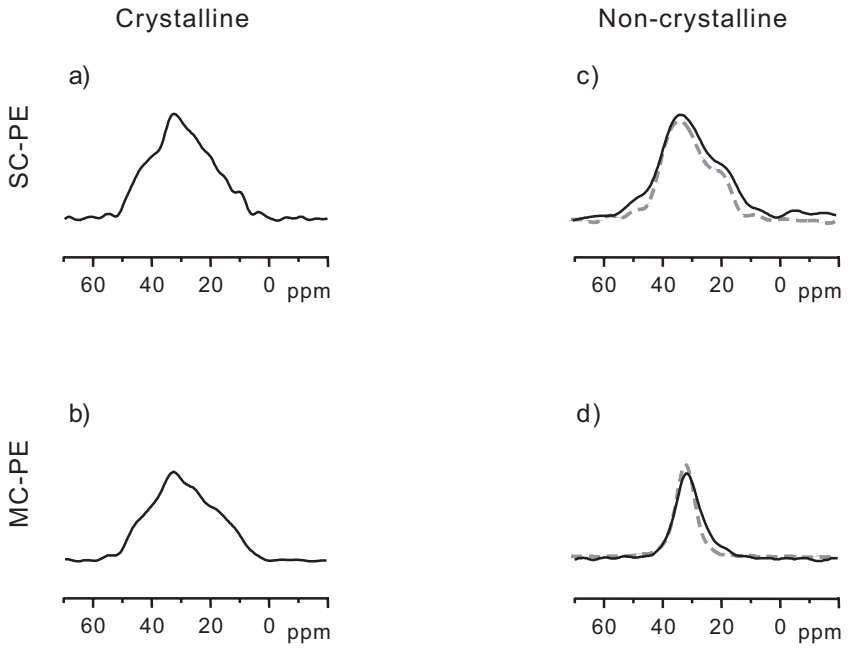

Figure 3.7: *The ^{13}C chemical shift anisotropy (CSA) patterns of two PEs: the crystalline pattern of SC-PE (a) and MC-PE (b); the non-crystalline patterns of SC-PE (c) and MC-PE (d). These patterns are taken from the slices of SUPER experiments, measured at 3k Hz MAS and T=320K. For a comparison two non-crystalline patterns of one sample are shown: the patterns drawn with the black line were measured via $^{1}H \rightarrow {}^{13}C$ cross-polarization, same as the crystalline patterns, and the patterns drawn with the gray dash line were measured via ^{13}C single pulse excitation.*

terns of the crystalline components (Fig. 3.7a, b) are very similar for the two samples, whereas significant differences have been observed for the non-crystalline components (Fig. 3.7c, d). The ^{13}C CSA powder line shape of non-crystalline regions in the solution crystallized sample shows features of an axial-symmetric CSA tensor, whereas the ^{13}C CSA pattern of non-crystalline regions of the melt crystallized sample is lacking typical features of tensorial powder lineshapes but resembles a broadened isotropic line.

The shape of ^{13}C CSA pattern is a good indication for the motion geometry of chain segments in this case. From the ab-initio simulation, we know that the all-trans conformer of PE CH_2 has three tensor principle values as: $\sigma_{11} = 50.0$ppm, $\sigma_{22} = 36.5$ppm, $\sigma_{33} = 12.5$ppm. For the gauche conformers, the three tensor principle values usually vary with the dihedral angle of involved carbon and the conformation of closely contacted carbons. Fig. (3.8) shows the tensor orientations in the molecular frame for the

all-trans conformer and the gauche conformer with a series as *ttgggt*.

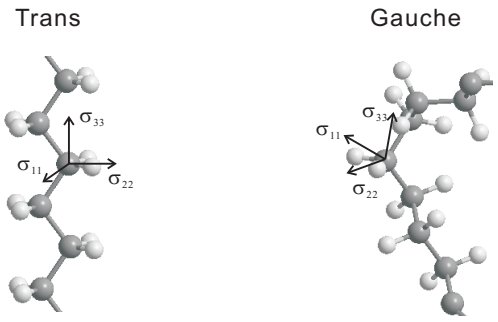

Figure 3.8: *PE ^{13}C CSA tensor orientation in different conformers. For the all-trans conformer, three tensor principle values are $\sigma_{11} = 50.0ppm$, $\sigma_{22} = 36.5ppm$, $\sigma_{33} = 12.5ppm$. For the gauche conformer with a series as $ttg^{*}ggt$, three tensor principle values of middle carbon are $\sigma_{11} = 84.0ppm$, $\sigma_{22} = 24.1ppm$, $\sigma_{33} = 20.4ppm$. The tensor orientations in the molecular frame are indicated by the direction of arrows.*

If there is no molecular motion involved, the three principle values of CSA tensor determine the shape of CSA pattern. However, in NMR practice the molecular motions in a sample always give perturbations to the pattern shape. The degree of perturbation is determined by the motion frequency as well as the geometry of motion. The isotropic chain motion usually averages these three values and give an isotropic resonance line, which is the case shown in MC-PE. In the case of SC-PE, the ^{13}C CSA pattern of non-crystalline regions shows features of an axial-symmetric CSA tensor. To keep this axial-symmetric tensor shape for the moving CH_2 units in non-crystalline regions, the most probable way is to let the CH_2 rotate along the chain backbone, which also matches the helical jumps of CH_2 units inside PE crystals. The rotation frequency should be faster than $|\sigma_{11} - \sigma_{22}|$ to get the axial symmetric tensor. In the case of SC-PE, the rotation frequency will be faster than 1.7kHz. Compared to the fast isotropic motion existing in non-crystalline regions of MC-PE, the molecular motion in non-crystalline regions of SC-PE is still highly restricted.

In literatures, the presence of an interphase with intermediate order located between non-crystalline and crystalline regions has been proposed based on both theoretical [Flory 84, Balijepalli 98, Gautam 00] as well as experimental approaches [Kitamaru 77, Mandelkern 90, Chen 92, Uehara 00]. In solid state NMR, this aspect can be addressed

varying the initial source of polarization of the ^{13}C CSA recoupling experiment. If the experiment is started with an initial cross polarization step using a short contact time, the acquired signal result predominantly from sites with a strong heteronuclear dipolar coupling and thus crystalline regions and the non-crystalline regions in close proximity to crystalline areas. In contrast, when the experiment is started with the direct excitation using a short relaxation delay (2s), the signals resulting from the mobile non-crystalline regions of sample dominate the acquired spectrum, due to the long ^{13}C T_1 relaxation in crystalline regions of PE. The non-crystalline patterns of the two samples obtained from these two kinds of experiments are exhibited in Fig. (3.7c, d). As shown in Fig. (3.7c), the line shapes of non-crystalline patterns of SC-PE acquired with both experimental approaches match very well, indicating that a homogeneous behavior with restricted anisotropic dynamics is present in non-crystalline areas in SC-PE. As to MC-PE shown in Fig. (3.7d), the Lorentzian line shape obtained from the CP method is broader than that obtained from direct excitation, however, the line shape stays Lorentzian and does not show any features of a powder line shape resulting from an axial-symmetric CSA tensor. Combining the results from dipolar and CSA recoupling experiments, it can be concluded that the conformational exchange in non-crystalline areas of the solution crystallized sample is highly restricted whereas the conformational space of the polymer chain in the melt crystallized sample seems largely accessible leading to a more isotropic segmental dynamic.

3.4 Temperature dependence of local chain dynamics

Fig. (3.9) shows the $^{1}H-^{13}C$ REREDOR sideband patterns for non-crystalline regions in these two samples at different temperatures. The corresponding $^{1}H-^{13}C$ dipolar couplings are listed in Table 3.4. A striking observation from these REREDOR experiments is that for SC-PE the residue $^{1}H-^{13}C$ dipolar coupling hardly changes with increasing temperature, indicating that the motional anisotropy in non-crystalline regions of SC-PE is maintained even at the relatively high temperatures. On the contrary, in the melt crystallized sample the residual $^{1}H-^{13}C$ dipolar coupling decreases with increasing temperature, indicating an increase in the local chain dynamics.

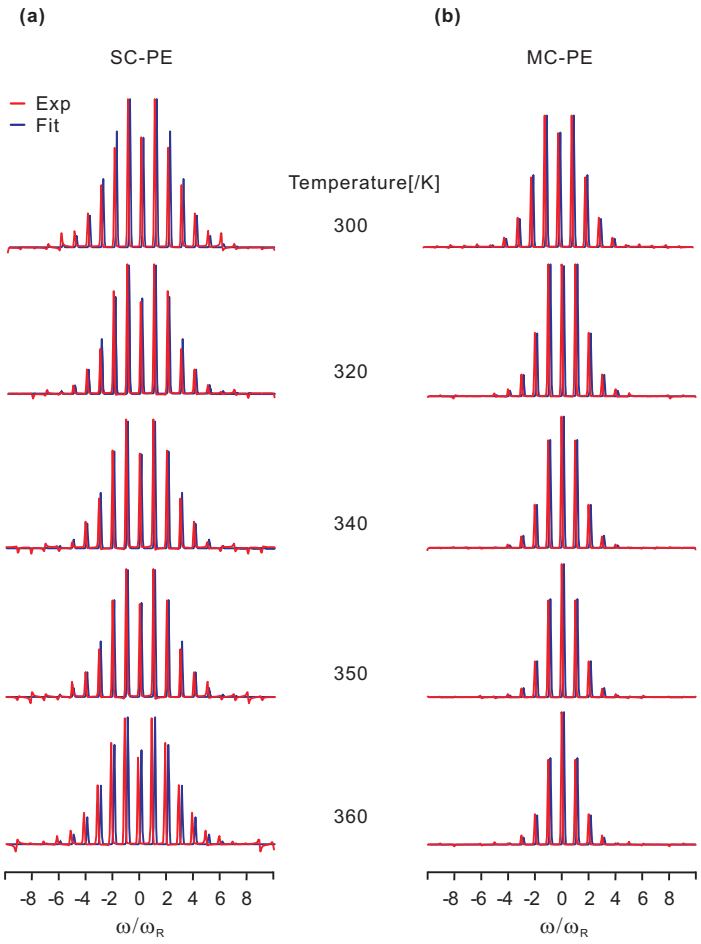

Figure 3.9: *The spinning sideband patterns of* $^{1}H-{}^{13}C$ *spin pairs in non-crystalline regions of the PEs, obtained from the REREDOR experiments at different temperatures.*

A similar phenomenon was observed in the ^{13}C CSA patterns of non-crystalline regions at different temperatures, which are shown in Fig. (3.10). In Fig. (3.10), for MC-PE with increasing temperature, the width of resonance line decreases, but the powder lineshape always keeps the isotropic feature. Whereas, the lineshape of^{13}C CSA pattern of SC-PE always shows features of an axial-symmetric CSA tensor. This phenomenon further confirms that the motional anisotropy in non-crystalline regions of SC-PE is maintained at relatively high temperatures, indicating the maintenance of folding structure in non-crystalline regions of SC-PE at the relatively high temperatures.

T[/K]	$D_{IS}/2\pi$ [/kHz] of SC-PE	$D_{IS}/2\pi$ [/kHz] of MC-PE
300	9.1	6.9
320	9.1	6.3
340	8.9	5.6
350	8.9	5.3
360	8.8	5.0

Table 3.1: *The $^1H-{}^{13}C$ dipolar coupling constant $D_{IS}/2\pi$ (kHz) in non-crystalline regions of PEs at different temperatures. These constants are from the simulations of the experimental spinning sideband patterns.*

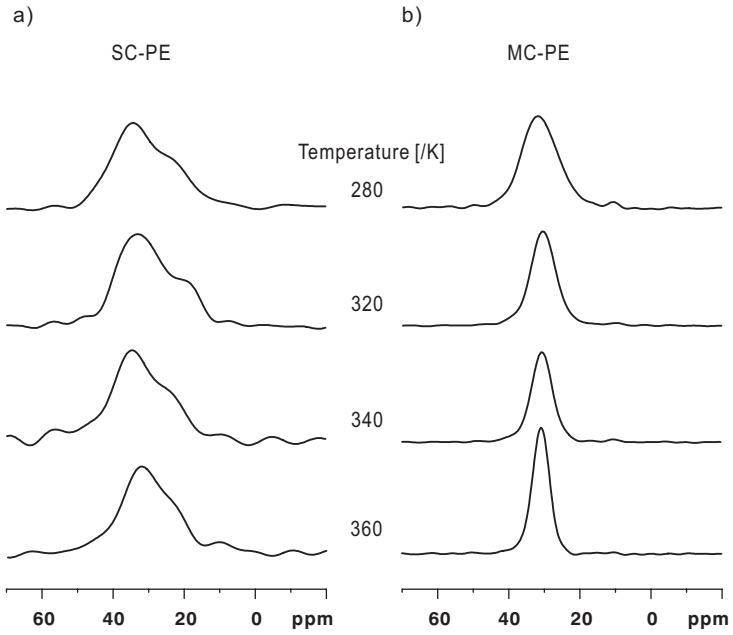

Figure 3.10: *The non-crystalline ^{13}C CSA patterns of two PEs at different temperatures: (a) SC-PE; (b) MC-PE. These patterns are taken from the slices of SUPER experiments, measured via ^{13}C single pulse excitation at 3k Hz MAS.*

3.5 Chain diffusion between crystalline and non-crystalline regions in the linear UHMW-PEs

The methods applied so far, probe the local dynamic behavior of chain segments, but do not elucidate the long range chain diffusive motion. Exchange NMR methods can provide this information, since the polymer segments change their conformation and thus their isotropic chemical shift when moving between the crystalline environment to non-crystalline areas [Schmidt-Rohr 91]. The remarkable difference of ^{13}C T_1 re-

laxation times in non-crystalline and crystalline regions facilitates to record 1D ^{13}C exchange NMR spectra using T_1 filtration (saturation of ^{13}C polarization followed by a short relaxation delay) to provide a selective polarization of non-crystalline areas. Cooperative chain motion from non-crystalline regions to crystalline areas is then observed via the increase of polarization in crystalline regions on time scales significantly shorter than the ^{13}C T_1 relaxation times of these sites. The chain motion process and the idea to monitor this process via NMR exchange methods are illustrated in Fig. (3.11).

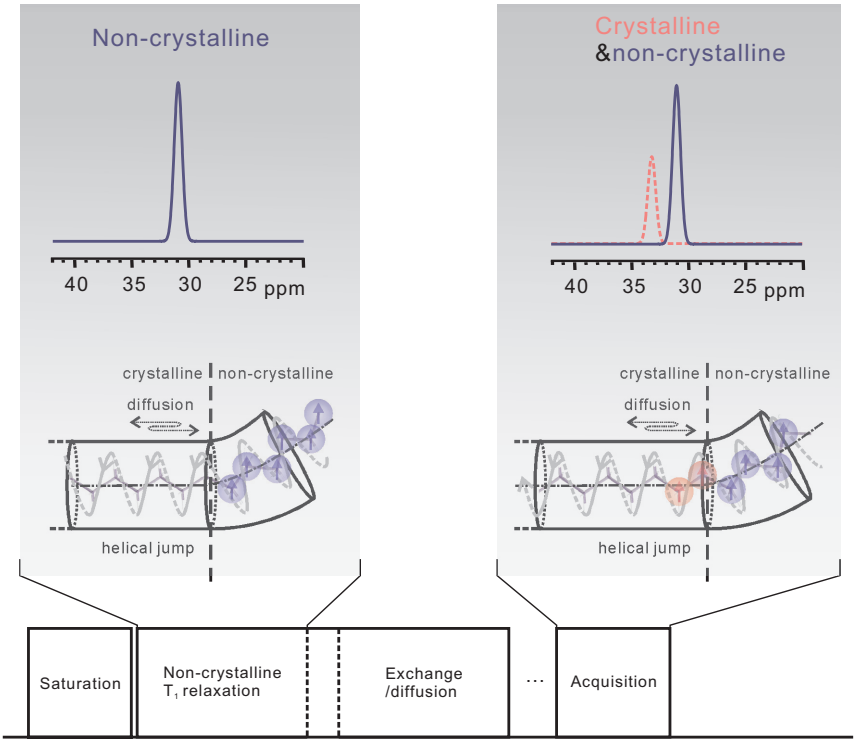

Figure 3.11: *The schematic illustration of the idea how to monitor the chain diffusive motion using the NMR exchange experiment.*

Based on the idea illustrated in Fig. (3.11), the 1D ^{13}C exchange NMR spectra of both samples were recorded, which are shown in Fig. (3.12). Fig. (3.12a) shows the exchange NMR spectra of both samples recorded at T = 320 K with various exchange times, whereas in Fig. (3.12b) the temperature dependence of 1D ^{13}C exchange NMR spectra acquired with a constant exchange time of 5s is given.

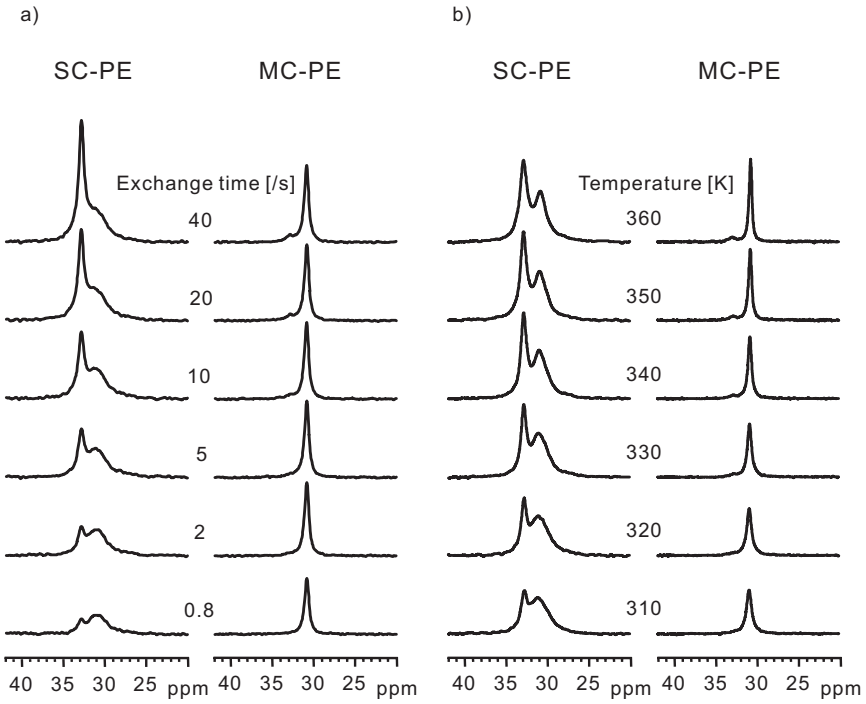

Figure 3.12: *The ^{13}C MAS exchange spectra of SC-PE and MC-PE: (a) measured at 6k Hz MAS, T=320K with different exchange times; (b) measured at 6k Hz MAS, a fixed exchange time (5s) and with different experimental temperatures.*

In MC-PE the build up of signal arises mainly from the relaxation process of non-crystalline regions. Whereas, in SC-PE with increasing waiting time two peaks are observed. The peak positions match with the non-crystalline and crystalline chemical shifts. The intensity of the crystalline peak increases rapidly with the exchange time. Considering the large relaxation time required for the crystalline component, the build up of the crystal peak is attributed to the exchange process of the chain segments from non-crystalline to crystalline regions. Such exchange, though very weak, is also observed in MC-PE at a large exchange time of 40s.

To quantify the rate of chain diffusion, the crystallinity of sample has to be taken into account. From single pulse ^{13}C MAS spectra, the crystallinity of these two samples were determined to $75 \pm 5\%$ for SC-PE, and $44 \pm 5\%$ for MC-PE at 320K. Then after normalizing the intensities of crystalline signals in the spectra shown in Fig. (3.12a), we know that with a 40s exchange time nearly 70% of the crystallites in SC-PE got polarized. Whereas only $\sim 10\%$ of the crystallites in MC-PE got polarized within the same exchange time. This difference clearly shows two different chain diffusive

motions existing in these two samples. Considering the same chemical natures of the samples, this difference thus can be reasonably related to the different arrangement of chains in non-crystalline regions, which has already been indicated by the different local chain dynamics in the above discussion.

When combined with the data reported in Fig. (3.6) and (3.7), it can be conclusively stated that though local chain dynamics in non-crystalline regions of the solution crystallized sample is restricted, the motional anisotropy present in non-crystalline regions favors the cooperative motion between non-crystalline and crystalline regions. On the contrary in the melt crystallized sample, though local chain dynamics is high, hardly any cooperative motion between non-crystalline and crystalline regions is observed. These observations at a temperature below the α-relaxation temperature of PE (Chapter 5, [Strobl 97]) reported for the first time are counterintuitive.

The chain exchange process in linear polyethylenes, above the α-relaxation temperature has been reported earlier by Schmidt-Rohr and Spiess. Fig. (3.12b) shows the exchange process at different temperatures at fixed exchange time of 5s. With increasing temperature, close to the α-relaxation temperature the exchange process starts appearing in MC-PE, whereas in SC-PE the process increases with temperature.

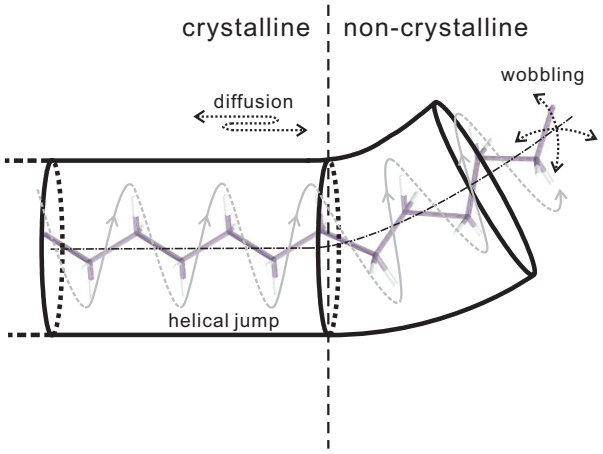

Figure 3.13: *The motions of PE chain. The individual helical jump generates the translation of chain stem by one CH_2 unit. This chain translative motion occurs many times then gives rise to the chain diffusive motion between crystalline and non-crystalline regions, which is observed in NMR experiments. The tube represents the restriction of the PE chain from its environment.*

The cartoon picture in Fig. (3.13) gives an explanation for this counterintuitive chain dynamics observed in SC-PE and MC-PE. In this picture, a chain stem is moving between the non-crystalline region (the right side) and the crystalline region (the left side). The tube represents the restriction of the PE chain from its environment and the diameter of tube indicates the degree of restriction. In this model the chain diffusion is achieved by the sliding of the chain stem in the tube. Due to the chain connectivity, the motion of non-crystalline chain portion somehow is connected with that of crystalline chain portion. Taking into account the fact that the chain diffusion in the crystal is always along the chain backbone, it is easy to imagine that the favorable chain motion in non-crystalline regions is the one with a direction along the chain backbone, whereas the random motion such as the wobbling of chain segments is not compatible with the diffusive motion, even can be an obstacle of chain diffusion. Following this point, reducing the freedom of the non-crystalline chain motion, i.e. from random motion to the motion along the chain backbone, thus would favor the chain diffusive motion. In the thermodynamics, the reduction in the freedom of the chain motion in fact is lowering the entropy change involved in the motion. Hence, besides the activation energy which relates to the change of chain conformation involved in the motion, the entropy change in the chain diffusive motion could also play an important role. An experimental confirmation of this viewpoint will be given in Chapter 6.

3.6 Conclusions

The above observations clearly demonstrate that the restricted local chain mobility present in non-crystalline regions of the solution crystallized sample plays a conclusive role in the cooperative chain motion. Absence of such restriction in the melt crystallized sample of the same polymer shows suppressed cooperative motion from non-crystalline to crystalline regions. This has implications in our understanding of crystal thickening, for an example the solution crystallized sample shows enhanced chain mobility along the crystallographic *c*-axis, ultimately leading to doubling of the initial crystal thickness after annealing [Rastogi 97].

Chapter 4

Morphological Effects on Molecular Dynamics in Non-crystalline Regions of Linear LMW-PE

In this chapter the molecular dynamics in non-crystalline regions of the low molecular weight polyethylenes (LMW-PE) will be investigated. The investigation represents the continuation of the analogous work on the UHMW-PEs in the last chapter. Again, the motional anisotropy in non-crystalline regions of the LMW-PEs and its implication on the chain diffusive motion between non-crystalline and crystalline regions, will be focused in the discussion.

The local chain dynamics in non-crystalline regions of the LMW-PEs was studied via analyzing the peak width of non-crystalline signals in the CP/MAS spectra, the motionally reduced $^{1}H - ^{13}C$ dipolar coupling and the line shape of the ^{13}C CSA powder pattern. Different with the case of UHMW-PEs, the motional anisotropy in non-crystalline regions of the LMW-PEs is present not only in the solution crystallized samples but also in the melt crystallized samples. Similar as the case of the last chapter, the motional anisotropy is thought to be caused by spatial constraints from the chain folds present in non-crystalline regions of the LMW-PEs.

The implication of anisotropic motion on the chain diffusive motion in the LMW-PEs was studied with the help of ^{13}C exchange experiment. The experimental data show that all the studied LMW-PEs with residual CSA present in non-crystalline regions ex-

hibit a significant chain diffusion between crystalline and non-crystalline regions. This observation further reveals the influence of the anisotropic motion on the chain diffusive motion between crystalline and non-crystalline regions. In the last part of this chapter the molecular weight dependence of the chain diffusive motion is discussed shortly.

Two LMW-PEs were investigated in the work of this chapter. One is named as LMW-PE1 with a molecular weight $M_w = 52kg/mol$, polydispersity index (PDI) 2.54. The other is named as LMW-PE2 with a molecular weight $M_w = 87kg/mol$, PDI=2.46. The variation of sample morphology was still achieved by melt/solution crystallization process. The solid state NMR techniques performed to study the morphological influence on the chain dynamics are similar to those used in the last chapter.

4.1 Partially ordered component and motional anisotropy

From the discussion in the last chapter, the presence of the anisotropic motion in non-crystalline regions of UHMW-PE has been clearly demonstrated with the help of various advanced NMR techniques. The origin of this anisotropic motion is related to the chain folding structure, which is often present in non-crystalline regions of solution crystallized PE samples. In this section, we will have a short discussion about the relationship between the motional anisotropy and the partially ordered component, the latter, that is often used to describe the interfacial component between crystalline and non-crystalline regions of polymer (Chapter 4, [Sperling 92]). With the knowledge of the motional anisotropy and the partially ordered component in PE, a comparison of their detection methods (X-ray vs. NMR) will be given in the last part of this section.

4.1.1 Partially ordered component and motional anisotropy in PE

The microstructure of a semi-crystalline polymer is often described by a two-component model, of crystalline regions embedded in a matrix of non-crystalline part [Flory 53, Mandelkern 64, Mandelkern 83]. In this model, non-crystalline chains are usually believed to approach random coil conformations and crystalline chains take regular conformations and align parallel to each other to fulfill the requirement of crystal lattice. Besides random non-crystalline regions and regular crystalline regions,

a third component with intermediate order has been proposed to explain some special physical properties of polymers, such as the unexpected high density of non-crystalline region [Robertson 65]. For polyethylene the molecular chains have no special interaction such as H-bonding in non-crystalline regions. The partially ordered component in non-crystalline regions thus is believed to be present only in the crystalline/non-crystalline boundary [Baker 01, Rastogi 05]. Hence this component in PE is often called as the interfacial component referring to its location. The introduction of this partially ordered non-crystalline component is necessary, because long PE chains are unlikely to tolerate the necessary discontinuity in molecular order at the crystalline/non-crystalline interface, which means that a sharp demarcation line between crystalline and non-crystalline regions is very unlikely. The density constraints between crystalline and non-crystalline regions also propose this partially ordered component [Hoffman 83, Frank 79, Di Marzio 84]. The existence of partially ordered component in non-crystalline regions of PE has been proven from both theoretical [Balijepalli 98, Flory 84, Gautam 00] and experimental works [Axelson 85, Kitamaru 77, Mandelkern 90, Mowery 06, Uehara 00].

With the above knowledge the appearance of the partially ordered component in PE can be described as the following. Assuming that the crystallites are of infinite extent in the basal plane, then at small distances away from each crystallite surface, most of the chains present will have originated from the crystallite. The average chain orientation then will not be as random as that in the bulk amorphous matrix but will be distributed around the normal to the crystallite surface: this is the proposed partially ordered interfacial component. With this picture in mind, one then could envisage the relationship between the motional anisotropy and the partially order component in PE: it is the spatial constraints from the sample morphology that restrict the motion of partially ordered components, then lead to the observed motional anisotropy. Hence, to some extend the motional anisotropy in nature can be considered as the dynamic behavior of partially ordered component. The degree of the motional anisotropy depends on the type of involved dynamic process and the degree of restriction on the partially ordered component.

By varying crystallization condition, the degree of order of the partially ordered component can be changed. In the case of solution crystallized PE, if the chains which

emanate from the crystallite surface immediately fold back into the crystallite, by the adjacent reentry, it is conceivable that due to the spatial constraints the formed chain folds in nature is the partially ordered component. Whereas, if the morphology of PE is similar to that described by the switchboard model, the persistence of chain order, i.e. all-trans in the crystal, will be quite weak since the chains are about to enter the completely random state. As a consequence the partially ordered component in this case will be present only in the region which is very close to the crystal surface. From the computer simulation, Rutledge and coworker [Gautam 00, Balijepalli 98] have reported that a ~ 0.6nm layer with the chains inside possessing intermediate order bridges crystalline region and non-crystalline regions.

4.1.2 Detection of the partially ordered component and the motional anisotropy

Although the presence of the partially ordered component in non-crystalline regions of PE has been proven necessary, the detection and characterization of this component experimentally are not easy, because this partially ordered component does not exhibit a clear first-order melting transition or a clear x-ray diffraction. The spectroscopic studies have provided most of the evidence for the presence of partially ordered component in non-crystalline regions of PE (X-ray diffraction [Tanabe 86, Baker 01], solid state NMR spectroscopy [Kitamaru 86, Cheng 94] and Raman spectroscopy [Wang 91]). Besides, differential scanning calorimetry (DSC) [Mandelkern 85] and dielectric relaxation and dynamic mechanical studies [Popli 84] also gave some experimental evidences. In addition the discrepancies in crystallinity values determined from different techniques have been attributed in part to the fact that some techniques include the contribution from the partially ordered component, others don't. However, the above experimental evidence for the partially ordered component in PE is better to be considered as the proof of the presence of this component rather than an investigation of the behavior of this component itself.

Compared to the techniques or methods mentioned above, the methods used in this work, i.e. monitoring the anisotropy of chain motion via the $^{1}H-{}^{13}C$ dipolar coupling constant and the line shape of the ^{13}C CSA, gives a way that not only evidences the presence of the partially ordered component, but also reveals the dynamic behavior of

this component. To elucidate this point, a comparison between the wide angle X-ray diffraction (WAXD) and the detection of local anisotropic interactions with NMR will be given in the following.

WAXD is one of the most used techniques to determine the ordered structure of polymers. In principle the WAXD pattern is produced by the diffraction of X-rays through the periodically spaced atoms (or precisely the electrons that surround the atoms). According to the range of diffraction angle, the ordered structure revealed in the WAXD pattern usually has periodicity on the sub-nanometer scale, which is the reason that WAXD is often used for the characterization of crystal structure of polymer. To monitor the partially ordered component in PE, however, WAXD is not suitable. Several factors limit its application. First, the partially ordered component, just as its name implies, doesn't contain the completely periodical and ordered structure, thus can cause a strong broadening on the diffraction lines. Second, the content of this component in PE is also a problem. The results from computer simulations reveal that the semicrystalline component between the crystal and the amorphous is a layer with a thickness of $\sim 6\mathring{A}$ [Gautam 00]. Compared to the usual lamellar thickness of PE crystallites $> 100\mathring{A}$, the content of partially ordered component in PE is quite low. Furthermore, the small thickness of this component would cause a broadening effect on its diffraction lines as indicated by the Debye-Scherrer formula. As a result, the investigation of this component with WAXD becomes even more difficult.

In contrast to WAXD, the NMR methods used in this thesis monitor the motionally averaged local NMR interactions and derive the structural information from the dynamic properties of chain motion. We monitored the motionally averaged $^1H - ^{13}C$ dipolar coupling and ^{13}C CSA of CH_2 units in non-crystalline regions of PE. These motionally averaged interactions reveal some spatial restriction on the motion of CH_2 units. Since there are no specific interaction such as H-bonding existing in non-crystalline regions of PEs, the restriction on the motion of CH_2 units can be reasonably attributed to the organization of PE chains, which then can be related to the structure or the morphology in the sample. The difference of WAXD detection and our methods for detecting the partially ordered components in PE has been illustrated in Fig. (4.1).

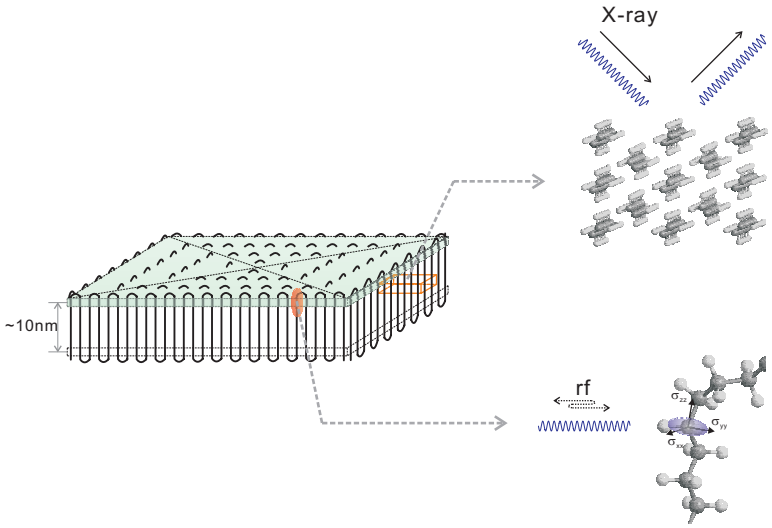

Figure 4.1: *The illustration of detection ways in X-ray and NMR.*

As the diffraction peak in WAXD originates from the periodic structure, the observed motionally averaged anisotropic NMR interaction can be considered as the result from the more or less ”ordered” molecular motion. This ”ordered” molecular motion serves as a bridge connecting the motionally averaged local interaction with the ”ordered” structure. However, one thing to be kept in mind is that the anisotropic chain motion is only a dynamical property of polymer chain units, and to derive the structural information from the dynamic behavior, one has to be very careful to the model dependence of the method. In most cases an observed dynamical property can ”fit” for several equivalent motional modes. In order to remove such ambiguities, it is necessary to acquire other data or the knowledge from other source and check their consistency. In the case of our work, the restriction on the PE chain units as revealed from $^{1}H-{}^{13}C$ dipolar coupling is consistent with the axial pattern of ^{13}C CSA, and the proposed motional mode from the analysis of ^{13}C CSA does not contradict the chain translation motion observed in the ^{13}C exchange experiment.

4.2 Possible morphology in melt crystallized LMW-PE

The morphology of a polymer varies with crystallization conditions, such as the polymer concentration (if crystallized from solution), state of entanglement, rate of crystallization, chemical nature of polymer chain and other factors [Gedde 04, Sperling 92, Strobl 97, Ungar 01]. The variation of morphology essentially is an indication of the

strong kinetic factor involved in the crystallization process, which partially results from the long chain nature of polymer. Generally when polymers crystallize from a dilute solution, a morphology close to the regular adjacent reentry is possible. Whereas, when crystallization occurs from a melt, where entanglements dominate, a morphology close to the switchboard model is expected. In the case of UHMW-PE these rules are applicable, as shown in the last chapter. In the case of LMW-PE, however, the solution/melt crystallization process doesn't always lead to the formation of the two different morphologies mentioned above.

In fact the morphology developed from melt crystallization is a highly debated topic in polymer crystallography. The central point of contention ultimately is about the nature of the crystal surface. Hoffman and Keller pushed the idea of adjacent reentry as the primary mechanism. In their views the morphology developed from the melt crystallization should also contain a significant amount of regular chain folds. This has been supported by the polymer decoration technique developed by Lotz [Wittmann 85]. Other known scientists from the field such as Flory and Fischer propose the switchboard model. Strobl also favors less ordered reentry models in his text book [Strobl 97]. Yet we still lack a technique to monitor each polymer chain to see how it is organized between crystalline and non-crystalline regions. The experimental and theoretical studies actually always take a "mean-field" approach by simplifying the individual behavior into an average form. So, if the morphology of polymer had a composite nature, e.g. the coexistence of adjacent reentry structure and switchboard model structure, the experimental results could be explained by both sides. Evidently, the separation would come up if one took a selective view of results.

Compared to UHMW-PE, LMW-PE have two distinct features, that is, the relatively low molecular weight and high content of mobile chain ends. These two features have a strong effect on the morphology of LMW-PE developed during melt crystallization. During melt crystallization, the conditions are far away from equilibrium, the polymer chains must adopt a regular conformation from the highly entangled, disordered melt and align parallel together to form the crystallites. The relatively short chains of LMW-PE, which can get disentangled, thus will be less constrained by the chain entanglements during the formation of the crystallites. As a consequence, the morphology of LWM-PE developed from melt crystallization could contain a considerable

similarity with that obtained from solution crystallization of the same sample, where the crystals are assumed to be formed from the fully disentangled chains.

This similarity in the morphology consequently leads to a similarity in the morphological effect on the chain dynamics, especially for the chains in non-crystalline regions. Therefore, in contrast to UHMW-PE, where the anisotropic molecular motion in non-crystalline regions only can be found in the solution crystallized sample, in the case of LMW-PE the anisotropy could be observed in non-crystalline regions of the solution crystallized samples as well as the melt crystallized samples.

4.3 Local chain dynamics in non-crystalline regions of the LMW-PEs

We start our discussion from the $^{13}C-CP/MAS$ spectra of LMW-PEs in Fig. (4.2), where the spectra of UHMW-PEs are also given for comparison. Fig. (4.2a) shows the spectra of solution crystallized samples, whereas Fig. (4.2b) shows the spectra of all melt crystallized analogues. Comparing the broad non-crystalline peaks in Fig. (4.2a) with the relatively sharp non-crystalline peaks in Fig. (4.2b), one could easily realize that the molecular dynamics present in non-crystalline regions of solution crystallized samples is much more restricted than that in non-crystalline regions of melt crystallized samples, indicating the strong influence of crystallization conditions on the chain dynamics in non-crystalline regions of PEs, a point that has been already mentioned in the last chapter.

An interesting phenomenon is indicated by the comparison of the spectra in Fig. (4.2a), where the spectra of LMW-PEs look very similar with that of UHMW-PE, especially for their broad non-crystalline peaks. Considering the big difference in the molecular weight of these samples, this similarity reveals a point that the chain segments in non-crystalline regions of these samples experience more influence from their local environments (or structure) rather than the molecular weights. This point has an important implication on the chain diffusive motion between crystalline and non-crystalline regions of PE, which will be discussed later.

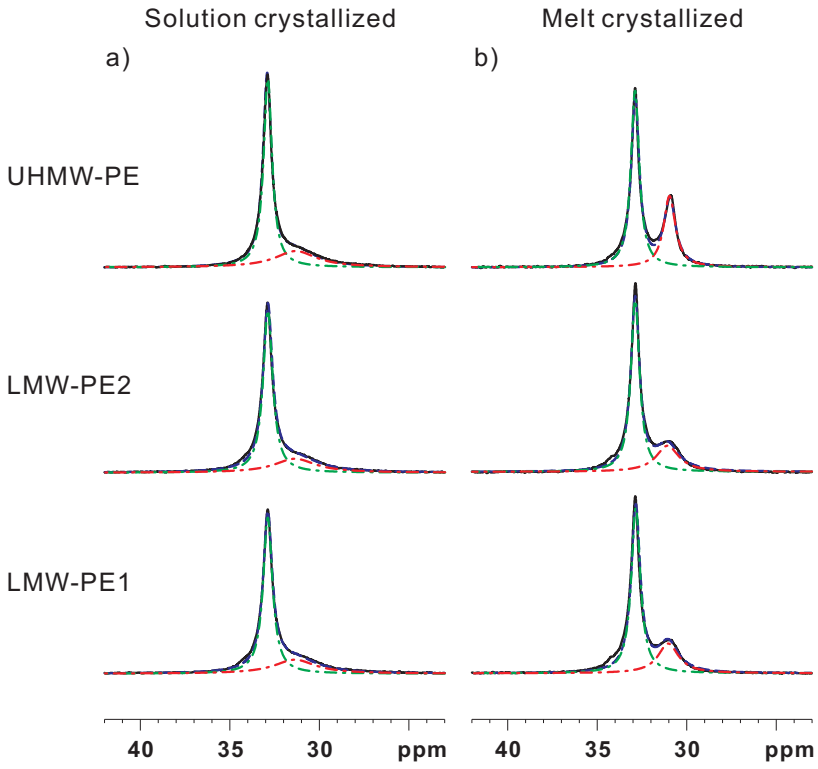

Figure 4.2: *The ^{13}C CP/MAS spectra of PEs at 320K: (a) for the solution crystallized samples; (b) for the melt crystallized samples.*

In contrast to the very similar spectra shown in Fig. (4.2a), the spectra of the melt crystallized PE samples in Fig. (4.2b) show a significant variation with the molecular weight. In Fig. (4.2b) the non-crystalline peaks of the melt crystallized LMW-PEs appear smaller and wider than that of the melt crystallized UHMW-PE. The smaller non-crystalline peaks of LMW-PEs suggest higher crystallinity in these samples, and the relatively big width of the non-crystalline peaks suggests the presence of some restriction on the chain dynamics in non-crystalline regions of these samples. However, compared to the corresponding solution crystallized samples, the non-crystalline peaks of the melt crystallized LMW-PEs are still sharper, which means that the restriction on chain dynamics in non-crystalline regions of the melt crystallized LMW-PEs might exist, but should be much weaker than those in the solution crystallized samples. In the other words, the intermediately broad non-crystalline peaks in the melt crystallized LMW-PEs could be a hint towards the coexistence of a mobile component and a restricted component in their non-crystalline regions. This composite nature of non-crystalline regions in the melt crystallized LMW-PEs is also indicated by the

measurement of the $^{1}H-{}^{13}C$ heteronuclear dipolar coupling of CH_2 units in non-crystalline regions of the samples.

Due to its orientation dependence, the $^{1}H-{}^{13}C$ heteronuclear dipolar coupling can be averaged by different dynamic processes, leading to different degrees of reduction of the observed $^{1}H-{}^{13}C$ dipolar coupling constant [Fischbach 03, Saalwachter 02]. Hence the $^{1}H-{}^{13}C$ heteronuclear dipolar coupling constant gives a measure of the molecular dynamics. In this work the $^{1}H-{}^{13}C$ heteronuclear dipolar coupling constants in non-crystalline regions of the LMW-PEs were obtained via the REREDOR experiment. The resulting spinning sideband patterns and $^{1}H-{}^{13}C$ heteronuclear dipolar coupling constants taken at the isotropic chemical shift of the non-crystalline signals are shown in Fig. (4.3).

With the observed $^{1}H-{}^{13}C$ dipolar coupling constants one could have several comparisons to see different dependences of the non-crystalline chain dynamics in the LMW-PEs. From the comparison of the patterns in Fig. (4.3a) and those in Fig. (4.3b), it is evident that the profiles of the spinning sidebands for the solution crystallized LMW-PEs and UHMW-PE are much broader than those of the melt crystallized analogues, indicating the presence of stronger dipolar couplings in non-crystalline regions of the solution crystallized samples. This result is consistent with the different width of non-crystalline peaks in the solution crystallized and melt crystallized samples shown in Fig. (4.2).

Because of the long chain nature of PE, the molecular dynamics in PE usually includes the local dynamics of chain segments and the long range dynamics concerning the motion of several chain segments or even the whole chain. Due to their different scales in time and space, the local dynamics does not necessarily have a direct relationship with the long range dynamics of polymer chain, which usually has a dependence on the molecular weight. Therefore, it is not very surprising to see the effective $^{1}H-{}^{13}C$ coupling constants in non-crystalline regions of the LMW-PEs are the same as that of the solution crystallized UHMW-PE in spite of their huge molecular weight difference, when comparing the sideband patterns and relevant $^{1}H-{}^{13}C$ coupling constants. These similar effective $^{1}H-{}^{13}C$ coupling constants result from a similar local molecular dynamics present in non-crystalline regions of the PE samples and thus

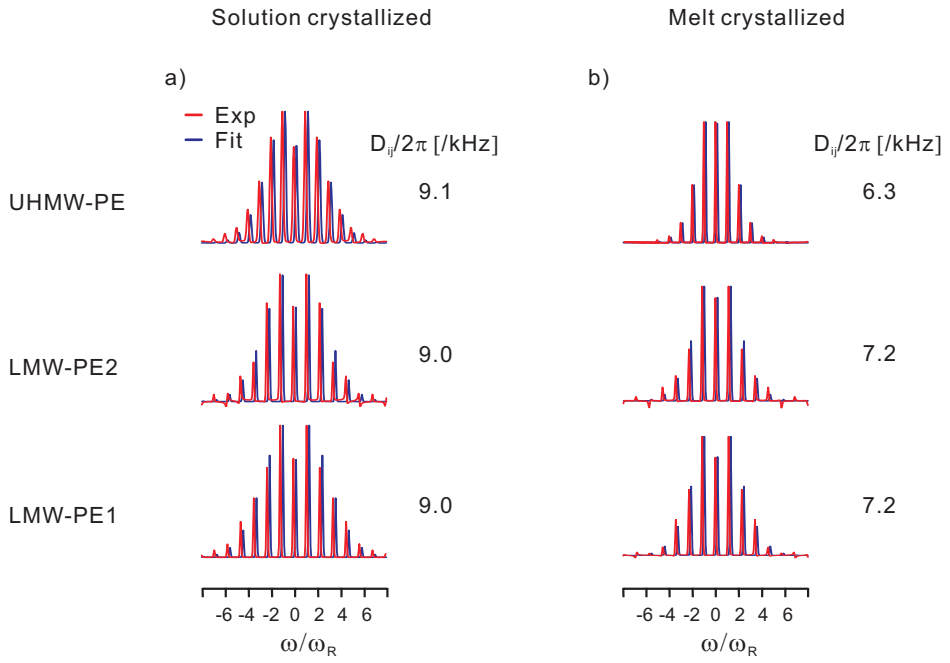

Figure 4.3: *The non-crystalline REREDOR spinning sideband patterns of PEs at 320K: (a) for the solution crystallized samples; (b) for the melt crystallized samples.*

indicate a similar local environment in non-crystalline regions of the solution crystallized samples. However, different with the case in the solution crystallized samples, the $^{1}H-{}^{13}C$ coupling constants in non-crystalline regions of melt crystallized samples seem to vary with the molecular weights of samples. The quantitative analysis of the sideband patterns yields the effective residual heteronuclear coupling constants 7.2 kHz for non-crystalline components in the two melt crystallized LMW-PEs. A coupling of 6.3 kHz was obtained for the melt crystallized UHMW-PE. The higher effective $^{1}H-{}^{13}C$ coupling constants in the melt crystallized LMW-PEs indicate a certain degree of restriction present in non-crystalline regions of these samples. If one recalls the ^{13}C CP/MAS spectra of these samples shown in Fig. (4.2b), this observation matches the interpretation of their relatively wide non-crystalline NMR signals.

The above observations from the ^{13}C CP/MAS spectra and the analysis of $^{1}H-{}^{13}C$ coupling constants indicate the influence of the crystallization conditions on the local chain dynamics present in non-crystalline regions of the LMW-PEs. If crystallized from solution, the chain dynamics in non-crystalline regions of the LMW-PEs experiences a similar degree of restriction as that in UHMW-PEs. Whereas, if crystallized

from melt, the LMW-PEs seem to have a certain restriction of the chain dynamics in non-crystalline regions, which does not exist in UHMW-PE. Considering the chemical structure of PE, the different chain dynamics in non-crystalline regions of PEs most probably is caused by the different spatial constraints originating from the organization of non-crystalline chains. For the solution crystallized LMW-PEs, this constraints are very likely to arise from the chain folds in non-crystalline regions as the case of the solution crystallized UHMW-PE. As to the melt crystallized LMW-PEs, the origin of the constraints is not clear so far. In the following static ^{13}C CSA patterns of the solution/melt crystallized LMW-PEs will be analyzed to provide the geometrical information about the dynamic processes of non-crystalline chains, which could be very helpful to elucidate the nature of the spatial constraints in non-crystalline regions of the LMW-PEs.

The static ^{13}C CSA patterns of LMW-PEs were recorded via the SUPER experiment. The crystalline ^{13}C CSA patterns of LMW-PEs in Fig. (4.4) look similar. This similarity indicates that the major parts of crystalline components in these samples are similar, although non-crystalline regions of these samples might possess a big difference. However, compared to the solution crystallized samples, the crystalline pattens of the melt crystallized LMW-PEs always only show soft features. These soft features of the patterns probably is indicative of the strong molecular motion, i.e. the chain diffusion, present in the crystallites of these melt crystallized samples, which will be discussed in detail later.

Different with the crystalline ^{13}C CSA patterns in Fig. (4.4), the non-crystalline ^{13}C CSA patterns in Fig. (4.5) show evident variations. The line shape of the non-crystalline ^{13}C CSA patterns for the solution crystallized LMW-PEs show features of an axial-symmetric CSA tensor, whereas the CSA patterns of non-crystalline regions for the melt crystallized LMW-PEs resemble a broadened isotropic resonance line. These different ^{13}C CSA patterns indicate the different geometry of chain dynamics in non-crystalline regions of the samples, i.e., non-crystalline chains in the solution crystallized LMW-PEs follow a more restricted anisotropic motion close to a locally axial motion along the chain backbone, whereas non-crystalline chains in the melt crystallized LMW-PEs undergo a more isotropic motion. This observation is consistent with the observations in UHMW-PE.

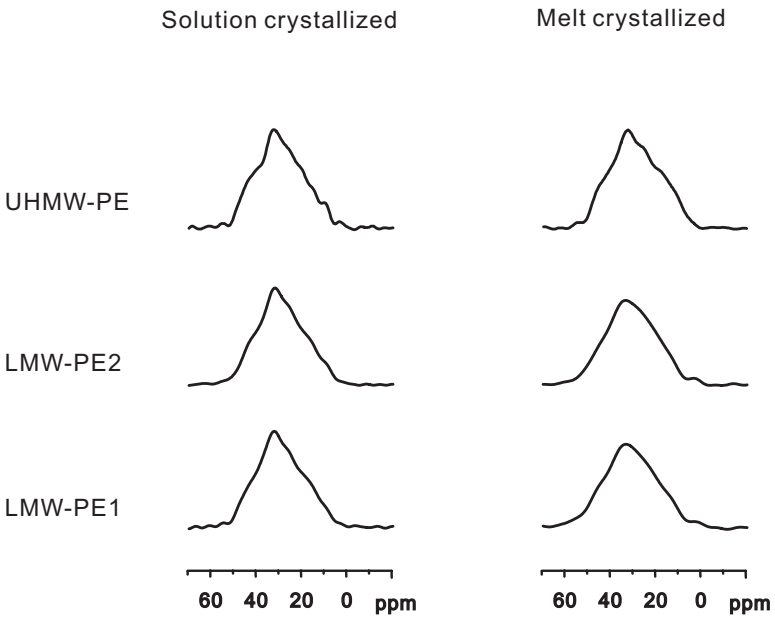

Figure 4.4: *The crystalline ^{13}C CSA patterns of the solution crystallized and melt crystallized PE samples. These patterns are extracted from the SUPER experiments, which were performed at T=320K.*

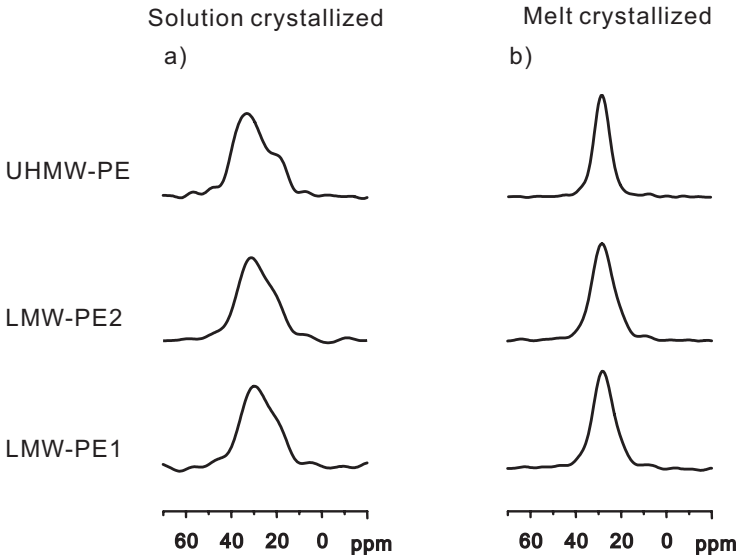

Figure 4.5: *The non-crystalline ^{13}C CSA patterns of: (a) solution crystallized PEs; (b) melt crystallized PEs. These patterns are extracted from the SUPER experiments, which were performed at T=320K.*

As a local interaction, ^{13}C CSA in nature is only sensitive to the local electronic en-

vironment of the observed ^{13}C nucleus. Hence, for the solution crystallized PEs the axial motion along the chain backbone in non-crystalline regions, as indicated by the ^{13}C CSA patterns, would not be strongly influenced by the molecular weight, i.e. the length of polymer chain. This is indicated by the similar ^{13}C CSA patterns in Fig. (4.5a). However, comparing carefully the ^{13}C CSA patterns of LMW-PEs with that of UHMW-PE in Fig. (4.5a), there are still some difference present in those spectra. Less distinct features of an axial-symmetric CSA tensor show up in the patterns of LMW-PEs. This difference might be related to the different molecular weights of samples, but could also originate from other reasons, such as the not completely equivalent crystallization condition of sample.

A comparison of ^{13}C CSA patterns in Fig. (4.5b) shows that the patterns of LMW-PEs are wider than that of UHMW-PE. This indicates a more restricted chain dynamics present in non-crystalline regions of the melt crystallized LMW-PEs compared to UHMW-PE. The difference becomes more pronounced in the ^{13}C CSA patterns of melt crystallized samples shown in Fig. (4.6), where the initial sources of polarization of the ^{13}C CSA patterns are varied. If the experiment is started with a direct excitation of ^{13}C and with the chosen relaxation delay in the experiments (2s), the acquired signal originates from the most mobile part in non-crystalline regions of sample. Whereas, if the experiment is started with an initial cross polarization step, the acquired signal results predominantly from sites with a strong heteronuclear dipolar coupling and thus, immobile sites in close proximity to crystalline areas. On shortening the contact time the immobile component in the signal becomes more and more pronounced (see Fig. 4.6a, b).

In Fig. (4.6a, b), with a relatively long contact time (1ms), only a slight asymmetric feature has been observed in the line shape of the ^{13}C CSA patterns for the two LMW-PEs, but the whole profiles of patterns still resemble broad isotropic resonance lines as those from the single pulse excitation method. As the contact time was reduced, the features of the axial-symmetric CSA tensor show up in the ^{13}C CSA patterns of the two LMW-PEs. When the contact time was set to 0.1ms, the ^{13}C CSA patterns of the two melt crystallized LMW-PEs become very similar to the patterns of the solution crystallized analogues. This similarity shows that the motion of some immobile non-crystalline components in the melt crystallized LMW-PEs has a similar geometrical

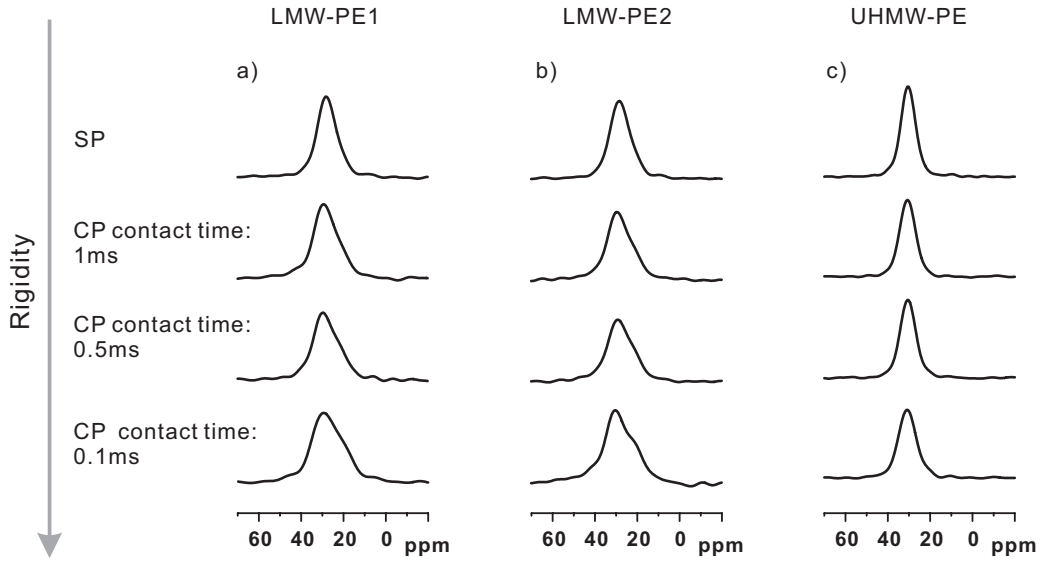

Figure 4.6: *The non-crystalline ^{13}C CSA patterns of melt crystallized PE samples. (a) the patterns of LMW-PE1; (b) the patterns of LMW-PE2; (c) the patterns of UHMW-PE. These patterns are extracted from the SUPER experiments performed at 320K. The initial sources of polarization of the CSA patterns vary from the single pulse excitation to the $^{1}H - ^{13}C$ cross polarization with different contact time.*

property as that in the solution crystallized analogues. Considering the most probable origin of the ^{13}C CSA pattern shape, this similarity can be indicative of the presence of the chain folds in these melt crystallized LMW-PEs. In contrast, the ^{13}C CSA patterns of the melt crystallized UHMW-PE in Fig. (4.6c) do not show any similar tendency. This indicates that the immobile components in the two melt crystallized LMW-PEs are not present in the melt crystallized UHMW-PE. However, although the immobile components in the two melt crystallized LMW-PEs has been clearly shown up in Fig. (4.6a, b), the quantification of these components is hampered by the dependence of the polarization transfer efficiency of the CP method.

Combining the data reported above altogether, one could figure out some characteristics of the chain dynamics and possible structure in non-crystalline regions of the LMW-PEs. For solution crystallized PE, a well accepted morphology model is that the crystals are formed by the folded chains and, the chain folds next to the crystal surface are non-crystalline regions as that shown in Fig. (4.1). The observation in the solution crystallized LMW-PEs approves of this kind of morphological picture. The restricted chain dynamics in non-crystalline regions of the solution crystallized LMW-PEs most

likely arises from the chain folds in non-crystalline regions, which are restricted by the two anchor points in the crystal surface and their neighboring chains. This morphology can favor the chain units to perform a rotation combined with a translation along the chain backbone. The rotation of the non-crystalline CH_2 units is consistent with the motional anisotropy as revealed by the ^{13}C CSA patterns and the translation motion which will be shown with the ^{13}C exchange experiment in the following sections. For the melt crystallized PE, the sample morphology is more complicated. Chiefly, two kinds of morphologies, i.e. the adjacent reentry chain folding model and the random reentry switchboard model, have been proposed to exist in non-crystalline regions of PE. Our observations show an intermediate restricted chain dynamics present in non-crystalline regions of the melt crystallized LMW-PEs. The motional anisotropy revealed in the ^{13}C CSA patterns shows the geometrical information of the restricted chain dynamics, and thus indicates that this restricted chain dynamics in the melt crystallized LMW-PEs could also originate from the chain folds, similar as that in the solution crystallized analogues. Hence, from our observations the crystals in the two LMW-PEs can in no way be of the complete random reentry switchboard type. The gradual line shape variation of the ^{13}C CSA patterns in Fig. (4.6a, b) indicates that combination of both limiting models, chain folding and switchboard structures, are present in non-crystalline regions of the melt crystallized LMW-PEs. However, the average scenario will be located between the two limiting models, and may depend on the molecular weight and the crystallization procedure. In contrast, the ^{13}C CSA patterns in Fig. (4.6c) indicate that the predominating structure in the melt crystallized UHMW-PE seems to be the switchboard model.

In order to see how the chain dynamics in non-crystalline regions of the LMW-PEs varies with the temperature, REREDOR experiments of the two LMW-PEs were performed at different temperatures. The resulting spinning sideband patterns and $^{1}H-^{13}C$ coupling constants in non-crystalline regions of the LMW-PEs are shown in Fig. (4.7) and Table. (4.3) respectively.

From the $^{1}H-^{13}C$ dipolar coupling constants listed in the Table (4.3), it is easy to find that, for a chemically identical PE sample the solution crystallized material always shows a lower temperature dependence of the effective $^{1}H-^{13}C$ dipolar coupling constants than the comparable melt crystallized one. However, the stability of this chain

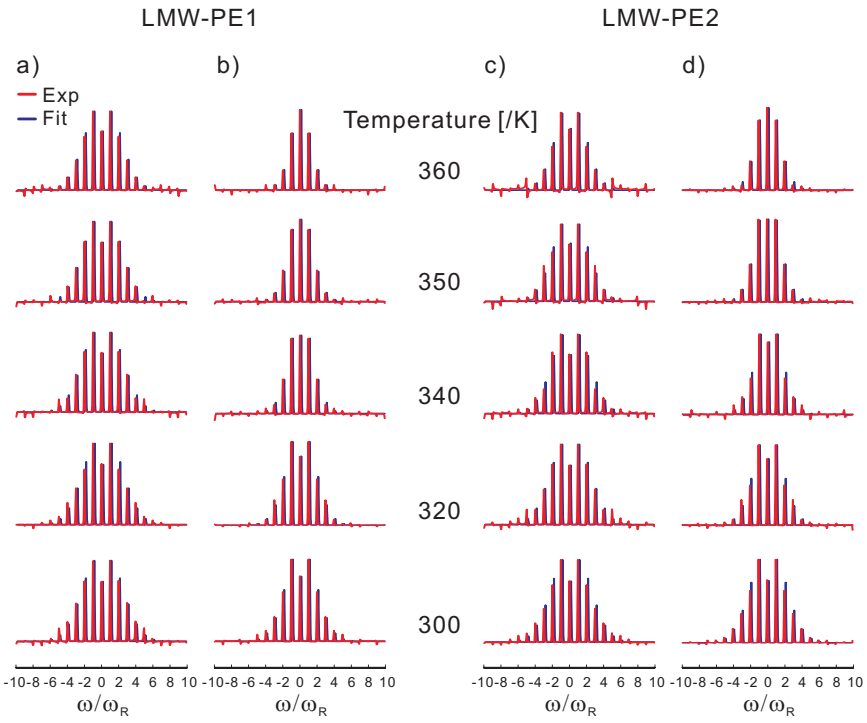

Figure 4.7: *The non-crystalline REREDOR spinning sideband patterns at different temperatures of: (a) solution crystallized LMW-PE1; (b) melt crystallized LMW-PE1; (c) solution crystallized LMW-PE2; d) melt crystallized LMW-PE2.*

	LMW-PE1		LMW-PE2		UHMW-PE	
T[/K]	SC	MC	SC	MC	SC	MC
360	8.5	5.2	7.5	5.7	8.8	5.0
350	8.8	5.8	8.3	6.2	8.9	5.3
340	9.1	6.1	8.6	6.7	8.9	5.6
320	9.1	7.2	9.0	7.2	9.1	6.3
300	9.1	7.6	9.0	8.5	9.1	6.9

Table 4.1: *The $^1H-{}^{13}C$ dipolar couplings constant $D_{IS}/2\pi$ (kHz) in the non-crystalline regions of the solution crystallized (SC) and melt crystallized (MC) LMW-PEs at different temperatures. For the comparison the $^1H-{}^{13}C$ dipolar coupling constants in the non-crystalline regions of solution/melt crystallized UHMW-PEs are also listed in this table. All of these constants are from the simulations of the corresponding experimental spinning sideband patterns.*

folding structure in the solution crystallized samples seems to have a dependence on the molecular weight. This is revealed by the experimental fact, that the temperature dependence of the $^1H-{}^{13}C$ dipolar coupling constants in the two LMW-PEs is

higher than that in the UHMW-PE, where the $^{1}H-{}^{13}C$ dipolar coupling constants hardly changes with increasing temperature. As to the melt crystallized sample, due to the completely different sample morphology the temperature dependence of the $^{1}H-{}^{13}C$ dipolar coupling constants then becomes a different scenario. In melt crystallized UHMW-PE, the most probable structure in its non-crystalline regions would be the random-coiled structure. With increasing temperature, the random motion of the chain segments in this structure will be gradually increased, leading to the gradual decreasing of the observed non-crystalline $^{1}H-{}^{13}C$ dipolar coupling constants. For the melt crystallized LMW-PEs, depending on the molecular weight and the conditions of melt crystallization, the structure present in non-crystalline regions would be a combination of the random-coiled structure and the chain folding structure. The observed non-crystalline $^{1}H-{}^{13}C$ dipolar coupling constants decrease with increasing temperature, indicating the presence of the random-coiled structure like the case of the melt crystallized UHMW-PE. However, at every specific temperature, the non-crystalline $^{1}H-{}^{13}C$ dipolar coupling constants in the melt crystallized LMW-PEs are always bigger than that of the melt crystallized UHMW-PE, which probably indicates the presence of the chain folding structure in the samples.

4.4 Chain diffusion in the LMW-PEs

After the discussion of the local chain dynamics in the LMW-PEs, in this section we will show how the local chain dynamics, e.g. the motional anisotropy, would influence the chain diffusive motion between non-crystalline and crystalline regions in the LMW-PEs.

Fig. (4.8) exhibits 1D ^{13}C exchange NMR spectra of the two LMW-PEs samples recorded at T=320K with various exchange times. From Fig. (4.8) one could see that the exchange spectra of all LMW-PEs show a fast intensity increase of the crystalline peak with increasing exchange time. Analyzing the time dependence of the crystalline signal build-up processes reveals a clear diffusive behavior, indicating that the crystalline signal build-up processes in all these LMW-PEs result from the chain diffusion process. As mentioned in the previous sections, all the LMW-PEs show the motional anisotropy in non-crystalline regions, no matter it is crystallized from melt or solution. The motional anisotropy in non-crystalline regions of PE has a geometry compatible

to a hopping motion of chain units inside crystals and thus favors the chain diffusive motion between non-crystalline and crystalline regions. This leads to the explanation that all the LMW-PEs, which posses the motional anisotropy in their non-crystalline regions, show up the clear chain diffusion between the non-crystalline and crystalline region.

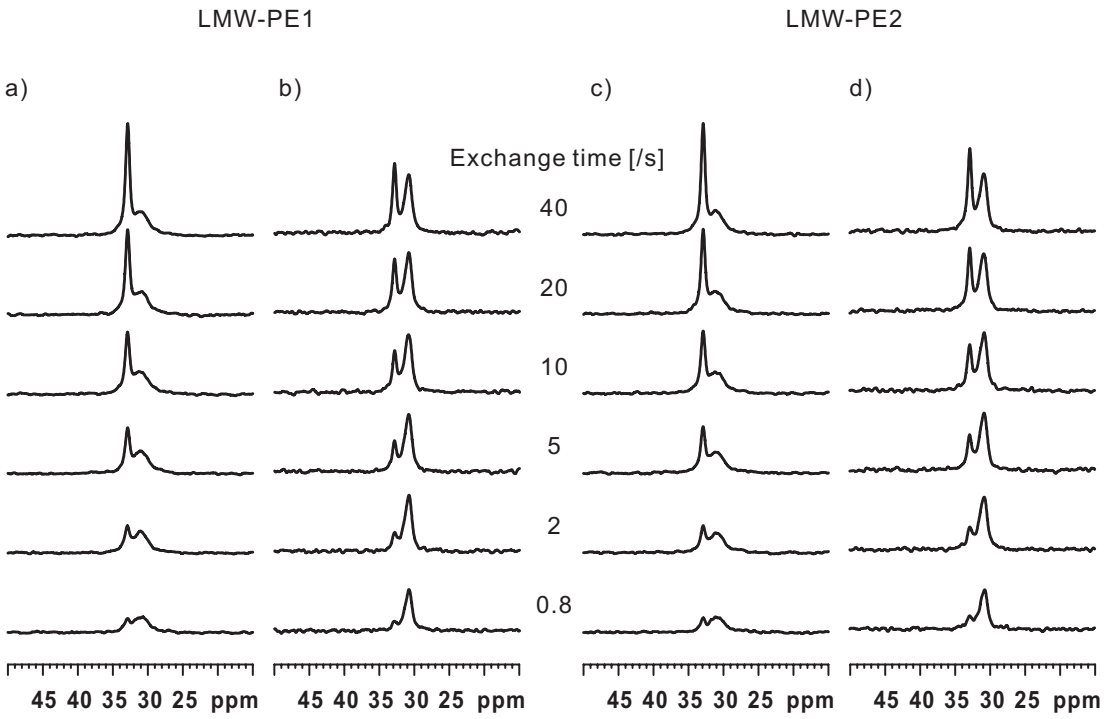

Figure 4.8: *The ^{13}C MAS exchange spectra of: (a) solution crystallized LMW-PE1; (b) melt crystallized LMW-PE1; (c) solution crystallized LMW-PE2; (d) melt crystallized LMW-PE2. All the experiments were measured at 6k Hz MAS, T=320K with different exchange times.*

The temperature dependence of the chain diffusion behavior in the LMW-PEs is shown in Fig. (4.9), where the 1D ^{13}C exchange NMR spectra of LMW-PEs were acquired at different temperatures but with a constant exchange time of 5s. With increasing temperature, the exchange spectra in Fig. (4.9) show a gradual increase of crystalline signals, indicating the accelerated chain diffusion in these samples.

However, although the increase of chain diffusion rate in the LMW-PEs on elevating the temperature has been expected, the temperature dependence of the chain diffusion

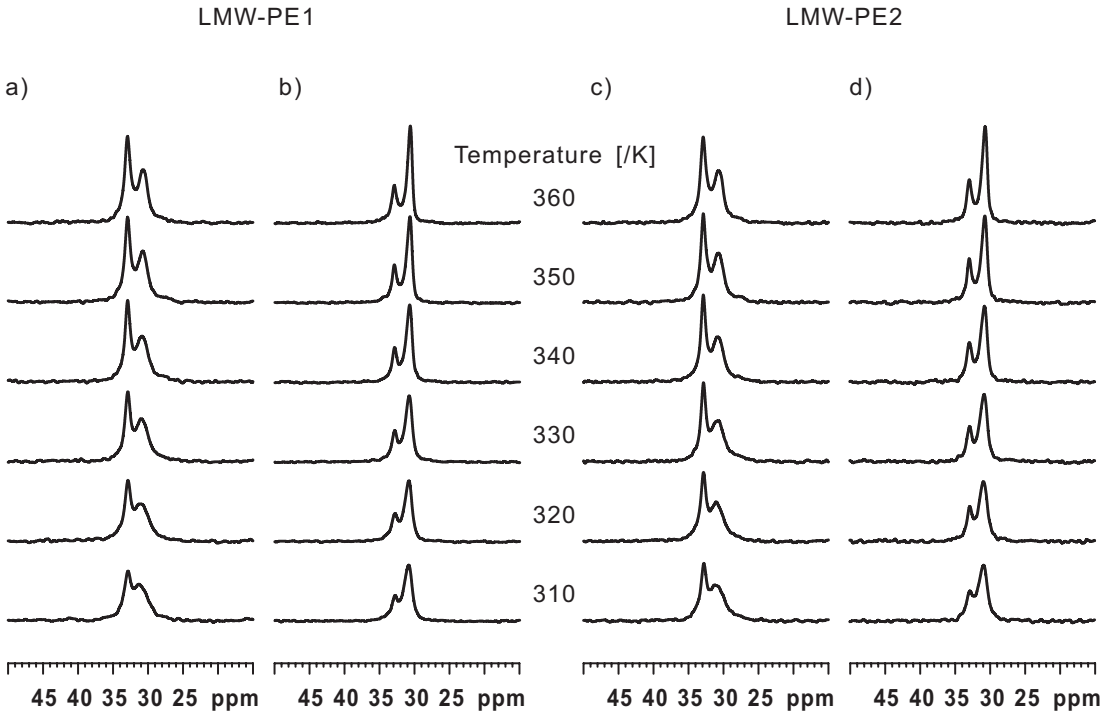

Figure 4.9: *The temperature varied ^{13}C MAS exchange spectra of: (a) solution crystallized LMW-PE1; (b) melt crystallized LMW-PE1; (c) solution crystallized LMW-PE2; (d) melt crystallized LMW-PE2. All the experiments were measured at 6k Hz MAS and with a fixed exchange time (5s)*

behavior in the LMW-PEs is not so easy to understand. Compared to the solution crystallized UHMW-PE, the chain diffusive behaviors in the LMW-PEs always show a lower temperature dependence. For the melt crystallized LMW-PEs, the temperature dependence of their chain diffusion behaviors might be caused by their complicated morphologies. Whereas, for the solution crystallized LMW-PEs, which are supposed to have a similar morphology as the UHMW-PE, their lower temperature dependence of chain diffusive behavior thus is unexpected. In the following, the exchange spectra of the solution crystallized UHMW-PE and LMW-PE2 acquired at different temperatures will be analyzed to give an explanation for their different temperature dependence of the chain diffusive behavior. Comparing the spectra of UHMW-PE in Fig. (4.10a) and LMW-PE2 in Fig. (4.10b), one could conclude that at low temperatures (300K and 320K) the chain diffusion behaviors in these two samples are quite similar, indicating the similar morphology, i.e. the chain folding, present in these two samples at these temperatures. When the temperature increases further, however, the chain diffusive behaviors in these two samples differ. For the UHMW-PE, the chain diffusion

rate gets a further enhancement with increasing temperature. At 340K and 360K, the increase of crystalline signal intensity in the UHMW-PE shows up a clear plateau, indicating that the crystals in the sample reach a fully polarized state. In contrast, for the LMW-PE2 no obvious enhancement of the chain diffusion rate with increasing temperature was observed in the spectra. Even at the high temperature (360K) the increase of the crystalline signal in the spectra still looks like the case at 300K. Considering the similar crystallinity and lamellar thickness in the UHMW-PE and LMW-PE2, one possible explanation for their different temperature dependency of chain diffusion behavior could be related to the stability of the structures in non-crystalline regions of the sample. As already discussed above, the chain diffusive motion between non-crystalline and crystalline regions in solution crystallized PE samples is facilitated by the motional anisotropy present in non-crystalline regions of sample, which requires the spatial restriction from the chain folding structure in the solution crystallized PE samples. Therefore, the change of chain folding structure will influence the chain diffusion in the sample. In the case of solution crystallized LMW-PE2, due to its relatively high content of chain ends, the chain folding structures in non-crystalline regions are easier to become loose compared to that in the UHMW-PE, when the temperature is elevated. The loose chain folding structures then lead to a less chain motional anisotropy in non-crystalline regions of sample, which is consistent with the decrease of the $^{1}H-{}^{13}C$ dipolar coupling constant in non-crystalline regions of solution crystallized LMW-PE2 at high temperatures. As a result, due to the relatively unstable structure in non-crystalline regions of the LMW-PEs the increase of temperature then gives more contribution to the isotropic chain motion rather than the translational motion of non-crystalline chains.

4.5 Conclusions

In the LMW-PEs the motional anisotropy of non-crystalline chains has been observed in solution crystallized samples as well as in melt crystallized samples. Since this motional anisotropy most probably originates from the chain folding structure, this observation indicates that the chain folding structure can be formed in non-crystalline regions of the solution and melt crystallized LMW-PEs. All the LMW-PEs, which posses the motional anisotropy in non-crystalline regions, show a clear chain diffusive

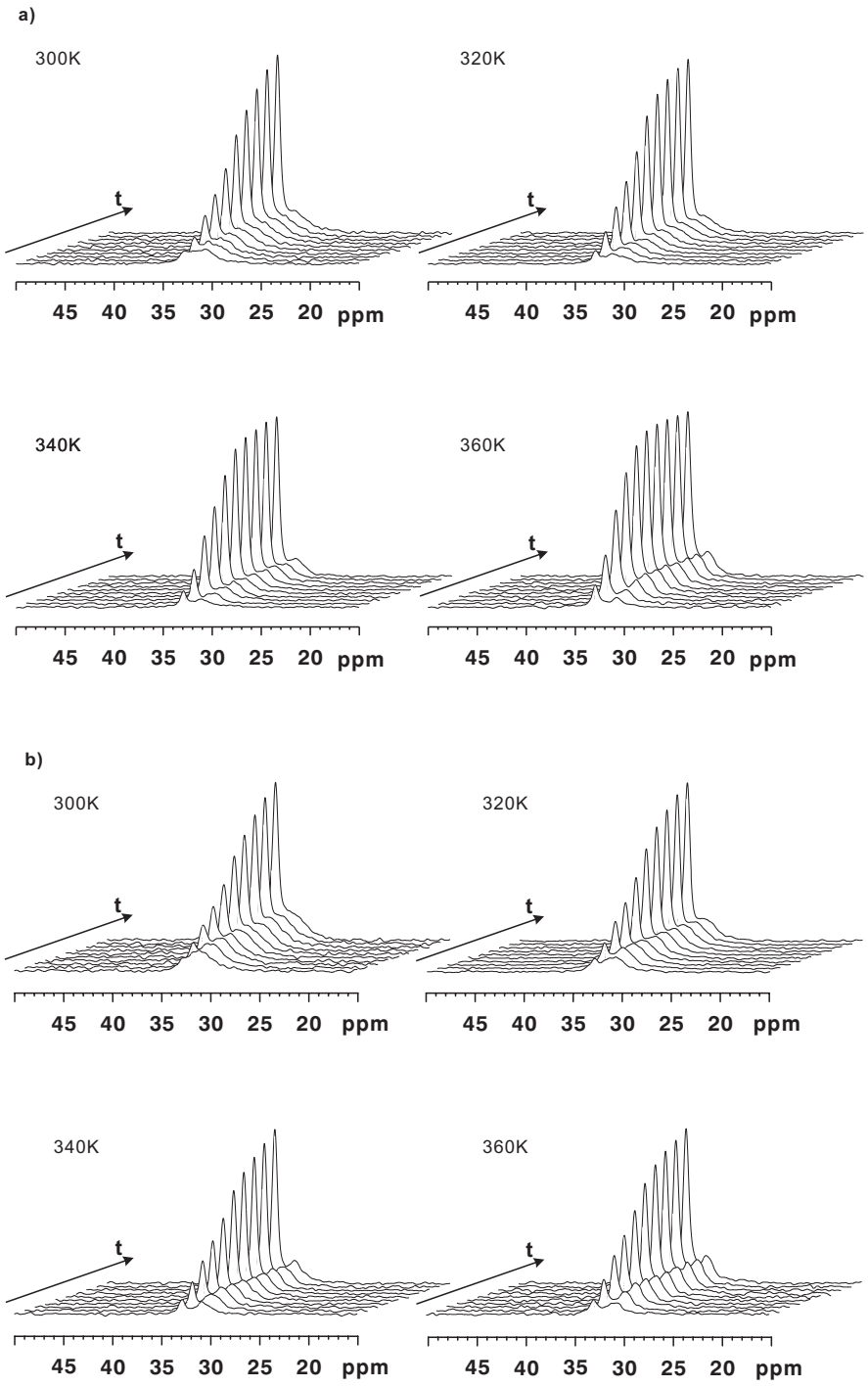

Figure 4.10: *The ^{13}C exchange spectra of two solution crystallized PE samples at different temperatures: (a) for the UHMW-PE; (b) for the LMW-PE2. The range of exchange time t in all of these exchange experiments was chosen from 0.8s to 120s.*

behavior. However, for the solution crystallized LMW-PEs, the chain diffusive behavior shows a lower temperature dependence compared to that of UHMW-PE. Combined with the observation of the non-crystalline $^{1}H - ^{13}C$ dipolar coupling constants at different temperatures, this difference may be explained by a possible structure variation (the loosening of chain folding) with increasing temperature.

Chapter 5

Morphological Influence on Molecular Dynamics of UHMW-PE Fiber

In this chapter we will change our subject to the molecular motion in the UHMW-PE fiber. The sample morphology will still be considered as the key to understand the specific features of molecular dynamics in the sample.

The UHMW-PE fiber investigated in this work is the product from DSM (Dyneema SK75), produced via the gel-spun procedure [Smith 79, Smith 80, Smith 81]. The chain-extended structure [Van Aerle 88] is considered to be present in this fiber sample, which gives rise to the very high mechanical performance. In a microscopic view, this specific chain-extended structure in the fiber apparently has an influence on the molecular motion, which will be studied in this chapter.

In the beginning of this chapter, a short introduction about the drawing process of PE and the morphology of resulting PE fiber will be given as a prerequisite knowledge for the following discussion. The next part of this chapter is the discussion about local chain dynamics and long range chain diffusive motion in the sample. Since the morphologies of the solution crystallized UHMW-PE and this fiber sample have some inherent similarity, a comparison of molecular dynamics between these two samples will be given. The solution crystallized UHMW-PE sample studied here is the one which has been investigated in Chapter 3. This sample has a similar molecular weight and molecular weight distribution as the fiber sample and thus is comparable with the fiber sample. Taking advantage of the chain diffusion behavior in the fiber sample, a

method for determination of crystallinity of PE fiber is proposed afterwards.

5.1 Drawing of PE sample and the fiber morphology

The chain-extended structure of PE fiber is created from the drawing process. To understand its characteristic, the knowledge about the possible change in the sample morphology during the drawing process is helpful. Following Peterlin's model [Peterlin 71], drawing of PE sample involves three stages of changes in the sample morphology: (1) the plastic deformation of the crystallites at low draw ratios; (2) the transformation of the lamellar structure into the fibrillar structure; and (3) the deformation of the fibrillar structure, when the drawing ratio λ is bigger than 15. However, depending on the initial morphology of sample and the drawing conditions, the demarcation between these stages usually is not very clear. For the solution crystallized UHMW-PEs in the hot drawing procedure, a refined drawing model has been proposed [Van Aerle 88], which stresses the transformations from the lamellar structure into the fibrillar structure and from the fibrillar structure to the chain-extended structure, because the lamellar break-down and formation of the fibrillar structure usually happen at the same time. In the following discussion we will follow this drawing model and consider the drawing process as a two-stage process, that is, the first stage for the lamellar break-down and formation of the fibrillar structure, and the second stage for the further change of fibrillar structure to the chain-extended structure. A schematic representation of this drawing process model is shown in Fig. (5.1).

The stage (i) in Fig. (5.1) happens when a sample is drawn at a low draw ratio. Even at a low draw ratio, the lamellar structure of sample might been destroyed to some extent, as has been supported by experimental observations from SAXS, electron microscopy, and neutron scattering experiment [Van Aerle 88, Petermann 79, Chuah 86, Adams 86, Wu 92]. In these observations the existing lamellar crystallites are broken by the shear forces and then form the fibrillar structure accompanied with some changes in the crystal thickness, decreased lateral dimensions and reduced perfection. As the draw ratio increase, the fibrillar structure will get a further extension and change into the stage (ii). However, to have a high draw ratio in a PE sample, some conditions in the sample morphology have to be fulfilled, such as an easy chain sliding inside crystallites and

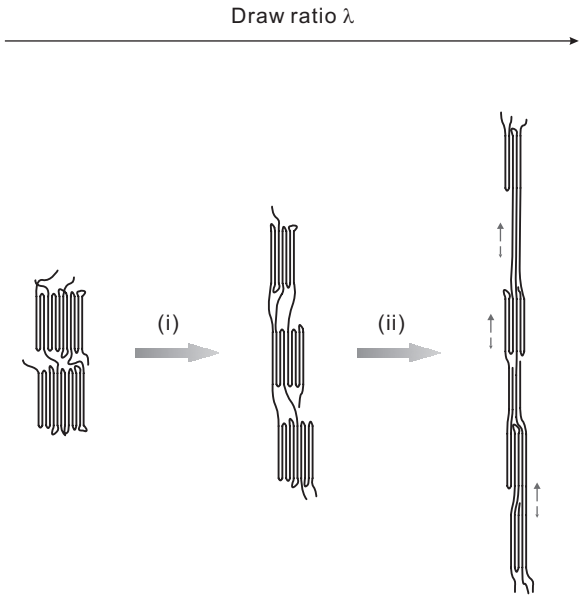

Figure 5.1: *Schematic illustration of drawing process. The stage (i): the break-down of lamellae and the formation of microfibril; the stage (ii): the extension of the microfibrillar structure. The bidirectional arrows indicate the chain diffusion inside the structure.*

sufficiently low level of chain entanglements in non-crystalline regions. These preconditions can be fulfilled by the suitable processing history of the initial sample. After stage (ii), the polymer chains get more and more extended, which is illustrated by the cartoon picture in the right side of Fig. (5.1).

In literature, there are two models available for the description of the fiber structure, that is, the continuous crystalline model and the microfibrillar model [Berger 03]. The continuous crystalline model assumes the macrofibril consisting of a more or less continuous crystalline phase with dispersed defects. On the other hand, the microfibrillar model describes the macrofibril of fiber as a bundle of highly extended chains with a diameter of $15-20nm$. These models have been illustrated in Fig. (5.2). The big difference between these models lies in the way how the stress transfers to the fiber. Concerning the molecular dynamics, these two models will not give too much difference. The prominent chain-extended structure favors the chain slippage in the sample as indicated by the results from the creep experiments [Ward 84, Govaert 92]. However, the highly extended chains in the fiber do not mean that the PE chains form crystalline lamellae with the thickness equal to the contour length of chain. In fact

the fiber crystals usually do not have a lamellar structure any more. Concerning the crystal size in PE fibres, the lateral dimensions were found to be of about 13 to 15 nm [Nakamae 91, Grubb 92], but the crystalline length in chain direction usually varies with the fiber type, i.e. a length of 71 nm for the Dyneema fiber [Nakamae 91]; 5-13 nm for Spectra 900 fibres and 15-43 nm for Spectra 1000 fibres [Grubb 92].

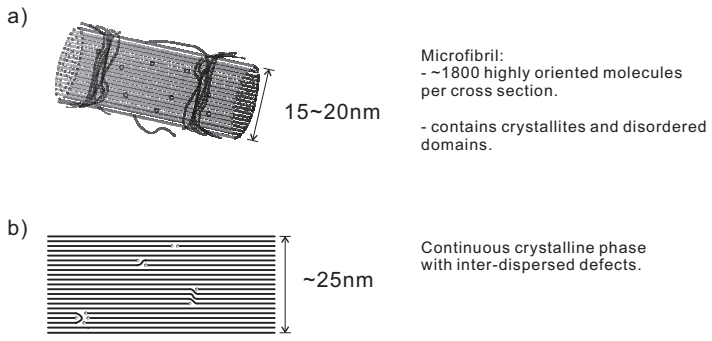

Figure 5.2: *The illustration of fiber structural models: (a) the microfibrillar model; (b) the continuous crystalline model. The lines denote the molecular chains and the small spheres denote the chain ends. This model illustration is taken from the Ref. [Berger 03].*

5.2 Structural irregularity and molecular motion in the UHMW-PE fiber

UHMW-PE fibers have a high Young's modulus and a high tensile strength, which originate from the highly extended chain structure [Ward 88]. However, the results from computer simulation demonstrate that a fully extended PE chain could give a tensile strength of 7*GPa* [Crist 95], which is much higher than the strength of UHMW-PE fiber in practice ($3 \sim 4GPa$). This difference between the theoretical and practical strength values has been attributed to the structural irregularity and the chain slippage in the fiber [Chodák 98, Berger 03]. In literatures the structural irregularity in PE fiber includes the irregular crystalline part and the non-crystalline part [Lagaron 99, Lagaron 00, Mowery 06]. The degree of structural irregularity depends on the properties of the starting material (molecular weight, linearity of chain, degree of entanglement, cross-linking, sample morphology) and on the processing procedure (solid state

or melt extrusion, gel spinning, hot drawing).

The presence of the irregular crystalline part in PE fiber has been revealed by many phenomena. The crystallinity value of PE fiber vary when determined with different measuring techniques [Berger 03, Karacan 06, Mowery 06]. This variation is considered as a reflection of the presence of the irregular crystalline part in the PE fibers. The broadening effect in the WAXD patterns of the PE fiber is also considered to result from this irregular crystalline part [Baker 01]. For the molecular motion, the presence of the irregular crystalline part apparently will give some influence on the chain motion inside the crystallites. It is easy to envisage that the chain units in the irregular crystalline part will be less restricted by the crystal lattice and thus could have a higher mobility compared to those in the regular crystalline part. Recently people found that the chain segments in the irregular "crystalline" region of PE fiber undergo a wiggling motion around the chain axis with an intermediate amplitude, whereas the all-trans conformation of chain units is still kept unchanged [Mowery 06]. Combined to the observed chain diffusion in the fiber crystallites [Hu 99a, Hu 00], the local motion of chain units in the irregular crystalline part thus may play an important role in accelerating or even initiating the chain diffusion in the fiber crystallites. Towards a better understanding of its implications on the chain diffusion in the fiber crystallites, a detailed discussion about the location and geometry of the local motion of chain units in the irregular crystalline part will be given in the following section.

5.3 Standard ^{13}C solid state NMR spectra of the UHMW-PE fiber

In the last two chapters, a strong relationship between the sample morphology and the molecular dynamics has been found in several PEs. Similarly, for the specific morphology in the fiber sample, one would also expect it to show some influences on the molecular dynamics in the fiber. Some influences have been evidenced by the standard ^{13}C solid state NMR spectra of the UHMW-PE fiber in Fig. (5.3). For a comparison, the spectra of melt and solution crystallized UHMW-PEs are also shown in Fig. (5.3)

The three spectra in the left column in Fig. (5.3) are the ^{13}C CP/MAS spectra of the melt crystallized UHMW-PE (Fig. (5.3)a), the solution crystallized UHMW-PE

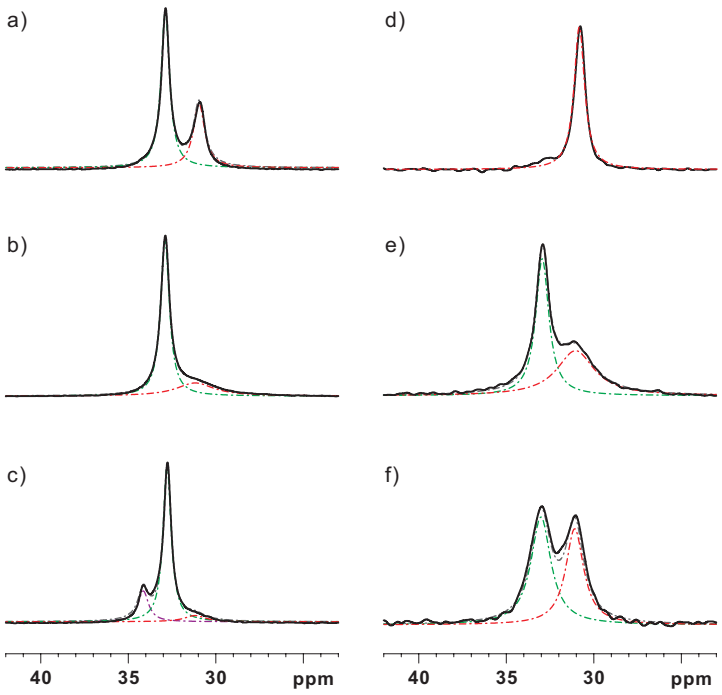

Figure 5.3: *The ^{13}C solid state NMR spectra of different PE samples at 320K: the CP/MAS spectrum of (a) melt crystallized UHMW-PE, (b) solution crystallized UHMW-PE, (c) fiber sample; the SP/MAS spectrum of (d) melt crystallized UHMW-PE, (e) solution crystallized UHMW-PE, (f) fiber sample.*

(Fig. (5.3)b) and the UHMW-PE fiber (Fig. (5.3)c). All these spectra were recorded at 320K. In these spectra the strong signals at $\sim 33 ppm$ are assigned to CH_2 units in orthorhombic crystals and the relatively weak signals at $\sim 31 ppm$ are assigned to the units in non-crystalline regions. Because of the different crystallinities and different chain mobilities in non-crystalline regions of the samples, these non-crystalline signals differ in intensity and peak width. With a normalized intensity of the crystalline signals in these ^{13}C CP/MAS spectra, the different signal intensities from non-crystalline regions in the spectra indicate that the fiber sample has the highest crystallinity and the melt crystallized UHMW-PE the lowest. The peak width of non-crystalline signal is indicative of the local chain mobility in non-crystalline regions of these PE samples. In the three spectra, one could easily see that the melt crystallized sample shows a sharp non-crystalline peak, indicating a fast molecular dynamics present in its non-crystalline area. The solution crystallized sample shows a wide non-crystalline peak, which can be attributed to the spatial constraints from the chain folds as discussed in Chapter 3. For the fiber sample, although the intensity is low, the non-crystalline peak

in the fiber sample shows an intermediate peak width, indicating that the local molecular dynamics in non-crystalline regions of the fiber is less mobile than that of the melt crystallized sample but more mobile than that of the solution crystallized one. Associated with the sample morphology, one would expect that this partially restricted molecular dynamics most probably originates from the spatial constraints of the special morphology of the fiber. In addition, for the ^{13}C CP/MAS spectrum of fiber, an additional signal appears at a chemical shift of $\sim 34 ppm$. The signal can be assigned to the monoclinic crystal phase [VanderHart 84], which usually appears in fiber samples when the orthorhombic crystal experiences a deformation [Painter 77, Holland-Morit 81].

The three spectra in the right column of Fig. (5.3) were acquired at 320K via the single pulse excitation with a 5s recycle delay. As mentioned in Chapter 3 & 4, the signals in this single pulse excitation routine have different origins with those from a CP routine. In this routine the acquired non-crystalline signals represent the whole non-crystalline phase because of its short ^{13}C T_1 relaxation time ($\sim$ 0.6s) and, the crystalline signal is from the surface of the crystallites due to the short diffusion time (the 5s recycle delay). From the discussion in Chapter 3 & 4, one knows that the fast chain diffusive motion in the sample has a close relationship with the chain folding structure in non-crystalline regions of sample. As to the fiber sample, it is interested to find that a crystalline peak appears in its spectrum (Fig. 5.3f). Although the crystalline peak in the spectrum of fiber is not as strong as that in the spectrum of solution crystallized sample, the appearance of this crystalline signal indicates that the chain segments in this fiber sample can still easily move between crystalline and non-crystalline regions in spite of the big crystal thickness of sample. Concerning how the chains in the fiber sample can have an easy diffusive motion and whether the motional anisotropy is also present in this sample, the above standard ^{13}C solid state NMR spectra cannot give the answer. In order to find the answer, several advanced solid state techniques will be applied to the fiber sample, which is given in the following sections.

5.4 Motional anisotropy in the UHMW-PE fiber

In this section the ^{13}C CSA patterns of the fiber sample were obtained from the "isotropically" distributed fiber sample, that is the chains in the fiber sample have an almost

isotropic orientation with respect to B_0. In order to achieve this isotropic orientation distribution, the fiber sample was cut to small pieces before packing into the rotor, as illustrated by the cartoon picture in Fig. (5.4).

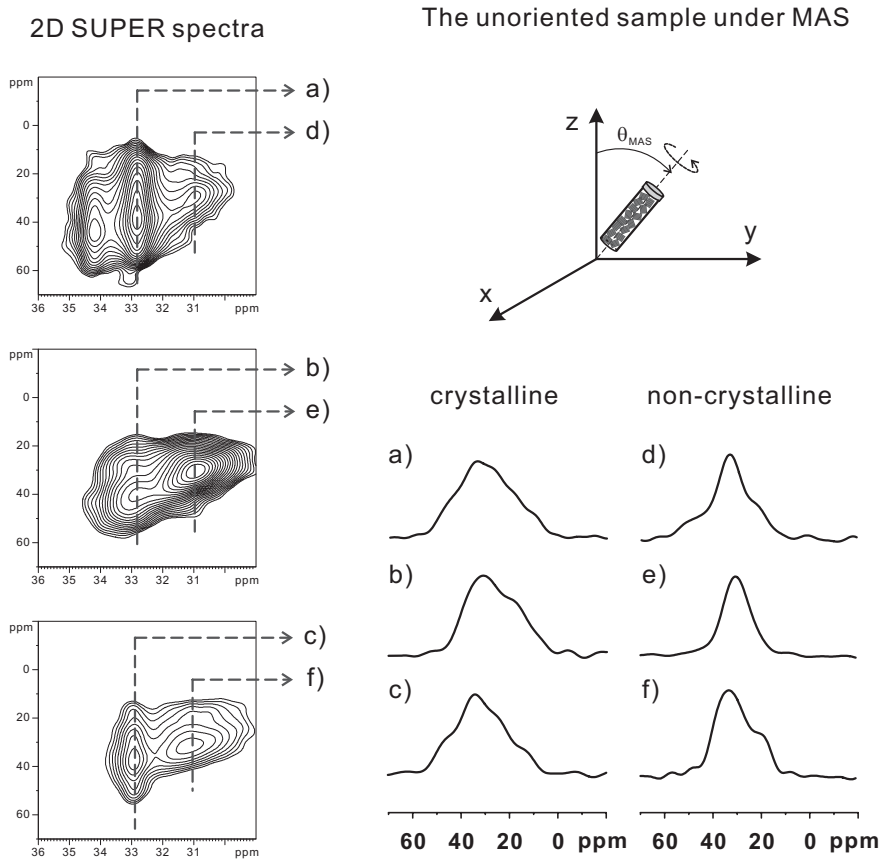

Figure 5.4: *^{13}C CSA patterns of unoriented fiber sample at 320K. (a) the crystalline pattern and (d) the non-crystalline pattern of fiber. The initial ^{13}C polarization in these two patterns is from CP step; (b) the crystalline pattern and (e) the non-crystalline pattern of fiber. The initial ^{13}C polarization in these two patterns is from the single pulse excitation. (c) the crystalline pattern and (f) the non-crystalline pattern of solution crystallized UHMW-PE. The initial ^{13}C polarization is from the single pulse excitation.*

To monitor the crystalline/non-crystalline components in the fiber sample the initial source of polarization in the SUPER experiment was varied. The patterns in Fig. (5.4a, d) are from the experiment which starts with an initial CP step. Due to the dependence on the CP efficiency, the acquired signals in this way strengthen the components with strong heteronuclear dipolar coupling, e.g. the crystalline component and non-

crystalline component with restricted molecular dynamics. In contrast, the patterns in Fig. (5.4b, e) recorded using the ^{13}C single pulse excitation with a shot relaxation delay (2s). In this case, non-crystalline signals with a short ^{13}C T_1 relaxation time are predominant. And the crystalline signal in this case results from the chain diffusion between non-crystalline and crystalline regions. Due to the short diffusion time ($\sim$ 2s), the pattern in Fig. (5.4b) exhibits predominant signals from the surface of crystallites. As a comparison, the ^{13}C CSA patterns of solution crystallized UHMW-PE obtained under equal experimental conditions are also shown in Fig. (5.4c and f).

The CSA pattern shown in Fig. (5.4a) looks similar to the ^{13}C crystalline patterns of UHMW-PE samples shown in Chapter 3. This similarity indicates that the main parts of crystallites in this fiber are similar as those in the other UHMW-PEs. An interesting phenomenon is observed from the pattern in Fig. (5.4b), where the signal originates from the surface of the fiber crystallites. The shape of this pattern shows features of an axial-symmetric CSA tensor, similar to the shape of the non-crystalline pattern in solution crystallized samples in Fig. (5.4f). As already mentioned before, this kind of shape indicates that the involved chains follow a restricted anisotropic motion close to a locally axial motion around the local chain backbone. Analogous as the case in the solution crystallized UHMW-PE, this motion anisotropy in the fiber sample will be expected to favor the chain diffusive motion.

With the same experimental condition, the ^{13}C CSA pattern from the surface of crystallites in the solution crystallized UHMW-PE were also obtained, which is shown in Fig. (5.4c). Obviously, the shape of this pattern does not exhibit features of an axial-symmetric CSA tensor, although this pattern shape looks complicated. This special pattern shape might originate from the overlap of two components, that is, the normal crystalline pattern from the deeper part of crystal, and the pattern with the axial-symmetric tensor feature from the surface of crystal. This kind of complicated shape actually also appears in the crystalline ^{13}C CSA patterns in the other PE samples in our study. In literature, people has found that these two components could exchange together [Edzes 84]. The $^{13}C - {}^{13}C$ spin diffusion was used to explain the exchange phenomenon. However, the exchange between these two components can be explained as well by the fast chain diffusion present in the sample.

Now one could compare the motional anisotropy in the fiber sample and the solution crystallized UHMW-PE. In the fiber sample, this motional anisotropy is present in the surface of the crystallites. Whereas, in the solution crystallized UHMW-PE, this motional anisotropy is found in non-crystalline regions. Considering the morphology of the solution crystallized UHMW-PE, its non-crystalline component, which is likely to be the chain folds, is also located in the crystal surface. This similarity indicates that the motional anisotropy in the fiber sample might also play a role for facilitating the chain diffusive motion.

Compared to the ^{13}C CSA patterns of crystalline component, the patterns of non-crystalline component in the fiber sample, however, are not very informative. The ^{13}C CSA pattern from the bulk non-crystalline part shows a wide but almost isotropic line (Fig. (5.4e)), whereas the ^{13}C CSA pattern from the restricted non-crystalline part, obtained experimentally with an initial CP step, shows a strange lineshape (Fig. 5.4d), indicating the presence of some restriction on this non-crystalline component. However, without additional information, it is not possible to get the proper geometry information of the restriction just from the line shape in Fig. (5.4d). Nevertheless, from the comparison of the patterns in Fig. (5.4d) and Fig. (5.4e), one still can draw the conclusion that the non-crystalline part of fiber sample at least consists of two components with different degrees of restriction on their local dynamics.

5.5 Structural irregularity in the UHMW-PE fiber

Taking advantage of the presence of chain orientation in the fiber, it is possible to record the ^{13}C CSA pattern of fiber when it is oriented at a certain angle. In this case all of the molecular chains in the fiber are more or less oriented along a direction, which will leads to some orientation effects shown in the pattern shape [VanderHart 84, Mowery 06]. In our experiments the fiber (the fiber drawing axis) was aligned at the magic angle, i.e. $\sim 54.7^\circ$ with respect to the external magnetic field B_0 and the resulting patterns are exhibited in Fig. (5.5).

The crystalline pattern in Fig. (5.5a) was recorded via a CP step for the creation of the initial polarization. In contrast to the pattern of the ”isotropic” fiber sample, the

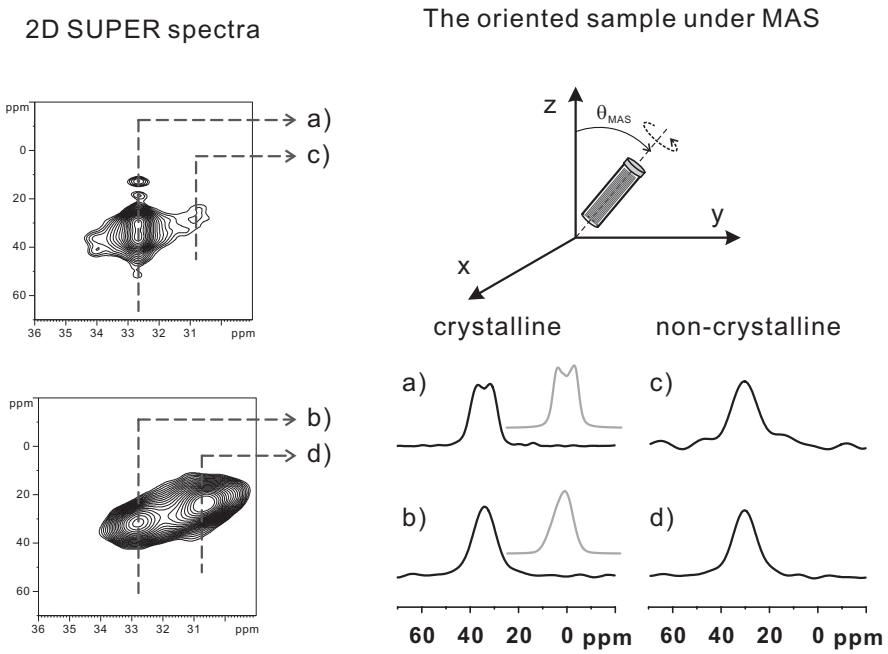

Figure 5.5: ^{13}C *CSA patterns of oriented fiber sample at 320K. (a) The crystalline pattern and (d) the non-crystalline pattern of oriented fiber. The initial* ^{13}C *polarization in these two patterns is from CP step; (b) the crystalline pattern and (e) the non-crystalline pattern of oriented fiber. The initial* ^{13}C *polarization in these two patterns is from the single pulse excitation. Two simulated patterns (the grey lines) are plotted close to the relevant experimental ones.*

pattern in Fig. (5.5a) shows a specific two-horn shape, which actually originates from the chain orientation in the fiber. A short interpret about the origin of this pattern shape is given in the following. First, one recalls the formula of CSA in the rotating frame:

$$\omega^*_{csa} = \frac{1}{2}\Delta(3cos^2\theta - 1 - \eta sin^2\theta cos2\phi) \tag{5.1}$$

In our case, θ in this formula is equal to the magic angle, i.e. $3cos^2\theta - 1 = 0$. Therefore, Eq. (5.1) can be simplified as:

$$\omega^*_{csa} = -\frac{\Delta\eta}{3}cos2\phi \tag{5.2}$$

Then, if ϕ distribution $P(\phi)$ of the sample is known, the pattern $S(\omega_{csa})$ can be obtained by:

$$S(\omega_{csa}) = P(\phi)|\frac{d\theta}{d\omega_{csa}}| \tag{5.3}$$

Substituting $\frac{d\theta}{d\omega_{csa}}$ in Eq. (5.3) with the relationship of $\omega_{csa} \sim \theta$ given in Eq. (5.2) leads a new form of $S(\omega_{csa})$:

$$S(\omega_{csa}) = P(\phi)|\frac{3}{2\Delta\eta sin2\phi}| \tag{5.4}$$

For a uniform axial distribution, $P(\phi)$ is equal to 1. Therefore, finally $S(\omega_{csa})$ has a formula:

$$S(\omega_{csa}) = |\frac{3}{2\Delta\eta sin2\phi}| \tag{5.5}$$

$$= |\frac{3}{2\Delta\eta\sqrt{1-\frac{9}{\Delta^2\eta^2}\omega_{csa}^2}}| \tag{5.6}$$

Eq. (5.6) shows that the two singular points of $S(\omega_{csa})$ will appear at $\omega = \pm\frac{\Delta\eta}{3}$, which actually give rise to the two horns in the pattern of oriented fiber. In our experimental condition, Δ and η have the values of -20.5 and 0.659 respectively. Thus, for a PE fiber with a perfect chain orientation, the distance between two singularities is $\sim 9ppm$, which is quite close to the observation in the experiment here ($\sim 6ppm$). The difference between the theoretical and experimental value originates from the orientation distribution present in the fiber sample. Computer simulation revealed that a fit for the pattern in Fig. (5.5a) needs a Gaussian distribution of the oriented chains with $\sigma = 2^\circ$. The simulated pattern is plotted as the gray line in Fig. (5.5a) and is in good agreement with the experimental pattern. From the simulation results, it is known that the main part of crystalline chains in the fiber has a high degree of orientation. However, the 2° deviation can originate from the alignment of the fibers in the MAS rotor as well from a misalignment of the polymer chains in the fiber. Varying the initial polarization of the ^{13}C CSA pattern from a CP method to a single pulse excitation, the degree of chain orientation at the surface of fiber crystallites can be monitored. This kind of pattern is exhibited in Fig. (5.5b). Different with the pattern in Fig. (5.5a), the pattern from the surface component of fiber crystallites looks like a wide isotropic resonance line. The disappearance of the two-horn feature indicates the presence of a broader orientation distribution in this component. Computer simulation showed that in order to get this line shape a Gaussian distribution with $\sigma = 10^\circ$ is needed. This broader orientation distribution of chain is indicative for structural irregularity present at the surface of fiber crystallites. In a dynamic picture, this orientation distribution probably reflects

the wiggling motion of chain present in the surface of fiber crystallites. Combined with the above observations from the unoriented sample, the local chain motion in the surface of fiber crystallites thus seems to be a combination of wiggling and rotation around the chain backbone.

Because of the special morphology of fiber, the chains in non-crystalline regions of fiber could also have a certain degree of orientation [VanderHart 84, Mowery 06]. However, from our observations, only the restricted non-crystalline chains possess a certain degree of orientation, whereas the chains in the main part of non-crystalline regions can still have an almost isotropic distribution. This point can be concluded from the comparison between Fig. (5.4d) and Fig. (5.5c), as well as Fig. (5.4e) and Fig. (5.5d). Because the initial polarization is created via CP method, the patterns in Fig. (5.4d) and Fig. (5.5c) show the feature of the restricted non-crystalline component in the sample. When the sample changes from the unoriented state to the oriented state, the strange pattern shape in the unoriented sample changes to the almost ”isotropic” line in the oriented sample. This change indicates the presence of orientation in this non-crystalline component. In contrast, the patterns in Fig. (5.4e) and Fig. (5.5d), which are from the major part of non-crystalline component, do not show a clear difference when the sample changes from the unoriented state to the oriented state. This means that the chains in the major part of non-crystalline regions in the fiber sample almost have no orientation.

5.6 Chain diffusion in the UHMW-PE fiber and its application for the determination of crystallinity

Similar to solution crystallized UHMW-PE, the polymer chains in the PE fiber are well-organized and rarely entangled. Thus, if considering the morphology of PE fiber, one actually might expect the presence of a fast chain diffusive motion in the fiber sample. One possible obstacle for the chain diffusion in the fiber could be the crystal thickness of fiber, which is usually much bigger than that in the solution crystallized UHMW-PE. However, in literatures the chain diffusive motion is considered to be initiated by a local 180°-twist and passes through the crystal in a very short time [Reneker 62, Mansfield 78]. The crystal thickness thus would not be a big obstacle

for the chain diffusive motion. The obstacle of chain diffusion is rather the crystallographic a, b value of crystal lattice but not the lamellar thickness. This point is supported by the appearance of crystalline peaks in Fig. (5.6).

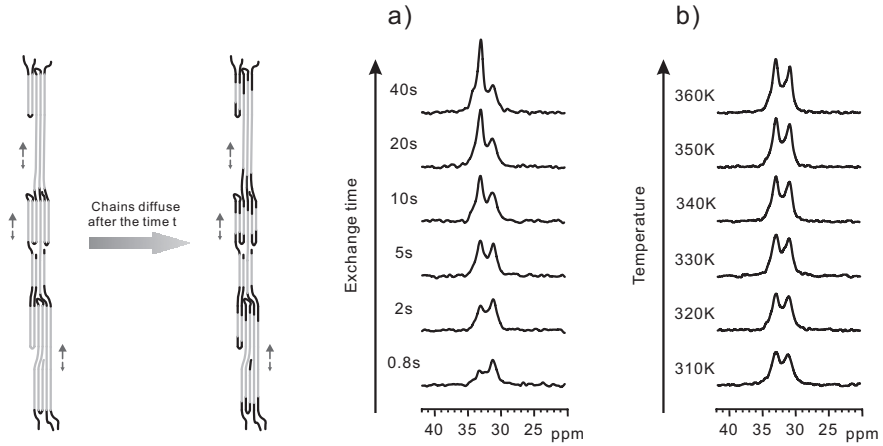

Figure 5.6: *^{13}C exchange spectra of fiber sample. (a) The ^{13}C exchange spectra of fiber sample at 320K with different exchange times. (b) The ^{13}C exchange spectra of fiber sample at different temperatures with a constant exchange time of 5s. The left cartoon picture illustrates how the ^{13}C polarization (the black color) diffuses from non-crystalline to crystalline regions.*

In the 1D ^{13}C exchange spectra shown in Fig. (5.6a) the crystalline peak of the fiber sample increases quite fast with increasing the exchange time. The spectra were recorded at 320K, which is far below the α-transition temperature of PE. The appearance of the crystalline peak here is a good indication of a fast chain diffusion present in the fiber sample. In Fig. (5.6b) 1D ^{13}C exchange spectra acquired with a constant exchange time of 5s at different temperatures are exhibited. In these spectra, the intensities of crystalline and non-crystalline signals both increase with increasing temperature. As one knows, crystalline signals in these exchange spectra result from ^{13}C polarization transfer due to the chain diffusion. Thus, the increase of the crystalline signal in the spectra indicates the increase of the chain diffusion rate in the sample. For the non-crystalline signal, there are two possible explanations for the observed temperature dependence in the spectra. One explanation is based on a variation of the crystallinity of sample. If the crystallinity of the fiber sample decreases at higher temperatures, the intensity of the non-crystalline signal in the spectra apparently will

increase due to the increase of the non-crystalline component. The second possible explanation is based on a variation of the relaxation behavior of non-crystalline regions of the fiber sample. In a simple case, one could assume that two non-crystalline components with different restrictions in the molecular dynamics are present in the fiber sample. The highly restricted one has a longer relaxation time and the less restricted one has a shorter relaxation time. At low temperature, the signal from the component with a short relaxation time will be predominant when spectra were recorded with a short recycle delay. With increasing temperature, the chain mobility in non-crystalline regions increases, which accelerates the ^{13}C T_1 relaxation process for all non-crystalline components. The restricted component thus could give more contributions to the non-crystalline signal in the spectra, leading to an increase of the non-crystalline signal intensity at the high temperature.

The two explanations above both can explain the temperature dependence of the 1D ^{13}C exchange spectra of the fiber sample in Fig. (5.6b). However, only with the information obtained from the spectra in Fig. (5.6b), we are not able to decide which explanation is the correct description in this case. In fact, when increasing temperature the crystallinity of the fiber sample will decrease and at the same time, the restricted components in non-crystalline regions will relax faster. The temperature dependence of the non-crystalline signal of the fiber sample as indicated in Fig. (5.6b), therefore, most likely results from a combination of both processes.

To quantify the rate of chain diffusion one needs the crystallinity value of sample. Although there are several techniques available to determine the crystallinity of the fiber, the different techniques are based on different mechanisms and usually give systematically different crystallinity values. In NMR, in principle the single pulse with an infinite long relaxation delay can be used to determine the crystallinity for the fiber sample. But because of the very long intrinsic ^{13}C relaxation time in the fiber crystals, this simple single pulse method cannot be used in practice. Taking advantage of the chain diffusion behavior in the fiber sample, an easy way to determine the crystallinity of fiber sample is present in the following.

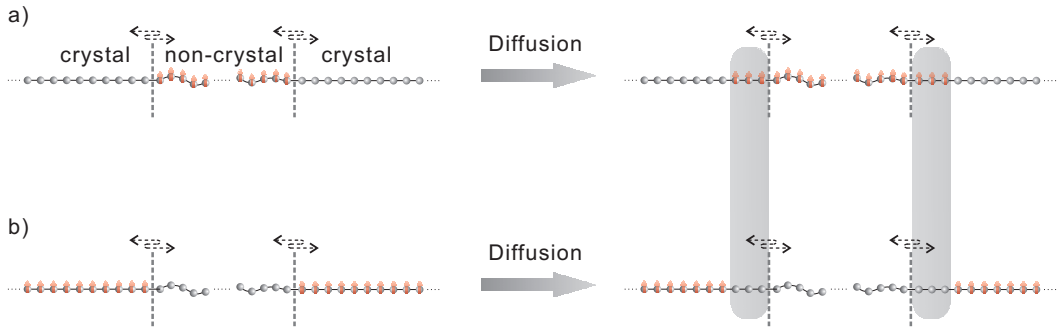

Figure 5.7: *The illustration of polarizing/depolarizing process induced by the chain diffusion. (a) the polarization transfer in the single pulse based ^{13}C exchange experiment; (b) the "depolarization" process in the CP based ^{13}C exchange experiment.*

As mentioned above, the failure of the single pulse method for the crystallinity determination is its requirement for a very long relaxation delay. If the relaxation delay is not long enough, the ^{13}C polarization will not get fully relaxed and the obtained crystallinity from the single pulse method will underestimate the actual crystallinity of the sample. But if one can know how the intensity of crystalline signal changes with the recycle delay in the single pulse method, the partially relaxed crystalline signal still can be used to determine the crystallinity of the sample, which actually is the basic idea of the method mentioned here. The whole procedure of this crystallinity determination is the following. First, one could use the CP method to get the crystallites polarized and then monitor the time dependence of the depolarization for the crystalline signal. Since this depolarization process results from the chain diffusion, the decrease of the normalized crystalline signal follows the diffusion process, which can be described as:

$$S_1 = C - D \cdot t^{\frac{1}{2}} \tag{5.7}$$

Second, one needs to record a series of single pulse based exchange spectra to have a signal increasing curve. As illustrated in Fig. (5.7), the polarizing/depolarizing of the crystalline signal via the chain diffusion mechanism are equivalent (excluding any external source or sink of polarization). Thus, the increase of the whole signal also follows the diffusion function if the exchange time t is much bigger than the relaxation time of the non-crystalline component:

$$S_2 = A + D \cdot t^{\frac{1}{2}} \tag{5.8}$$

With a proper normalization to let these two curve have a same slope D, the crystallinity of the sample is then given by $\frac{C}{C+A}$.

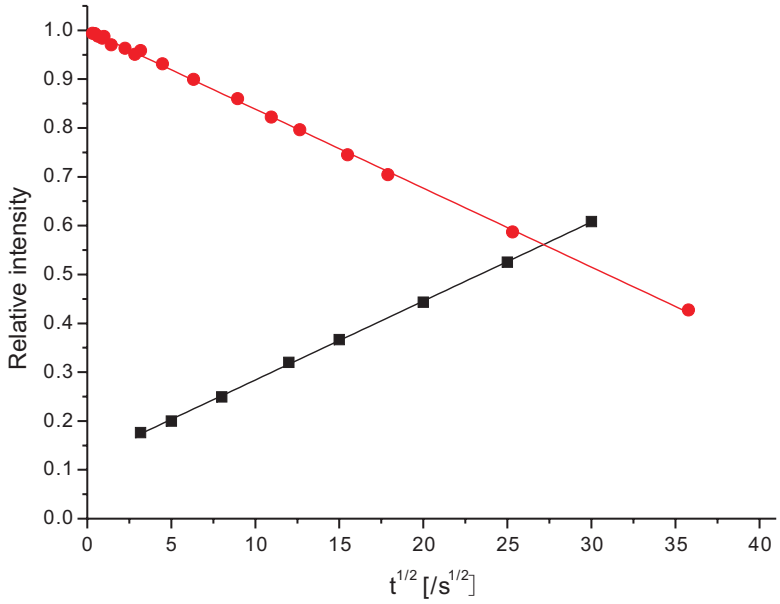

Figure 5.8: *Signal variation induced by the diffusion process in the fiber sample. The normalized crystalline signal from the CP exchange experiment (●), and the normalized total signals, i.e. the crystalline and non-crystalline signals, from the SP exchange experiment (■) are plotted against the square root of the diffusion time. The way for the signal normalization is explained in the text.*

Now we apply this crystallinity determination method to our fiber sample. In Fig. (5.8) the signal S against the square root of exchange time $t^{\frac{1}{2}}$ is plotted. The red points are the data from the exchange experiment based on the CP method. The black squares are the data from the exchange experiment based on the single pulse method. In both cases, the signals are linear to the square root of exchange time, indicating the diffusive origin of the signal change. Fitting these two data sets with a same slope $D = 0.01616$ yields two intercepts $C = 1$ and $A = 0.1224$. The crystallinity of this sample then can be calculated by $\frac{C}{C+A} = 89.1\%$, which is in good agreement with values given in the literature [Karacan 06].

5.7 Conclusions

With the help of NMR techniques, detailed information of the motional anisotropy and the fast chain diffusive motion in the UHMW-PE fiber were revealed. The location and geometry of the motion anisotropy in the PE fiber indicate that this motion anisotropy has a strong relationship with the fast chain diffusive motion in the fiber. The molecular dynamics of fiber sample are well explained with the known chain-extended morphology of PE fiber. The findings reported here again exhibit a good example about the correlation between the sample morphology and the molecular dynamics in PE. Concerning the mechanical properties of PE fiber, the findings here also give a microscopic explanation for the origin of creep in PE fiber.

Chapter 6

Topological Influences on the Chain Diffusion in PE

In the previous chapters it was shown that the morphology of a linear PE sample has a strong influence on the local chain dynamics. Based on that knowledge, we will now concentrate on how the chain diffusion is influenced by the topology of the samples. The morphological factors, such as lamellar thickness, chain organization in non-crystalline regions and chain entanglements, will be discussed in this chapter.

In chemistry, diffusion usually refers to the spontaneous migration of particles from regions of high concentration to regions with low concentration. However, the chain diffusion in PEs is not driven by a concentration gradient. Considering its situation, the chain diffusion in PEs is more like a self-diffusion of liquids or gases. In the beginning of this chapter, we will give a short discussion about the thermodynamics involved in the chain diffusion. The transition state theory will be used for the description of this motion. The second part of this chapter consists of a comparison between two NMR methods for the detection of the chain diffusion, which actually both are based on the ^{13}C exchange experiment. One is to first polarize the ^{13}C spins in non-crystalline regions and then monitor how the polarization diffuses into crystalline regions. The other is to first polarize the ^{13}C spins in crystalline regions and then monitor how the polarization diffuses into non-crystalline regions leading to the decay of the monitored crystalline signal intensity. A detailed analysis of the advantage and disadvantage of these two methods will be given in this section. In the third part, the chain diffusion in the PE samples with the different topological constraints will be studied. The activa-

tion energy of chain diffusion and the relationship between the local jump motion and chain diffusion in PE crystals will be discussed. In this context a concept of effective jump motion was introduced to explain the difference between the jump rates derived from the chain diffusion coefficients and the literature values.

6.1 Thermodynamics of the chain diffusion

The simplest theory which attempts to deal with the temperature dependence of chain diffusion behaviour is the transition state or barrier theory. This theory stems from the theory of chemical reactions. The basic idea of this theory is that a system has to adopt a transition state before changing into the final state. The following discussion is based on this theory.

6.1.1 A description of chain diffusion with the transition state theory

First, we simplify the chain motion between crystalline and non-crystalline regions in PEs as a translative movement of chain stem, which is illustrated by the cartoon picture in Fig. (6.1). In literature, the chain diffusion was proposed to result from the traversing of chain defect in the crystallites [Mansfield 78, Syi 88, Schmidt-Rohr 91]. Following this idea, in Fig. (6.1) we plot the change in potential energy when the chain stem makes a movement and changes from the state A (before the movement) to the state A' (after the movement). The intermediate step is the state when the chain defect is created and travelling through the crystallites, which is denoted by A^*.

Based on the transition state theory, the diffusion rates now can be considered to be the product of two quantities, the probability of forming the intermediate state A^* and the effective rate of crossing the energy barrier by the system. Under this assumption the effective rate of crossing the energy barrier can be shown to equal kT/h (k is Boltzmann's constant, T is the temperature, and h is Planck's constant). This effective rate can be considered as a kind of vibration of chain stem from the intermediate state A^* to the final state A'. Thus, its value is dependent only on the temperature and usually is independent of nature of the experienced change. Since there is an equilibrium between

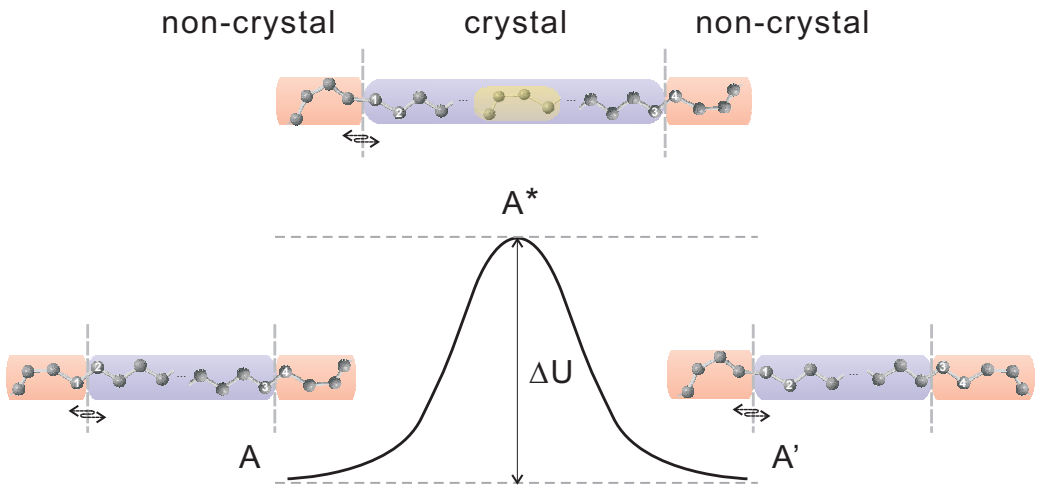

Figure 6.1: *Change of potential energy in the chain diffusion of PE. It is assumed that the system has a same potential energy before and after the movement of chain stem (i.e. a dynamic equilibrium). The transition state is the state when the chain defect is created and travelling through crystallites. The translative movement of chain stem is achieved via the traversing of chain defect through crystallites.*

the initial state A and the intermediate state A^*, the probability of forming the intermediate state at constant pressure is determined in absolute terms by the Boltzmann factor $e^{\Delta G/RT}$, where ΔG is the free energy difference per mole between the initial state A and intermediate state A^*. Then the diffusion rate ν of a chain stem is given by:

$$\nu = \frac{kT}{h} e^{-\Delta G/RT} \tag{6.1}$$

Eq. (6.1) states that the diffusion rate ν depends on the energy difference between the initial state A and the intermediate state A^* and not on the free energy difference between the initial state A and the final state A'. If substituting ΔG with $\Delta H - T\Delta S$, Eq. (6.1) can be written as:

$$\nu = \frac{kT}{h} e^{\Delta S/R} e^{-\Delta H/RT} \tag{6.2}$$

The form of Eq. (6.2) emphasizes the way in which temperature affects ν primarily through the activation energy ΔH (actually an enthalpy). To a good approximation the

activation energy for this kind of process is given by the Arrhenius equation:

$$\nu = \nu_0 e^{-\Delta H/RT} \tag{6.3}$$

with $\nu_0 = \frac{kT}{h} e^{\Delta S/R}$.

Eq. (6.3) can be written in the following form:

$$\ln\nu = \ln\nu_0 - \frac{\Delta H}{R}\frac{1}{T} \tag{6.4}$$

Assuming that ν_0 is almost constant in the experimental temperature range, the activation energy for the process can therefore be obtained plotting $\ln\nu$ against the reciprocal of the absolute temperature ($\frac{1}{T}$), where the slope is given by $\frac{\Delta H}{R}$ and the intercept contains $\frac{\Delta S}{R}$.

The above description of chain diffusion, however, is a very rough one based on an over simplified model. In practice the chain diffusion in PEs is much more complicated. For instance, the ν_0 in Eq. (6.3) usually will not have the formula of $\frac{kT}{h} e^{\Delta S/R}$. The prefactor $\frac{kT}{h}$ actually is derived from the molecular motion in the gas state and most probably will not be valid for the chain diffusion in PEs. Nevertheless, ν_0 will still have a dependence on the temperature T and be proportional to $e^{\Delta S/R}$. Thus, a new formula of ν_0 then could be written as:

$$\nu_0 = f(T) e^{\Delta S/R} \tag{6.5}$$

where $f(T)$ is a function of temperature T, describing the temperature dependence of ν_0.

6.1.2 The origin of the activation energy ΔH

In looking for the origin of ΔH, one should first consider the way how a chain stem achieves a movement in the diffusion motion. From literature, it's known that the crystalline chain units in PEs undergo a 180° jump motion. Following this point, the movement of a chain stem is considered as the result of a traveling chain defect,

combining the rotation of chain with a translation by one CH_2 unit along the crystallographic *c*-axis. The "size" of the defect and how the defect travel in the crystallites thus will be the factors determining the activation energy of the chain diffusion. Reneker proposed the old but widely known model, which requires $2 \sim 3$ CH_2 units to be involved in one defect [Reneker 62]. In this model, the traveling of defect needs a relatively high energy [Mansfield 78]. Later Mansfield and Boyd proposed another model, which describes a more extended defect, i.e. ~ 12 CH_2 units involved in one defect [Mansfield 78]. In this model, the defect consists of a fairly uniform succession of slightly twisted chain bonds, leading to a relatively low energy requirement for the movement of defect.

Based on the fact that the chain diffusion traverses crystalline and non-crystalline regions, the activation energy could be influenced by the non-crystalline regions. Considering the situation of the non-crystalline portion of a diffusing chain, it is easy to envisage that chain entanglements in non-crystalline regions will have some influences on the chain diffusion. However, the influence of chain entanglements will depend on the length scale of chain diffusion. If the chain diffusion happens on a very local scale, the diffusing chain most likely will not experience the presence of chain entanglements. If the chain had a large scale of diffusive motion, chain entanglements in non-crystalline regions then will give a retardance to the chain diffusion. However, due to the molecular motion in non-crystalline regions, entanglements usually are not a static structure, which makes it difficult to quantify the influence of chain entanglements on the chain diffusion. Nevertheless, the activation energy of chain diffusion could contain some contributions from chain entanglements.

In literature the presence of interphase between the non-crystalline and crystalline region has been proved. For the chain diffusion, the presence of this interphase bridges the different molecular motions in non-crystalline and crystalline regions and thus could have an influence on the chain diffusion. As already shown in the previous chapters, a suitable interphase like the chain folds in the solution crystallized PE can facilitate the chain diffusion. However, since the exact structure and modes of chain motion in the interphase are still not fully elucidated, it is difficult to propose a relationship between the activation energy and the interphase. In fact the influence of the interphase on the chain diffusion is related to both the entropy change ΔS and the

activation energy change ΔH, as indicated in Eq. (6.2). Besides the energy barrier, a lower entropy change ΔS is favorable to make an efficient transfer, which could be a thermodynamical explanation for the different diffusion rates in melt crystallized and solution crystallized UHMW-PE.

6.2 NMR detections of the chain diffusion

6.2.1 Two types of 1D ^{13}C exchange experiments: SPEX and CPEX

Based on the idea of 1D ^{13}C exchange experiment, there are two ways to detect the chain diffusion between crystalline and non-crystalline regions of PEs. One way is to first selectively polarize non-crystalline regions and monitor how the polarization "diffuses" into crystalline regions. Taking advantage of the short ^{13}C T_1 relaxation time in non-crystalline regions, the single-pulse excitation can be used for this purpose. In the following discussion we will call this experiment the single-pulse based exchange experiment (SPEX). The second way is to first selectively polarize crystalline regions via CP and then monitor how the polarization "diffuses" into non-crystalline regions and relaxes there. In the following discussion this experiment will be called the CP based exchange experiment (CPEX). The two pulse sequences are illustrated in Fig. (6.2).

Fig. (6.2a) sketches the pulse sequence of SPEX, which is well known as the saturation recovery pulse sequence used for T_1 relaxation time measurement. The first part of this pulse sequence is the recycle delay D_1. The delay time should be chosen long enough to avoid possible NOE effect on the ^{13}C signal. After D_1 a set of saturation pulses is applied on the ^{13}C channel. The following time τ is used to create the non-crystalline polarization by the fast relaxation process in non-crystalline regions and, the crystalline polarization by chain diffusion, carrying polarization from non-crystalline to crystalline regions. Due to the very long intrinsic ^{13}C T_1 relaxation time of crystalline component in PEs with natural abundant ^{13}C, the chain diffusion process is the only possible way to create the polarization in crystalline regions during the short τ time. If the crystalline signal build-up is based on the chain diffusion, one could expect that the plot of crystalline signal intensity against the square root of time τ will give a straight line and the slope of this line can be used to extract the chain diffusion coefficient of

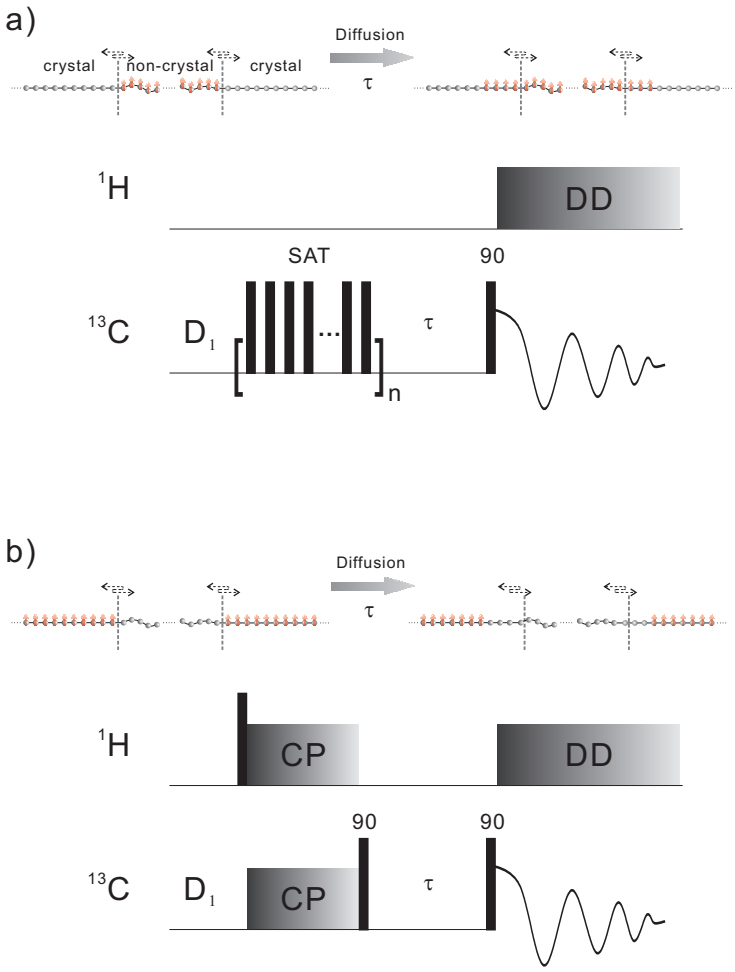

Figure 6.2: *Demonstration of 1D ^{13}C exchange pulse sequences: (a) SPEX; (b) CPEX. The explanation about the design of SPEX can be found in the main text. The pulse sequence of CPEX is the same as the Torchia pulse sequence [Torchia 78]. The cartoon pictures indicate the change of polarization during the experiments.*

this sample.

Different with SPEX shown in Fig. (6.2a), the pulse sequence of CPEX shown in Fig. (6.2b) utilizes a CP block as the first part of pulse sequence to create initial polarization in the rigid regions of sample, that is the crystalline part and some restricted non-crystalline parts. After CP, a 90° pulse is applied on the ^{13}C channel to flip the ^{13}C magnetization along the z (or -z) direction. Subsequently, in the τ time two processes happen: the fast relaxation of non-crystalline component and the chain diffusion between crystalline and non-crystalline regions. The presence of fast chain diffusion in

PEs could let the polarized chains in crystalline areas move into non-crystalline regions and lose their polarization by the fast T_1 relaxation in non-crystalline regions. Similar to SPEX, if the chain diffusion process is the only process which could relax the crystalline signal, the plot of crystalline signal against the square root of time τ will also give a straight line and the slope of this line gives the chain diffusion coefficient.

A basic prerequisite of these two methods is the combination of the very slow ^{13}C T_1 relaxation in crystalline regions and the fast ^{13}C T_1 relaxation in non-crystalline regions. The fast ^{13}C relaxation in non-crystalline regions assures the chain units there to get fully relaxed very quickly. In the case of SPEX the fast ^{13}C relaxation in non-crystalline regions supplies the ^{13}C polarization to diffuse into the crystallites. In the case of CPEX, the fast ^{13}C relaxation in non-crystalline regions depolarizes the chain units before moving back into crystallites. The very slow ^{13}C relaxation in crystalline regions assures that the change of crystalline signal does not originate from the ^{13}C relaxation processes in crystallites. In the experimental practice this assumption is satisfied quite well. At 320K the ^{13}C relaxation time of the non-crystalline component in PEs usually is less than one second, whereas the intrinsic ^{13}C relaxation time of the crystalline component in PEs is usually more than several hundreds seconds [Axelson 83]. Fig. (6.3) plots the increasing/decreasing of relative signal intensity against the square root of exchange time t for the UHMW-PE fiber. The linear curves of the plots strongly indicates a typical diffusive behavior of polymer chain present in this fiber sample.

6.2.2 Comparison of SPEX and CPEX

SPEX and CPEX both can be used to study the chain diffusion in PEs. By making a plot of normalized signal intensity against the square root of exchange time t, one could get the chain diffusion coefficient by determining the slope of curve. Via measuring the chain diffusion coefficients at different temperatures one could make an Arrhenius plot to determine the activation energy of chain diffusion. At a first glance it seems that there is no difference between these two kinds of 1D ^{13}C exchange experiments.

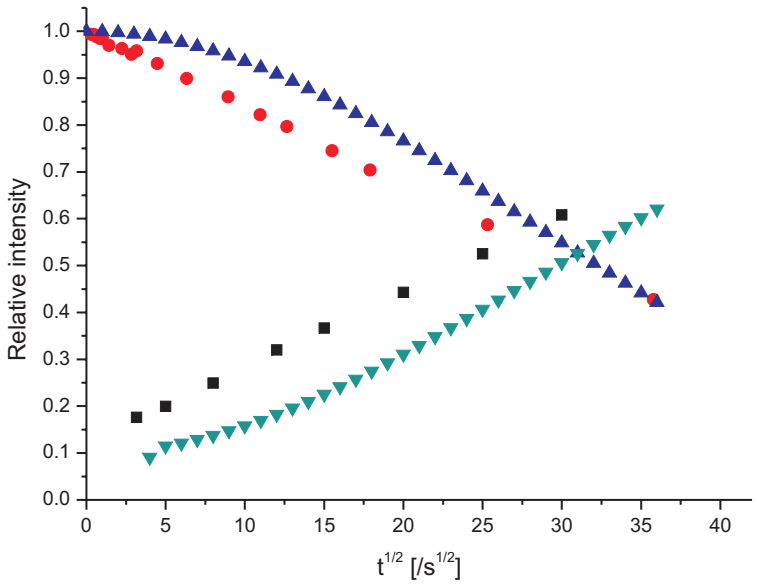

Figure 6.3: *The signal variation induced by the diffusion process in the UHMW-PE fiber. The normalized crystalline signal from the CPEX experiment (●), and the normalized whole signals, i.e. the crystalline and non-crystalline signals, from the SPEX experiment (■) are plotted against the square root of the diffusion time. The way for the signal normalization is explained in Chapter 5. For a comparison the exponential decay curve with a relaxation time 1500s (▲) and the exponential increase curve with the relaxation times 0.6s and 1500s (▼) are also plotted.*

In practice, the CPEX experiment has several advantages compared to the SPEX experiment.

Compared to SPEX a big advantage of CPEX is related to the signal normalization procedure, which becomes very important for the quantitative evaluation of the experiments. For the CPEX experiment, the normalization procedure is very simple, since the CP process in the CPEX experiment polarizes the whole crystalline component. The intensity of the crystalline signal at the exchange time $t = 0$ can be utilized to normalize the intensity of crystalline signal at the exchange time $t = \tau$. Whereas, in the SPEX experiment this normalization procedure requires the value of the sample crystallinity determined via the ^{13}C spectrum. Due to the very long intrinsic ^{13}C relaxation time in PE crystals, the accurate determination of sample crystallinity via the ^{13}C spectrum usually is very difficult. The uncertainty in the crystallinity determination thus will give some uncertain scaling factor to the plot of normalized signal intensity against the square root of exchange time t, and affect the accuracy of chain

diffusion coefficient determination.

Another advantage of CPEX actually is a disadvantage of SPEX, which is related to the NOE phenomenon in the experiment. For SPEX, the crystalline signal is obtained as follows: the polarization is created first in non-crystalline regions by the fast ^{13}C relaxation there, then via the chain diffusion the polarization is transfered into crystalline regions. During this process, if the protons of polymer are not in thermal equilibrium the ^{13}C polarization may gain some polarization from a NOE type polarization transfer. Since the NOE has transient contributions, the NOE enhancement factor varies with the exchange time. This will influence the crystalline signal intensity, leading to a complicated relationship between the change in the crystalline signal intensity and the exchange time. To avoid this problem, one way is to let the system get a constant NOE factor, which can be simply achieved by saturating the ^{1}H signal all the time. By doing this, the ^{13}C signal will get an constant enhancement due to the NOE. But the method also create a new problem that the signal normalization for the plot ($I \sim t^{1/2}$) become difficult. An alternative to avoid this problem is to get rid of the NOE signal enhancement. In this case the normalization process will become relatively easy, but significant signal sensitivity is lost. The pulse sequence of SPEX shown in Fig. (6.2a) is designed to get the spectrum without the influence of NOE.

In the CPEX experiment (6.2b), NOE does not play an important role. The ^{13}C polarization is transfered from ^{1}H via the CP process. During this process the ^{13}C polarization gains a certain enhancement factor. After the CP process, the polarization is flipped back along $+z$ or $-z$ axis. In the following exchange time due to the chain diffusion some portion of the polarized crystalline chains will move into non-crystalline regions and then lose their polarization due to the fast T_1 relaxation process there. The remaining portion of the chain, which always stays inside the crystallites during the chain diffusion, will still keep the polarization with the enhancement factor. Thus, the crystalline signal decay in CPEX is not influenced by the enhancement factor of CP. With long exchange times it is possible that non-crystalline chains are polarized by the relaxation process in non-crystalline regions and move into crystalline regions. The presence of this process could make the data analysis become complicated. However, a suitable phase cycling of CPEX pulse sequence can easily cancel out signals from

this kind of process.

6.2.3 Limitation of SPEX and CPEX

As already mentioned above, a basic assumption of the two methods is the combination of the very slow ^{13}C T_1relaxation in crystalline regions and the fast ^{13}C T_1 relaxation in non-crystalline regions. This assumption requires that the ^{13}C crystalline signal does not decay via its T_1 relaxation process, whereas the ^{13}C non-crystalline signal is relaxed immediately. In NMR practice, the former one usually can be easily fulfilled in the case of PE, because of its very long intrinsic crystalline ^{13}C T_1 relaxation time. However, due to the short, but not infinitely short ^{13}C T_1 relaxation time in non-crystalline regions of PE, the latter one usually cannot be fulfilled. This situation then gives rise to some features in the plot of signal intensity again the square root of exchange time t.

First, let's consider a standard diffusion case, which is shown in Fig. (6.4a). In this case the polarization is assumed to diffuses from non-crystalline to crystalline regions. At the time $t = 0$, only non-crystalline regions contain the polarization. Then at the time $t = t_m$ the obtained crystalline signal intensity I_C via the chain diffusion can be calculated from the following equation:

$$< I_C > \propto D^{1/2}\, t^{1/2} \tag{6.6}$$

where D is the diffusion coefficient. Eq. (6.6) actually is a derivative of the Einstein relation describing the relationship between the mean-square displacement of a particle and the consumed time. The plot of $I_C \sim t^{1/2}$ will give a straight line as exhibited by the red line in Fig. (6.4c).

However, in the practice at the time $t = 0$, there is no polarization present in non-crystalline regions. Before transferring the polarization to crystalline regions, the chains in non-crystalline regions must gain the polarization via the T_1 relaxation process. In this case, one could divide the practical diffusion process into two steps. Step (i) is the combination of polarization build-up in non-crystalline regions and simultaneously the polarization transfer via the chain diffusion. Step (ii) is the polarization

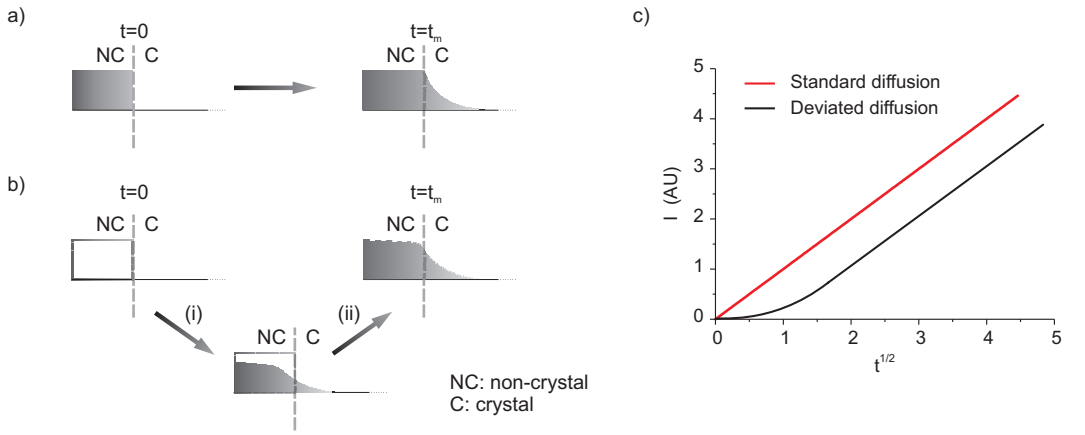

Figure 6.4: *The illustration of ^{13}C polarization transfer in SPEX experiment from: (a) the standard diffusion; (b) the deviated diffusion. The black color indicates the polarization. (c) The increasing behavior of crystalline signal intensity in the standard and deviated diffusion monitored via SPEX experiment.*

transfer via the chain diffusion. These two steps are illustrated in Fig. (6.4b). It is easy to see that if the ^{13}C T_1 relaxation process in non-crystalline regions becomes shorter or the chain diffusion rate becomes lower, step (i) will become shorter and then the experimental diffusion process will be closer to the ideal diffusion process as shown in Fig. (6.4a). For the PE samples used in this study, the ^{13}C T_1 relaxation time in non-crystalline regions of PEs at 320K is always close to 0.6s. Although this relaxation time is quite short, it still can cause some deviation in the beginning of the diffusion curve, which is illustrated in Fig. (6.4c).

As to CPEX the situation is comparable to SPEX. For the standard diffusion, the loses of the crystalline polarization can be considered as the result from the diffusion of the "blank". For the deviated diffusion, the description for the loses of the crystalline polarization is complicated. In a certain diffusion time the polarization can move from crystalline regions to non-crystalline regions via the chain diffusion. But since the ^{13}C T_1 relaxation time in non-crystalline regions is not infinitely short, the partially relaxed polarization can move back into crystalline regions, leading to a retarded decay process of the crystalline polarization. The illustration of the polarization decay process and the plot of $I_C \sim t^{1/2}$ is given in Fig. (6.5).

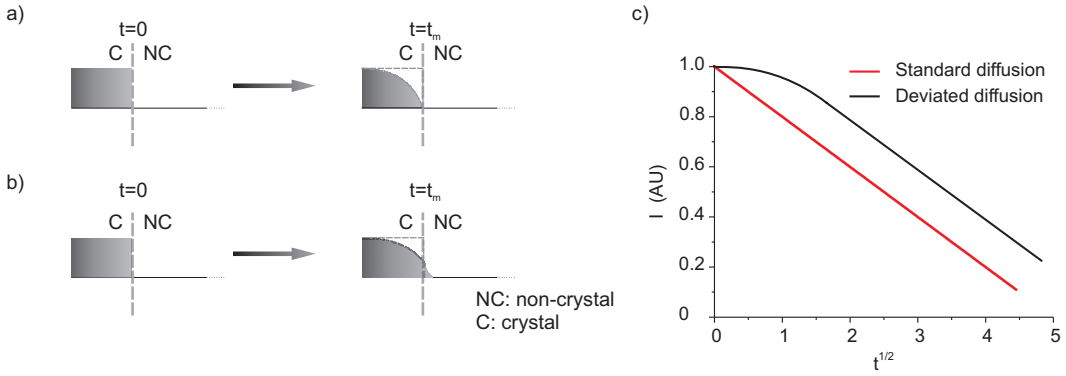

Figure 6.5: *The illustration of ^{13}C polarization decay in the CPEX experiment from: (a) the standard diffusion; (b) the deviated diffusion. The black color indicates the polarization. (c) The decaying behavior of crystalline signal intensity in the standard and deviated diffusion monitored via the CPEX experiment.*

6.3 Morphological influence on the chain diffusion of PE

In this section we will focus on the morphological influences on the chain diffusion of PE. The morphological factors include lamellar thickness, chain organization in non-crystalline region and chain entanglements. The CPEX method will be used for this study.

6.3.1 Influence of lamellar thickness on the chain diffusion

Three samples were chosen to demonstrate the influence of lamellar thickness on the chain diffusion. One is the solution crystallized UHMW-PE (SC-PE), which has a lamellar thickness $\sim$ 12nm. The second is made from SC-PE by annealing at 120$^{\circ}C$. After the annealing process the lamellar thickness of SC-PE is doubled, but the structures in non-crystalline regions of sample stay almost the same [Rastogi 97]. The third is the UHMW-PE fiber, which usually has a very big crystal thickness. The chain diffusive behaviors in these samples are exhibited in Fig. (6.6a).

The signal intensity in the plots of Fig. (6.6a) is normalized with the intensity of crystalline signal at the exchange time $t = 0$. (Experimentally, the intensity of crystalline signal at the exchange time $t = 1$ms is used for the normalization.) The initial normal-

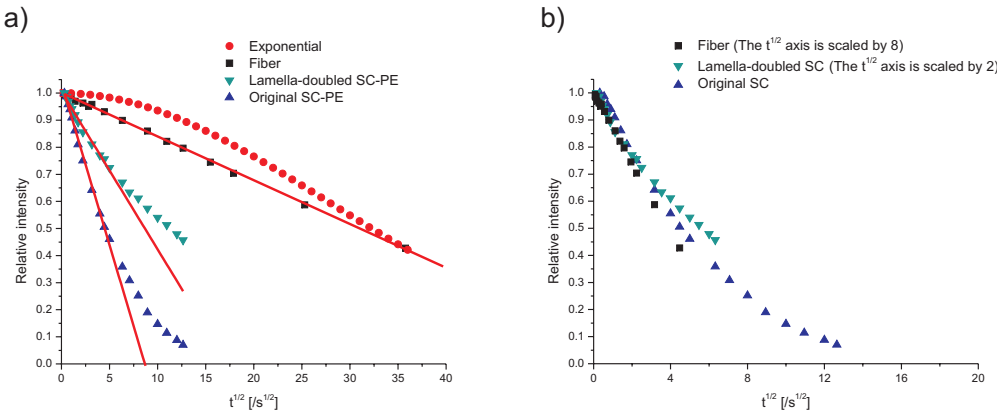

Figure 6.6: *(a) The decay of crystalline signal intensity in: (▲) the original SC-PE; (▼) the lamellar-doubled SC-PE; (■) the UHMW-PE fiber, plotted against the square-root of the exchange time. (b) The decay of crystalline signal intensity in the same PEs, but plotted against the scaled square-root of the exchange time. The scaling factor of $t^{1/2}$ axis relates to the lamellar thickness of sample. Using the lamellar thickness of original SC-PE as the unit, the factors of (▲) the original SC-PE; (▼) the lamellar-doubled SC-PE; (■) the UHMW-PE fiber are 1, 2, and 8 respectively. These data were acquired from the CPEX experiment performed at 320K. The pure exponential decay curve with a relaxation time* $\sim 1500s$ *(●) is shown in the plots for a comparison.*

ized signal decay thus fulfills the following equation:

$$\frac{<\mathrm{I_C}>}{\mathrm{I_0}} = 1 - S \cdot t^{1/2} \tag{6.7}$$

where $\mathrm{I_0}$ is the intensity of crystalline signal at the exchange time $t = 0$ and S is the slope in the plot of $\frac{<\mathrm{I_C}>}{\mathrm{I_0}} \sim t^{1/2}$. One knows that the signal intensity in this case is proportional to the polarized crystalline portion. Thus, if the sample has a typical lamellar structure, it is easy to derive the following equation:

$$\frac{<\mathrm{I_C}>}{\mathrm{I_0}} = \frac{<L>}{L_0} \tag{6.8}$$

where L_0 is the lamellar thickness of SC-PE and $<L>$ is the averaged thickness of polarized crystalline portion after the chain diffusion in the time t. Now, Eq. (6.7) can be re-written as:

$$\frac{<L>}{L_0} = 1 - S \cdot t^{1/2} \tag{6.9}$$

The diffusion coefficient D can be derived from the slope S:

$$D = g \cdot (L_0 \cdot S)^2 \tag{6.10}$$

where g is the so-called geometry factor of the diffusion. In this case, g is equal to 1/2, because we observe a 3D diffusion in one direction.

Now one could look at the chain diffusion behavior in the original SC-PE and the lamella-doubled SC-PE. These two samples are supposed to have a quite similar morphology except their different lamellar thickness [Rastogi 97]. As shown in Fig. (6.6a) in the first 40s these two samples both show the fast signal decay, which are quite linear to $t^{1/2}$. Fitting their signal decay curves yields a slope of -0.119 for the original SC-PE and -0.058 for the lamella-doubled SC-PE. It is interesting to see that the absolute slope value for the original SC-PE (0.119) is two times bigger compared to that of the lamella-doubled SC-PE (0.058). From Eq. (6.10) one can realize that the chain diffusion coefficients D in these two samples are similar. The different signal decay behaviors shown in Fig. (6.6a) thus are only due to their different lamellar thickness. The chain diffusion behavior of the UHMW-PE fiber shown in Fig. (6.6a) shows a straight line, indicating a typical chain diffusion behavior present in this sample. Fitting this straight line yields a slope -0.0162. This absolute slope value (0.0162) is ~ 8 times smaller than that of original SC-PE (0.119). Assuming that the chain diffusion coefficient in this fiber is similar to that in the original SC-PE, using Eq. (6.10) one can roughly estimate the averaged length of extended all-trans conformations in this fiber, which will be close to 100nm. In Fig. (6.6b) we made the plot that the $t^{1/2}$ axis is scaled by the factor which is proportional to the lamellar thickness of sample, that is, if considering the factor for the original SC-PE as 1, the factor for the lamella-doubled SC-PE is 2 and the fiber sample is 8. Before the signal intensity decays to 65%, the chain diffusion behaviors in these samples are quite similar. For longer time scales, the signal decays then begin to show a bending-up curvature. This deviation may result from some topological constraints imposed on the chain diffusion when the chains diffuse a long distance. The origin of this bending-up curvature has a very complicated nature, which will be discussed in the next section.

6.3.2 Influence of crystallization conditions on the chain diffusion

Two samples are chosen to show the influence of crystallization conditions on the chain diffusion. One is the solution crystallized UHMW-PE (SC-PE) and the other is the melt crystallized UHMW-PE (MC-PE). These two samples have the same crystal structure (orthorhombic) and a similar lamellar thickness (see Appendix F.3). Due to their different chain organizations in non-crystalline regions, different topological constraints are imposed on the chain diffusion in these two samples, leading to the different chain diffusive behaviors there.

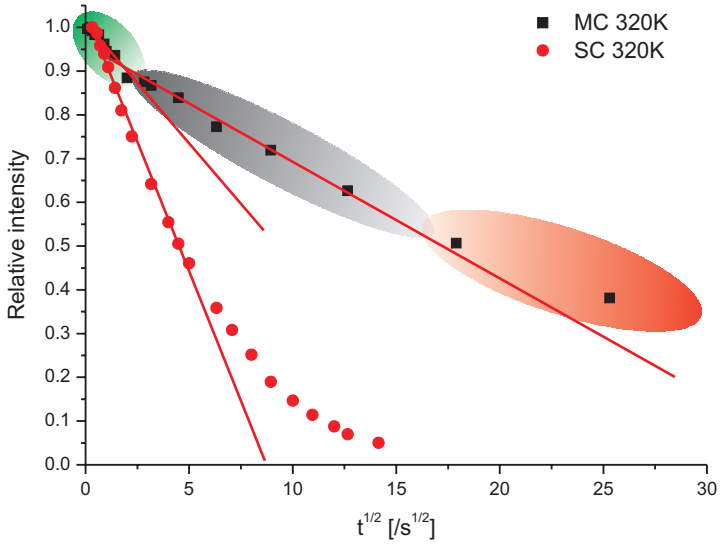

Figure 6.7: *The decay of crystalline signal intensity in: (●) SC-PE and (■) MC-PE, plotted against the square-root of the exchange time t. These data were acquired from the CPEX experiments performed at 320K.*

Fig. (6.7) shows the chain diffusion behaviors of SC-PE and MC-PE. From Fig. (6.7), it is easy to see that the signal intensity of SC-PE decays much faster than MC-PE. Since these two samples have a similar lamellar thickness, the faster signal decay in SC-PE indicates a faster chain diffusion present in this sample. From the discussion in the previous chapters, one knows that the chain folding structure present in non-crystalline regions of SC-PE favors the chain diffusion, whereas the random structure in non-crystalline regions of MC-PE does not. The different chain organizations in non-crystalline regions of the samples thus can be a reasonable explanation for the different rates of chain diffusion in SC-PE and MC-PE.

Another interesting feature in Fig. (6.7) is that, in the beginning of the decay curve the signal intensity of MC-PE shows a relatively fast linear decay against the square root of time t and the decay rate is close to that of SC-PE at the same temperature. This fast signal decay indicates the presence of some non-crystalline component in MC-PE, which contains the conformations favoring the chain diffusion as the case in SC-PE. Concerning its behavior, this non-crystalline component could be some chain folds or the so-called "interphase", which is located between crystalline and non-crystalline regions and contains favorable conformations for the chain diffusion. Fig. (6.8a) shows the signal decay curves of MC-PE at different temperatures. This figure shows that at high temperatures the fast signal decay seems to disappear, indicating that the favorable conformations for the chain diffusion in non-crystalline regions of MC-PE disappear at high temperatures. The disappearance of the favorable conformations can be attributed to the fast conformation exchange resulting from the increase of the chain mobility in non-crystalline regions of MC-PE at high temperatures. This finding is consistent with the observation in Chapter 3, where it is shown that non-crystalline components of MC-PE become more and more mobile with increasing temperature, as indicated by the temperature dependence of the $^{1}H - {}^{13}C$ dipolar coupling in non-crystalline regions. The temperature dependence of the fast decay can be seen more clearly in Fig. (6.8b), where the scaled plots have been made with the same data sets from Fig. (6.8a).

In Fig. (6.7) the decay curves of SC-PE and MC-PE both bend up when the chains diffuse a long distance. This bending-up curvature should not originate from the ^{13}C T_1 relaxation process in the PE crystallites, since the relaxation process would speed up the signal decay, leading to a bending-down curvature. This obviously is not the case in Fig. (6.7). The bending-up curvature of the curves in Fig. (6.7) indicates a slowing down of diffusion, and thus is rather indicative of some additional constraint imposed on the chain diffusion. The origin of this bending-up curvature thus could be related to the chain entanglements, which could retard the chain diffusion after the chains diffuse a certain distance. Besides the chain entanglements, actually the chain diffusion itself could also give a contribution to the bending-up curvature, which is discussed in the following.

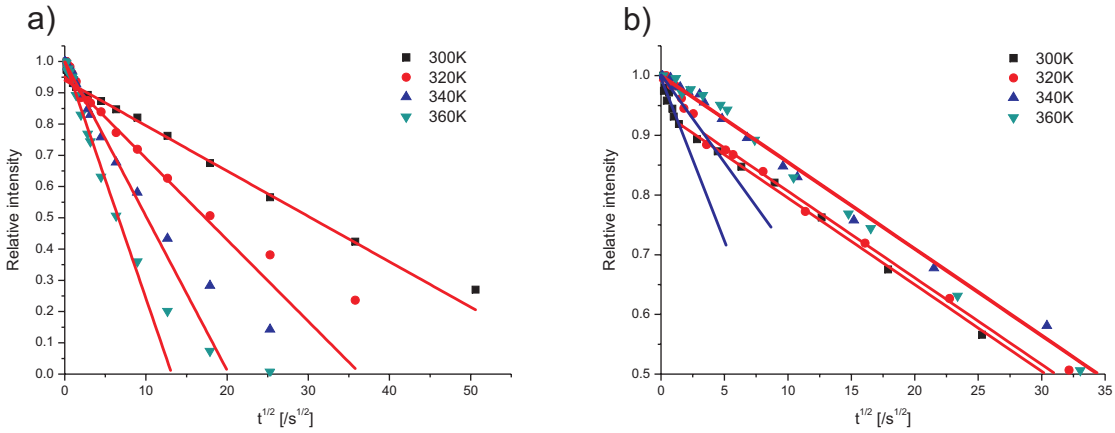

Figure 6.8: *(a) The decay of crystalline signal intensity in MC-PE at different temperatures, plotted against the square-root of the exchange time t. (b) The decay of crystalline signal intensity in the same sample, but plotted against the scaled square-root of the exchange time t. The scaling factor of $t^{1/2}$ axis is chosen in such way that the decay curves have the same slope after the fast decay in the beginning. The curve at 300K is used as the unit to scale the others.*

So far, the chain diffusion in PEs is described by the Einstein relation. In this consideration the diffusion of polymer chains is simplified to be accomplished by moving a chain stem in the crystal as a whole. In a real system, however, a chain stem more likely undergoes a curvilinear diffusion, where the diffusion path is almost confined in a tube which represents the restrictions of neighboring polymer chains. The chain diffusion is accomplished by randomly moving the chain back and forth inside the tube. This situation is analogous to that of a reptating chain in a fixed network (Chapter 6, [Doi 86], [Klein 02]). Based on the tube-reptation model, the fraction of the chain remaining in the tube, ψ, at some time, t, is given by:

$$\psi = \sum_{p;odd} \frac{8}{p^2\pi^2} \exp(-p^2 t/\tau_D) \tag{6.11}$$

where τ_D is the reptation time, the time taken for the chain to disengage from the tube in which it was confined at $t = 0$. Note that the tube here actually represents the restriction of chains from the crystal lattice, thus it doesn't have the same meaning as that often appears in polymer dynamics. From Eq. (6.11) one can model the signal

decay curve in CPEX with the following equation:

$$\frac{< I_C >}{I_0} = \sum_{p;odd} \frac{8}{p^2\pi^2} \exp(-p^2 t/\tau_D) \tag{6.12}$$

Using the signal decay curve of SC-PE as an example to fit it with Eq. (6.12), the graph shown in Fig. (6.9) is obtained.

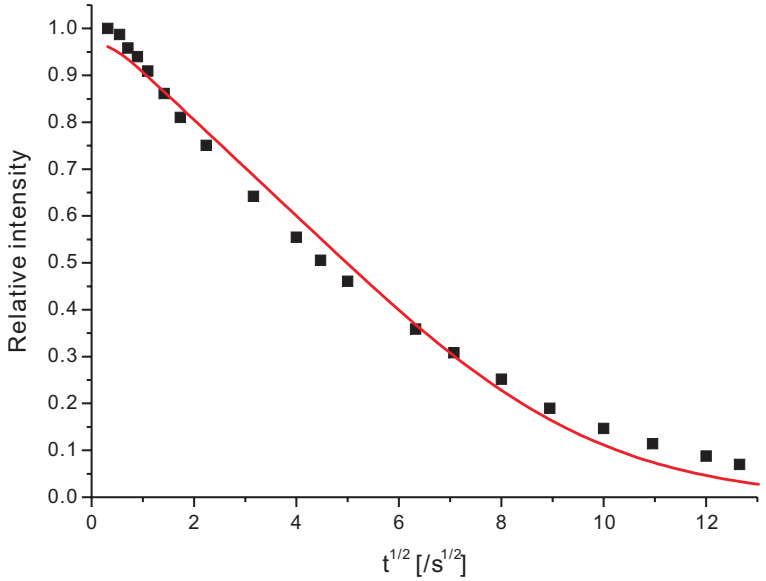

Figure 6.9: *The best fit for the decay of crystalline signal intensity in SC-PE using Eq. (6.12). The experimental data were acquired using CPEX at 320K.*

Although a clear bending-up curvature is shown for longer times, the fitting curve in Fig. (6.9) doesn't fit the experimental data very well, indicating that Eq. (6.12) does not provide an exact description for the chain diffusion process here. However, considering the broad linear region in the beginning of the fitting curve, one may ask if Eq. (6.12) can be used to fit the linear region of the signal decay curve. By doing so, the fitting curve in Fig. (6.10) is obtained.

The curvilinear approach fits very well with the experimental data in the linear region of signal decay, but in the bending-up region, the bending curvature of the fitting curve still does not fit the experimental data, indicating that the reptation like chain diffusion in crystallites gives only a partial contribution to the bending-up curvature of the ex-

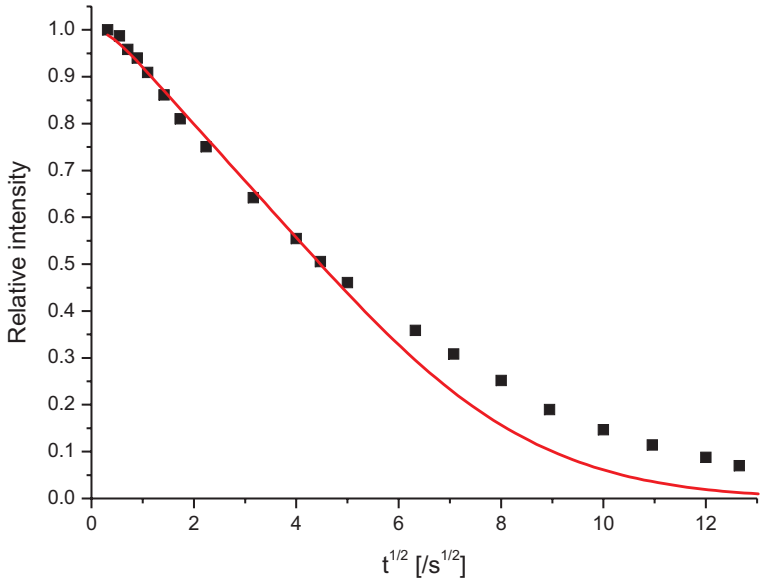

Figure 6.10: *The best fit for the linear region in the decay of the crystalline signal intensity in SC-PE with Eq. (6.12). The experimental data were acquired using CPEX at 320K.*

perimental data.

Via fitting the linear region of the signal decay curve, one is able to extract the diffusion coefficient D from the Einstein approach or the reptation time τ_D from the curvilinear analysis. One could wonder if these two approaches are equivalent. Fig. (6.11) shows the best fits for the linear region in the signal decay of SC-PE with Eq. (6.12) (the blue line) and the Einstein relation (the red line). In the linear region of signal decay the fitting curves are almost superimposed and both fit very well with the experimental data points. Determining the temperature dependence of these two parameters can yield the activation energies of the chain diffusion. In the latter part of this chapter, we will show that these two approaches give similar activation energies for the chain diffusion, which further confirms the equivalence of these two approaches. For its simplicity, the linear fitting approach based on the Einstein relation will be used for most cases in the following discussion.

For the decay curve of MC-PE, one may argue that this kind of signal decay could be a kind of multi-component exponential decay, which often is used to explain the ^{13}C T_1 relaxation behavior in PE crystallites. But for the MC-PE used in this study, it seems

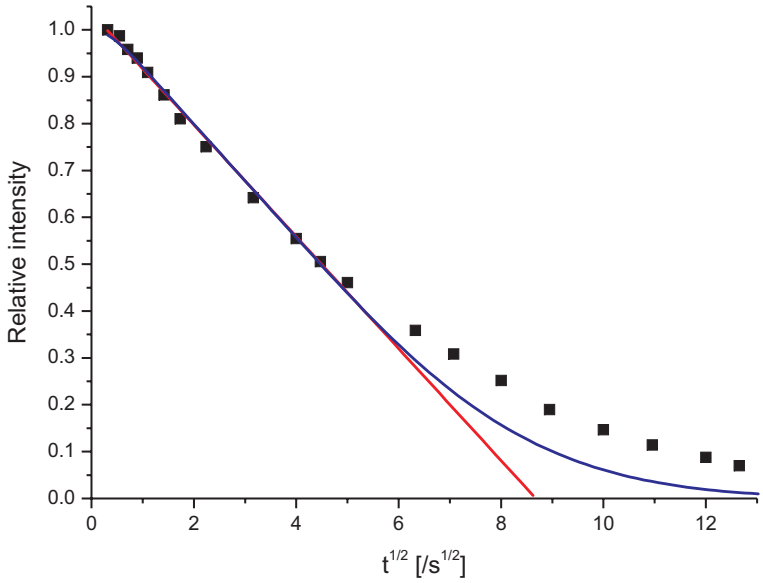

Figure 6.11: *The best fits for the linear region in the decay of crystalline signal intensity in SC-PE with Eq. (6.12) (the blue line) and the Einstein relation (the red line). The fitting procedure gives the reptation time* $\tau_D = 29.6s$ *and the diffusion coefficient* $D = 1.42 \times 10^{-18} m^2 s^{-1}$. *The experimental data were acquired using CPEX at 320K.*

that the multi-component exponential decay cannot be used to properly describe the signal decay. We fitted the crystalline signal decay curve of MC-PE with a two exponential decay function $I_C = a * \exp(-t/T_1) + (1-a) * \exp(-t/T_2)$, which yields two relaxation time: the short one is 15.9s with a fraction of 27.1% and the long one is 831.9s with a fraction of 72.9%. The best fit for the crystalline signal decay curve of MC-PE with two exponential components is ploted in Fig. (6.12).

At the first glance, one could think that the fitting of signal decay curve in Fig. (6.12a) is not very bad. But actually it is the linear t axis that hides the detail of the fitting. When enlarging the area indicated by the gray ellipse in Fig. (6.12a), one immediately realizes that the two-exponential fitting is not appropriate for the decay (see Fig. (6.12b)). Adding more exponential components could improve this fitting. But more exponential components in the curve means more components in crystalline regions of sample, which usually does not have a clear physical meaning.

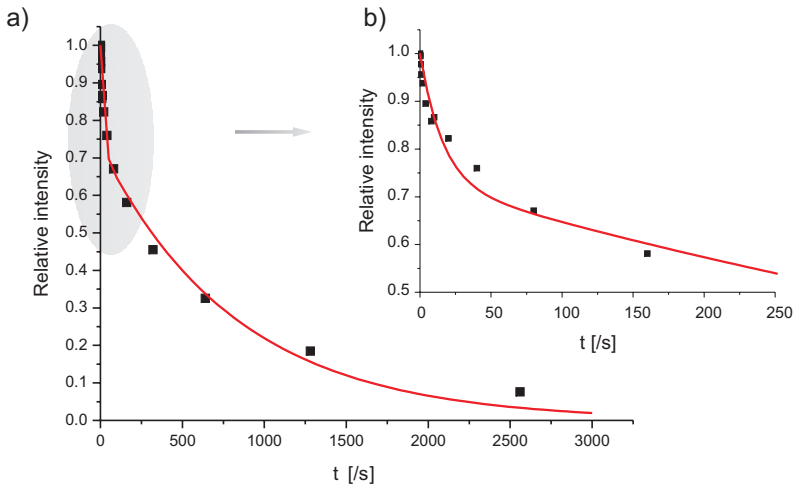

Figure 6.12: *(a) The best fit for the crystalline signal decay curve of MC-PE with two exponential components. (b) The enlarged region of (a).*

6.3.3 Influence of drawing process on the chain diffusion

As already mentioned in the last chapter, drawing PE samples could induce substantial changes in the morphology of sample, which would lead to changes in the chain diffusion behavior. In this section several UHMW-PE samples will be investigated to show how the chain diffusion can be affected by the drawing process. One sample is the original undrawn SC-PE. The another two drawn samples were prepared from the original SC-PE, with different draw ratios: one was drawn with a draw ratio $\lambda = 5$ and the other was drawn to $\lambda = 30$. The drawing has been done at $T = 90℃$. For comparison, the fiber is also chosen as the sample which has the highest draw ratio. The signal decay behaviors of all these samples are exhibited in Fig. (6.13).

From Fig. (6.13) it is easy to see that with increasing draw ratio the signal decay is slowed down. For the original undrawn SC-PE sample, it shows the fastest signal decay. For the sample with the draw ratio $\lambda = 5$, the signal decay shows only a minor deviation from the behavior of undrawn sample. When the draw ratio λ is increased to 30, the signal decay seems to slow down and a clear bending-up curvature is observed. For the fiber sample, the signal decay curve differs from those of all the other samples. A typical linear behavior and the slowest signal decay are found in this sample.

The origin of the different signal decay behavior in these samples can be related to their

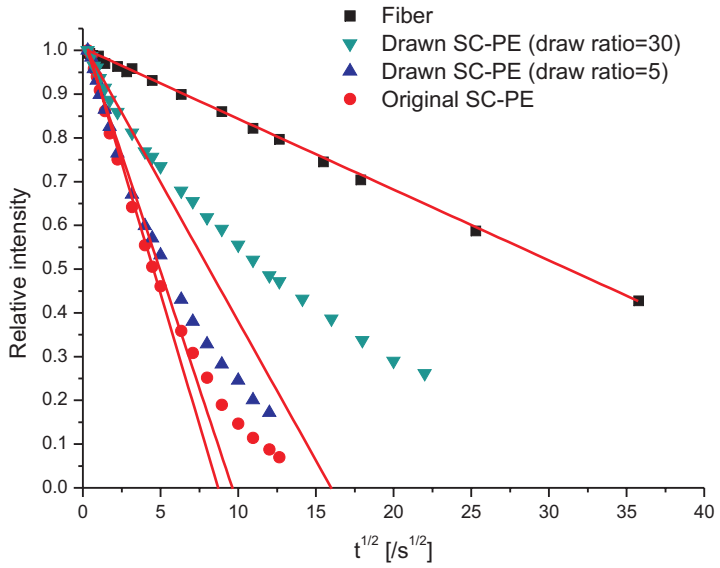

Figure 6.13: *The decay of crystalline signal intensity in: (●) the original SC-PE; (▲) the drawn SC-PE sample with $\lambda = 5$; (▼) the drawn SC-PE sample with $\lambda = 30$; (■) the UHMW-PE fiber, plotted against the square-root of the exchange time. These data were acquired from the CPEX experiments performed at 320K.*

different lamellar thickness and the different topological constraints, which vary with draw ratio of sample. First, let's consider what is the influence of lamellar thickness of sample on the signal decay curve. In order to avoid the influence of the chain entanglements, which could bend up the signal decay curve, we will focus on the signal in the linear decay region. For the drawn sample with $\lambda = 30$, the linear region is the initial 20% signal decay. For all the other samples the linear region is the initial 50% signal decay. Fitting the curves in these linear regions yields four slopes, that is, -0.119 for the undrawn SC-PE, -0.107 for the drawn SC-PE with $\lambda = 5$, -0.063 for the drawn SC-PE with $\lambda = 30$ and -0.016 for the fiber. Assuming that the variation of these slopes is only due to the change of lamellar thickness, with Eq. (6.10) one could roughly estimate the lamellar thickness in these samples. For the slightly drawn sample ($\lambda = 5$), the lamellar thickness becomes a little bit bigger after drawing. Whereas, for the drawn sample ($\lambda = 30$) the lamellar thickness is nearly doubled after drawing. This observation is in good agreement with results from SAXS experiments [Van Aerle 88, Van Aerle 89].

Now let's consider the influence of topological constraints on the chain diffusion of sample. One knows that chain organization in non-crystalline regions of sample changes during the drawing process. If the polymer chains do not disentangle during

drawing, the drawing process will increase the ”density” of the chain entanglements in the non-crystalline regions because the content of non-crystalline component in the drawn sample decreases. The increase of chain entanglements in non-crystalline regions apparently will give more retardance to the chain diffusion in the sample, which explains why in Fig. (6.13) the bending-up curvature of the drawn samples appears earlier than the original undrawn sample. The fiber sample shows a linear decay against $t^{1/2}$ in Fig. (6.13) until the signal decay to $\sim 55\%$ of the intial, which could be indicative of very rare chain entanglements in this fiber sample, resulting from being gel-spun.

A very wide distribution of lamellar thickness in a PE sample actually can also give a contribution to the bending-up feature in the signal decay curve obtained from the CPEX experiment, since the slope of the curve is influenced by lamellar thickness. However, evaluating this contribution requires the knowledge of the thickness and content distributions of crystalline lamellae in a sample. Drawing solution crystallized PEs increases the distribution of lamellar thickness in the sample, as indicated by an increase in the width of the SAXS peaks [Van Aerle 88, Van Aerle 89]. Therefore, the bending-up feature of the signal decay curves in Fig. (6.13) could also contain some contributions from the thickness distribution of lamellae in the samples, which increases with increasing draw ratio.

6.3.4 Activation energy of the chain diffusion

Using CPEX experiment the diffusion coefficient of polymer chains in PEs can be measured. Analyzing the temperature dependence of chain diffusion coefficient, the activation energy of the chain diffusion can be determined. Two samples were chosen for this study. One is SC-PE and the other is MC-PE. These two samples were made from the same UHMW PE powder and have a similar thickness of $\sim$ 12nm.

Fig. (6.14) shows the plot of crystalline signal intensity of SC-PE and MC-PE as a function of the square root of exchange time t at different temperatures. Fitting the linear region of the signal decay curves yields the chain diffusion coefficients (For MC-PE, the data points after the fast decay were chosen for the fitting.). These temperature dependent diffusion coefficients can be combined in an Arrhenius plot, which

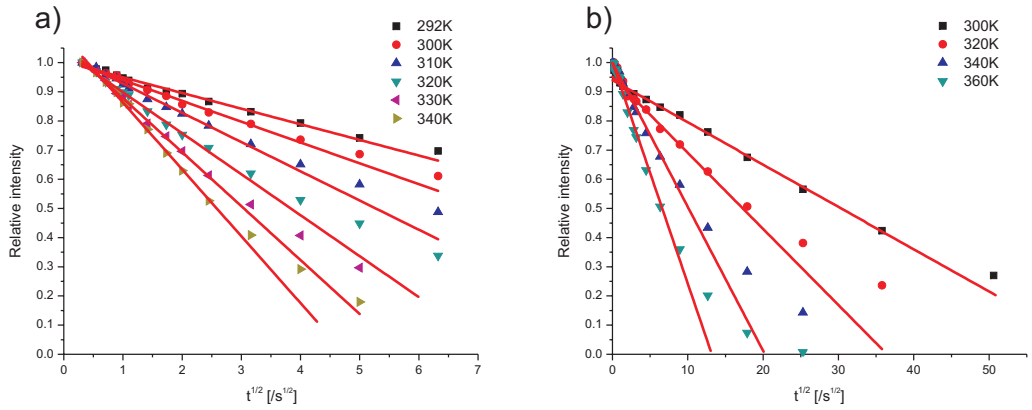

Figure 6.14: *The decay of crystalline signal intensity in (a) SC-PE and (b) MC-PE at different temperatures, plotted against the square root of the exchange time t. For MC-PE, the data points after the fast decay are chosen for fitting.*

is given in Fig. (6.15).

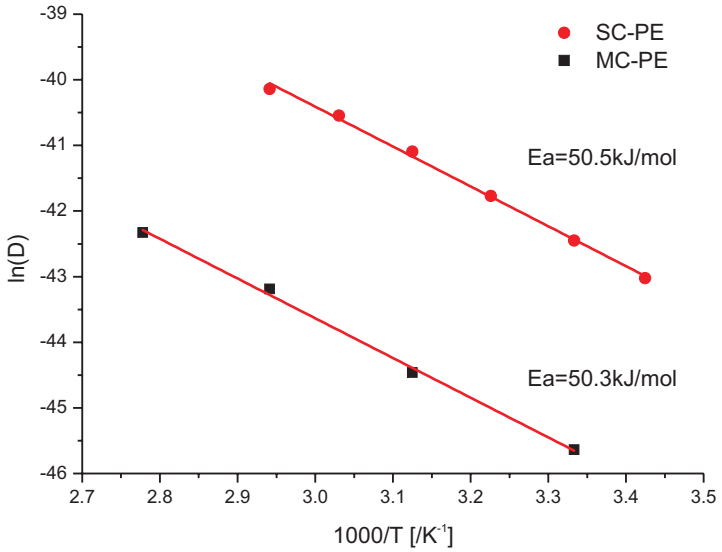

Figure 6.15: *Arrhenius plots of the chain diffusion coefficients in: (●) SC-PE and (■) MC-PE.*

The chain diffusion coefficients D plotted in Fig. (6.15) are calculated with Eq. (6.10). The lamellar thickness of the two samples used in the calculation is 12nm. In the temperature range of the experiments, the lamellar thickness of sample is considered to be unchanged. Fitting the curves in Fig. (6.15) yields an activation energy of 50.5 kJ/mol for SC-PE and 50.3 kJ/mol for MC-PE, which both are two times smaller than the

values given in literature [Schmidt-Rohr 91]. The difference in the values of the activation energies probably reflects the difference between the "apparent" and "effective" jumps of CH_2 in PE crystals, the latter, that leads to the chain diffusion. The detailed discussion about the "apparent" and "effective" jumps of CH_2 in PE crystals will be given below.

Concerning the very different chain diffusion rates in the two samples at a given temperature, it is remarkable to see that the chain diffusion in the two samples have a similar activation energy. To elucidate the different chain diffusive behaviors of the two samples, Eq. (6.2) can be taken into account, indicating that the rate of chain diffusion actually is controlled not only by the change of activation energy ΔH but also by the change of entropy ΔS in the motion. For these two samples the activation energies ΔH involved in the motion are quite similar. Thus, the different entropy change ΔS in the motion probably contributes to the different chain diffusion rates in the two samples. From the y-axis intercept of the Arrhenius plot in Fig. (6.15) one could extract the entropy change in the motion via the following equation:

$$\text{y-axis intercept} = \ln f(T)_\infty + \frac{\Delta S}{R} \tag{6.13}$$

From the fitting one obtains the y-axis intercept of -22.2 for SC-PE and -25.5 for MC-PE. In order to obtain the absolute value for ΔS, one has to know the value of $\ln f(T)_\infty$ for both samples, which cannot be measured in our experiments. However, the y-axis intercepts still can be used to compare the entropy change in the two samples. Assuming that both samples have a similar $f(T)_\infty$, one can easily derive Eq. (6.14) from Eq. (6.13):

$$\Delta S_{SC} - \Delta S_{MC} = \big((\text{y-axis intercept})_{SC} - (\text{y-axis intercept})_{MC}\big) \cdot R \tag{6.14}$$

If the entropy change of the chain diffusion is related to a group of CH_2, which consists in the chain defects moving from non-crystalline regions into crystalline regions in the chain diffusion, the entropy change during this movement thus can be written as:

$$\Delta S = S^* - S \tag{6.15}$$

where S denotes the entropy of the CH_2 units before moving and S^* denotes the entropy

for the CH_2 units in the transition state. With Eq. (6.15) one could re-write Eq. (6.14) as:

$$(S^*_{SC} - S_{SC}) - (S^*_{MC} - S_{MC}) = 3.3 \cdot R \quad (6.16)$$

$$(S^*_{SC} - S^*_{MC}) + (S_{MC} - S_{SC}) = 3.3 \cdot R \quad (6.17)$$

It is easy to envisage that in SC-PE and MC-PE there is no difference in the entropy of chain defects when they travel through the crystallites. Thus, it is reasonable to assume that S^*_{SC} is equal to S^*_{MC}. With Eq. (6.17) one thus can get the entropy difference of $S_{MC} - S_{SC} \approx 27.4$J/K. This entropy difference indicates that CH_2 units involved in the chain diffusion have bigger change in entropy in MC-PE than that in SC-PE, which consists with the observation shown in Chapter 3.

As mentioned before, the linear fitting based on the Einstein relation is equivalent to the curvilinear approach based on the tube/reptation model. We also can use the curvilinear approach to extract the activation energy and entropy difference. Fitting the data with Eq. (6.12) yields the reptation time τ_D. The activation energy then can be extracted from the temperature dependence of τ_D. Fig. (6.16) show the fittings of the crystalline signal decay curves of SC-PE and MC-PE at different temperatures.

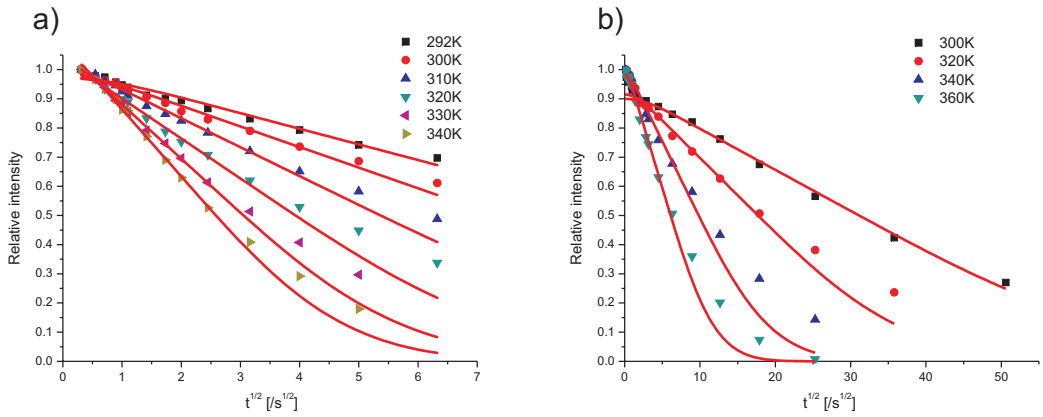

Figure 6.16: *The decay of crystalline signal intensity in (a) SC-PE and (b) MC-PE at different temperatures, plotted against the square root of the exchange time t. The fitting curves are created by Eq. (6.12). For MC-PE, the data points after the fast decay are chosen for fitting.*

The Arrhenius plot of the reptation time τ_D is shown in Fig. (6.17).

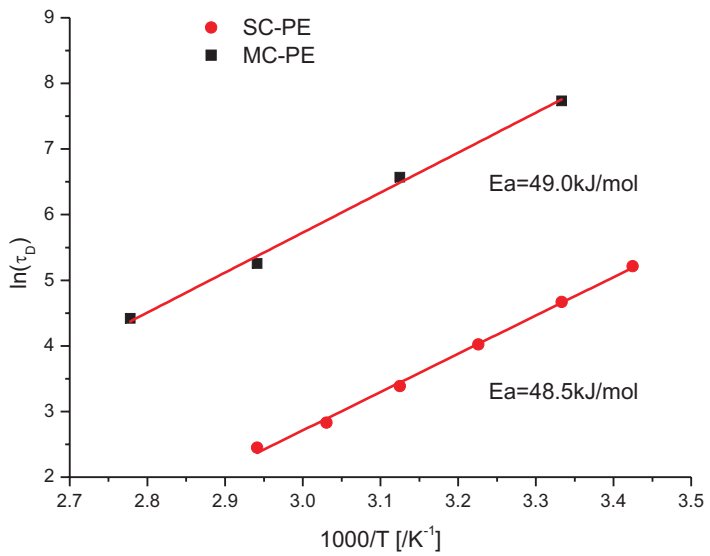

Figure 6.17: *Arrhenius plots of the reptation time* τ_D *in: (●) SC-PE and (■) MC-PE.*

This fitting procedure yields an activation energy of 48.5 kJ/mol for SC-PE and 49.0 kJ/mol for MC-PE and the corresponding entropy difference is $S_{MC} - S_{SC} \approx 23.3$J/K, which are similar to the values determined by the linear fitting approach.

The phenomenological diffusion coefficient D obtained from the exchange experiment can be used to calculate the jump rate of CH_2 groups in PE crystals. Eq. (6.18) gives the expression of D in terms of the lattice constant a and jump rate v:

$$D = g' \cdot a^2 \cdot v \tag{6.18}$$

where g' is the geometry factor of the jump motion. It takes into account that for jump motions with all directions, only some orientations contribute to the diffusion motion. In the case of the jump motion in PE crystals, g' is about 1. Since the unit cell of PE crystal contains two CH_2 groups, the lattice constant a is equal to the half of the crystallographic c, which is $\sim 1.267\AA$.

Using Eq.(6.18) the jump rate of CH_2 groups in PE crystals can be calculated from the chain diffusion coefficient D. However, the jump rate obtained in this way corresponds to the jump motion, where every jump leads to a translative movement of chain

stem. Thus, this jump rate is better to be term as the ”effective” jump rate to differentiate with the ”apparent” jump rate in PE crystals. In literature the apparent jump rates of CH_2 groups in crystals of melt crystallized PE sample at different temperatures have been measured by dipolar ^{13}C NMR [Hu 99a] and DQ-DQ MAS exchange NMR [Schnell 01a]. The values of jump rates obtained in this work using Eq. (6.18) have been combined with the literature values together in the Arrhenius plot given in Fig. (6.18).

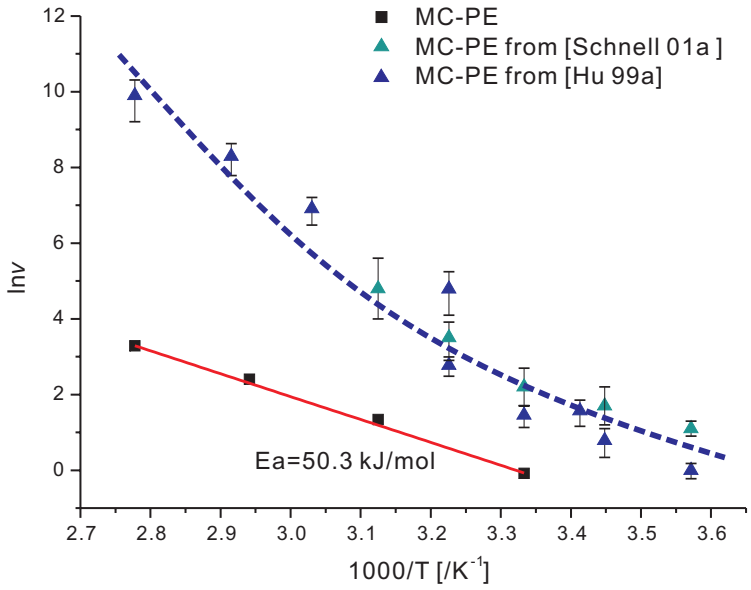

Figure 6.18: *Arrhenius plots of the apparent jump rates (▲, ▲) and the effective jump rates (■) in the MC-PEs. The data points plotted as (▲) are taken from [Schnell 01a] and the data points bolted as (▲) are taken from [Hu 99a].*

Comparing the two kinds of jump rates shown in Fig. (6.18), it is easy to see that at a given temperature the apparent jump rate is always higher than the effective jump rate determined in this work, indicating that the jump motion of CH_2 groups in PE crystals does not always lead to the translative movement of chain stem. However, since the PE samples in the literature [Hu 99a, Schnell 01a] are not the same as that we used in this work, the point derived from the direct comparison between the values of jump rates seems not to be very persuasive. But a further proof for the above point can be found from the different temperature dependence of the effective and apparent jump rates in Fig. (6.18). With increasing the temperature, although the effective and apparent jump rate both increase, the fraction of the effective jumps decreases, as indicated by

the increase of the difference between the effective and apparent jump rates at higher temperatures. The decrease of the fraction of the effective jumps indicates that in the high temperature range the jump motion in the PE crystals becomes more and more ineffective.

The above comparison gives us a picture of the chain diffusion in PE crystals. In literature people have proposed that the movement of a whole chain stem in PE crystals is accomplished by transferring defects through the crystallites. In this scenario, a defect is created at one side of the crystal surface. In order to make a successful movement of the whole chain stem, the defects have to move through the crystallite to the other side and finally leave the crystallite. However, when the defects travel inside the crystallites, they could be reflected back by some hindrances such as disordered crystalline parts or the interphase between crystalline and non-crystalline regions. If this reflection happens, the chain stem then will not achieve a movement, since all the involved CH_2 groups will jump back to their previous sites. In this case the CH_2 groups perform the jump motions forwards and backwards, but the whole chain stem stays, which explains the difference between the effective jump rate and the apparent jump rate. To achieve a movement for chain stem, the defects have to leave crystallites and thus must pass through the interphase. The conformers in the interphase and their dynamic modes thus become quite important for the transfer of defects between crystalline and non-crystalline regions. Following this idea, it will be very interesting to compare the effective and apparent jump rates in the solution crystallized PE sample. But so far there are no apparent jump rates available in literature for the solution crystallized PE sample.

The nonlinear behavior in the Arrhenius plot of apparent jump rates shown in Fig. (6.18) is another remarkable phenomenon. As indicated by the slope of the spline in Fig. (6.18), the apparent activation energy of the jump motion increases with increasing temperature. Assuming that the apparent activation energy relates to the defects in PE crystals, this temperature dependence of the apparent activation energy indicates the increase of the defect number in the PE crystals at high temperatures, which probably originates from the lattice expansion of PE crystals [Strobl 78]. As the lattice expands, the likelihood of defects will increase, yet many of those apparently are not effective for chain diffusion, leading to a decreasing fraction of effective jumps. Since the

percentage of the effective jumps decreases with increasing temperature, in the high temperature range the activation energy determined via the effective jump rates (from the ^{13}C exchange experiment) differs from that determined via the apparent jump rates. However, from Fig. (6.18) one could see that in the low temperature range the slopes of the spline and the straight line (derived from the efficient jump rates) are similar. This indicate that the percentage of the effective jump stays almost constant in this temperature range, and thus the activation energies determined from the apparent jump rate and from the effective jumps become similar, which both are close to the half of the values given in literature [Hu 99a, Schnell 01a] (actually determined from the high temperature range). Recently, mechanical measurements showed a similar temperature dependence of the activation energy from relaxation processes in PEs [Matsuo 03]. The finding here thus give a microscopic picture to explain the results revealed by the mechanical measurements.

6.4 Conclusions

In this chapter, we studied the influences of sample morphology on the chain diffusion, which includes lamellar thickness, chain organization in non-crystalline regions and chain entanglements. These morphological factors explain the different chain diffusion behavior in the different PE samples. The activation energies of the chain diffusion in two UHMW-PEs were measured via determining the temperature dependence of the chain diffusion coefficients and the reptation time. From the chain diffusion coefficients, the rates of jump motion in the melt crystallized UHMW-PE were calculated. Compared to literature values, the jump rates obtained in this way are always smaller at a given temperature. A concept of effective jump motion was introduced to explain the difference. Since the chain diffusion is considered as the microscopic mechanism of the α-process in PE, related to crystal thickening, drawability, the creep behavior of PE fiber, etc, the study in this chapter then has implications in our understanding of all these α-process related phenomena.

6.5 Outlook

The chain diffusion in PEs is a quite complicated phenomenon influenced by many factors. In this chapter the influences of lamellar thickness, crystallization conditions and drawing processes were discussed. But in fact some other factors such as cross-linking, chain branching and molecular weight, also can have strong influences on the chain diffusion. Since all the PE samples used in this work are linear ones, we did not consider the influence of cross-linking. As to the influence from chain branching, it includes length of chain branch, branch degree, branch distribution, etc. In this chapter the influence of chain branching was not discussed because the PE samples studied in this chapter have a very low branch degree ($\leq$ 1 branch per 10000 CH_2 backbone units.). However, how chain branching would influence the chain diffusion in PEs could be an interesting topic, which will be studied in the future.

The influence of molecular weight is another topic, which is not covered in the discussion of this chapter. Following the polymer dynamics theory, the diffusion property of polymer chains in melts usually shows a strong dependence on molecular weight [Doi 86]. Different chain entangled states in melts give rise to different power relationships between the chain diffusion coefficient and molecular weight of the sample. However, for the chain diffusion of PE in the solid samples, it does not show a clear molecular dependence on the chain diffusion coefficient. Preliminary results have shown that there is almost no difference in the diffusion rate between the solution crystallized UHMW-PE and LMW-PE, although the molecular weight of UHMW-PE is $\sim$ 100 times bigger than LMW-PE. This remarkable phenomenon reveals that the chain diffusion in polymeric solids does not follow the classic Rouse model and tube-reptation model which were developed from polymeric melts. But to quantify the influence of molecular weight a similar molecular weight distribution of sample is required, which usually is difficult for the sample synthesis.

Summary

In this thesis, morphological influences on the molecular dynamics of PE were investigated. Several PE samples were used for this investigation. Via the different processing histories these samples have different morphologies, leading to different molecular dynamics present in these samples. A broad variety of solid state NMR techniques were used to investigate the chain dynamics in these PE samples. The local chain dynamics in non-crystalline regions of the samples was studied via measuring $^{1}H - ^{13}C$ heteronuclear dipolar coupling and ^{13}C CSA. The long range chain diffusion motion of PE was monitored via ^{13}C exchange experiment.

In the first part of this work (Chapter 3, 4 and 5) the morphological influence on the local chain dynamics in non-crystalline regions of PE was focused. In Chapter 3 two linear UHMW-PE samples (SC-PE and MC-PE) were used as representative examples to demonstrate the morphological influence on the molecular dynamics of PE. The two samples were prepared from the same UHMW-PE powder but with different crystallization conditions. One was crystallized from a melt and the other was crystallized from a dilute solution. Solid state NMR studies were performed to follow chain mobility in the non-crystalline regions of these two samples. The chains in non-crystalline regions of the melt crystallized sample show largely isotropic motion, whereas the solution crystallized sample reveals anisotropy. The anisotropy present in non-crystalline regions is maintained at higher temperatures. The location, frequency and geometry of this motion favor the chain diffusion between non-crystalline and crystalline regions of PE.

In Chapter 4, our study was extended to linear LMW-PE samples. Different from the case in the UHMW-PE samples, the motional anisotropy present in non-crystalline regions of LMW-PE was found not only in the solution crystallized sample but also in the melt crystallized sample. This phenomenon was explained as the result of residual

chain folding structure present in the melt crystallized LMW-PE samples. All of the LMW-PEs, which posses motional anisotropy in non-crystalline regions, exhibit clear chain diffusion, providing evidence of the role of motional anisotropy on the chain diffusion in PEs. The chain diffusion in the LMW-PEs, however, show a lower temperature dependence compared to the UHMW-PEs in Chapter 3. Combined with the observation of the $^{1}H - ^{13}C$ dipolar coupling constants in the non-crystalline areas at different temperatures, this difference was explained by the possible structure variation (e.g. the loosening of chain folds) with increasing temperature.

In Chapter 5, an UHMW-PE fiber was chosen for studying the morphological influence on the molecular dynamics. The morphology of this UHMW-PE fiber has the chain-extended structure, which is significant different from the sample morphology developed from quiescent crystallization condition, i.e. solution and melt crystallizations. This special morphology leads to special molecular dynamics in the fiber. The motion anisotropy was found present in the surface of fiber crystallites. The detailed information of this motion anisotropy shows that the involved chain units in this motion combine wiggling and rotation around the chain backbone, while their all-trans conformations are kept more or less unchanged. Considering its location and geometry, this motional anisotropy in the PE fiber is considered to have a strong relationship with the chain diffusion in the fiber.

In Chapter 6, the chain diffusion between non-crystalline and crystalline regions of PE is focused. The influences of lamellar thickness, crystallization conditions and drawing process on the chain diffusion of PE were studied via the ^{13}C exchange experiment. The different chain diffusive behaviors in the different PE samples were explained based on the knowledge of the sample morphology. A thermodynamic treatment of the chain diffusion in two UHMW-PEs has been taken into consideration, which reveals the entropy-controlled feature of the chain diffusion in PE. This is consistent with the observation in Chapter 3 that the sample with a restricted local chain mobility shows a fast chain diffusion between non-crystalline and crystalline regions. Using the chain diffusion coefficient, the rates of the jump motion in the crystals of the melt crystallized PE have been calculated, which are always smaller than those in literature at a given temperature. To explain this difference, a concept of ”effective” jump motion has been proposed.

Appendix A

Irreducible Spherical Representation

A.1 Definition of irreducible spherical tensor

A convenient way to describe the rotation of a tensor in Cartesian coordinate is to use the irreducible spherical tensor [Spiess 78]. A spherical tensor of rank l is a set of $2l+1$ objects with the property that when any of them is rotated in 3 dimensions, the result is a linear superposition of the same set of objects. The rank of a spherical tensor indicates different mathematical groups. Particularly important in solid state NMR is the irreducible spherical tensor of rank 2, which can be constructed from a Cartesian 3×3 matrix R as:

$$\begin{aligned}
R_{0,0} &= \frac{1}{3}\,(R_{xx}+R_{yy}+R_{zz}) \\
R_{1,0} &= -\frac{\mathbf{i}}{\sqrt{2}}\,(R_{xy}-R_{yx}) \\
R_{1,\pm1} &= -\frac{1}{2}\,[(R_{zx}-R_{xz}) \pm \mathbf{i}(R_{zy}-R_{yz})] \\
R_{2,0} &= \sqrt{\frac{3}{2}}\,(R_{zz}-R_{00}) \\
R_{2,\pm1} &= \mp\frac{1}{2}\,[(R_{zx}+R_{xz}) \pm \mathbf{i}(R_{zy}+R_{yz})] \\
R_{2,\pm2} &= \frac{1}{2}\,[(R_{yy}-R_{xx}) \pm \mathbf{i}(R_{xy}+R_{yx})]
\end{aligned} \tag{A.1}$$

where the Cartesian matrix R is defined as:

$$R = \begin{pmatrix} R_{xx} & R_{xy} & R_{xz} \\ R_{yx} & R_{yy} & R_{yz} \\ R_{zx} & R_{zy} & R_{zz} \end{pmatrix} \tag{A.2}$$

$R_{0,0}$ is the trace of the matrix, which is rotationally invariant and thus is interpreted as a tensor of rank zero. And $R_{1,m}$ can be called as a tensor of rank 1. This tensor is equivalent to the antisymmetric part of the matrix, which has the rotation behavior as a vector. $R_{2,m}$ is the second rank spherical tensor from the rearrangement of the traceless symmetric part of the matrix R.

A.2 Irreducible spherical representation of spin interaction

In NMR the Hamiltonian of interaction has a general form:

$$\hat{H} = \underline{\hat{I}}\,\underline{\underline{A}}\,\underline{\hat{J}} = \underline{\underline{A}} \cdot \underline{\underline{\hat{T}}} \tag{A.3}$$

where $\underline{\underline{A}}$ is the spherical tensor related to the spatial part of Hamiltonian and $\underline{\underline{T}}$ is the spin operator tensor, constructed from the dyadic-product matrix with elements $(\underline{\hat{J}} \otimes \underline{\hat{I}})_{kn} = \hat{J}_k \hat{I}_n$, which is shown in Table A.1. Via the scalar product of two spherical tensor, the Hamiltonian in Eq. (A.3) can be constructed as:

$$\hat{H} = \sum_{L=0}^{2} \sum_{m=-L}^{L} (-1)^m A_{Lm} \hat{T}_{L-m} \tag{A.4}$$

Interaction	T_{00}	T_{10}	$T_{1\pm1}$	T_{20}	$T_{2\pm1}$	$T_{2\pm2}$
Chemical shift	$-\frac{1}{\sqrt{3}}\hat{I}_z B_0$	0	$-\frac{1}{2}\hat{I}_\pm B_0$	$\sqrt{\frac{2}{3}}\hat{I}_z B_0$	$\mp\frac{1}{2}\hat{I}_\pm B_0$	0
Dipole-dipole	0	0	0	$\frac{1}{\sqrt{6}}(3\hat{I}_z\hat{S}_z - \underline{\hat{I}}\cdot\underline{\hat{S}})$	$\mp\frac{1}{2}(\hat{I}_z\hat{S}_\pm + \hat{I}_\pm\hat{S}_z)$	$\frac{1}{2}\hat{I}_\pm\hat{S}_\pm$
Quadrupole	0	0	0	$\frac{1}{\sqrt{6}}(3\hat{I}_z\hat{S}_z - I(I+1)$	$\mp\frac{1}{2}(\hat{I}_z\hat{I}_\pm + \hat{I}_\pm\hat{I}_z)$	$\frac{1}{2}\hat{I}_\pm\hat{I}_\pm$

Table A.1: *Spherical tensor representation of spin operators (with $\hat{I}_\pm = \hat{I}_x \pm \mathbf{i}\hat{I}_y$)*

To show how to use this representation to construct Hamiltonians two examples will be given in the following.

Dipolar Hamiltonian

Using Table (A.1) one could write the spin part of dipolar Hamiltonian:

$$\underline{\underline{\hat{T}_2}} = \begin{pmatrix} T_{22} \\ T_{21} \\ T_{20} \\ T_{2-1} \\ T_{2-2} \end{pmatrix} = \begin{pmatrix} \frac{1}{2}\hat{I}_+\hat{S}_+ \\ -\frac{1}{2}(\hat{I}_z\hat{S}_+ + \hat{I}_+\hat{S}_z) \\ \frac{\sqrt{6}}{6}(3\hat{I}_z\hat{S}_z - \underline{\hat{I}}\cdot\underline{\hat{S}}) \\ \frac{1}{2}(\hat{I}_z\hat{S}_- + \hat{I}_-\hat{S}_z) \\ \frac{1}{2}\hat{I}_-\hat{S}_- \end{pmatrix} \tag{A.5}$$

After the secular approximation one gets:

$$\underline{\underline{\hat{T}_{2,sec}}} = \begin{pmatrix} 0 \\ 0 \\ \frac{\sqrt{6}}{6}(3\hat{I}_z\hat{S}_z - \underline{\hat{I}}\cdot\underline{\hat{S}}) \\ 0 \\ 0 \end{pmatrix} = T_{20}\cdot\begin{pmatrix} 0 \\ 0 \\ 1 \\ 0 \\ 0 \end{pmatrix} \tag{A.6}$$

For the spatial part $\underline{\underline{A_2}}$ of dipolar Hamiltonian, one knows that in PAF it has a diagonal matrix, which is symmetric and traceless. Therefore, via the definition in Eq. (A.1)

$\underline{\underline{A_2^{PAF}}}$ has a form as:

$$\underline{\underline{A_2^{PAF}}} = \sqrt{\frac{3}{2}}\delta\ [0,\ 0,\ 1,\ 0,\ 0] \tag{A.7}$$

In order to construct the Hamiltonian one has to get A_{20}^{LAB}. This can be achieved by the frame transformation:

$$\begin{aligned} A_{20}^{LAB} &= \sum_{m=-2}^{2} A_{2m}^{PAF} Y_{Lm}(\beta, -\gamma)(\frac{4\pi}{2L+1})^{\frac{1}{2}} \\ &= \sqrt{\frac{3}{8}}\delta(3cos^2\beta - 1) \end{aligned} \tag{A.8}$$

The detail about the frame transformation will be discussed in the next section. With the tensors in Eq. (A.6) and Eq. (A.8), therefore, one can easily construct the formula of dipolar Hamiltonian:

$$\hat{H}_{dd,sec} = A_{20}^{LAB}\hat{T}_{20} = \delta\frac{1}{2}(3cos^2\beta - 1)\frac{1}{2}(3\hat{I}_z\hat{S}_z - \underline{\hat{I}}\cdot\underline{\hat{S}}) \tag{A.9}$$

Here, δ is equal to $2D$ if comparing with the formula given in Chapter 1.

Chemical shift anisotropy

The Hamiltonian of chemical shift is a little bit special, since its "spin part" $\underline{\underline{\hat{T}_2}}$ includes the spatial information $\underline{B_0}$. One still can try to construct the "spin part" $\underline{\underline{\hat{T}_2}}$ from the dyadic-product matrix with elements $(\underline{\hat{J}}\otimes\underline{\hat{I}})_{kn} = \hat{J}_k\hat{I}_n$:

$$\underline{\underline{\hat{T}_2}} = \begin{pmatrix} 0 \\ 0 \\ B_0 \end{pmatrix} \otimes (I_x,\ I_y,\ I_z) = \begin{pmatrix} 0 & 0 & 0 \\ 0 & 0 & 0 \\ B_0I_x & B_0I_y & B_0I_z \end{pmatrix} \tag{A.10}$$

Via the definition in Eq. (A.1) one could write down the spin part of CSA Hamiltonian

in the spherical representation:

$$\underline{\underline{\hat{T}_2}} = \begin{pmatrix} T_{22} \\ T_{21} \\ T_{20} \\ T_{2-1} \\ T_{2-2} \end{pmatrix} = \begin{pmatrix} 0 \\ -\frac{1}{2}B_0 I_+ \\ \sqrt{\frac{2}{3}}B_0 I_z \\ +\frac{1}{2}B_0 I_- \\ 0 \end{pmatrix} \tag{A.11}$$

After the secular approximation, one gets:

$$\underline{\underline{\hat{T}_{2,sec}}} = \begin{pmatrix} 0 \\ 0 \\ \sqrt{\frac{2}{3}}B_0 I_z \\ 0 \\ 0 \end{pmatrix} \tag{A.12}$$

For the spatial part $\underline{\underline{A_2}}$ of CSA Hamiltonian, it has a form as:

$$\underline{\underline{A_2^{PAF}}} = \sqrt{\frac{3}{2}}\delta\,[\frac{\sqrt{6}}{6}\eta,\ 0,\ 1,\ 0,\ \frac{\sqrt{6}}{6}\eta] \tag{A.13}$$

Its formula in the laboratory frame can be achieved by the frame transformation:

$$\begin{aligned} A_{20}^{LAB} &= \sum_{m=-2}^{2} A_{2m}^{PAF} Y_{Lm}(\beta,-\gamma)(\frac{4\pi}{2L+1})^{\frac{1}{2}} \\ &= \sqrt{\frac{3}{8}}\delta(3cos^2\beta - 1 + \eta sin^2\beta cos2\gamma) \end{aligned} \tag{A.14}$$

Therefore, the formula of CSA Hamiltonian in the laboratory frame reads as:

$$\hat{H}_{CSA,sec} = A_{20}^{LAB}\hat{T}_{20} = B_0\delta\frac{1}{2}(3cos^2\beta - 1 + \eta sin^2\beta cos2\gamma)I_z \tag{A.15}$$

Appendix B

Rotation and Coordinate Transformation

B.1 Rotation and coordinate transformation

In NMR one always deals with rotation of interaction tensor. In mathematics any three dimensional rotation can be achieved via three subsequent rotations with three Euler angles α, β and γ. On a fundamental level it is useful to distinguish between the active and passive rotations.

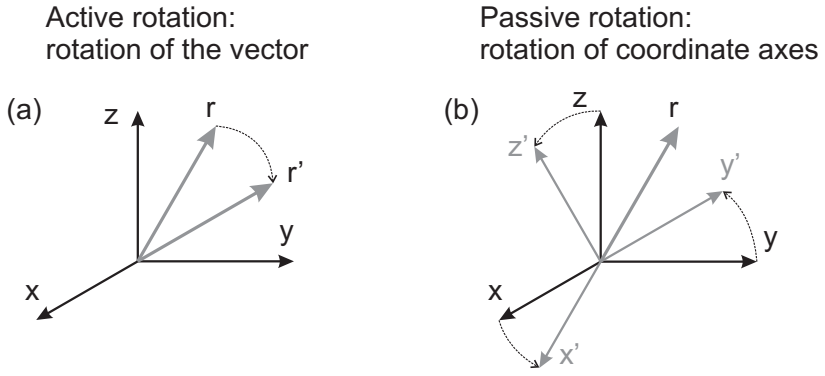

Figure B.1: *Active vs. passive rotations. (a) An active rotation rotates the vector in a fixed coordinate system. (b) A passive rotation: the vector is fixed in space, while the coordinate system is rotated.*

Active rotation Rotation of the objects without changing the coordinate system.
Passive rotation Keep the objects fixed and rotating the coordinate system.
These two rotations are visualized in Fig. (B.1).

Normally people are more familiar with the active rotation since this one is directly performed on the object. Whereas, the passive rotation is directly performed on the coordinate axes, which in fact is the case of coordinate transformation.

The definition of Euler angle depends on the chosen rotation type. In this thesis we follow the convention of Rose. Assuming the original coordinate has an index **a** and the new coordinate has **b**, the Euler angles are defined as:

α : rotation about the original $z^{\mathbf{a}}$ axis
β : rotation about the intermediary y' axis
γ : rotation about the final $z^{\mathbf{b}}$ axis

This definition involving the rotation of the coordinate axes, represents a passive rotation as defined above.

An alternative method for determining α, β and γ is to follow these facts:

(β, α) are the polar coordinates of the $z^{\mathbf{b}}$ axis in the frame **a**
$(\beta, 180^\circ - \gamma)$ are the polar coordinates of the z^{a} axis in the frame **b**

Mathematically, the rotation is carried out by multiplication with the rotation matrix $\underline{\underline{R}}(\alpha, \beta, \gamma)$:

$$\underline{\underline{R}}(\alpha, \beta, \gamma) = \underline{\underline{R_{z^{\mathbf{b}}}}}(\gamma)\underline{\underline{R_{y'}}}(\beta)\underline{\underline{R_{z^{\mathbf{a}}}}}(\alpha) \tag{B.1}$$

The rotation matrix describes a unitary transformation, exhibiting the following properties:

$$det\underline{\underline{R}} = 1 \quad \text{and} \quad \underline{\underline{R}}^{-1} = \underline{\underline{R}}^{T} \tag{B.2}$$

In order to treat the Euler rotation like the more familiar active rotations, it is customary to introduce the 'pseudo-active' Euler rotation matrix $\underline{\underline{\tilde{R}}}$:

$$\underline{\underline{\tilde{R}}}(\alpha,\beta,\gamma) = \underline{\underline{R}}^{-1}(\alpha,\beta,\gamma) = \underline{\underline{R}}^{T}(\alpha,\beta,\gamma) \tag{B.3}$$

$$= \begin{pmatrix} cos\gamma & sin\gamma & 0 \\ -sin\gamma & cos\gamma & 0 \\ 0 & 0 & 1 \end{pmatrix} \begin{pmatrix} cos\beta & 0 & -sin\beta \\ 0 & 1 & 0 \\ sin\beta & 0 & cos\beta \end{pmatrix} \begin{pmatrix} cos\alpha & sin\alpha & 0 \\ -sin\alpha & cos\alpha & 0 \\ 0 & 0 & 1 \end{pmatrix} \tag{B.4}$$

Concerning rotation of tensor, the transformation of a Cartesian tensor $\underline{\underline{T}}$ reads as:

$$\begin{aligned} \underline{\underline{T}}^{\mathbf{b}} &= \underline{\underline{\tilde{R}}}(\alpha,\beta,\gamma)\, \underline{\underline{T}}^{\mathbf{a}}\, \underline{\underline{\tilde{R}}}^{-1}(\alpha,\beta,\gamma) \\ &= \underline{\underline{R}}^{-1}(\alpha,\beta,\gamma)\, \underline{\underline{T}}^{\mathbf{a}}\, \underline{\underline{R}}(\alpha,\beta,\gamma) \end{aligned} \tag{B.5}$$

Eq. (B.5) actually is equivalent to rotate the coordinate axes of frame **a** with the Euler angles $(-\alpha,-\beta,-\gamma)$:

$$\begin{aligned} \underline{\underline{T}}^{\mathbf{b}} &= \underline{\underline{R}}(-\alpha,-\beta,-\gamma)\, \underline{\underline{T}}^{\mathbf{a}}\, \underline{\underline{R}}^{-1}(-\alpha,-\beta,-\gamma) \\ &= \underline{\underline{R}}^{-1}(\alpha,\beta,\gamma)\, \underline{\underline{T}}^{\mathbf{a}}\, \underline{\underline{R}}(\alpha,\beta,\gamma) \end{aligned} \tag{B.6}$$

With the rotation matrix $\underline{\underline{R}}(\alpha,\beta,\gamma)$ one can perform a rotation to a vector $\underline{r}$:

$$\underline{r}^{\mathbf{b}} = \underline{\underline{\tilde{R}}}(\alpha,\beta,\gamma)\underline{r}^{\mathbf{a}} \tag{B.7}$$

or a (wave) function $\psi(\underline{r})$:

$$\psi^{\mathbf{b}}(\underline{r}) = \hat{P}(\alpha,\beta,\gamma)\psi^{\mathbf{a}}(\underline{r}) \tag{B.8}$$

$$= \psi^{\mathbf{a}}(\underline{\underline{\tilde{R}}}\,\underline{r}) \tag{B.9}$$

or an operator $\hat{T}^{\mathbf{a}}$:

$$\hat{T}^{\mathbf{b}} = \hat{P}\hat{T}^{\mathbf{a}}\hat{P}^{-1} \tag{B.10}$$

Here, $\hat{P}(\alpha,\beta,\gamma)$ is called the rotation operator.

Since performing rotation in Cartesian coordinate always relates to tedious matrix multiplications, it is convenient to describe rotation via the the spherical tensor representation. As mentioned in the last section, if rotating a spherical tensor $\underline{\underline{\hat{T}}}^{\mathbf{a}}$ the new tensor $\underline{\underline{\hat{T}}}^{\mathbf{b}}$ is just a new linear combination of the tensor element $\hat{T}^{\mathbf{a}}_{Lm}$:

$$\underline{\underline{\hat{T}}}^{\mathbf{b}} = \hat{P}(\alpha,\beta,\gamma)\,\underline{\underline{\hat{T}}}^{\mathbf{a}}\,\hat{P}^{-1}(\alpha,\beta,\gamma) \tag{B.11}$$

$$= \sum_{m'=-L}^{L} \hat{T}^{\mathbf{a}}_{Lm'} D^{L}_{m'm}(\alpha,\beta,\gamma) \tag{B.12}$$

where the coefficients $D^{L}_{m'm}(\alpha,\beta,\gamma)$ is the Wigner rotation matrix, with the Euler angles (α,β,γ) specifying the coordinate transformation. The dependence of $D^{L}_{m'm}(\alpha,\beta,\gamma)$ on α and γ is simply $e^{-\mathbf{i}m'\alpha}e^{-\mathbf{i}m\gamma}$:

$$D^{L}_{m'm}(\alpha,\beta,\gamma) = d^{L}_{m'm}(\beta)e^{-\mathbf{i}m'\alpha}e^{-\mathbf{i}m\gamma} \tag{B.13}$$

The nontrivial dependence on β is described by the "reduced rotation matrix" element $d^{L}_{m'm}(\beta)$ which is listed in Table B.1.

In most cases, only a limited set of the elements is relevant: if there is no dependence on γ (or α) only the elements:

$$D^{L}_{m0}(\alpha,\beta,\gamma) = Y_{Lm}(\beta,-\alpha)\left(\frac{4\pi}{2L+1}\right)^{\frac{1}{2}} \tag{B.14}$$

$$D^{L}_{0m}(\alpha,\beta,\gamma) = (-1)^{m}Y_{Lm}(\beta,-\gamma)\left(\frac{4\pi}{2L+1}\right)^{\frac{1}{2}} \tag{B.15}$$

where the spherical harmonics $Y_{Lm}(\beta,\gamma)\quad L=0,1,2$ are :

$$Y_{0,0} = 1(\frac{1}{4\pi})^{\frac{1}{2}} \tag{B.16}$$

$$Y_{1,0} = cos\beta\,(\frac{3}{4\pi})^{\frac{1}{2}} \tag{B.17}$$

$$Y_{1,\pm1} = \mp sin\beta\, e^{\pm i\gamma}\,(\frac{3}{8\pi})^{\frac{1}{2}} \tag{B.18}$$

$$Y_{2,0} = \frac{1}{2}(3cos^2\beta-1)\,(\frac{5}{4\pi})^{\frac{1}{2}} \tag{B.19}$$

$$Y_{2,\pm1} = \mp sin\beta\, cos\beta\, e^{\pm i\gamma}\,(\frac{15}{8\pi})^{\frac{1}{2}} \tag{B.20}$$

$$Y_{2,\pm2} = sin^2\beta\, e^{\pm i2\gamma}\,(\frac{15}{32\pi})^{\frac{1}{2}} \tag{B.21}$$

B.2 Rotating frame

In NMR the rotating frame usually is introduced to ”get rid of” the effect of Zeeman interaction. Essentially, moving from the laboratory frame to the rotating frame is just a case of coordinate transformation.

Assuming that the density operator (magnetization) at time 0 $(t=0)$ is $\hat{\rho}(0)=\hat{I}_\alpha$, it

Table B.1: β-*dependent factor* $d^2_{mn}(\beta)$ *of the Wigner function* $D^2_{mn}(\alpha,\beta,\gamma)$

n	2	1	0	-1	-2
m					
2	a	-b	c	-d	e
1	b	f	-g	h	-d
0	c	g	i	-g	c
-1	d	h	g	f	-b
-2	e	d	c	b	a

a=$\frac{1}{4}(1+cos\beta)^2$ d=$\frac{1}{2}(1-cos\beta)sin\beta$ g=$\sqrt{\frac{3}{8}}sin2\beta$
b=$\frac{1}{2}(1+cos\beta)sin\beta$ e=$\frac{1}{4}(1-cos\beta)^2$ h=$\frac{1}{2}(cos\beta+1)-cos^2\beta$
c=$\sqrt{\frac{3}{8}}sin^2\beta$ f=$\frac{1}{2}(cos\beta-1)+cos^2\beta$ i=$\frac{1}{2}(3cos^2\beta-1)$

evolves under the Zeeman interaction in the laboratory frame:

$$\hat{\rho}(t) = e^{-\mathbf{i}\omega_L t\hat{I}_z}\,\hat{\rho}(0)\,e^{\mathbf{i}\omega_L t\hat{I}_z} \tag{B.22}$$

This Eq. (B.22) describes a rotation of $\hat{I}_\alpha$ by an angle $\omega_L t$ about the z-axis. The effect of this rotation is eliminated by a transition to a frame that rotates with a frequency $\omega_R = \omega_L$. Then the density operator in Eq. (B.22) in this rotating frame can be written as:

$$\begin{aligned}
\hat{\rho}_R(t) &= e^{\mathbf{i}\omega_R t\hat{I}_z}\,\hat{\rho}(t)\,e^{-\mathbf{i}\omega_R t\hat{I}_z} \\
&= e^{-\mathbf{i}(\omega_L-\omega_R)t\hat{I}_z}\,\hat{I}_\alpha\,e^{\mathbf{i}(\omega_L-\omega_R)t\hat{I}_z} && \text{(B.23)} \\
&= \hat{I}_\alpha \qquad (if\ \ \omega_R = \omega_L) && \text{(B.24)}
\end{aligned}$$

where the rotation operator $\hat{P} = e^{\mathbf{i}\omega_R t\hat{I}_z}$.

In Eq. (B.24) it shows that if choosing the rotating frame with a frequency $\omega_R = \omega_z$ the Zeeman interaction disappears. And this rotating frame can be called $\hat{H}_z$-interaction representation, where the direct effect of Zeeman interaction has been transformed away. For internal spin Hamiltonians they have to take the same kind of transformation:

$$\hat{H}_{int,R}(t) = e^{\mathbf{i}\hat{H}_z t}\,\hat{H}_{int}\,e^{-\mathbf{i}\hat{H}_z t} \tag{B.25}$$

Then the density operator of our system in $\hat{H}_z$-interaction representation reads as:

$$\frac{d}{dt}\hat{\rho}_R(t) = -\mathbf{i}[\hat{H}_{int,R}, \hat{\rho}_R(t)] \tag{B.26}$$

Appendix C

Action of Hamiltonian on $\hat{\rho}$: Time Evolution

The time evolution of a spin system can be described by the Liouville-von Neumann equation:

$$\frac{d}{dt}\hat{\rho} = -\mathbf{i}[\hat{H}, \hat{\rho}] \tag{C.1}$$

The density operator $\hat{\rho}(t)$ describes the state of the spin system, while the Hamiltonian represents the ”force”, or interaction, that try to change the state of system.

For a Hamiltonian $\hat{H}$ acting constantly on the system, i.e., $\partial\hat{H}/\partial t = 0$, the formal solution of the Liouville-von Neumann equation is given by:

$$\hat{\rho}(t) = e^{-\mathbf{i}\hat{H}t}\hat{\rho}(0)e^{\mathbf{i}\hat{H}t} \tag{C.2}$$

To evaluate this formal solution, one can make use of the Baker-Hausdorff relation

("time-evolution series"):

$$\begin{aligned}\hat{\rho}(t) &= e^{-\mathbf{i}\hat{H}t}\hat{\rho}(0)e^{\mathbf{i}\hat{H}t} \\ &= \hat{\rho}_0 + [-\mathbf{i}\hat{H}t, \hat{\rho}_0] + \frac{1}{2}[-\mathbf{i}\hat{H}t, [-\mathbf{i}\hat{H}t, \hat{\rho}_0]] + \frac{1}{6}[-\mathbf{i}\hat{H}t, [-\mathbf{i}\hat{H}t, [-\mathbf{i}\hat{H}t, \hat{\rho}_0]]] + \cdots \\ &= \hat{\rho}_0 - \frac{\mathbf{i}t}{1!}[\hat{H}, \hat{\rho}_0] + \frac{(\mathbf{i}t)^2}{2!}[\hat{H}, \underset{=\hat{r}_1}{\uparrow}] - \frac{(\mathbf{i}t)^3}{3!}[\hat{H}, \underset{=\hat{r}_2}{\uparrow}] + \cdots \qquad \text{(C.3)}\end{aligned}$$

According Eq. (C.3) the state of spin system at time t is described by an infinite series of commutators. This description, although looks complicated, proves to be harmless in some cases. In the following two examples are given to show how to use Eq. (C.3) to calculate the time evolution of spin state and yield an explicit formula in the end.

Example 1: $\hat{r}_2 = \omega^2\hat{\rho}_0$
In this case, one finds that:

$$\begin{aligned}\hat{r}_1 &= \hat{r}_1 & \hat{r}_2 &= \omega^2\hat{\rho}_0 \\ \hat{r}_3 &= \omega^2\hat{r}_1 & \hat{r}_4 &= \omega^4\hat{\rho}_0 \\ \hat{r}_5 &= \omega^4\hat{r}_1 & \hat{r}_6 &= \omega^6\hat{\rho}_0\end{aligned}$$

This results in:

$$\begin{aligned}\hat{\rho}(t) &= \hat{\rho}_0\Big(1 + \frac{(\mathbf{i}\omega t)^2}{2!} + \frac{(\mathbf{i}\omega t)^4}{4!} + \cdots\Big) - \frac{\hat{r}_1}{\omega}\Big(\frac{(\mathbf{i}\omega t)^1}{1!} + \frac{(\mathbf{i}\omega t)^3}{3!} + \cdots\Big) \\ &= \hat{\rho}_0 cos(\omega t) - \mathbf{i}\frac{\hat{r}_1}{\omega}sin(\omega t) \qquad \text{(C.4)}\end{aligned}$$

Chemical shift, dipolar coupling of isolated spin-1/2 pair, and quadrupolar coupling of $I = 1$ belong to this case.

Example 2: $\hat{r}_3 = \omega^2\hat{r}_1$

In this case, one finds that:

$$\begin{aligned} \hat{r}_1 &= \hat{r}_1 & \hat{r}_2 &= \hat{r}_2 \\ \hat{r}_3 &= \omega^2 \hat{r}_1 & \hat{r}_4 &= \omega^2 \hat{r}_2 \\ \hat{r}_5 &= \omega^4 \hat{r}_1 & \hat{r}_6 &= \omega^4 \hat{r}_2 \end{aligned}$$

This results in:

$$\begin{aligned} \hat{\rho}(t) &= \hat{\rho}_0 + \frac{r_2}{\omega^2}\left(\frac{(\mathbf{i}\omega t)^2}{2!} + \frac{(\mathbf{i}\omega t)^4}{4!} + \cdots\right) - \frac{r_1}{\omega}\left(\frac{(\mathbf{i}\omega t)^1}{1!} + \frac{(\mathbf{i}\omega t)^3}{3!} + \cdots\right) \\ &= \hat{\rho}_0 - \frac{r_2}{\omega^2} + \frac{r_2}{\omega^2}\, cos(\omega t) - \mathbf{i}\frac{\hat{r}_1}{\omega}\, sin(\omega t) \end{aligned} \tag{C.5}$$

The action of the averaged Hamiltonians in CP and spin diffusion belong to this case.

Appendix D

Average-Hamiltonian Theory

The "average-Hamiltonian theory" (AHT) was developed by Haeherlen and Waugh [Haeberlen 68]. The main idea of this theory is to introduce an interaction representation, where the immediate action of pulse is transformed away and the effect of local field can be calculated to the first order as a simple average. The introduced interaction representation usually is visualized as a transition into a frame "toggling" with the pulses. The AHT originally is designed to facilitate the analysis of the action of multiple-pulse sequences, which are used for the homonuclear decoupling. Nevertheless, it can be also applied to many other NMR problems, e.g. heteronuclear decoupling, cross polarization and some recoupling sequences like REDOR,BABA $\cdots$. In the following we will give a short introduction of this theory.

As shown in Chapter 1, one can calculate the density operator describing a spin system $\rho(t)$ at time t, from that at time $t = 0$ via the equation:

$$\hat{\rho}(t) = \hat{U}(t)\hat{\rho}(0)\hat{U}^{\dagger}(t) \tag{D.1}$$

where the propagator $\hat{U}(t)$ is given by:

$$\hat{U}(t) = \exp(-\mathbf{i}\hat{H}t) \tag{D.2}$$

Generally, the Hamiltonian $\hat{H}$ has a time dependence. In this circumstance Eq. (D.2)

becomes:

$$\hat{U}(t) = \exp(-\mathbf{i}\hat{H}_n t_n)\cdots\exp(-\mathbf{i}\hat{H}_1 t_1) \tag{D.3}$$

where the Hamiltonian which operates in the first time period t_1 is $\hat{H}_1$ and so on.

One could replace the series of exponential functions in Eq. (D.3) for the propagator with a single exponential one relying on an average Hamiltonian $\bar{\hat{H}}$ which has the same effect as the series of Hamiltonians $\hat{H}_1\hat{H}_2\cdots\hat{H}_n$, i.e.

$$\hat{U}(t) = \exp(-\mathbf{i}\hat{H}_n t_n)\cdots\exp(-\mathbf{i}\hat{H}_1 t_1) = \exp(-\mathbf{i}\bar{\hat{H}}t) \tag{D.4}$$

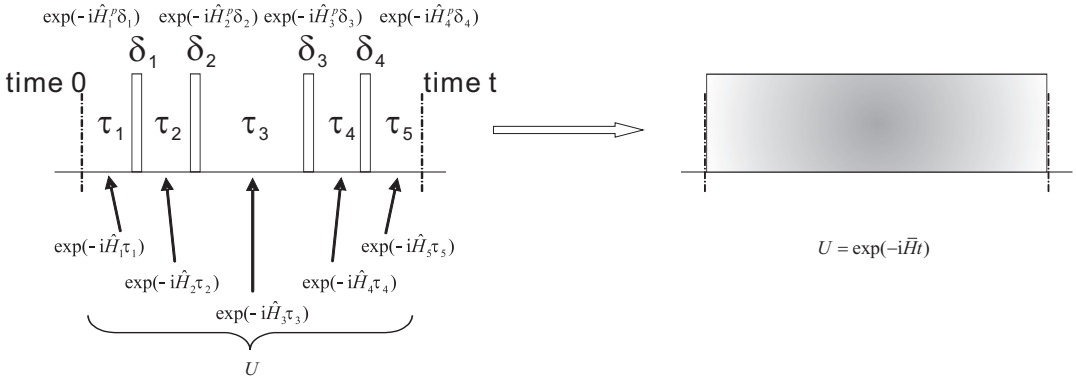

Figure D.1: *The idea behind average Hamiltonian theory*

This replacement is always possible but not always useful, because in general the appropriate average Hamiltonian $\bar{\hat{H}}$ will depend on t, the time at which one wishes to know the propagator. However, when the Hamiltonian (or series of Hamiltonian) describing the spin system is periodic in time, one only wish to know about the state of spin system at some specific time points spaced by the periodical Hamiltonians. And it is always possible to calculate a single average Hamiltonian which correctly describes the behaviour of the spin system at those time points.

A way to evaluates the series of exponential operators in Eq. (D.3) is to use the Magnus

expansion:

$$e^{\hat{A}}e^{\hat{B}} = \exp\Big\{\hat{A}+\hat{B}+\frac{1}{2}[\hat{A},\hat{B}]+\frac{1}{3}([\hat{A},[\hat{A},\hat{B}]]+[[\hat{A},\hat{B}],\hat{B}])+\cdots\Big\} \tag{D.5}$$

Applying this expansion to the series of exponential operators in Eq. (D.3) for a periodic Hamiltonian of period t_p, i.e. $t_1+t_2+\cdots+t_n=t_p$, one gets:

$$\hat{U}(t) = \exp(-\mathbf{i}\bar{\hat{H}}t_p) \tag{D.6}$$

where the Hamiltonian $\bar{\hat{H}}$ during t_p is given as:

$$\bar{\hat{H}} = \bar{\hat{H}}^{(0)}+\bar{\hat{H}}^{(1)}+\bar{\hat{H}}^{(2)}+\cdots \tag{D.7}$$

in which the different orders in the averaged Hamiltonian are given by:

$$\begin{aligned}
\bar{\hat{H}}^{(0)} &= \frac{1}{t_p}\int_0^{t_p} dt_1\hat{H}(t_1)\\
\bar{\hat{H}}^{(1)} &= -\frac{\mathbf{i}}{2t_p}\int_0^{t_p} dt_1\int_0^{t_1} dt_2[\hat{H}(t_1),\hat{H}(t_2)] \qquad \text{(D.8)}\\
\bar{\hat{H}}^{(2)} &= -\frac{1}{6t_p}\int_0^{t_p} dt_1\int_0^{t_1} dt_2\int_0^{t_2} dt_3\Big\{[\hat{H}(t_1),[\hat{H}(t_2),\hat{H}(t_3)]]+[\hat{H}(t_3),[\hat{H}(t_2),\hat{H}(t_1)]],\Big\}
\end{aligned}$$

Eq. (D.7) and Eq. (D.8) are not as daunting as they appear. The zero order term $\bar{\hat{H}}^{(0)}$ (the first order in the Hamiltonian) is simply the average of the piecewise Hamiltonian $\hat{H}_1,\hat{H}_2,\cdots,\hat{H}_n$ which operate during one period:

$$\begin{aligned}
\bar{\hat{H}}^{(0)} &= \frac{1}{t_p}\int_0^{t_p} dt_1\hat{H}(t_1)\\
&= \frac{1}{t_p}(\hat{H}_1t_1+\hat{H}_2t_2+\cdots+\hat{H}_nt_n) \qquad \text{(D.9)}
\end{aligned}$$

In the case where these Hamiltonians all commute with each other, or nearly so, all higher-order terms can be neglected and the zero-order term is a good description of the average Hamiltonian. Whereas, in case where the Hamiltonians which operate over the time period do not commute with each other, one could transform the Hamiltonians into a new frame, the so-called toggling frame, in which non-commuting terms disappear. It is then possible to approximate the average Hamiltonian in this frame by the first-order term in Eq. (D.8).

The purpose to introduce the toggling frame in NMR is to move the effect of pulses from the Hamiltonian to the spin state $\hat{\rho}$, since the Hamiltonian of pulses doesn't commute with the Zeeman interaction. Therefore, before introducing the toggling frame, one could consider what is the direct effect of pulse on the spin state. Assuming to apply an x-pulse on a spin state $\hat{\rho}(0)$, then the spin state after the pulse $\hat{\rho}(t)$ is given by:

$$\hat{\rho}(t) = \exp(-\mathbf{i}\omega_{RF}\hat{I}_x t)\hat{\rho}(0)\exp(\mathbf{i}\omega_{RF}\hat{I}_x t) \tag{D.10}$$

where the Hamiltonian of this x-pulse is given by:

$$\hat{H}_{RF} = \omega_{RF}\hat{I}_x \tag{D.11}$$

From the discussion in Appendix B.1, one knows that $[\exp(-\mathbf{i}\omega_{RF}\hat{I}_x t)\hat{\rho}(0)\exp(\mathbf{i}\omega_{RF}\hat{I}_x t)]$ can be regarded as an active rotation of $\hat{\rho}(0)$ by the angle $(\omega_{RF}t)$ about x-axis; or a passive rotation of the frame, where the $\hat{\rho}(0)$ is defined, by the angle $(-\omega_{RF}t)$ about x-axis. It means that, if one enters a new frame via rotating the old one by the angle $(-\omega_{RF}t)$ about x-axis, the density operator $\hat{\rho}(0)$ in this new frame will gain the same change as rotating it by $(+\omega_{RF}t)$ via the pulse. This new frame is the so-called toggling frame, where the direct effect of pulses has been transformed into the density operator.

Due to the change of the frame, the Hamiltonian could also change it formula. With the example given above, one could write down the Hamiltonian in the toggling frame:

$$\hat{H}_T(t) = \hat{R}_x^{-1}\hat{H}\hat{R}_x - \omega_{RF}\hat{I}_x \tag{D.12}$$

where $\hat{R}_x = \exp(\mathbf{i}\omega_{RF}\hat{I}_x t)$ represents the rotation operator for the rotation of the original axis frame.

So, in the case where $\hat{H} = \hat{H}_{RF} = \omega_{RF}\hat{I}_x$, its Hamiltonian in the toggling frame $\hat{H}_{T,RF}$ is:

$$\hat{H}_{T,RF} = \omega_{RF}\hat{R}_x^{-1}\hat{I}_x\hat{R}_x - \omega_{RF}\hat{I}_x = 0 \tag{D.13}$$

As expected, in this frame the effect of pulse is nulled. The frame transformation on the density operator takes account of the pulse effect. Now suppose that the Hamiltonian in the rotating frame is:

$$\hat{H} = \hat{H}_{int} + \hat{H}_{RF} \tag{D.14}$$

Transforming this Hamiltonian to the toggling frame, one gets:

$$\hat{H}_T(t) = \hat{R}_x^{-1}\hat{H}\hat{R}_x - \omega_{RF}\hat{I}_x = \hat{R}_x^{-1}\hat{H}_{int}\hat{R}_x \tag{D.15}$$

It means that the Hamiltonian in the toggling frame depends only on the spin interaction $\hat{H}_{int}$ and not on the pulse part.

If a series of pulses are applied to the spin system, the toggling frame will change with time due to the change of the pulses. As a result, the Hamiltonians in the toggling frame could also change with time. Providing that the Hamiltonians in the toggling frame commute with each other at different time, the average Hamiltonian in this frame can be calculated only to the first order term $\bar{\hat{H}}_T^{(0)}$:

$$\bar{\hat{H}}_T^{(0)} = \frac{1}{t}(\hat{H}_1 t_1 + \hat{H}_2 t_2 + \cdots + \hat{H}_n t_n) \tag{D.16}$$

where $t = t_1 + t_2 + \cdots + t_n$ is the total time of the pulses.

Then, $\bar{\tilde{H}}_T^{(0)}$ can be used to calculate the density operator $\hat{\rho}_T(t)$ in the toggling frame:

$$\hat{\rho}_T(t) = \exp(-\mathbf{i}\bar{\tilde{H}}_T^{(0)}t)\hat{\rho}_T(0)\exp(\mathbf{i}\bar{\tilde{H}}_T^{(0)}t) \tag{D.17}$$

If the pulses are periodic, i.e. the frame transformation on the density operator will have no effects on the density operator after the pulse train, the averaged Hamiltonian calculated from the toggling frame then is completely equivalent to that from the usual rotating frame.

Appendix E

Powder Average

In solid state NMR the powder sample means a sample consisting of many crystallites with random orientations. Therefore, when carrying out simulations of solid state NMR experiment on a powder sample a proper powder averaging procedure has to be applied [Fischbach 03, Duer 04]. Assuming one gets a signal $s(t,\alpha,\beta,\gamma)$ after the calculation of the spin evolution, the signal of a powder sample $S(t)$ then is given by:

$$S(t) = \frac{1}{8\pi^2}\int_0^{2\pi} d\alpha \int_0^{\pi} sin\beta d\beta \int_0^{2\pi} d\gamma\, s(t,\alpha,\beta,\gamma) \tag{E.1}$$

where $s(t,\alpha,\beta,\gamma)$ describes the time evolution of a single crystallite, and α, β and γ are the Euler angles denoting the orientation of the molecular frame (MF) in the rotor frame. Note that if only one interaction is considered, the three Euler angles can be regarded as the orientation of PAS in the rotor frame. If not, it is then necessary to do the frame transformation for the interactions from PAS to MF before performing the powder average. And this frame transformation usually needs the information of the molecular structure.

In the case of MAS, the angle γ is considered as the initial rotor phase, which usually is taken into account separately. Therefore, the signal of a powder sample under MAS only involves the integrations of α and β:

$$S(t) = \frac{1}{4\pi}\int_0^{2\pi} d\alpha \int_0^{\pi} sin\beta d\beta\, s(t,\alpha,\beta) \tag{E.2}$$

For the computer simulation, the integration for the powder average needs to be implemented in discrete steps. For instance, Eq. (E.2) needs to be approximated as the following:

$$S(t) = \sum_{i=1}^{N} \sum_{j=1}^{M} s(t, \alpha_{ij}, \beta_{ij})\, \sigma_{ij} \tag{E.3}$$

where the subscripts i and j are introduced to indicate the Euler angles and σ_{ij} is the weighting factor for the corresponding Euler angle $(\alpha_{ij}, \beta_{ij})$, which is normalized according to $\sum_{i=1}^{N} \sum_{j=1}^{M} \sigma_{ij} = 1$. For $S(t)$ in Eq. (E.3), there are two ways to carry it out: (i) to increase the three angles linearly in two nested loops (ii) to use numerous random angles (Monte-Carlo integration). But for these methods they usually need a lot of powder angles and thus a long calculating time to achieve the convergence. In literatures some methods, such as "ZCW" and "REPULSION", are presented, which generate the Euler angle sets for a faster and more efficient powder average.

Appendix F

Experimental Details and Sample Characterizations

F.1 Instrumentation and experimental parameters

The NMR experiments were carried out on the digital BRUKER Avance-type spectrometer, with B_0 field corresponding to ^{1}H resonance frequencies of 500.12 MHz (DSX500, 11.74 T, 89 mm bore magnet). MAS experiments were carried out using commercial 2.5 mm or 4mm MAS double-resonance probes, also manufactured by BRUKER. The spinning speeds of rotor typically is 3 kHz for the SUPER experiment, 6 kHz for the ^{13}C exchange experiment in the 4mm MAS probe and 25 kHz for the REREDOR experiment in the 2.5mm MAS probe. The 90° pulse lengths in the 4mm MAS probe vary between 3 and 4 μs on both channels, corresponding to $\omega_1/2\pi \approx 63-83$ kHz. The 90° pulse length in the 2.5mm MAS probe is 2.5 μs on both channels, corresponding to $\omega_1/2\pi = 100$ kHz. In all ^{13}C-detected experiments, the CW or TPPM scheme were applied for dipolar decoupling. The decoupling frequencies in the CW method varied between $83-89$ kHz. In the TPPM method the approximate 170° pulses ($5.3-5.7$ μs) and a phase-modulation angle of 15° were used. Ramped-CP was used for the experiments with an initial cross-polarization step.

SUPER. The SUPER experiments were performed at 3 kHz MAS with a scaling factor $\chi' = 0.155$ resulting in an effective spectral width of the indirect dimension of = 45 kHz, which is sufficiently large for the CSAs of CH_2 in PEs. The offset was set on the resonance of interest. For the ^{13}C 360° recoupling pulses the $\omega_{1,C} = 12.12\omega_R$ condition was satisfied by choosing the pulse strength to be 36.4 kHz. Special care has to be taken to apply sufficient heteronuclear decoupling during the ^{13}C 360° recoupling pulses. Optimum decoupling would be achieved with $\omega_{1,H}/\omega_{1,C} \geq 2$. In the experiments presented here, the decoupling during the ^{13}C 360° recoupling pulses was chosen to be 125 kHz.

SAXS. For the characterization of the lamellar thickness of PE, small-angle X-ray scattering (SAXS) was used. The SAXS setup consisted of a Rigaku rotating anode X-ray source (Cu K_α, 1.54A), typically operated at 30 kV, 50 mA. The X-rays were nearly monochromatized by Osmic Mirror. A two-dimensional CCD detector [Bruker-AXS high star 1024*1024 pixels 100mm] at a typical sample to detector distance of 1780 mm was used to record the diffraction patterns. The beam stop was a round lead disk of 6mm in diameter. The powder pattern rings were azimuthally integrated around the incident beam direction to yield one-dimensional traces of diffracted intensity vs $q = 4\pi sin\theta/\lambda$ where 2θ is the angle between the incident and scattered beam directions. These traces were divided by q to normalize to X-rays per unit area in the detector plane.

F.2 Sample characterizations

Several PE samples were used in this thesis to correlate the molecular dynamics to the sample morphology. The molecular properties of these samples are described in Table (F.2).

The branch degree of PE was determined by melt-state NMR [Klimke 06]. The measurements were carried out on a Bruker Avance 500 dedicated solid-state NMR spectrometer operating at a proton and carbon Larmor frequency of 500.13 and 125.75 MHz respectively. A commercial Bruker, $^{13}C - {}^{1}H$ optimized, high temperature, 7 mm MAS probehead was used in the measurements. Nitrogen gas was used for all pneumatics to limit thermal oxidation. All measurements were conducted at 3 kHz

Sample	M_w $[/(g \cdot mol^{-1})]$	M_w/M_n	Branch degree
SC-PE	4.5×10^6	8	0.55
MC-PE	4.5×10^6	8	0.55
Fiber	$> 10^6$	$\sim$	1.1
LMW-PE1	5.2×10^4	2.54	8.0
LMW-PE2	8.7×10^4	2.46	9.3

Table F.1: *Molecular properties of PE samples. The value of branch degree is defined as the branch number per 10000 CH_2 backbone units.*

spinning speed at 150℃ sample temperature, whilst compensating for thermal MAS effects. The quantification of the branch degree of PE is achieved by comparing the peak areas of end group and backbone in the ^{13}C single pulse excitation (SPE) spectrum, which was acquired using 10 μs ^{13}C 90° excitation pulses and 180° pulse-train heteronuclear dipolar decoupling. The branch degree values in Table (F.2) are extracted from the following spectra:

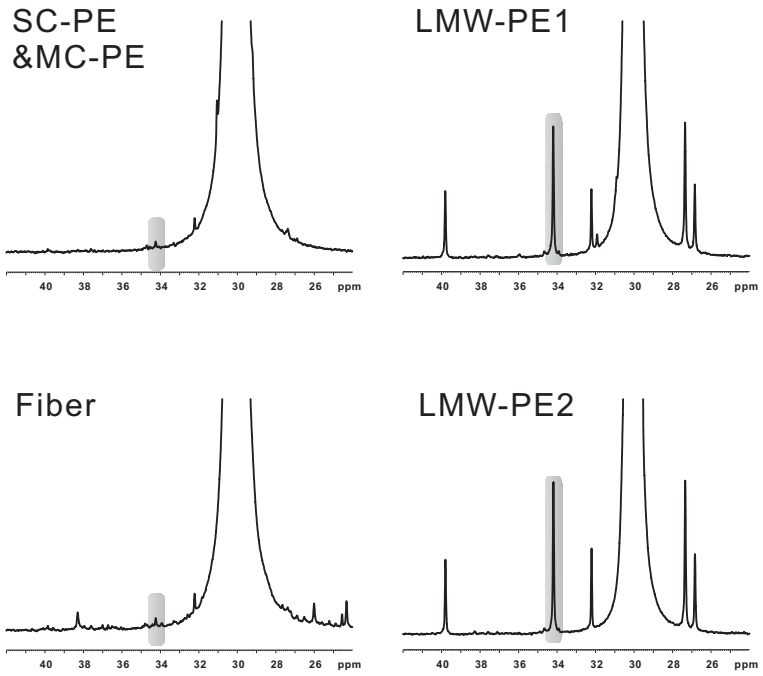

Figure F.1: *The normalized melt-state ^{13}C spectra of PEs at 500 MHz, using the 7 mm MAS setups. The signals assigned to* α *carbon next to the branch point in the PE backbone are noted with the grey color in the spectra. These* α *carbon peaks are used for the branch degree determination.*

F.3 Lamellar thickness of UHMW MC-PE

The SAXS experiment has been performed on the UHMW MC-PE at room temperature. The decay of X-ray intensity plotted against q is shown in Fig. (F.2).

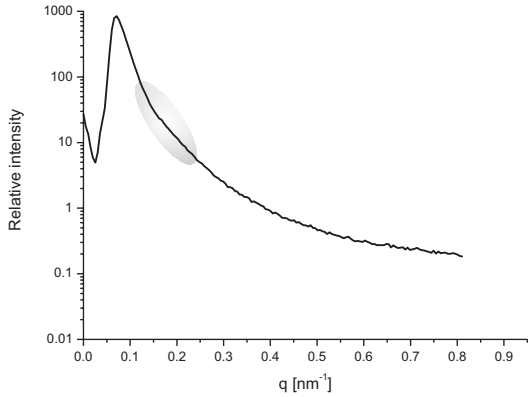

Figure F.2: *Raw SAXS intensity plotted against q. The SAXS experiment was performed at room temperature.*

The decay curve in Fig. (F.2) shows a bending at $q \approx 0.2\text{nm}^{-1}$, which relates to a long period of $L = 2\pi/q \approx 31\text{nm}$. According to the crystallinity of sample (44%), the averaged lamellar thickness in MC-PE then is $\sim 14\text{nm}$, which is close to that in SC-PE.

References

[Abragam 61] A. Abragam. The Principles of Nuclear Magnetism. Oxford University Press Inc., Oxford (1961).

[Adams 86] W. Wade Adams, D. Yang, L. Thomas Edwin. Direct visualization of microstructural deformation processes in polyethylene. *Journal of Materials Science* **V21**(7), 2239–2253 (1986).

[Axelson 83] D. E. Axelson, L. Mandelkern, R. Popli, P. Mathieu. C-13 Nmr of Polyethylenes - Correlation of the Crystalline Component T1 with Structure. *Journal of Polymer Science Part B-Polymer Physics* **21**(11), 2319–2335 (1983).

[Axelson 85] D. E. Axelson, K. E. Russell. Characterization of polymers by means of ^{13}C NMR spectroscopy : (a) Morphology by Solid-State NMR (b) End-Group Studies. *Progress in Polymer Science* **11**(3), 221–282 (1985).

[Baker 01] A. M. E. Baker, A. H. Windle. Evidence for a partially ordered component in polyethylene from wide-angle X-ray diffraction. *Polymer* **42**(2), 667–680 (2001).

[Balijepalli 98] S. Balijepalli, G. C. Rutledge. Molecular simulation of the intercrystalline phase of chain molecules. *Journal of Chemical Physics* **109**(16), 6523–6526 (1998).

[Berger 03] L. Berger, H. H. Kausch, C. J. G. Plummer. Structure and deformation mechanisms in UHMWPE-fibres. *Polymer* **44**(19), 5877–5884 (2003).

[Billmeyer 84] Fred W. Billmeyer. Textbook of Polymer Science. Wiley, New York, 3rd. edition (1984).

[Bloch 46] F. Bloch. Nuclear Induction. *Physical Review* **70**(7-8), 460 (1946).

[Chen 92] Qun Chen, Takeyoshi Yamada, Hiromichi Kurosu, Isao Ando, Takeshi Shiono, Yoshiharu Doi. Dynamic study of the noncrystalline phase of ^{13}C-labeled polyethylene by variable-temperature ^{13}C CP/MAS NMR spectroscopy. *Journal of Polymer Science Part B-Polymer Physics* **30**(6), 591–601 (1992).

[Cheng 94] Jinlong Cheng, Matilda Fone, Vijay N. Reddy, Kenneth B. Schwartz, Howard P. Fisher, Bernhard Wunderlich. Identification and quantitative analysis of the intermediate phase in a linear high-density polyethylene. *Journal of Polymer Science Part B-Polymer Physics* **32**(16), 2683–2693 (1994).

[Chodák 98] I. Chodák. High modulus polyethylene fibres: preparation, properties and modification by crosslinking. *Progress in Polymer Science* **23**(8), 1409–1442 (1998).

[Chuah 86] Hoe Hin Chuah, J. S. Lin, Roger S. Porter. On deformation of polyethylene: the question of melting and recrystallization. *Macromolecules* **19**, 2732–2736 (1986).

[Corbeij-Kurel 01] Lada Corbeij-Kurelec. *Chain Mobility in Polymer System: On the Borderline between Solid and Melt*. Dissertation, Technische Universiteit Eindhoven (2001).

[Crist 95] B. Crist. The Ultimate Strength and Stiffness of Polymers. *Annual Review of Materials Science* **25**(1), 295–323 (1995).

[Di Marzio 84] E. A. Di Marzio. A simple explaination of the polymer collapse transition: the (6/5)ths and the (2/3)rds laws. *Macromolecules* **17**, 969–971 (1984).

[Doi 86] M Doi, S F Edwards. The Theory of Polymer Dynamics. Oxford University Press, Oxford (1986).

[Duer 04] M. J. Duer. Introduction to Solid-State NMR Spectroscopy. Blackwell, Oxford (2004).

[Earl 79] W. L. Earl, D. L. Vanderhart. Observations in Solid Polyethylenes by Carbon-13 Nuclear Magnetic Resonance with Magic Angle Sample Spinning. *Macromolecules* **12**, 762–767 (1979).

[Eden 03] Mattias Eden. Computer simulations in solid-state NMR. III. Powder averaging. *Concepts in Magnetic Resonance Part A* **18A**(1), 24–55 (2003).

[Edzes 84] H. T. Edzes, Jan P. C. Bernards. Two-dimensional exchange NMR in static powders: interchain ^{13}C spin exchange in crystalline polyethylene. *JACS* **106**, 1515–1517 (1984).

[Ernst 65] R. R. Ernst, W. A. Anderson. Sensitivity Enhancement in Magnetic Resonance. II. Investigation of Intermediate Passage Conditions. *Review of Scientific Instruments* **36**(12), 1696–1706 (1965).

[Ernst 66] R. R. Ernst. Sensitivity Enhancement in Magnetic Resonance. *Advances in Magnetic and Optical Resonance* **2**, 1 (1966).

[Ernst 87] R. R. Ernst, G. Bodenhausen, A. Wokaun. Principles of Nuclear Magnetic Resonance in One and Two Dimensions. Oxford University Press Inc., Oxford (1987).

[Fischbach 03] I. Fischbach. *Supermolecular order and dynamics of discotic materials studied by solid-state NMR recoupling methods*. Dissertation, Johannes Gutenberg University (2003).

[Flory 53] P. J. Flory. Principle of Polymer Chemistry. Cornell University Press, New York (1953).

[Flory 62] P. J. Flory. On the Morphology of the Crystalline State in Polymers. *J. Am. Chem. Soc.* **84**(15), 2857–2867 (1962).

[Flory 84] P. J. Flory, D. Y. Yoon, K. A. Dill. The Interphase in Lamellar Semicrystalline Polymers. *Macromolecules* **17**(4), 862–868 (1984).

[Frank 79] F. C. Frank. General Introduction. *Faraday Discuss. Chem. Soc.* **68**, 7 (1979).

[Gautam 00] S. Gautam, S. Balijepalli, G. C. Rutledge. Molecular simulations of the interlamellar phase in polymers: Effect of chain tilt. *Macromolecules* **33**(24), 9136–9145 (2000).

[Gedde 04] Ulf W. Gedde, Alessandro Mattozzi. Polyethylene Morphology. *Advances in Polymer Science* **169**, 29–73 (2004).

[Govaert 92] L. E. Govaert, P. J. Lemstra. Deformation behavior of oriented UHMWPE fibers. *Colloid & Polymer Science* **V270**(5), 455–464 (1992).

[Grubb 92] David T. Grubb, Keshav Prasad. High-modulus polyethylene fiber structure as shown by x-ray diffraction. *Macromolecules* **25**(18), 4575–4582. (1992).

[Gullion 89] Terry Gullion, Jacob Schaefer. Rotational-echo double-resonance NMR. *Journal of Magnetic Resonance (1969)* **81**(1), 196–200 (1989).

[Haeberlen 68] U. Haeberlen, J. S. Waugh. Coherent Averaging Effects in Magnetic Resonance. *Physical Review* **175**(2), 453–467 (1968).

[Hartmann 62] S. R. Hartmann, E. L. Hahn. Nuclear Double Resonance in Rotating Frame. *Physical Review* **128**(5), 2042–2053 (1962).

[Hoffman 83] J. D. Hoffman. Regime III crystallization in melt-crystallized polymers: The variable cluster model of chain folding. *Polymer* **24**, 3–26 (1983).

[Holland-Morit 81] K. Holland-Moritz, K. Van Werden. FTIR-spectroscopic studies on polyethylene during elongation. *Die Makromolekulare Chemie* **182**(2), 651–655 (1981).

[Hu 99a] W. G. Hu, C. Boeffel, K. Schmidt-Rohr. Chain Flips in Polyethylene Crystallites and Fibers Characterized by Dipolar ^{13}C NMR. *Macromolecules* **32**(5), 1611–1619 (1999).

[Hu 99b] W. G. Hu, K. Schmidt-Rohr. Polymer ultradrawability: the crucial role of alpha-relaxation chain mobility in the crystallites. *Acta Polymerica* **50**(8), 271–285 (1999).

[Hu 00] W. G. Hu, K. Schmidt-Rohr. Characterization of ultradrawn polyethylene fibers by NMR: crystallinity, domain sizes and a highly mobile second amorphous phase. *Polymer* **41**(8), 2979–2987 (2000).

[Karacan 06] Ismail Karacan. Molecular structure and orientation of gel-spun polyethylene fibers. *Journal of Applied Polymer Science* **101**(3), 1317–1333 (2006).

[Kitamaru 77] R. Kitamaru, F. Horii, S. H. Hyon. Proton Magnetic-Resonance Studies of Phase Structure of Bulk-Crystallized Linear Polyethylene. *Journal of Polymer Science Part B-Polymer Physics* **15**(5), 821–836 (1977).

[Kitamaru 86] Ryozo Kitamaru, Fumitaka Horii, Koichi Murayama. Phase structure of lamellar crystalline polyethylene by solid-state high-resolution carbon-13 NMR detection of the crystalline-amorphous interphase. *Macromolecules* **19**(3), 636–643 (1986).

[Klein 02] P. G. Klein, M. A. N. Driver. Chain Diffusion in Ultralong n-Alkane Crystals Studied by ^{13}C NMR. *Macromolecules* **35**(17), 6598–6612 (2002).

[Klimke 06] Katja Klimke. *Optimised Polyolefin Branch Quantification by ^{13}C NMR Spectroscopy*. Dissertation, Johannes Gutenberg University (2006).

[Lagaron 99] J. M. Lagaron, N. M. Dixon, W. Reed, J. M. Pastor, B. J. Kip. Morphological characterisation of the crystalline structure of cold-drawn HDPE used as a model material for the environmental stress cracking (ESC) phenomenon. *Polymer* **40**(10), 2569–2586 (1999).

[Lagaron 00] J. M. Lagaron, S. Lopez-Quintana, J. C. Rodriguez-Cabello, J. C. Merino, J. M. Pastor. Comparative study of the crystalline morphology present in isotropic and uniaxially stretched ”conventional” and metallocene polyethylenes. *Polymer* **41**(8), 2999–3010 (2000).

[Lee 65] Moses Lee, Walter I. Goldburg. Nuclear-Magnetic-Resonance Line Narrowing by a Rotating rf Field. *Physical Review A* **140**, 1261–1271 (1965).

[Levitt 01] Malcolm H. Levitt. Spin Dynamics: Basics of Nuclear Magnetic Resonance. John Wiley & Sons, New York, 1st. edition (2001).

[Levitt 02] M. H. Levitt. Encyclopedia of Nuclear Magnetic Resonance, Volume 9 (*Advances in NMR*). John Wiley & Sons, Ltd., Chichester (2002).

[Liu 02] S. F. Liu, J. D. Mao, K. Schmidt-Rohr. A robust technique for two-dimensional separation of undistorted chemical-shift anisotropy powder

patterns in magic-angle-spinning NMR. *Journal of Magnetic Resonance* **155**(1), 15–28 (2002).

[Mandelkern 64] L Mandelkern. Crystallization in Polymers. McGraw-Hill, New York (1964).

[Mandelkern 83] L Mandelkern. An Introduction to Macromolecules. Springer-Verlag, New York (1983).

[Mandelkern 85] L Mandelkern. The Relation between Structure and Properties of Crystalline Polymers. *Polymer J.* **17**, 337–350 (1985).

[Mandelkern 90] L. Mandelkern, R. G. Alamo, M. A. Kennedy. Interphase Thickness of Linear Polyethylene. *Macromolecules* **23**(21), 4721–4723 (1990).

[Mansfield 78] Marc Mansfield, Richard H. Boyd. Molecular motions, the alpha relaxation, and chain transport in polyethylene crystals. *Journal of Polymer Science Part B-Polymer Physics* **16**(7), 1227–1252 (1978).

[Matsuo 03] Masaru Matsuo, Yuezhen Bin, Chunye Xu, Lin Ma, Takahiko Nakaoki, Takenori Suzuki. Relaxation mechanism in several kinds of polyethylene estimated by dynamic mechanical measurements, positron annihilation, X-ray and ^{13}C solid-state NMR. *Polymer* **44**(15), 4325–4340 (2003).

[Mehring 83] M. Mehring. High Resolution NMR of Solids. Springer-Verlag, Berlin (1983).

[Meier 92] B. H. Meier. Cross polarization under fast magic angle spinning: thermodynamical considerations. *Chemical Physics Letters* **188**(3-4), 201–207 (1992).

[Mowery 06] D. M. Mowery, D. J. Harris, K. Schmidt-Rohr. Characterization of a Major Fraction of Disordered All-Trans Chains in Cold-Drawn High-Density

Polyethylene by Solid-State NMR. *Macromolecules* **39**(8), 2856–2865 (2006).

[Nakamae 91] K. Nakamae, T. Nishino, H. Ohkubo. Elastic-Modulus of Crystalline Regions of Polyethylene with Different Microstructures - Experimental Proof of Homogeneous Stress-Distribution. *Journal of Macromolecular Science-Physics* **B30**(1-2), 1–23 (1991).

[Neuhaus 89] D Neuhaus, M. P. Williamson. The Nuclear Overhauser Effect and Conformational Analysis. VCH publishers, New York (1989).

[Organ 85] S. J. Organ, A. Keller. Solution crystallization of polyethylene at high temperatures. *Journal of Materials Science* **20**(5), 1571–1585 (1985).

[Painter 77] P. C. Painter, J. Havens, W. W. Hart, J. L. Koenig. A fourier transform infrared spectroscopic investigation of polyethylene single crystals. II. Fine structure of the CH_2 rocking mode. *Journal of Polymer Science: Polymer Physics Edition* **15**(7), 1237–1249 (1977).

[Peterlin 71] A. Peterlin. Molecular model of drawing polyethylene and polypropylene. *Journal of Materials Science* **V6**(6), 490–508 (1971).

[Petermann 79] J. Petermann, W. Kluge, H. Gleiter. Electron microscopic investigation of the molecular mechanism of plastic deformation of polyethylene and isotactic polystyrene crystals. *Journal of Polymer Science: Polymer Physics Edition* **17**(6), 1043–1051 (1979).

[Popli 84] R. Popli, M. Glotin, L. Mandelkern, R. S. Benson. Dynamic mechanical studies of alpha and beta relaxations of polyethylenes. *Journal of Polymer Science Part B-Polymer Physics* **22**(3), 407–448 (1984).

[Porter 66] Roger S. Porter, Julian F. Johnson. The Entanglement Concept in Polymer Systems. *Chem. Rev.* **66**(1), 1–27 (1966).

[Purcell 46] E. M. Purcell, H. C. Torrey, R. V. Pound. Resonance Absorption by Nuclear Magnetic Moments in a Solid. *Physical Review* **69**(1-2), 37 (1946).

[Rastogi 97] S. Rastogi, A. B. Spoelstra, J. G. P. Goossens, P. J. Lemstra. Chain Mobility in Polymer Systems: on the Borderline between Solid and Melt. 1. Lamellar Doubling during Annealing of Polyethylene. *Macromolecules* **30**(25), 7880–7889 (1997).

[Rastogi 05] S. Rastogi, A. E. Terry. Morphological implications of the interphase bridging crystalline and amorphous regions in semi-crystalline polymers. *Advances in Polymer Science* **180**, 161–194 (2005).

[Reneker 62] D. H. Reneker. Point dislocations in crystals of high polymer molecules. *Journal of Polymer Science* **59**(168), S39–S42 (1962).

[Robertson 65] Richard E. Robertson. Polymer Order and Polymer Density. *J. Phys. Chem.* **69**(5), 1575–1578 (1965).

[Saalwachter 02] K. Saalwachter, I. Schnell. REDOR-based heteronuclear dipolar correlation experiments in multi-spin systems: Rotor-encoding, directing, and multiple distance and angle determination. *Solid State Nuclear Magnetic Resonance* **22**(2-3), 154–187 (2002).

[Schmidt-Rohr 91] K. Schmidt-Rohr, H. W. Spiess. Chain Diffusion between Crystalline and Amorphous Regions in Polyethylene Detected by 2d Exchange C-13 Nmr. *Macromolecules* **24**(19), 5288–5293 (1991).

[Schmidt-Rohr 94] K. Schmidt-Rohr, H. W. Spiess. Multidimensional Solid-State NMR and Polymers. Academic Press, London (1994).

[Schnell 01a] I. Schnell, A. Watts, H. W. Spiess. Double-quantum double-quantum MAS exchange NMR spectroscopy: Dipolar-coupled spin pairs as probes

for slow molecular dynamics. *Journal of Magnetic Resonance* **149**(1), 90–102 (2001).

[Schnell 01b] Ingo Schnell, Hans Wolfgang Spiess. High-Resolution ^{1}H NMR Spectroscopy in the Solid State: Very Fast Sample Rotation and Multiple-Quantum Coherences. *Journal of Magnetic Resonance* **151**(2), 153–227 (2001).

[Slichter 90] C. P. Slichter. Springer Series in Solid-State Sciences, Volume 1 (*Principles of Magnetic Resonance*). Springer-Verlag, Berlin, 3rd. edition (1990).

[Smith 79] Paul Smith, Piet J. Lemstra. Ultrahigh-strength polyethylene filaments by solution spinning/drawing: 2. Influence of solvent on the drawability. *Macromolecular Chemistry and Physics* **180**(12), 2983–2986 (1979).

[Smith 80] P. Smith, P. J. Lemstra. Ultrahigh Strength Polyethylene Filaments by Solution Spinning-Drawing .3. Influence of Drawing Temperature. *Polymer* **21**(11), 1341–1343 (1980).

[Smith 81] P. Smith, P. J. Lemstra, J. P. L. Pijpers, A. M. Kiel. Ultra-drawing of high molecular weight polyethylene cast from solution. *Colloid & Polymer Science* **259**(11), 1070–1080 (1981).

[Sperling 92] L. H. Sperling. Introduction to physical polymer science. Wiley, New York, 2nd. edition (1992).

[Spiess 78] H. W. Spiess. NMR basic principles and progress, Volume 15 (*Dynamic NMR spectroscopy*). Springer-Verlag, Berlin (1978).

[Strobl 78] G. B. Strobl. Molekulare Deutung der Umwandlungswaermen bei den Modifikationsuebergaengen des n-Tritriacontans. *Colloid & Polymer Science* **V256**(5), 427–445 (1978).

[Strobl 97] G. Strobl. The Physics of Polymers. Springer-Verlag, Berlin, 2nd. edition (1997).

[Syi 88] Jia-Lin Syi, Marc L. Mansfield. Soliton model of the crystalline [alpha] relaxation. *Polymer* **29**(6), 987–997 (1988).

[Tanabe 86] Y. Tanabe, G. R. Strobl, E. W. Fischer. Surface melting in melt-crystallized linear polyethylene. *Polymer* **27**, 1147–1153 (1986).

[Torchia 78] D. A. Torchia. The measurement of proton-enhanced carbon-13 T1 values by a method which suppresses artifacts. *Journal of Magnetic Resonance* **30**(3), 613–616 (1978).

[Uehara 00] H. Uehara, T. Yamanobe, T. Komoto. Relationship between solid-state molecular motion and morphology for ultrahigh molecular weight polyethylene crystallized under different conditions. *Macromolecules* **33**(13), 4861–4870 (2000).

[Ungar 01] G. Ungar, X. b Zeng. Learning Polymer Crystallization with the Aid of Linear, Branched and Cyclic Model Compounds. *Chem. Rev.* **101**(12), 4157–4188 (2001).

[Van Aerle 88] N. A. J. M. Van Aerle, A. W. M. Braam. A structural study on solid state drawing of solution-crystallized ultra-high molecular weight polyethylene. *Journal of Materials Science* **23**, 4429–4436 (1988).

[Van Aerle 89] N. A. J. M. Van Aerle, A. W. M. Braam. A real-time drawing study on solution-crystallized UHMW-polyethylene - comparison with conventional x-ray results. *Colloid & Polymer Science* **V267**(4), 323–329 (1989).

[Vanderhart 81] D. L. Vanderhart. Influence of molecular packing on solid-state ^{13}C chemical shifts: The n-alkanes. *Journal of Magnetic Resonance* **44**(1), 117–125 (1981).

[VanderHart 84] D. L. VanderHart, F. Khoury. Quantitative determination of the monoclinic crystalline phase content in polyethylene by ^{13}C n.m.r. *Polymer* **25**(11), 1589–1599 (1984).

[Vinogradov 99] Elena Vinogradov, P. K. Madhu, Shimon Vega. High-resolution proton solid-state NMR spectroscopy by phase-modulated Lee-Goldburg experiment. *Chemical Physics Letters* **314**(5-6), 443–450 (1999).

[Wang 91] Li Hui Wang, Porter Roger S., Stidham Howard D., Hsu Shaw L. Raman spectroscopic characterization of the morphology of polyethylene reactor powder. *Macromolecules* **24**, 5535–5538 (1991).

[Ward 84] I. M. Ward, M. A. Wilding. Creep behavior of ultrahigh-modulus polyethylene: Influence of draw ratio and polymer composition. *Journal of Polymer Science: Polymer Physics Edition* **22**(4), 561–575 (1984).

[Ward 88] IM Ward. Developments in Oriented Polymers. Elsevier, New York, 2nd. edition (1988).

[Wittmann 85] J. C. Wittmann, B. Lotz. Polymer decoration: The orientation of polymer folds as revealed by the crystallization of polymer vapors. *Journal of Polymer Science Part B-Polymer Physics* **23**(1), 205–226 (1985).

[Wu 92] W. Wu, G. D. Wignall, L. Mandelkern. A SANS study of the plastic deformation mechanism in polyethylene. *Polymer* **33**(19), 4137–4140 (1992).